Titre: Title:	Advancements in Multimodal Endoscopic Optical Coherence Tomography: Novel Hardware, Software, and Optical Strategies
Auteur: Author:	Xavier Attendu
Date:	2022
Type:	Mémoire ou thèse / Dissertation or Thesis
Référence: Citation:	Attendu, X. (2022). Advancements in Multimodal Endoscopic Optical Coherence Tomography: Novel Hardware, Software, and Optical Strategies [Thèse de doctorat, Polytechnique Montréal]. PolyPublie. https://publications.polymtl.ca/10561/

URL de PolyPublie: PolyPublie URL:	https://publications.polymtl.ca/10561/
Directeurs de recherche: Advisors:	Caroline Boudoux, & Ton Van Leeuwen
Programme: Program:	Génie physique

POLYTECHNIQUE MONTRÉAL
affiliée à l'Université de Montréal

Advancements in Multimodal Endoscopic Optical Coherence Tomography: Novel Hardware, Software, and Optical Strategies

XAVIER ATTENDU
Département de génie physique

Thèse présentée en vue de l'obtention du diplôme de *Philosophiæ Doctor*
Génie physique

Septembre 2022

POLYTECHNIQUE MONTRÉAL
affiliée à l'Université de Montréal

Cette thèse intitulée :

Advancements in Multimodal Endoscopic Optical Coherence Tomography: Novel Hardware, Software, and Optical Strategies

présentée par **Xavier ATTENDU**
en vue de l'obtention du diplôme de *Philosophiæ Doctor*
a été dûment acceptée par le jury d'examen constitué de :

Frédéric LEBLOND, président
Caroline BOUDOUX, membre et directrice de recherche
Ton VAN LEEUWEN, membre et codirecteur de recherche
Lucien WEISS, membre
Adrien E. DESJARDINS, membre externe

DEDICATION

"In theory, there is no difference between theory and practice.
But in practice, there is."
– Benjamin Brewster 1882

To my family and friends.

ACKNOWLEDGEMENTS

Many years ago, back in high school, my biology teacher, Mr. Marsh, wrote a note in my yearbook: "What is the sound of one hand clapping?" I guessed it implied something about teamwork and collaboration at the time, but I did not think much of it. However, I have often thought about this quote/riddle throughout my graduate studies and doctoral research. Each time I have found a new appreciation for the sentiment it expresses, which culminated during the composition of this thesis. It is very difficult to imagine getting this far without the incredible support of those listed below. As such, I would like to acknowledge here the people that contributed, in one way or another, to the completion of my Ph.D.

First and foremost, I would like to thank my Ph.D. advisor Caroline Boudoux. Your passion for science, your ambition, and your unrelenting enthusiasm have been an inspiration from day 1. Along with your infectious drive, your great generosity created many invaluable opportunities for both my professional and personal development. Your guidance has shaped me as a scientist, teacher, and mentor. I am very proud of what I achieved under your tutelage and glad that we will still be able to work together towards even greater things in the future.

I would also like to thank my Dutch co-supervisors Ton van Leeuwen and Dirk Faber. I remember how my move to Amsterdam was decided in no more than 15 minutes during a discussion at Photonics West. It felt like a very rapid decision at the time, but I couldn't have asked for a better outcome. Being a part of your team these last few years has been a privilege. You have continuously guided, challenged, and supported me with your remarkable scientific insights and incredible kindness. Your door has always been open when I come up with something new, and, just as importantly, you have kept me in check when I get distracted with crazy side projects. I would be hard-pressed to imagine a better work environment than the one you have created. I am delighted to carry on with our work together in the coming years.

I also want to thank the extended LODI family or *Boudoux Crew* as we have started to call ourselves. To the old guard, Fouzi, Wendy-Julie, Etienne, Kathy, and Mathias: our time at the LODI only overlapped shortly, but you were always kind and helpful. You also set the very high standards for the next generation, and I hope my work lives up to them. Mathias thank you for being there to guide me at the beginning of my graduate studies and bearing with the million and a half questions I had for you. Your patience and helpfulness are something I will always try to emulate when guiding younger students. Thomas, Robin, Martin, Raphaël, Édith, Khaliun, Simon, and Rodrigo, I am lucky to call you both friends and colleagues. The time spent together at the LODI was/is always scientifically stimulating and plain good fun. I am excited to see all the remarkable things you will do and hope that I will still get to be a part of them. To all the students that passed through the LODI through the years that I had the privilege to supervise or assist, including Camille, Joannie, Billie, Marie-Hélène, Marie-Ève, Gianmarco, Chloe, Aude, Gabriel, Émilie, and Claudia, thank you. Your hard work was essential to many of the results presented here. Robin, a special nod to you. All of the work presented here is the continuation of our very first paper together. It is a little crazy to see how far it has come. Finally, I would like to acknowledge Prof. Nicolas Godbout, Mikaël Leduc, Lucas Majeau, and Xavier Daxhelet for their expertise and help in all fiber-related matters.

There are equally many people to acknowledge and thank in the Amsterdam group. Abel, you are one of the main reasons I came to Amsterdam. For that, I will always be grateful. Thank you also for the great work together and the fun times outside of the office. Thanks also to my very first office mates, Xu and Anouk, for welcoming me at the beginning of my time in Amsterdam. Anouk, I look forward to all the fantastic projects we will accomplish together. Roosje, thank you for being an awesome office buddy and working on our paper together. It was a blast every day, even when I was getting scolded. To Linda, Leah, Mitra, Anas, Vasudha, Jacob, Lionel, Arjan, Edwin, Dick, Carla, Judith, Richard, Maurice, Martijn, and the rest of the BMEP group (past and present), you are all wonderful friends and colleagues. It is a privilege to see and work with you every day. A special thank you to Paul and Niels. You were both instrumental in the success of several projects, and I would not be handing in this thesis if it was not for both of you. Just as importantly, I am so happy that we share the same passion for all manner of engineering problems. It has been a delight to tackle them all with the two of you. How well our little trio works together is something I value tremendously. I look forward to building all the things together in the future.

Thank you also to my friends for supporting me throughout this whole process. Your kind words, silly jokes, and shared adventures have given me all the support and motivation I needed to push through any hard times. Gwen, Caro, PJ, Chuck, Dion, Éric, Matt, Max, Tony, Franky vous serez ravis de savoir que je n'ai toujours pas trouvé de "vraie job" et que je compte encore vivre pendant un bon moment de vos impôts. Donc un grand merci pour ça! Blagues à part, merci de toujours être là, même lorsque nous ne nous voyons pas pour des mois. Vous me manquez tous beaucoup lorsque je ne suis pas au Québec et je n'ai pas abandonné espoir de faire migrer le groupe en Europe éventuellement. Tim and Alex, you guys are probably my oldest friends and you've seen me work towards this point since I was a nerdy highschool kid. Thank you for being there for the entire journey and all the fun times along the way. Lis and Gabi (and Maxi) thank you for all the walks in the forest together this last year, and for letting me vent on numerous occasions (and venting together). You undoubtedly helped me maintain my mental health and my sanity on many occasions. En tenslotte, lieve Wil, bedankt voor onze Nederlandse lessen. Ze waren ontzettend leuk, altijd gezellig, en een hoogtepunt van mijn week.

À ma famille québécoise: merci de m'avoir acceuilli à Montréal il y a déjà quelques années. Les dîners en famille et autres bons moments ont rendu mon temps à Montréal mémorable. Louise, Stéphane et Alex un grand merci à vous trois pour vous être si bien occupé de moi pendant toutes ces années. JM, merci de m'avoir aiguillé sur le chemin du génie physique. Cela à sans aucun doute été une des meilleures décisions de ma vie. To my dutch family, Tim, Lars, Martin and Jolanda (and Buster): thank you for all your support during our move to Amsterdam and especially in the last few months. I don't think I would have survived the rush leading up to handing in this thesis without you.

À mes parents et à mon frère: merci pour votre support inconditionnel. Pierre et Joelle, j'ai beaucoup de difficulté à trouver les mots qui expriment ma gratitude envers vous... Tous mes accomplissements petits ou grands sont grâce aux opportunités que vous m'avez offertes tout au long de ma vie. Merci pour chacune d'entre elles et d'être des modèles d'intelligence, de persévérance et de gentillesse. Louis je suis impressioné par les choses que tu accomplis tous les jours. Merci de toujours être la pour moi et de mettre la barre si haute. Je m'attends néanmoins à ce que tu m'appelles Dr. Xavier pour les quelques mois à venir!

And finally to Claire (although this applies to Sam too): thank you for being there every step of the way. Thank you for being my rock and the person I can always come home to. The love and happiness you give me every day are what allow me to pursue my passions to the fullest. This thesis is a testament to that and would not have been possible without you. You are the light of my life and I can't wait to see all the incredible things the future holds for us.

RÉSUMÉ

Le cancer de l'oesophage (CO) est une maladie dangereuse, principalement en raison de sa nature asymptomatique jusqu'à un stade avancé de son développement. Actuellement, la vidéo-endoscopie en lumière blanche combinée à des biopsies aléatoires constituent l'étalon-or pour la détection du CO. Cependant, ces méthodes sont invasives, manquent de sensibilité et ne sont pas rentables. La tomographie par cohérence optique (OCT) est une technique interférométrique qui permet d'obtenir une imagerie 3D de tissus biologiques en haute résolution et en profondeur. Son implémentation endoscopique est très prometteuse pour la détection précoce des CO. Cependant, à ce jour, l'OCT endoscopique n'a jamais atteint les performances requises pour remplacer complètement les protocoles standard de vidéo-endoscopie et biopsies aléatoires. Dans cette thèse doctorale, nous émettons l'hypothèse que la combinaison de l'OCT à des techniques d'imagerie spectroscopique, offrant un sensibilité accrue à la composition moléculaire des échantillons biologiques, pourrait améliorer le pouvoir diagnostique pour la détection précoce du cancer de l'oesophage.

Nous présentons tout d'abord une analyse critique de la littérature qui expose le principe de fonctionnement fondamental de l'OCT et de l'imagerie spectroscopique. Nous examinons ensuite les méthodes existantes pour augmenter le contraste de l'OCT, par le biais d'extensions fonctionnelles ou de combinaisons avec d'autres techniques et nous étudions leur compatibilité avec le format endoscopique. Nous présentons la fibre à double gaine (DCF) et les coupleurs de fibre à double gaine (DCFC), des technologies permettant le développement de systèmes multimodaux. De plus, ces technologies fibrées ont un haut potential de miniaturisation et pourraient être adaptées dans des sondes endoscopiques. La fibre DCF possède un coeur monomode (SM) et une gaine interne multimode (MM) qui peuvent chacun transporter un signal optique. L'on peut accéder à ces deux canaux éfficacement par le biais d'un DCFC, qui permet de combiner ou séparer les signaux. Dans les systèmes OCT multimodaux à base de DCFC, l'imagerie OCT est réalisée par le coeur tandis que l'imagerie avec la modalité supplémentaire est réalisée pas la gaine interne.

Dans la première partie de cette thèse, nous présentons trois systèmes qui combinent l'OCT avec différentes variantes de l'imagerie spectroscopique, en utilisant de la DCF et des DCFC. Ces systèmes sont progressivement de plus en plus compatibles avec l'imagerie dans un milieu clinique. Le premier système combine l'OCT avec l'imagerie hyperspectrale (HSI) en utilisant une source externe à large bande pour illuminer l'échantillon et en

collectant le signal réfléchi à travers la gaine interne pour une analyse spectroscopique. Ce système a été la première démonstration de la combinaison de l'OCT et de l'HSI dans une seule fibre. Cependant, ce système était limité par une faible vitesse d'imagerie et une faible résolution latérale pour l'HSI. Dans le second système, nous avons utilisé plusieurs lasers à longueur d'onde unique pour réaliser une imagerie multispectrale (MSI). De plus, ces multiples longueurs d'onde ont été multiplexées dans le domaine fréquentiel et combinées au signal OCT dans le coeur de la DCF avec un multiplexeur par division en longueur d'onde (WDM) fibré. Ce multiplexage en fréquence a permis une imagerie simultanée à grande vitesse (fréquence d'acquisition de 16 kHz) avec les deux modalités, garantissant ainsi leur co-localisation dans l'espace. L'illumination interne a également permis d'améliorer considérablement la résolution latérale de l'imagerie multispectrale. Cependant, ceci a également mis en évidence certains défis liés aux rétro-réflexions et aux aberrations chromatiques associées à l'optique réfractive, ainsi que des distorsions du signal OCT associées au WDM. Dans le troisième système, nous avons développé une tête d'imagerie entièrement réfléchissante pour une imagerie à large bande achromatique et sans rétro-réflexion dans les domaines spectraux du visible (VIS) et du proche infrarouge (NIR). Ce système souffre de la même limitation en vitesse d'imagerie que le premier, mais permet une imagerie à haute résolution pour l'OCT et l'imagerie spectroscopique. Son utilité est d'identifier des caractéristiques spectrales de tissus biologiques à des fins de diagnostic ou de classification.

Dans la deuxième partie de cette thèse, nous présentons deux sondes endoscopiques en format capsule attachée (TCE) développées pour l'imagerie de l'oesophage. La première est basée sur l'utilisation d'une lentille à gradient d'indice (GRIN). Nous avons effectué des simulations optiques pour concevoir le système optique et évaluer les effets dépendant de la longueur d'onde, notamment les décalages focaux et les rétro-réflexions. Il est rapidement devenu évident que les conceptions basées sur les lentilles GRIN étaient peu performantes sur ces deux aspects. Par conséquent, nous ne démontrons que l'imagerie OCT avec ce dispositif. Le deuxième TCE repose exclusivement sur des optiques réfléctives pour la focalisation et le balayage du faisceau. Nous avons d'abord décrit la conception optomécanique, centrée sur l'utilisation d'un miroir ellipsoïdal pour la focalisation, ainsi que les étapes d'assemblage du dispositif. Nous avons ensuite caractérisé les performances et démontré des images préliminaire combinant l'OCT et la spectroscopie de réflectance dans le visible. La conception d'une capsule entièrement réfléchissante est intéressante car elle fonctionne à toutes les longueurs d'onde, ce qui permet de combiner l'OCT avec d'autres modalités que l'imagerie spectroscopique, comme la fluorescence ou le marquage laser.

Dans la troisième partie de cette thèse, nous étudions des algorithmes de calibration et de traitement de données pour l'OCT. Nous présentons d'abord une procédure de calibration simple et robuste pour la linéarisation en nombre d'onde et la compensation de la dispersion, deux étapes critiques du traitement de données OCT. Ce protocole ne nécessite que deux mesures directement sur le dispositif expérimental et est intéressant car le développement du système nécessite des calibrations fréquentes en raison de petites modifications. Le deuxième algorithme est centré sur la suppression de l'artéfact miroir dans l'OCT à plage complète (FR-OCT), qui double effectivement la plage d'imagerie. La FR-OCT sans artéfact est pertinente en OCT endoscopique car le signal associé aux interfaces optiques à l'intérieur de la capsule peut être replié dans la plage d'imagerie. Cela peut réduire la plage d'imagerie utile et dégrader la qualité globale de l'image.

Enfin, nous considérons les liens entre les différents chapitres de cette thèse et évaluons la réalisation des objectifs de recherche, ainsi que les avantages et les limites des méthodologies proposées. Nous constatons que les développements technologiques présentés tout au long de cette thèse font effectivement progresser l'endoscopie multimodale pour l'imagerie de l'oesophage. En particulier, les méthodes proposées favorisent une approche modulaire de la conception de systèmes endoscopiques multimodaux. Dans ce paradigme, le système peut être ajusté ou modifié en changeant les modules d'illumination et de détection sans changer la sonde endoscopique, ce qui peut simplifier transfert des technologies vers la clinique.

ABSTRACT

Esophageal cancer (EC) is a deadly disease, primarily because of its asymptomatic nature until advanced stages in its development. Currently, white light video-endoscopy combined with random biopsies is the gold standard for the detection of EC. However, such methods are invasive and lack sensitivity and cost-effectiveness. Optical coherence tomography (OCT) is an interferometric technique that allows depth-resolved, high-resolution 3D imaging of biological tissue. Its endoscopic implementation for esophageal imaging has shown great promise for the early detection of EC but has, to this day, always fallen short of the required performance to replace video-endoscopy and biopsies outright. We hypothesize that combining OCT with spectroscopic imaging techniques that provide enhanced sensitivity to the molecular composition may enhance diagnostic performance for early esophageal cancer detection.

We first present a critical literature review that outlines the fundamental operating principle of OCT and spectroscopic imaging. We delve into existing methods for expanding OCT contrast through functional extensions or combinations with other techniques and consider their compatibility with endoscopic applications. We present double-clad fiber (DCF) and double-clad fiber couplers (DCFC) as viable candidates for developing fiber-based multimodal systems with the potential for miniaturization into endoscopic devices. DCF possesses a single-mode (SM) core and a multimode (MM) inner-cladding that can each transport complementary optical signals. These two channels may be efficiently accessed through a DCFC, which can combine or separate the signals. In DCF-based multimodal OCT systems, OCT is carried out through the fiber core and the additional modality through the inner cladding.

In the first part of this thesis, we present three systems that combine OCT with different implementations of spectroscopic imaging, using DCF and DCFCs and with progressive levels of compatibility with clinical imaging. The first system combines OCT with hyperspectral imaging (HSI) by utilizing an external broadband source to illuminate the sample and collecting the reflected signal through the inner cladding for spectroscopic analysis. This system was the first demonstration of combined OCT and HSI through a single fiber. However, this implementation suffered from low imaging speed and low lateral resolution for HSI. In the second system, we used multiple single-wavelength lasers to perform multispectral imaging (MSI). Furthermore, the multiple wavelengths of the MSI illumination were multiplexed in the frequency domain and combined with the OCT

signal in the DCF core with a fiber-based wavelength division multiplexer (WDM). This frequency multiplexing allowed high-speed (16 kHz A-line rate) concurrent imaging with both modalities, guaranteeing their co-registration. The internal illumination led to significantly improved lateral resolution for MSI. However, it also highlighted challenges associated with backreflections and chromatic aberrations associated with the refractive optics and distortions in the OCT signal associated with the WDM. In the third benchtop system, we developed an all-reflective scanner head for achromatic and backreflection-free broadband imaging across the visible (VIS) and near-infrared (NIR) spectral ranges. This system suffered from the same slow imaging speed as the first one but enabled high-resolution imaging with both the OCT and spectroscopic imaging channels. Its purpose was to identify spectral features in biological tissue for diagnosis or classification.

In the second part of this thesis, we present two tethered capsule endoscopic probes (TCE) developed for esophageal imaging. The first was based on the use of a gradient-index (GRIN) lens. We performed optical simulations to design the optics and assess the wavelength-dependent effects, including focal shifts and backreflections. It quickly became apparent that GRIN-based designs performed poorly in both these aspects. As such, we only demonstrated OCT imaging with this device. The second TCE relied exclusively on reflective optics for focusing and beam steering. We first outlined the optomechanical design, centered around the use of an ellipsoidal mirror for focusing, as well as the assembly steps of the device. We then characterized its performance and demonstrated preliminary combined imaging with OCT and VIS reflectance spectroscopy. The all-reflective design of the capsule is exciting because it allows operation at all wavelengths, enabling the combination of OCT with other modalities aside from spectroscopic imaging, such as fluorescence or laser marking.

In the third part of this thesis, we investigate algorithms for OCT calibration and data processing. We first presented a simple and robust calibration procedure for k-linearization and dispersion compensation, two critical steps in OCT data processing. This protocol requires only two measurements directly on the experimental setup and is interesting because system development requires frequent calibrations due to small alterations. The second algorithm was centered around removing the mirror artifact in full-range OCT (FR-OCT), which effectively doubles the imaging range. Artifact-free FR-OCT is relevant in endoscopic OCT because the signal associated with optical interfaces inside the endoscope is folded back into the imaging range. This can reduce the useful imaging range and degrade the overall image quality.

Finally, we reflect on the connection between the various chapters of this dissertation and evaluate the completion of the research objectives, as well as the advantages and limitations of the proposed methodologies. We find that the technological development presented throughout this thesis indeed advances multimodal endoscopy for esophageal imaging. In particular, the proposed methods promote a modular approach to the conception of multimodal endoscopic systems. In this paradigm, the system can be fine-tuned or altered with changes to illumination and detection modules without changing the endoscopic probe, which may simplify clinical translation.

TABLE OF CONTENTS

LIST OF TABLES

LIST OF FIGURES

LIST OF SYMBOLS AND ACRONYMS

ADC	analog to digital converter
AFI	autofluorescence imaging
ASIR	age-standardized incidence rate
BE	Barrett's esophagus
CMRR	common mode rejection ratio
DAC	digital to analog converter
DCF	double-clad fiber
DCFC	double-clad fiber coupler
DOCT	Doppler OCT
DOF	depth of focus
EAC	esophageal adenocarcinoma
EC	esophageal cancer
EM	ellipsoidal mirror
ESCC	esophageal squamous cell carcinoma
FD-OCT	fourier domain optical coherence tomography
FOV	field of view
FT	Fourier transform
FWHM	full-width at half-maximum
GERD	gastroesophageal reflux disease
GI	gastro-intestinal
GRIN	gradient index
HGD	high-grade dysplasia
HSI	hyperspectral imaging
JND	just noticeable difference
LGD	low-grade dysplasia
MMF	multimode fiber
MSI	multispectral imaging
MZI	mach-zender interferometer
NIR	near-infrared (~800-2500 nm)
OCT	optical coherence tomography
OCTA	OCT angiography
OFDI	optical frequency domain imaging
OPD	optical path difference

OPL	optical path length
PIC	photonic integrated chip/circuit
PS-OCT	polarization-sensitive OCT
PSF	point-spread function
ROI	region of interest
RSH	reflective scanner head
SBR	signal-to-background ratio
SD-OCT	spectral-domain optical coherence tomography
SFR	single fiber reflectance spectroscopy
SMF	single mode fiber
SNR	signal-to-noise ratio
SOCT	spectroscopic OCT
SS-OCT	swept-source optical coherence tomography
TCE	tethered-capsule endoscope
VIS	visible (~400-800 nm)
WDM	wavelength division multiplexer
WLE	white light endoscopy
WMC	wideband multimode circulator
ZD	zero-delay

LIST OF APPENDICES

CHAPTER 1 INTRODUCTION

1.1 An image is worth a thousand words

Imaging is undeniably a cornerstone of modern clinical practice in diagnosis, treatment planning and monitoring, and surgical guidance. Several well-known techniques include X-ray imaging, computed tomography (CT), magnetic resonance imaging (MRI), and ultrasound imaging (US). These modalities have become ubiquitous in many medical fields for their ability to resolve biological structures in large volumes. However, these methods do not allow analysis on a cellular scale which can be essential for assessing tissue health or identifying pathological tissue in the early stages of development. Optical methods represent a potential solution to this shortcoming. As depicted in Fig. 1.1, various optical techniques offer significant improvements in the achievable resolution, albeit at the cost of reduced penetration depth and total imaging volume. Moreover, many of these optical methods rely on different and complementary contrast mechanisms, enabling varying degrees of molecular sensitivity. Combining two or more techniques can provide insight into various structural, biochemical and physiological properties of the sample under investigation. This complementarity lies at the center of this thesis, in which we attempt to integrate multiple techniques to assess tissue morphology and molecular content simultaneously.

Applying optical imaging to medicine is not a novel idea. Microscopy has been a staple of histopathology since the late 19th century [5]. Many new microscopy techniques have been developed since, powered by the advent of the laser in the 1960s and the subsequent explosion of laser, fiber optic, and detector technologies. In the last two decades, the relative maturity of these technologies, along with advances in optical manufacturing, has opened the door to miniaturizing bulky microscopy systems into small endoscopes for in vivo imaging. As such, rather than bringing the biopsied sample to the histopathologist's microscope, it became possible to bring the microscope to the sample directly, to perform so-called *optical biopsies*. In principle, optical biopsies allow the diagnosis of various pathologies based on optical signals without physically extracting a sample from the tissue.

The concept of optical biopsies presents several crucial advantages over the conventional approach. Firstly, it enables non- or minimally invasive diagnosis and removes the risks associated with the biopsy procedure. Secondly, it bypasses the significant delays and

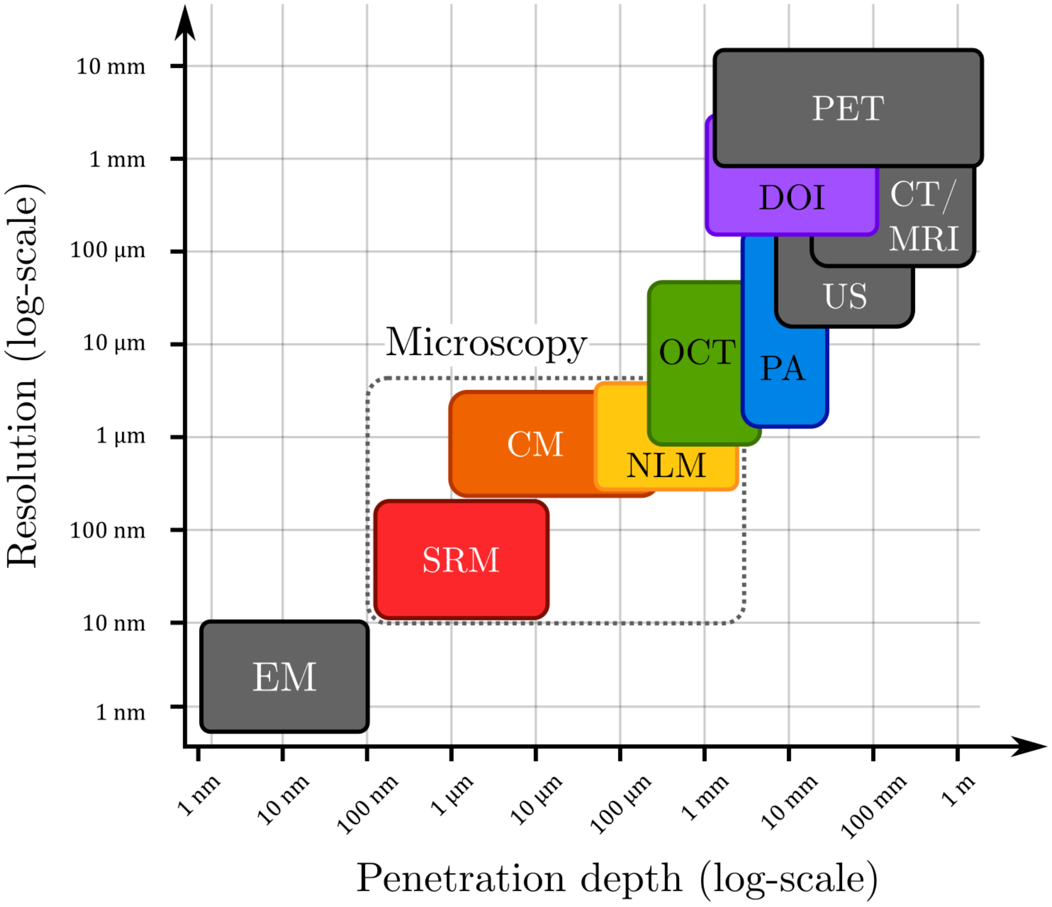

Figure 1.1 Imaging capabilities of various techniques in terms of resolution and penetration depth. Optical methods are indicated by colored boxes, while the other types of techniques are in grey. Depicted modalities include electron microscopy (**EM**), super-resolution microscopy (**SRM**), confocal microscopy (**CM**), non-linear microscopy (**NLM**), optical coherence tomography (**OCT**), photo-acoustic imaging (**PA**), ultrasound imaging (**US**), diffuse optical imaging (**DOI**), computed tomography (**CT**), magnetic resonance imaging (**MRI**), positron emission tomography (**PET**).

costs associated with the extraction, processing, and analysis of conventional biopsies. These advantages may have a tremendous impact on medical practice as they have the potential to allow low-risk and cost-effective screenings for various diseases, which would be impossible with conventional biopsies. Thirdly, through scanning or snapshot imaging, optical methods significantly improve the sampling density, potentially allowing the assessment of the whole organ rather than point measurements. Finally, the high speed of various optical methods enables real-time imaging, which could lead to novel theragnostic protocols, where pathological tissue is detected and treated within the same endoscopic procedure. As such, optical biopsies offer immense advantages over current practices.

However, significant challenges are associated with in vivo endoscopic imaging and obtaining reliable optical biopsies. In vivo imaging gives rise to numerous errors and artifacts such as background signals, motion artifacts, or aberrated and sub-optimal imaging quality compared to microscopy. Moreover, the design and fabrication of reliable devices are challenging due to the high degree of miniaturization and clinical requirements for safety and disinfection/sterilization. Finally, chemical or immunological labeling is complicated due to regulatory restrictions. Extracting sufficient diagnostic information from the intrinsic optical signal is a challenge that has yet to be solved. Moreover, solutions tailored to each disease are necessary and require carefully selecting the utilized optical technique(s). To our knowledge, no single optical method has been shown to reliably obtain in vivo optical biopsies that can replace conventional histopathology as the gold standard for diagnosis.

The core hypothesis of this thesis is that a multimodal approach, where multiple optical techniques are combined into a single device, may provide enhanced diagnostic capabilities compared to a single one. Specifically, we investigate the combination of optical coherence tomography (OCT) with various spectral imaging techniques to assess tissue morphology and molecular content simultaneously. We delve into the engineering challenges associated with fiber-based, multimodal endoscopic imaging and present several promising strategies for system development and data analysis. Furthermore, we propose that such a multimodal endoscopy system may be beneficial for the early detection of esophageal cancer, as discussed in the following section.

1.2 Clinical problem

Esophageal cancer (EC) was chosen as the target pathology for this research for two main reasons. The first (clinical) reason is that esophageal cancer is one of the deadliest cancers worldwide, with an average 5-year survival rate below 20% [6]. This poor prognosis is usually associated with the advanced stages of the ECs at diagnosis due to their asymptomatic nature and the lack of cost-effective screening protocols. As such, there is an unmet clinical need for improved early detection of esophageal cancer. The second (scientific) reason is that the simple, tubular geometry of the esophagus and its relative ease of access are attractive features for the validation of novel endoscopic imaging technologies that enhance the project's feasibility as a whole. Moreover, consequential literature already exists on applying optical methods to esophageal imaging. This existing art may serve as a baseline for demonstrating the benefit of the proposed multimodal approach, which has not been researched as extensively.

1.2.1 Epidemiology of esophageal cancer

EC is the 8th most prevalent cancer worldwide, with 604,000 new cases and 544,000 deaths in 2020 [7]. New cases, deaths, and incidences for several specific geographical locations are reported in Tab. 1.1. There exist two main histological subtypes of EC: esophageal adenocarcinoma (EAC) and esophageal squamous cell carcinoma (ESSC), which are strongly divided by geographic region. ESCC is most prevalent in East- and South-East Asia and sub-Saharan Africa, while EAC is most common in North America and North- and Western Europe [8].

Table 1.1 Esophageal cancer statistics: age-standardized incidence rates (ASIR) per 100k people (male/female), number of cases and deaths for different geographical locations

Location (date)	ASIR (M/F)	New Cases	Deaths	Ref.
Canada (2021)	9.2 / 2.4	2400	2300	[9]
USA (2022)	7.8 / 1.8	20,640	16,410	[10]
World (2020)	9.3 / 3.6	604,100	544,076	[7]

Globally, the incidence of EC has been steadily decreasing over the last decades. However, this is primarily caused by the decrease of ESCCs, which currently account for most cases (85% in 2018) [11]. On the other hand, EAC is rapidly becoming a significant issue in western countries as it has the highest reported rise in incidence of all cancers in the last 40 years [12, 13] increasing by over 700% between 1975 and 2017 [14]. It is expected that these trends will continue in the coming years and that EAC will become the leading form of EC in most western countries (where this is not already the case) and a significant clinical and economic burden. For example, projections for 2030 predict that in the United Kingdom and the Netherlands, over 1 in 100 men will be diagnosed with EAC during their lifetime [15]. Given this growing incidence and the geographical proximity, EAC was selected as the specific target. However, it should be noted that many of the technological developments presented in this thesis can also be applied to detecting ESCCs.

1.2.2 Screening & early diagnosis

As is generally the rule with cancer, early diagnosis of EC leads to significantly improved survival rates. The proportions of cancer stage at diagnosis, as well as the associated 5-year survival rates, are presented in Tab. 1.2 for ECs in general, with EACs following near-identical trends [16, 17]. This data shows that most ECs are only identified later in their development, leading to a low average survival rate. In both histological subtypes, this is primarily due to the diseases' asymptomatic nature until the advanced stages of their development.

Table 1.2 Survival rates by stage at diagnosis for EC in the 2000s decade

SEER stage at diagnosis	proportion [%]	5-yr. survival [%]
in situ	2	78
localized	27	43
regional	34	21
metastatic	37	4

Unfortunately, population screening is not viable due to the low prevalence of EC (and consequently EAC). Currently, screening for EAC is only carried out in at-risk groups. The inclusion criteria for the at-risk group vary by country but generally include persons of advanced age with a family history of EC, suffering from *gastroesophageal reflux disease* (GERD), and diagnosed with *Barrett's esophagus* (BE), a known precursor to EAC. Briefly, GERD is a medical condition where stomach acid frequently passes the esophageal sphincter and flows back into the esophagus, irritating the esophageal lining. Its prevalence is high in Western countries affecting between 10 and 20% of the population [18,19]. BE is defined as the appearance of gastric columnar epithelium and goblet cells in the esophagus [20] and often results from prolonged GERD. However, these risk factors are poor predictors of EAC occurrence, as over 40% of patients diagnosed with EAC never present with GERD [21], and only a minimal subset of patients diagnosed with BE will develop EAC. Indeed, the annual progression risk of BE to EAC is estimated at 0.14% [22,23].

In addition to the low prevalence of the EAC, screening strategies are further disadvantaged by several practical difficulties. Pre-cancerous tissue identification and EAC diagnosis currently rely on white-light video-endoscopy (WLE) and biopsies (targeted and random). However, WLE is ill-suited for detecting and differentiating the microscopic morpho-chemical changes in the esophageal tissue associated with cancerous growths [24]. Such tissue changes include the development of low- and high-grade dysplasia (LGD and HGD, respectively), both pre-cancerous lesions which require histological analysis of biopsied tissue. Because such lesions are difficult to visualize with WLE, endoscopists typically rely on random biopsies at regular intervals along the length of the esophagus to increase the total sampling volume. A common approach is the Seattle protocol, in which random biopsies are performed in four quadrants, every 2 cm of the organ [25, 26]. Nonetheless, the sampling volume remains exceedingly low, on the order of 4-6%, and biopsies are prone to sampling errors [22], due to the localized nature of the target pre-cancerous lesions [27]. Moreover, a high degree of interobserver variability exists when assessing non-dysplastic tissue, LGD, and HGD, which may lead to misdiagnosis [22]. As such, current screening methods by no means guarantee an accurate early diagnosis.

The issues mentioned above, combined with the high procedure costs of esophageal endoscopy, have led many to question the cost-effectiveness of BE surveillance programs. Several studies have attempted to answer this question through modeling, with the majority concluding that surveillance only remained viable with infrequent visits (every 4-5 years) [22, 28, 29]. One UK study even concluded that the costs outweighed the benefits and that surveillance of BE patients was not cost-effective at all [30]. In all cases, these analyses indicate a strong clinical need for a new generation of early diagnosis methods, which provide improved sensitivity, slashed costs, and reduced patient burden.

1.2.3 Novel diagnostic methods for BE, dysplasia, and EAC

In recent years, several optical methods have been proposed to address the limitations of current practice in esophageal endoscopy. Such techniques include high-definition WLE [31], narrow-band imaging (NBI) [32–34], various chromoendoscopies relying on different staining of fluorescent dyes [35,36], single fiber reflectance spectroscopy (SFR) [37], autofluorescence imaging (AFI) [38, 39], and optical coherence tomography (OCT) [40–44]. Each technique has demonstrated promising results in detecting pathological tissue and potentially differentiating various stages of advancement. However, no single modality has demonstrated that it may completely replace the standard WLE and biopsy protocol to this day. While these approaches may be further refined independently, co-registered multimodal imaging may provide the final improvements in diagnostic capabilities necessary to justify replacing current protocols. However, there still exist significant knowledge gaps in terms of technological means to achieve multimodal endoscopic imaging. Some unsolved challenges include accurate co-registration of two or more techniques, high-speed acquisition to enable whole organ imaging and avoid disrupting the clinical workflow, and interpretation of the combined datasets. Moreover, in the context of EC detection, these challenges must be addressed in endoscopic format, requiring advanced opto-mechanical engineering to satisfy the miniaturization requirements.

1.3 Project objectives

The general objective of this project is the development of a multimodal, fiber-based clinical endoscopy system that combines OCT with imaging spectroscopy. This system should address the limitations of the current methods mentioned in the previous sections. It is important to note that this project is centered around the technological developments associated with such a system, not its clinical validation.

Specific objectives

The specific objectives can be broken down into three sections: (1) systems development, (2) endoscopic probes, and (3) algorithms and signal processing.

Specific objective 1: Development of a proof-of-concept, fiber-based, bench-top systems combining OCT and imaging spectroscopy:

1.1. Development and validation of specialty fiber components for combined OCT and VIS/NIR spectral imaging;

1.2. Development of combined acquisition schemes, including hardware and software solutions for data acquisition, synchronization, system control, and real-time data processing;

1.3. Investigation of several candidate techniques for combination with OCT, including hyperspectral imaging (HSI), multispectral imaging (MSI), and single-fiber reflectance spectroscopy (SFR).

Specific objective 2: Development of a multimodal endoscopic probes:

2.1. Design and fabrication of tethered capsule endoscope (TCE) using existing gradient index (GRIN) optical designs;

2.2. Design and fabrication of an all-reflective capsule to enable multimodal imaging without back-reflections and chromatic aberrations.

Specific objective 3: Development of signal processing methods and algorithms for optimized operation and multimode analysis:

3.1. Development of calibration methods for k-linearization and dispersion compensation in OCT systems;

3.2. Development of calibration methods for full-range OCT (FR-OCT) with passive quadrature demultiplexing;

3.3. Study of light-tissue interaction for the accurate extraction of optical properties from non-contact imaging spectroscopy and OCT data.

1.4 Thesis outline

This thesis is split into five major parts. A schematic representation of the structure is presented in Fig. 1.2.

Part 1: Introduction includes the problem statement in **Chapter 1** and the literature review in **Chapter 2**. The literature review presents the technologies at the heart of this dissertation, including optical coherence tomography, hyper- and multispectral imaging, single fiber reflectance spectroscopy, and double-clad fiber technologies. A particular emphasis is placed on OCT, the central imaging modality investigated in this thesis, and the subject of the developed calibration methods.

Part 2: System development pertains to the development of bench-top systems combining OCT with different forms of spectral imaging. This section investigates the advantages and disadvantages of the different techniques and design choices. **Chapter 3** presents the first reported combination of OCT and hyperspectral imaging using a double-clad fiber coupler. In **Chapter 4**, we demonstrate the combination of OCT with frequency-encoded MSI, where MSI is optimized for color reconstruction. In **Chapter 5**, we present OCT combined with broadband, point-scanning, VIS/NIR spectroscopy (dubbed imaging SFR) using an all-reflective scanner head.

Part 3: Endoscopic probes discusses the design, fabrication, and characterization of different endoscopic probes. **Chapter 6** details a preliminary design for a GRIN-based endoscope and elaborates on why they are a poor choice for this project. **Chapter 7** presents the development of an all-reflective tethered capsule endoscope designed for double-clad fiber-based multimodal imaging in the esophagus.

Part 4: Signal processing and analysis showcases the various algorithms used to calibrate, process, and analyze the OCT data obtained with the developed multimodal systems. In **Chapter 8**, we outline a simple calibration procedure for k-linearization and dispersion compensation in OCT. In **Chpater 9**, we present another calibration procedure to remove the mirror artifact from full-range OCT images through passive quadrature demultiplexing.

Part 5: Discussion & Conclusion is comprised of a retrospective analysis of the presented research. In **Chapter 10**, we discuss the key insights and recommendations and the questions that remain unanswered. Finally, in **Chapter 11**, we briefly present future research avenues and provide concluding remarks.

All published scientific articles are incorporated into this thesis as independent chapters. A complete list of scientific contributions is provided in the appendix.

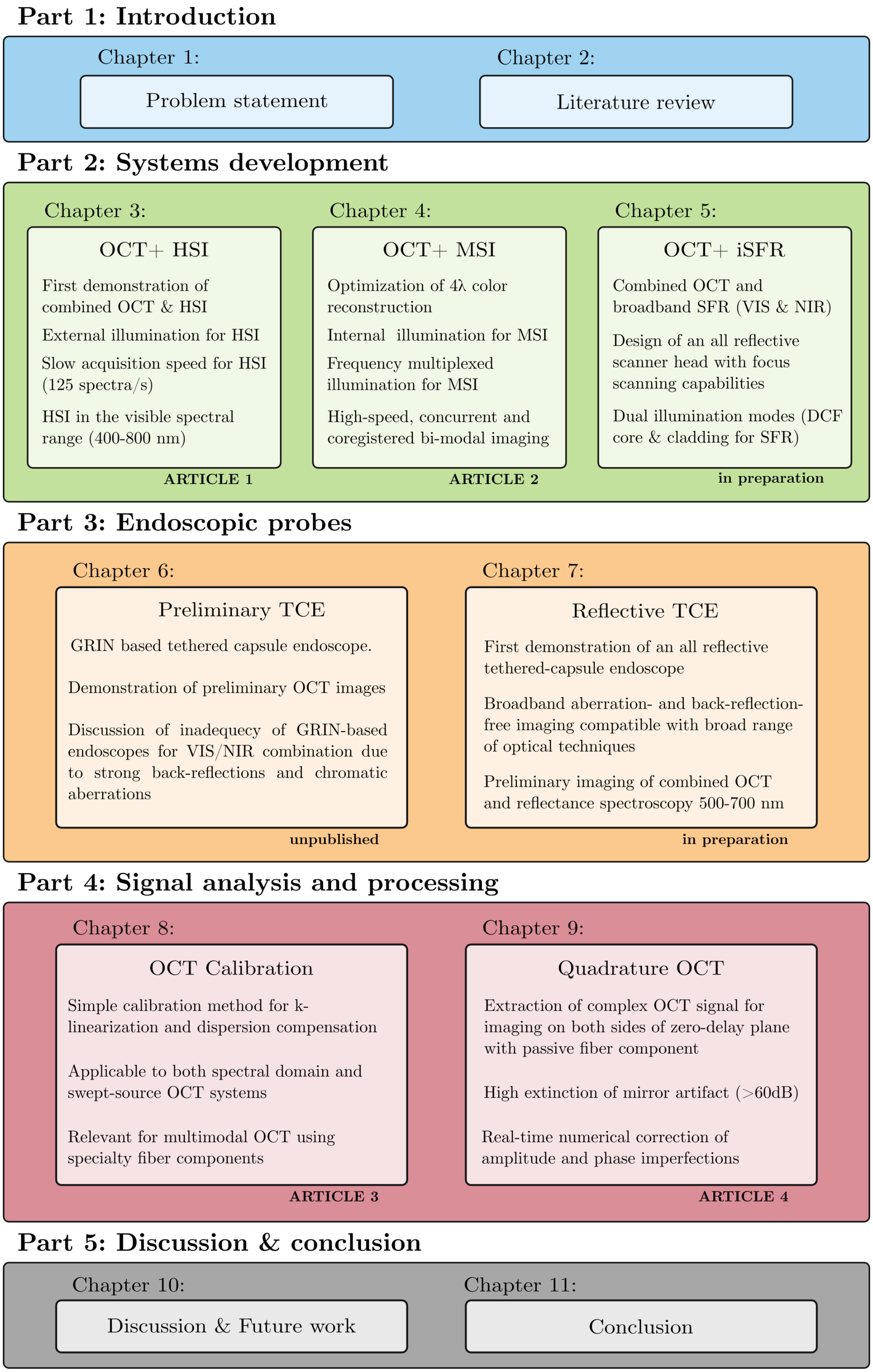

Part 1: Introduction

Chapter 1:
Problem statement

Chapter 2:
Literature review

Part 2: Systems development

Chapter 3:
OCT+ HSI
First demonstration of combined OCT & HSI
External illumination for HSI
Slow acquisition speed for HSI (125 spectra/s)
HSI in the visible spectral range (400-800 nm)
ARTICLE 1

Chapter 4:
OCT+ MSI
Optimization of 4λ color reconstruction
Internal illumination for MSI
Frequency multiplexed illumination for MSI
High-speed, concurrent and coregistered bi-modal imaging
ARTICLE 2

Chapter 5:
OCT+ iSFR
Combined OCT and broadband SFR (VIS & NIR)
Design of an all reflective scanner head with focus scanning capabilities
Dual illumination modes (DCF core & cladding for SFR)
in preparation

Part 3: Endoscopic probes

Chapter 6:
Preliminary TCE
GRIN based tethered capsule endoscope.
Demonstration of preliminary OCT images
Discussion of inadequecy of GRIN-based endoscopes for VIS/NIR combination due to strong back-reflections and chromatic aberrations
unpublished

Chapter 7:
Reflective TCE
First demonstration of an all reflective tethered-capsule endoscope
Broadband aberration- and back-reflection-free imaging compatible with broad range of optical techniques
Preliminary imaging of combined OCT and reflectance spectroscopy 500-700 nm
in preparation

Part 4: Signal analysis and processing

Chapter 8:
OCT Calibration
Simple calibration method for k-linearization and dispersion compensation
Applicable to both spectral domain and swept-source OCT systems
Relevant for multimodal OCT using specialty fiber components
ARTICLE 3

Chapter 9:
Quadrature OCT
Extraction of complex OCT signal for imaging on both sides of zero-delay plane with passive fiber component
High extinction of mirror artifact (>60dB)
Real-time numerical correction of amplitude and phase imperfections
ARTICLE 4

Part 5: Discussion & conclusion

Chapter 10:
Discussion & Future work

Chapter 11:
Conclusion

Figure 1.2 Thesis structure

CHAPTER 2 LITERATURE REVIEW

2.1 Optical coherence tomography

Optical coherence tomography (OCT) is an imaging technique that allows the reconstruction of high-resolution, depth-resolved reflectivity maps of biological tissue [45]. It is often described as the optical analog of ultrasound imaging (US). In US, sound waves are sent into a sample, and their echo time delay is measured, from which the depth-position of reflectors can be inferred. OCT operates on a similar principle but with electromagnetic waves. However, due to the speed of light, the echo time delay is too short for direct measurement. Instead, the delay is measured interferometrically relatively to a reference reflector.

2.1.1 Essential OCT terminology

Before diving into the theory of OCT, let us quickly define some of OCT-related terminology. OCT allows depth-resolved measurements of the reflectivity profile of a studied sample. This is typically performed in a point-scanning approach by scanning a focused laser beam across the sample. A single laser beam position provides a 1D measurement along the axial or z-direction. This 1D measurement is called an *A-line*. By scanning the focused beam's position along one lateral dimension, we obtain 2D, cross-sectional images called *B-scans*. Finally, if successive B-scans are acquired while incrementing the position along the other lateral dimension, we obtain a full 3D volume, called *C-scan*. These various scans are illustrated in Fig. 2.1. The axis along which multiple A-lines are acquired to build a B-scan is called the *fast scan axis*, while the other axis, along which multiple B-scans are performed to obtain a C-scan, is called the *slow axis*.

Another key performance specification of an OCT system is its resolution, both in the axial and lateral directions. In general, resolution refers to an imaging system's ability to distinguish two objects close to one another [46]. In the case of OCT, the lateral and axial resolutions are decoupled or independent of one another. The lateral resolution depends on the optics used for focusing the laser beam, while the axial resolution depends on the spectral bandwidth of the illumination source. A mathematical derivation for the axial resolution and some more explanations are provided in the following sections. While the axial resolution is independent of the lateral one, the choice of focusing optics does influence the divergence and, therefore, the depth of focus of the beam. The *depth of focus*

(DOF) refers to the distance over which the beam is considered in-focus, usually defined as 2× the Rayleigh length, z_{RL} [46,47]. Outside of this range, images tend to be strongly blurred. Assuming a Gaussian input beam, the expressions for the lateral resolution, Δx, and depth of focus are given by Eqs. 2.1 and 2.2 respectively [47]:

$$\begin{aligned} \Delta x &= \frac{\sqrt{2\ln 2}\lambda_0}{\pi NA} &\approx 0.37\frac{\lambda_0}{NA}, \qquad (2.1) \\ DOF &= \frac{2\lambda_0}{\pi NA^2} &\approx 0.64\frac{\lambda_0}{NA^2}, \qquad (2.2) \end{aligned}$$

where λ_0 is the center wavelength of the OCT system and NA is the numerical aperture of the input beam. It should be noted that the lateral resolution expression above uses the full-width at half-maximum (FWHM) spot size as the criterion for lateral resolution [47]. Typical OCT systems have axial resolutions ranging from 5-15 μm and lateral resolutions ranging from 5-30 μm [48–50]. Advanced OCT systems boasting axial and lateral resolutions ≤ 1 μm have been developed and are referred to as micro-OCT or μOCT [51]. The typical range of lateral resolutions results in DOF values from several hundreds of microns to several mm. Imaging depth is, however, usually limited to 0.5-2 mm by the penetration depth of light in biological tissue [52]. The resolution and imaging depth obtained with OCT makes it particularly apt for imaging tissue structure, although it typically does not permit cellular resolution.

Another key advantage of OCT is its high sensitivity. Thanks to its interferometric nature, it can measure samples with extremely low reflectivity values. The limit of this ability is called the *sensitivity* of a system, which refers to the sample reflectivity for which the *signal-to-noise ratio* (SNR) is equal to 1. The SNR is defined as follows:

$$\mathrm{SNR} = \frac{\langle I_D \rangle^2}{\sigma_N^2} \propto R_S, \qquad (2.3)$$

where $\langle I_D \rangle^2$ is the mean-square signal power at the detector, σ_N^2 is the noise variance, and R_S is the intensity reflectivity of the sample. Modern OCT systems often have sensitivity values of around 100–110 dB ($20\log_{10}$ scale), which means that they are capable of detecting reflectivities as small as 5×10^{-6}.

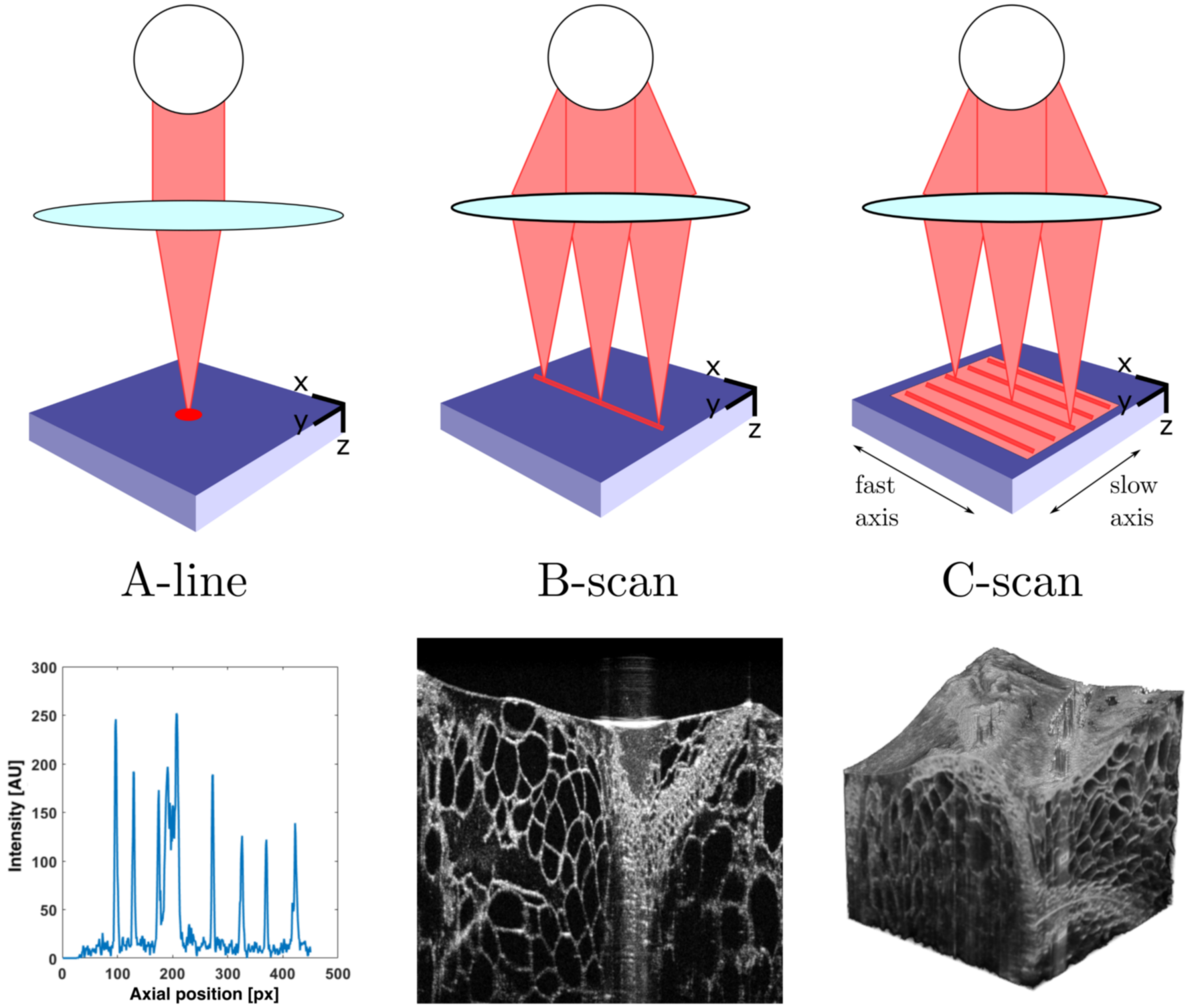

Figure 2.1 Schematic representation of various scan patterns, including an A-line, a B-scan, and a C-scan (top row, from left to right) with corresponding OCT signals/images of a mandarine slice (bottom row). The white circles in the top row represent a beam scanning mechanism such as galvo-mirrors.

2.1.2 Fundamental operating principle

The core operating mechanism of OCT is interference, a fundamental physical phenomenon caused by the superposition of two or more electromagnetic waves. One of the simplest methods to observe this phenomenon is through the use of a Michelson interferometer, such as the one depicted in Fig. 2.2, where a coherent laser beam is split into the two arms of the interferometer (called the reference and sample arms). When the optical path through these two arms is not identical, one beam accumulates a delay relative to the other, leading to constructive or destructive interference upon their recombination [53].

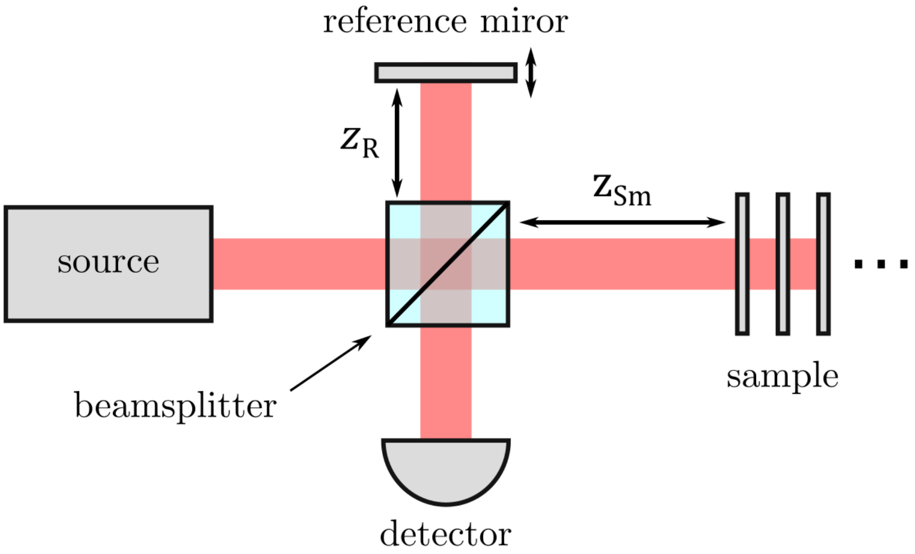

Figure 2.2 Schematic representation of a Michelson interferometer. z_R refers to the optical path length of the reference arm, while z_{Sm} refers to the optical path lengths of the various partial reflectors in the sample arm.

Mathematically, the electrical field incident on the detector can be expressed as the sum of the complex electrical fields from each arm of the interferometer, $\widetilde{E}_{\text{Ref}}$ and $\widetilde{E}_{\text{Sam}}$. If we further expand the complex fields of each arm and express them as complex phasors, we arrive at Eq. 2.4, where r_R and r_{Sm} are the amplitude reflectivity coefficients for the reference mirror and the m^{th} partial reflector in the sample arm, respectively, E_0 is the amplitude of the electrical field of the initial beam, k is the wavenumber, ω is the angular frequency, and t is the time. The $E_0/2$ factor in both terms accounts for the double pass through the beamsplitter.

$$\widetilde{E}_{det} = \underbrace{\frac{E_0}{2} r_R e^{i(2kz_R - \omega t)}}_{\widetilde{E}_{\text{Ref}}} + \underbrace{\frac{E_0}{2} \sum_m r_{Sm} e^{i(2kz_{Sm} - \omega t)}}_{\widetilde{E}_{\text{Sam}}} \tag{2.4}$$

The signal measured at the detector is, however, not the amplitude but the intensity of the electromagnetic radiation. This quantity is defined as the time-averaged square of the magnitude of the electrical field [46, 47]:

$$I_{det} = \langle |\widetilde{E}_{det}|^2 \rangle = \langle \widetilde{E}^*_{det} \cdot \widetilde{E}_{det} \rangle, \tag{2.5}$$

where $\widetilde{E}^*_{det}$ refers to the complex conjugate of $\widetilde{E}_{det}$. By inserting Eq. 2.4 into Eq. 2.5, we can express the intensity of the signal measured at detector as [49]:

$$\begin{aligned} I_{det}(z_R) = {} & \frac{I_0}{4} \cdot \left[R_R + \sum_m R_{Sm} \right] && \text{(DC terms)} \\ & + \frac{I_0}{2} \cdot \left[\sum_m \sqrt{R_R R_{Sm}} \cos\left(2k(z_{Sm} - z_R)\right) \right] && \text{(Cross-correlation terms)} \\ & + \frac{I_0}{4} \cdot \left[\sum_{m \neq n} \sqrt{R_{Sm} R_{Sn}} \cos\left(2k(z_{Sm} - z_{Sn})\right) \right], && \text{(Auto-correlation terms)} \end{aligned} \tag{2.6}$$

where I_0 refers to the initial intensity associated with the field E_0 and R_i represents the intensity reflectivity coefficients associated with the amplitude reflectivities r_i ($R_i = |r_i|^2$). As depicted above, Eq. 2.6 can be separated into three parts: DC, cross- and auto-correlation terms. The DC terms do not depend on the optical path difference (OPD) and therefore do not carry information about the reflectors' position in the sample. The cross-correlation terms represent the interference signals between the electric fields from the individual reflectors and the reference mirror. These terms contain the information of interest for OCT and allow the reconstruction of the depth-resolved reflectivity profile. Finally, the auto-correlation terms represent the interference between the different partial reflectors in the sample (i.e., without interaction with the reference arm). During imaging, these appear as artifacts that may degrade the overall image quality and are generally undesirable. Fortunately, the sample reflectivities are typically much lower than that of the reference mirror ($R_R \gg R_{Sm}$) in biological tissue. As such, the auto-correlation terms tend to be very small compared to the other two sets of terms and may be considered negligible [49]. For this reason, and to lighten the mathematical formalism, the auto-correlation terms are not considered in the following demonstrations.

Equation 2.6 describes the measured signal in the case of a monochromatic source. In this case, the signal measured will be a succession of constructive and destructive interference fringes as the position of the reference mirror (z_R) changes. Let us now consider the more realistic case where the laser source has a certain spectral bandwidth, described by a power spectrum $S(k)$, centered around a certain wavenumber k_0. Incorporating this wavelength dependence and neglecting the auto-correlation terms, we arrive at:

$$I_{det}(k,z_R) = \frac{S(k)}{4} \cdot \left[R_R + \sum_m R_{Sm} \right] + \frac{S(k)}{2} \cdot \left[\sum_m \sqrt{R_R R_{Sm}} \cos\left(2k(z_{Sm} - z_R)\right) \right]. \tag{2.7}$$

This equation lies at the heart of low-coherence interferometry and, therefore, of OCT. Depending on how this signal is measured, either as a function of the reference mirror position or as a function of wavenumber, it gives rise to two different OCT methods: time-domain (TD-OCT) and Fourier-domain OCT (FD-OCT). Both allow the recovery of the depth-resolved reflectivity map of the studied sample and will be discussed in further detail below. It is important to note that the equations above and those in the following sections detailing the operating principle of TD- and FD-OCT are for a free-space interferometer. They do not account for the propagation of light through dispersive media, where the total optical path length (OPL) varies with wavelength. This more advanced analysis is explored in detail in Chapter 8.

2.1.3 Time-domain OCT

Mathematical framework

In TD-OCT, the signal described in Eq. 2.7 is measured as a function of z_R using a single detection element. As such, for a given position of the reference mirror, the measured signal is given by $I_{det}(k,z_R)$ integrated over all wavelengths:

$$I_{TD}(z_R) = \int_0^\infty I_{det}(k,z_R)\,dk. \tag{2.8}$$

From Eq. 2.7, it is straightforward to see that the integral of the DC terms will be a constant multiplied by the integral of the power spectrum $S(k)$ over all wavelengths, which is also constant with regards to z_R. Equation 2.8 can then be expanded as:

$$\begin{aligned} I_{TD}(z_R) &= \text{const.} + \frac{1}{2}\int_0^\infty S(k)\sum_m \sqrt{R_R R_{Sm}}\cos\left(2k(z_{Sm}-z_R)\right)dk \\ &= \text{const.} + \frac{1}{2}\sum_m \sqrt{R_R R_{Sm}}\int_0^\infty S(k)\cos\left(2k(z_{Sm}-z_R)\right)dk \end{aligned} \tag{2.9}$$

The integration over wavenumber in the second formulation in Eq. 2.9 corresponds to the real part of the Fourier transform (FT) of the power spectrum, with the Fourier pair k and $2(z_{Sm}-z_R)$. Using the shifting property of the Fourier transform, we can re-write Eq. 2.9 as:

$$I_{TD}(z_R) = \text{const.} + \frac{1}{2}\sum_m \sqrt{R_R R_{Sm}}\underbrace{\cos\left(2k_0(z_{Sm}-z_R)\right)}_{\text{carrier}}\cdot\underbrace{\mathbb{R}\left[\mathcal{F}_k\{S(k)\}(z_{Sm}-z_R)\right]}_{\text{enveloppe}}, \tag{2.10}$$

where $\mathcal{F}_k$ is the Fourier transform with respect to k. Equation 2.10 can be visualized in Fig. 2.3, where we can observe the carrier cosine (in blue) and the envelope (in red), which has peaks centered around the position of each reflector (see graph below). We can also clearly see that height of each peak is directly proportional to the field/amplitude reflectivity of each reflector ($r_{Sm} = \sqrt{R_{Sm}}$). As such, the measured signal's envelope provides information on the reflectors' positions and their relative reflectivities. Conveniently, the single-frequency carrier cosine can be used to perform lock-in detection, which allows high sensitivity measurement of the envelope while removing the DC offset [49].

Another essential feature of Eq. 2.10 is that the shape and, more specifically, the width of the peaks is characterized by the Fourier transform of the input spectrum, $S(k)$, also called the axial *point-spread function* (PSF). Indeed, the peaks' width will determine the axial resolution achievable with OCT, or in other words, our ability to distinguish reflectors close to one another in the axial direction.

Physically, the Fourier transform of the input power spectrum in terms of wavenumber is equal to the auto-correlation function, $\Gamma(\delta z)$, of the input electrical field. This equality is also known as the Wiener-Khinchin theorem, although it is usually written in terms of optical frequency, ω, and temporal delay, $\Delta\tau$ [46,47,49,54]. The auto-correlation function informs us of a wave's ability to interfere with itself depending on the delay between the interfering fields. In the case of broadband light, strong interference is only possible when this delay is small, which is why the fringe bursts visible in the top graph of Fig. 2.3 only appear when the reference mirror is close to the position of a sample reflector. Two

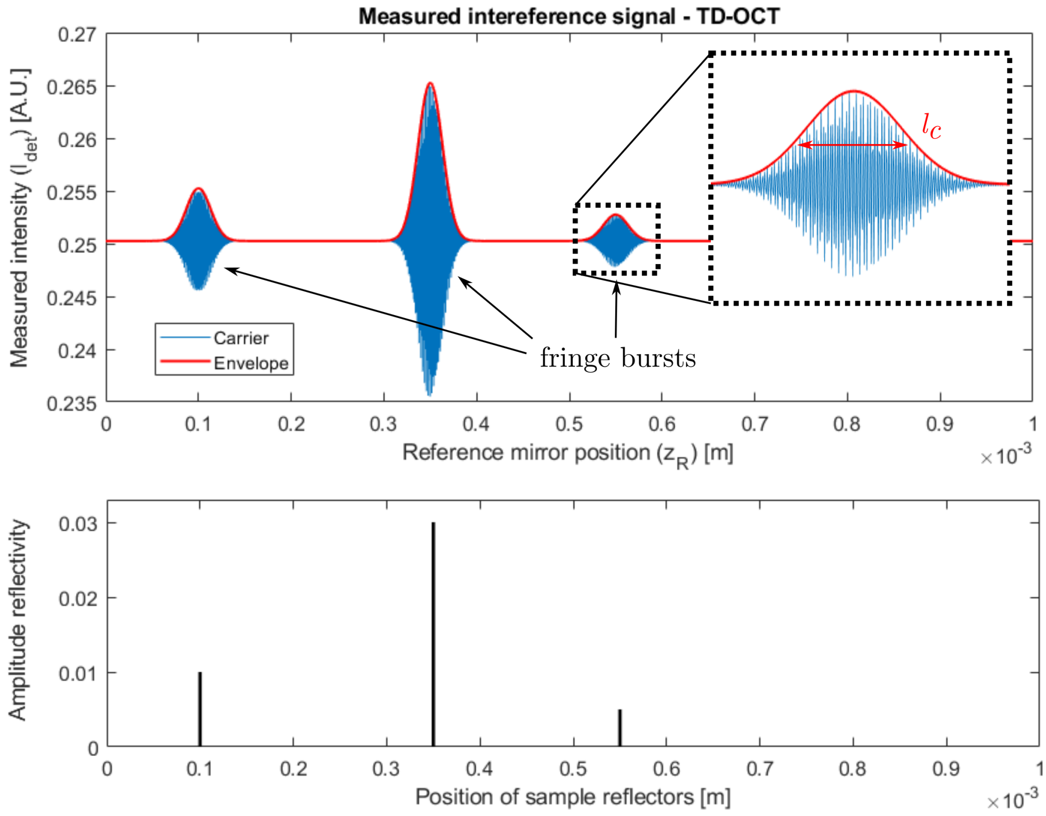

Figure 2.3 Example TD-OCT signal measured while varying the position of the reference mirror, z_R. The signal in the top graph is produced from reflectors whose positions, z_{Sm}, and amplitude reflectivities, r_m, are depicted in the bottom graph.

properties exist that describe this delay over which "strong" interference is achieved: the coherence time, τ_c, and the coherence length, l_c. These two parameters are related by Eq. 2.11.

$$l_c = c\tau_c \tag{2.11}$$

Both the coherence time and length can be derived from the normalized version of the auto-correlation function, also called the spatial complex degree of coherence or coherence function, $\gamma(\delta z)$, described in Eq. 2.12. The coherence length is usually defined as the FWHM of the coherence function [47, 49].

$$\gamma(\delta z) = \frac{\Gamma(\delta z)}{\Gamma(0)} = \frac{\langle \widetilde{E}^*(z)\widetilde{E}(z+\delta z)\rangle}{\langle \widetilde{E}^*(z)\widetilde{E}(z)\rangle} = \frac{\langle \widetilde{E}^*(z)\widetilde{E}(z+\delta z)\rangle}{I(z)} \tag{2.12}$$

As a consequence of the Wiener-Khinchin theorem, the envelope signal in Eq. 2.10 will have the same shape as the complex degree of coherence and, therefore, the same FWHM, equal to the coherence length. As such, l_c has become widely accepted as the metric for characterizing the axial resolution in OCT. Furthermore, this value can be predicted directly from the power spectrum of the broadband source used. For example, let us consider a normalized Gaussian spectrum given by:

$$S(k) = \frac{1}{\Delta k\sqrt{\pi}} e^{-\frac{(k-k_0)^2}{\Delta k^2}}, \tag{2.13}$$

where Δk is the half-width of the spectrum at $1/e$ of its maximum. The Fourier transform with respect to k is:

$$\mathcal{F}_k\{S(k)\} = \gamma(z) = e^{-z^2\Delta k^2}, \tag{2.14}$$

where $\gamma(\delta z)$ is the spatial equivalent of $\gamma(\tau)$. From Eq. 2.14, it is straightforward to find the FWHM, which is given by:

$$l_c = \frac{2\sqrt{\ln 2}}{\Delta k} = \frac{2\ln 2}{\pi}\frac{\lambda_0^2}{\Delta\lambda} \approx 0.44 \cdot \frac{\lambda_0^2}{\Delta\lambda}, \tag{2.15}$$

where the second equality performs the conversion back into wavelength values. In this expression, λ_0 refers to the center wavelength, related to the center wavenumber by $\lambda_0 = 2\pi/k_0$, and $\Delta\lambda$ refers to the FWHM of the wavelength spectrum, also called the spectral bandwidth [49]. The inverse relationship of l_c with the spectral bandwidth implies that sources with a broader spectrum will produce narrower peaks and, therefore, have an improved axial resolution.

Practical implementation

OCT imaging of biological tissue was first demonstrated in 1991 in a landmark paper by Huang et al. [45]. It was quickly followed by several more, notably *in vivo* measurements of eye structures such as the retina and macula [55, 56]. Ophthalmology was (and still is) the medical field where OCT has had the most significant impact. Due to the eye being optically accessible, it was the focus of many early clinical studies with OCT. However, a key advantage of OCT is its compatibility with optical fiber, which allows it to be implemented in an endoscopic format to image tissues deep inside the body. This enabled the application of OCT imaging to numerous other clinical fields, including cardiology, gastroenterology, pulmonology, and urology [57–62]. The use of optical fibers also offers several other advantages, including significantly increasing robustness to vibration or movement, reducing the need for sensitive free-space optical alignments and providing improved light containment for laser safety purposes.

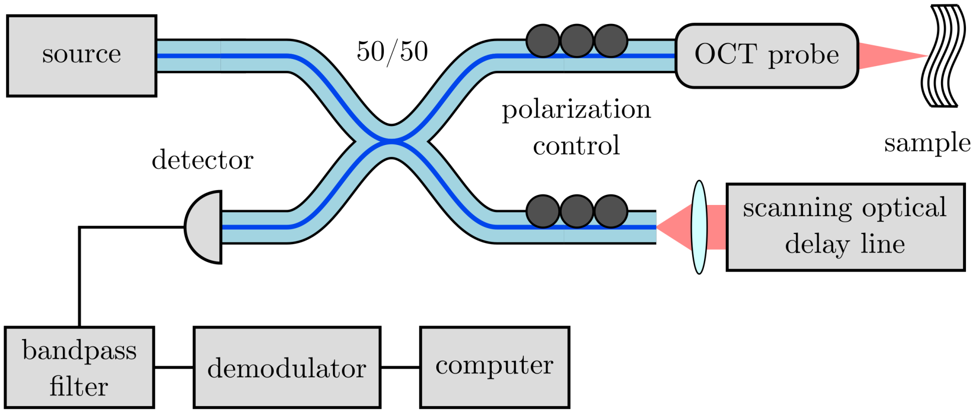

Figure 2.4 Schematic representation of a fiber-based TD-OCT system. All fibers are single mode. The 50/50 indicates the power split between the two output arms of the fiber coupler.

Figure 2.4 presents a standard fiber-based TD-OCT system compatible with endoscopic probes. In this diagram, light emitted from the broadband laser source is split by the 50/50 fiber coupler into the interferometer's arms. An endoscopic probe, connected at the distal end of the sample arm, can then be inserted into the body to image the tissue of interest. A scanning optical delay line, which performs the axial scan of the reference mirror, is connected to the reference arm. Light reflected from the reference arm and backscattered from the sample arm travels back along the fiber and interferes in the fused segment of the 50/50 coupler. The interference signal, described by Eq. 2.10, is then transported to the detector. The RF signal is then demodulated and digitized for display or further processing.

The repetition rate of the scanning optical delay line determines the TD-OCT system's A-line rate. As such, many research groups investigated various methods to increase this repetition rate. The simplest and slowest method was using motorized linear translation stages to translate the mirror physically. Such systems typically achieved up to several tens of A-lines per second [45, 56, 63], which did not allow for real-time image formation. Several other delay methods were developed that achieved varying A-line rates, including expanding piezo-electric modulators (~500 Hz) [64], piezo-electric transducers driving parallel mirror systems (~10 Hz) [65], Fourier-domain optical delay lines (~4 kHz) [57] and rotating beamsplitter cubes (~25 kHz) [66]. However, while these methods with kHz A-line rate allowed the acquisition of multiple B-scans per second, they remained sensitive to motion artifacts and required complex mechanical assemblies. Furthermore, increased acquisition speed and corresponding detector bandwidth (BW) reduced the OCT systems' overall sensitivity. Only with the development of FD-OCT systems did OCT achieve considerably higher acquisition speeds and significant clinical potential.

2.1.4 Fourier-domain OCT

Mathematical framework

Fourier-domain OCT refers to OCT where the interferometric signal described in Eq. 2.7 is measured spectrally (i.e., as a function of wavenumber). This aptly-named *interference spectrum* can be analyzed to provide depth-resolved reflectivity maps with the important advantage of not requiring the reference mirror to be scanned. Consider the following equation:

$$I(k) = \frac{S(k)}{4} \cdot \left[R_R + \sum_m R_{Sm} \right] + \frac{S(k)}{2} \cdot \left[\sum_m \sqrt{R_R R_{Sm}} \cos\left(2k(\delta z_m)\right) \right], \tag{2.16}$$

a copy of Eq. 2.7 where the terms $z_{Sm} - z_R$ have been replaced with δz_m. Since the reference mirror position no longer varies, the position of each partial reflector in the sample can be defined relative to that reference position, as illustrated in Fig. 2.5. The position of the reference mirror is usually called the *reference* or *zero-delay plane*. If we isolate the interference term in Eq. 2.16, we arrive at:

$$I_{int}(k) = \frac{S(k)}{2} \cdot \left[\sum_m \sqrt{R_R R_{Sm}} \cos(2k\delta z_m) \right]. \tag{2.17}$$

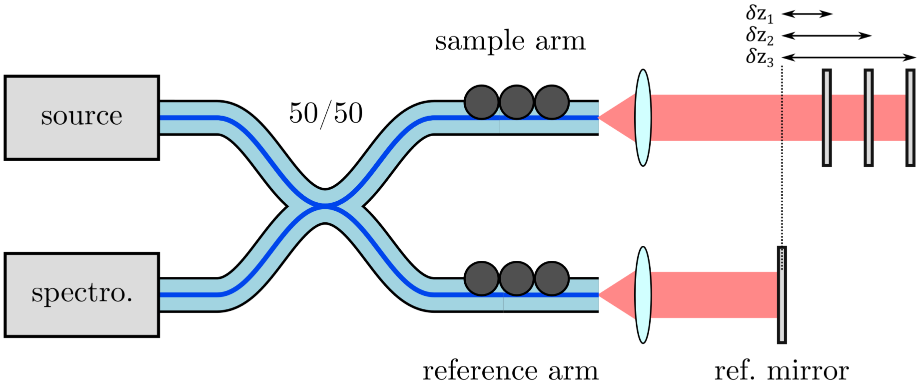

Figure 2.5 Schematic representation of a simplified FD-OCT system with multiple reflectors. The position of each reflector, δz_m, can be defined relative to the reference plane.

In practice isolating the interference term can be achieved by subtracting a background measurement from the signal. This background measurement can be obtained by acquiring the signal without a sample, where it is assumed that the DC signal from the sample is negligible compared to the DC from the reference arm ($R_R \gg \sum R_{Sm}$). Using the convolution theorem and the Fourier transform of a cosine:

$$\mathcal{F}\{f(k) \cdot g(k)\} = \mathcal{F}\{f(k)\} * \mathcal{F}\{g(k)\}, \tag{2.18}$$

$$\mathcal{F}_k\{\cos(k\delta z)\} = \frac{1}{2}\left[\delta(z - \delta z) + \delta(z + \delta z)\right], \tag{2.19}$$

where δ is the delta function and $*$ is the convolution operator, we can show that the Fourier transform with respect to k of Eq. 2.17 is given by:

$$\begin{aligned} \mathcal{F}_k\{I_{int}(k)\} &= \frac{1}{2}\mathcal{F}_k\{S(k)\} * \mathcal{F}_k\left\{ \sum_m \sqrt{R_R R_{Sm}} \cos(2k\delta z_m) \right\} \\ &= \frac{1}{2}\gamma(z) * \left[\frac{1}{2} \sum_m \sqrt{R_R R_{Sm}} \left(\delta(z - 2\delta z_m) + \delta(z + 2\delta z_m)\right) \right]. \end{aligned} \tag{2.20}$$

Finally, using the sifting property of the delta function we can re-write Eq. 2.20 as:

$$\mathcal{F}_k\{I_{int}(k)\} = \frac{1}{4}\sum_m \sqrt{R_R R_{Sm}}\left(\gamma(z-2\delta z_m)+\gamma(z+2\delta z_m)\right). \tag{2.21}$$

Qualitatively, Eq. 2.21 states that for each partial reflector in the sample arm, the Fourier transform of the dark-corrected interference spectrum will produce two symmetric peaks on either side of the zero-delay plane at positions, $\pm 2\delta z$, proportional to the real position of the reflector. As was the case for TD-OCT, the shape of these peaks is given by the Fourier transform of the normalized illumination spectrum, $S(k)$, and their relative heights are proportional to the amplitude reflectivity, r_{Sm}. However, it is important to note that, in FD-OCT, the Fourier transform is performed only over the measured spectral range. As such, the power spectrum $S(k)$ is not always perfectly gaussian, nor is it zero at the edges of the detected spectral range. Window functions are then often applied to the interference spectrum prior to FT to reduce side-lobes in the axial PSF. However, windowing also effectively reduces the spectral bandwidth, leading to reduced axial resolution. In this case, Eq. 2.15 becomes a poor estimation of the theoretical axial resolution of the OCT system. A better metric for the theoretical axial resolution is the FT of the envelope of the interference signal.

The steps outlined in equations 2.16 to 2.21 are also represented graphically in Fig. 2.6. Equation 2.21 and Fig. 2.6(d) both indicate that there is a duplication of the information on either side of the zero-delay plane. This is called the *mirror* or *complex conjugate artifact* and highlights that, in a standard configuration, FD-OCT systems cannot distinguish whether a reflector is located before or after the reference plane in the axial direction. As such, only the positive side of the Fourier transform is typically used when imaging samples. However, certain special OCT systems can remove this artifact by measuring both the amplitude and the phase of the complex interference signal. Such a system is presented in Chapter 9 of this thesis.

Practical implementations

In practice, two methods can measure the interference signal spectrally. The first is using a spectrometer, which uses a dispersive element (prism or grating) to spatially separate different spectral components across multiple detectors. This implementation is called *spectral-domain OCT* (SD-OCT). The second approach is to scan the illumination wavelength in time and record the interference signal's intensity using single-element detectors. This method is usually called *swept-source OCT* (SS-OCT), although it is also referred to as *optical frequency domain imaging* (OFDI). SD- and SS-OCT differ slightly in their op-

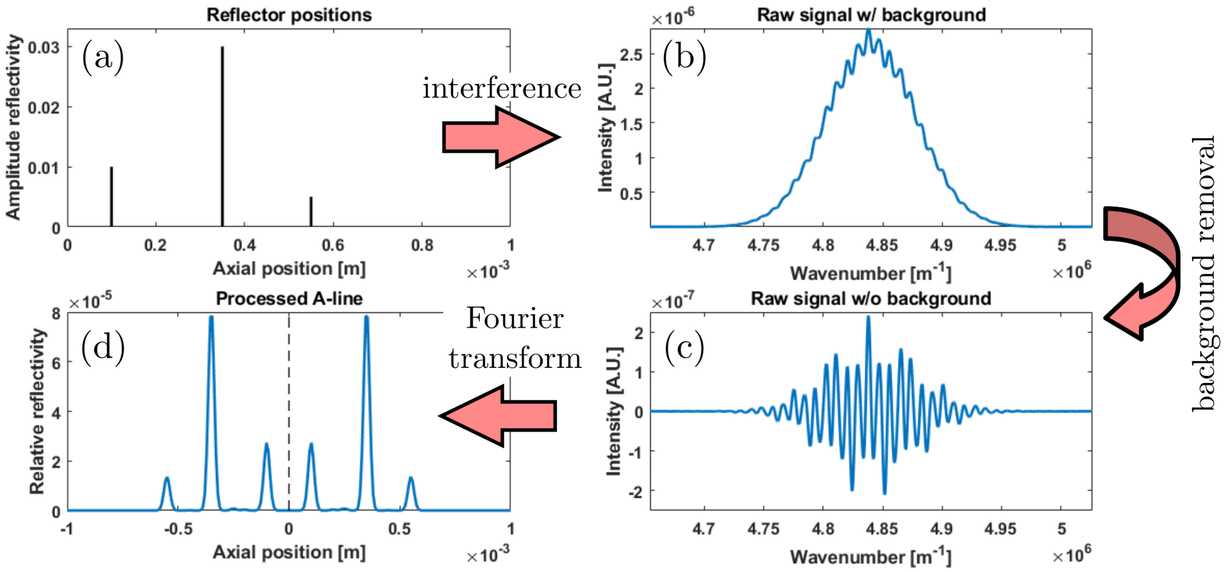

Figure 2.6 Example FD-OCT signal at different stages in acquisition and processing. (a) Positions and amplitude reflectivities of three reflectors in the sample arm. (b) Acquired interference spectrum containing both the DC and the interference component. (c) Dark-corrected interference spectrum, i.e., with DC component removed. (d) Fully processed A-line mapping the axial positions and relative reflectivities of the reflectors.

tical configuration, as illustrated in Figs. 2.7 and 2.8. While these two techniques provide the same fundamental information, some key differences exist between the two. SD-OCT systems rely on linear detector arrays to measure the interference spectrum at the output of a spectrometer system. The A-line rate is therefore determined by the integration time of the sensor as well as the read-out delay. In SS-OCT, the A-line rate is determined by the sweep rate of the wavelength-swept laser source. SS-OCT systems typically reach sweep rates of several hundreds of kHz, with some advanced experimental systems achieving A-line rates well into the MHz range [67, 68]. SD-OCT systems only achieve somewhat slower scan speeds of 100–250 kHz.

Another key difference between SD- and SS-OCT is the use of fiber-based optical circulators in SS-OCT (see Fig. 2.8). This enables enhanced collection efficiency of the backscattered light and balanced detection, which strongly attenuates the DC and autocorrelation components of the interference signal while doubling the cross-correlation term (see Eq. 2.6). Balanced detection in SS-OCT takes advantage of the fact that the interference signal (cross-correlation term) at the two output branches of the 50/50 coupler are out of phase by π radians, while the other terms (DC and autocorrelation) remain in phase. Both signals are measured and then subtracted from one another, resulting in the coherent addition of the interferometric signal and the attenuation of the other terms. The DC and autocorrelation signals would be suppressed entirely in ideal balanced detection. However, slight differences in the spectral response of the 50/50 fiber coupler and the two detectors lead to small residual signals. The effective attenuation is called the *common mode rejection ratio* (CMRR) and is typically on the order of 25–30 dB. Balanced detection is also possible in SD-OCT but is less common due to the high cost of having two spectrometers and the challenges associated with matching the two devices spectrally.

The two configurations also differ in their usual wavelength range. SS-OCT is typically limited to wavelength ranges above 1000 nm by the available wavelength-swept laser sources. SD-OCT, on the other hand, may operate below 1000 nm [69]. A typical wavelength range is around 800–900 nm, but systems operating in the VIS range have also been demonstrated. Lower center wavelengths for SD-OCT are favored by the availability of high-performance and affordable silicon and CMOS detectors in the sub-1000 nm range. The lower central wavelength of SD-OCT systems allows them to obtain much higher axial resolution than SS-OCT, reaching micron or sub-micron values. However, this gain in axial resolution also comes at the expense of the maximum imaging depth, limited by the penetration of light into the tissue. The choice of wavelength range, and therefore of system type, is usually dictated by the target application.

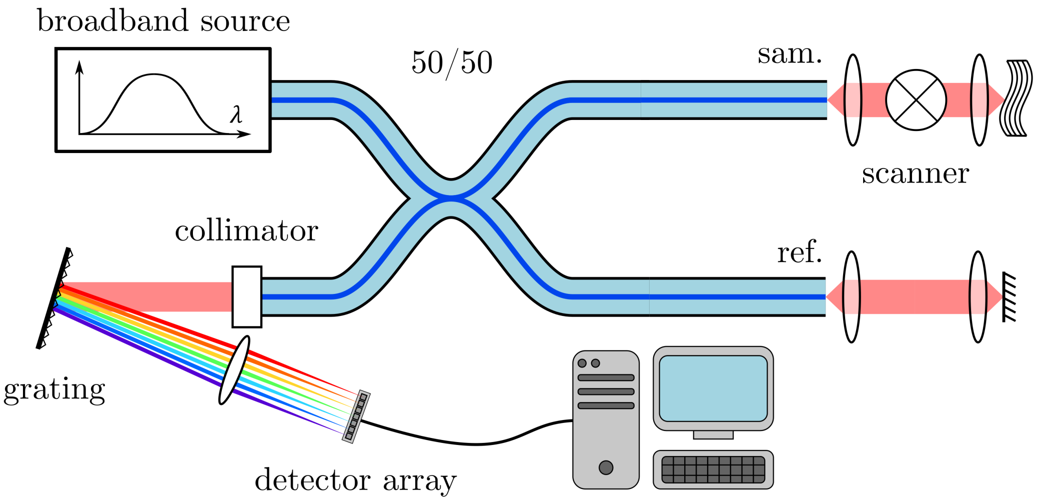

Figure 2.7 Example of an SD-OCT system. Spectral separation occurs during the detection using a spectrometer.

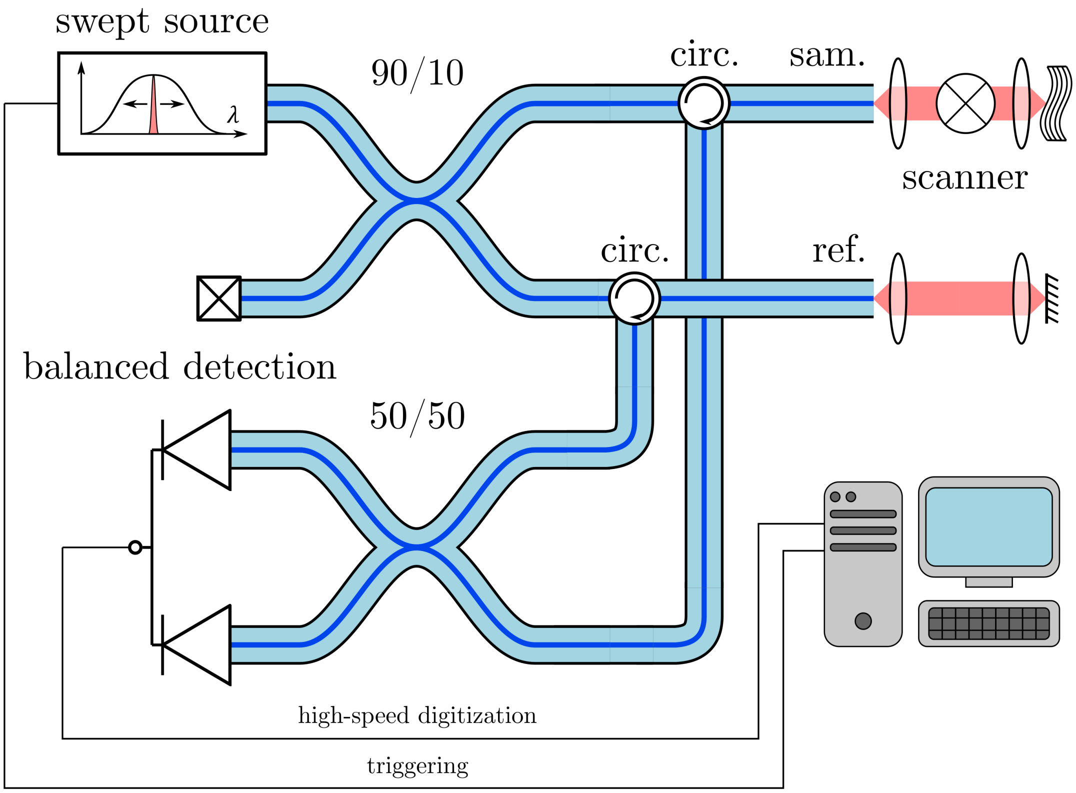

Figure 2.8 Example of an SS-OCT system. Spectral separation occurs during the illumination using a swept-source laser which continuously changes its wavelength in time.

Sensitvity advantage of FD-OCT

As demonstrated above, FD-OCT allows the retrieval of the same information of interest as TD-OCT: the axial position and reflectivity of reflectors in a sample. It also offers the advantage of not requiring a scanning optical delay line. However, the critical advantage of FD-OCT is a significant sensitivity enhancement. This was suggested in the literature in the late 90s [70–72], but was only widely accepted after 2003, when three publications provided the mathematical derivation and experimental validation for this sensitivity advantage, equivalent for both spectral-domain OCT and swept-source OCT [73–75]. Qualitatively, the gain provided by FD-OCT techniques can be explained in two ways, depending on the implementation (SD- or SS-OCT). In SD-OCT, the interference signal is spread onto M spectral bands that are summed coherently when reconstructing the signal. In addition, because FD-OCT only measures the real part of the complex interference, the signal level is reduced by a factor of 2. As a result, the signal level of SD-OCT systems is equal to that of TD-OCT, reduced by a factor of 2. Simultaneously, the noise contributions of each spectral channel are added incoherently, resulting in an overall decrease of the noise level by a factor of M. The resulting signal-to-noise ratio (SNR) of SD-OCT is given by Eq. 2.22 [73]. In SS-OCT, each spectral band can be delivered with a power equivalent to the total power of the broadband source in TD-OCT. The coherent addition of all spectral bands during signal reconstruction leads to an increase in signal level of M^2, while the incoherent addition of noise results in an increase of only a factor M. Similarly to SD-OCT, a signal reduction factor of 2 is also applied in SS-OCT. As such, the resulting SNR of SS-OCT systems is identical to that of SD-OCT and corresponds to a gain of $M/2$ over TD-OCT. It should be noted that Eq. 2.22 assumes a uniform power spectrum. Additional factors must be added for gaussian or other non-uniform spectral shapes, but the proportionality to M remains [49].

$$SNR_{SD} = SNR_{SS} = SNR_{TD} \cdot \frac{M}{2} \tag{2.22}$$

Most FD-OCT systems have a number of spectral channels M on the order of 1000–2000. The corresponding SNR gain compared to TD-OCT is about 500–1000. This allowed FD-OCT systems to measure deeper into tissue and, most importantly, to operate at significantly higher speeds without compromising image quality. Modern systems are routinely able to scan at A-line rates of several hundred kHz while maintaining sensitivities above 100 dB. This high-speed imaging has enabled real-time measurement protocols in various clinical fields and functional imaging modes, assessing the OCT signal's temporal evolution and related tissue properties.

2.1.5 Clinical applications of endoscopic OCT

The sensitivity and speed advantages of FD-OCT systems have led to an explosion of clinical applications in the last two decades, spearheaded by the field of ophthalmology, where OCT has become a gold standard for general retinal examination, diagnosis of various pathologies, and treatment monitoring [48, 76, 77]. Today, over 30 million retinal OCT scans are performed each year, corresponding to an incredible one procedure per second [77, 78]. This number is remarkable, especially considering that the technique was developed only 30 years ago [45]. Comparatively, endoscopic implementations of OCT have achieved less widespread acceptance. This can be attributed to several reasons, including the additional requirement for the design and fabrication of reliable and safe endoscopic probes, the need for the development of diagnostic criteria, and the competition with long-standing diagnostic methods [76]. Nonetheless, several applications have emerged as promising candidates in various fields, chief amongst which are cardiology and gastroenterology. Other disciplines where endoscopic OCT is applied include pulmonology, urology, gynecology, and laryngology.

In cardiology, intracoronary OCT has notably been applied to evaluating the vulnerability of atherosclerotic plaque [79, 80], guidance and assessment of percutaneous coronary interventions (i.e., stent placement in blood vessels) [81] and the characterization of arterial morphology [82]. In plaque assessment, in particular, OCT shines for its high resolution and ability to differentiate various types of atherosclerotic lesions based on signal intensity and attenuation [80]. However, several studies have shown that OCT may misclassify certain plaque types due to imaging artifacts or insufficient specificity of the scattering interactions occurring in the tissue on which the OCT signal is based [83–85]. Consequently, there has been significant effort in developing and validating multimodal intravascular probes, which supplement the morphological information from OCT with biochemical data from other techniques [86]. Some such combinations are listed in Table 2.1 in Section 2.1.7, where multimodal OCT is discussed in more detail.

OCT has also been implemented extensively in gastrointestinal (GI) imaging. The primary application, and also the target clinical application of this thesis, has been the early detection of cancerous and pre-cancerous lesions in the esophagus (both EAC and SCC). However, OCT is also being investigated as a means to image other organs and/or pathologies including eosinophilic esophagitis [87, 88], stomach cancer [89, 90], celiac disease by means of intestinal imaging [91, 92], colon cancer [93], differentiation of inflammatory bowel diseases [94, 95] and biliary tract strictures [96]. In the esophagus, OCT has been implemented for the detection of the various stages of progression from intestinal metaplasia (IM) and Barrett's esophagus (BE) through low- and high-grade dysplasia (LGD and HGD, respectively) to esophageal adenocarcinoma (EAC). Several descriptive studies have identified distinctive anatomical characteristics in OCT images that can be used for feature-based classification [1, 60, 90, 97, 98]. Examples of such features are presented in Fig. 2.9.

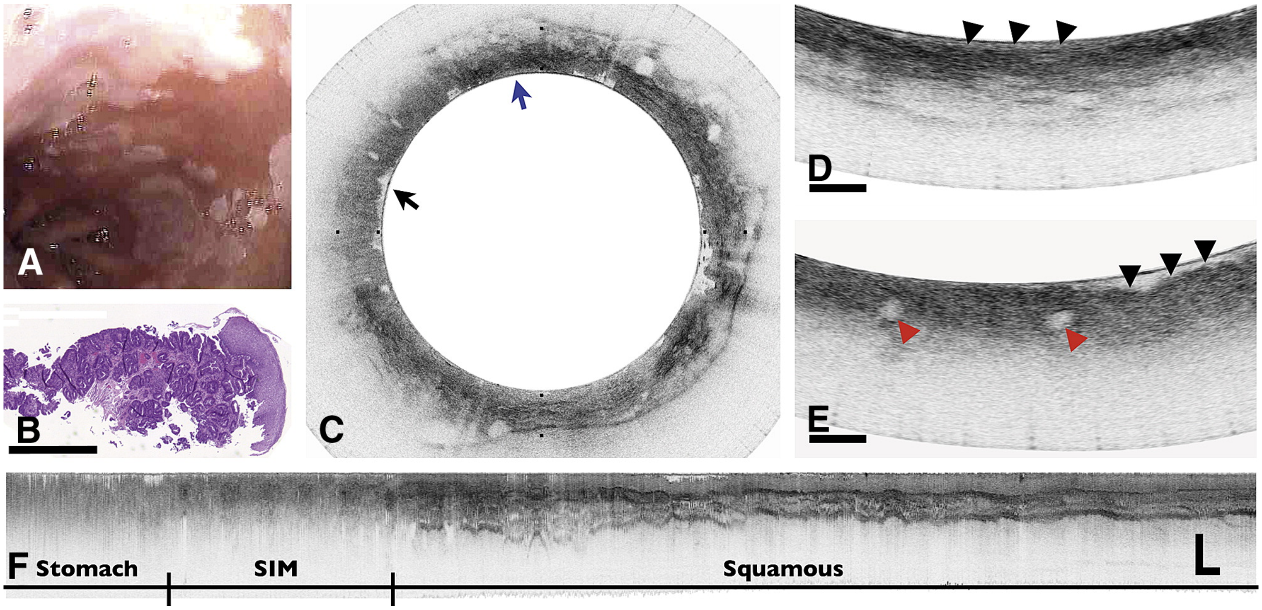

Figure 2.9 Barrett's esophagus with dysplasia. **(a)** Video endoscopic image reveals a patchy mucosa consistent with specialized IM (SIM). **(b)** Histopathologic image of biopsy with IM and LGD. **(c)** Cross-sectional OCT image highlighting regions with SIM without dysplasia (blue arrow) and SIM with HGD (black arrow). **(d)** Expanded view of (c) taken from the region denoted by the blue arrow, demonstrating good surface maturation (arrowheads), indicative of SIM without dysplasia. **(e)** Expanded view of (c) taken from the region denoted by the black arrow, demonstrating features consistent with HGD, including poor surface maturation (black arrowheads) and the presence of dilated glands (red arrowheads) in the mucosa. **(f)** A longitudinal slice highlights the transition from gastric cardia through a 9-mm segment of SIM and finally into squamous mucosa. Scale bars represent 1 mm. Image reprinted and caption extracted from Ref [1], Copyright (2008), with permission from Elsevier.

These anatomical features were incorporated into diagnostic algorithms and used in prospective studies to identify IM, dysplasia and/or cancer with reported sensitivity and specificity values ranging from 0.75–1 and 0.33–1 (values from individual studies) [41–44, 98–102]. Two meta-analyses incorporating the results of these trials determined combined sensitivities/specificities for the detection of dysplasia and early-stage cancer of 93%/54% [103] and 68–83%/75–82% [40]. Although these findings are promising, they fall short, albeit only slightly, of the criteria proposed by the American Society for Gastrointestinal Endoscopy of 90% sensitivity and 80% specificity for any imaging technique to replace the current random 4-quadrant biopsy protocol [104]. In the last few years, significant clinical and industrial efforts have been dedicated to improving the performance of OCT and making it a standard tool for esophageal imaging. Two approaches have been favored in this regard. The first is enhancing the system's overall performance in terms of resolution and speed, as well as implementing functional extensions of OCT. The second, and the premise of this thesis, is the multimodal approach where OCT imaging is complemented with other modalities that provide additional information.

2.1.6 Expanding OCT contrast

In the standard implementations presented in the previous sections, OCT only enables imaging of backscattered light. While this enables high-resolution imaging of sub-surface tissue morphology and the detection of various anatomical features, it only provides limited access to quantitative information about the sample properties. Several advanced data analysis methods and functional extensions of standard OCT have been developed to expand the technique's ability to measure various optical, chemical, or physiological properties and detect additional features. Such extensions include, but are not limited to, polarization-sensitive OCT (PS-OCT), OCT angiography (OCTA) and flow detection through doppler-OCT or speckle variance methods, spectroscopic OCT, and attenuation coefficient (μ_{OCT}) measurement. These methods are briefly discussed below, with an emphasis on their use in endoscopy. It is interesting to note that these extensions are not mutually exclusive or necessarily incompatible with the multimodal approach. As such, advanced multimodal OCT systems may well incorporate these functional extensions and the additional optical signal(s).

Polarization-sensitive OCT

Under the paraxial approximation, light waves are transverse electromagnetic (TEM), meaning that the electrical field vector is perpendicular to the propagation direction [47]. The exact orientation of the electrical field within the transverse plane and its evolution along the propagation vector is called the *polarization state* of light [47, 53]. This property is of particular interest in biomedical optics because many light-tissue interactions may change the polarization state and can be used as sources of contrast [105]. PS-OCT notably allows the measurement of tissue birefringence, optical axis, diattenuation (i.e., the variable absorption of light depending on polarization), and depolarization [105–107]. Birefringence occurs when materials have refractive indices dependent on the polarization state. In biological tissue, this occurs especially in the presence of structured fibrous materials such as muscle, collagen, or nerve fiber, and is called form birefringence [108–111]. Given this enhanced sensitivity to fiber structures, PS-OCT has been used in various applications of ophthalmology and dermatology. Endoscopic applications have only recently emerged due to the technical difficulty associated with polarization control in optical fibers. Indeed, optical fibers exhibit birefringence due to imperfections and mechanical stress, such as bends or torsion. However, advanced processing and calibration methods have been developed recently to account for fiber-induced birefringence and perform measurements in-vivo [112–114]. Endoscopic applications include the evaluation of atherosclerotic plaques in cardiology [115, 116] and, more recently, the measurement of smooth airway muscle in pulmonology [113, 117, 118].

While PS-OCT offers a wealth of additional information compared to classical OCT, this comes at the cost of some additional system complexity and advanced data processing [106]. The added contrast is also specific to certain tissue types exhibiting sufficient form birefringence. As such, the application should be carefully evaluated to determine the benefit of implementing PS-OCT.

OCT angiography

OCT angiography (OCTA) refers to imaging vasculature in biological tissue. Tissue vascularization holds valuable clinical information as numerous pathological conditions can be associated with irregular vessel structures and abnormal vessel growth or reduction [119, 120]. A few examples of such conditions include cancer [121], inflammation [120], burns and wounds [122], and diabetic retinopathy [123]. OCTA is performed by measuring the motion of scatterers within blood vessels. This motion is detected by observing variations in the OCT signal between two time points. Several different methods exist to quantify these changes based either on the intensity or the phase of the signal [124].

Phase-based methods include Doppler OCT (DOCT), which, in modern FD-OCT systems, measures the depth-resolved phase shift between two overlapping A-lines [125]. DOCT has the advantage that it can directly provide absolute quantification of flow speed and direction, but the disadvantage that it may only do so for the flow component in the axial direction. Several methods with advanced data processing, special beam-scanning patterns, or multi-beam acquisition have been proposed to overcome this limitation, but at the cost of enhanced system complexity and computationally heavy, non-real-time signal processing [125]. Moreover, most implementations have been demonstrated for retinal or dermatological imaging and far less extensively in endoscopic applications, although some research does exist [126]. Phase-based methods have the additional limitation that they are sensitive to bulk tissue motion and the overall phase-stability of the system, both of which are more difficult to control in an endoscopic setting than in bench-top systems [124].

Intensity-based methods offer several advantages over their phase-based counterparts. Firstly, they are sensitive both to transverse and axial flow. Secondly, as they rely on the magnitude of the OCT signal, they do not depend on the phase stability of the system. Intensity methods measure temporal variations of the OCT signal from B-scan to B-scan to detect the presence of flow. This can be achieved in several different ways, including image correlation metrics [127, 128] and by analyzing speckle variance [129, 130]. While these methods can detect flowing scatterers and thus map the microvasculature network, they do not provide direct information on the absolute flow velocities as is possible with phase-based methods. Intensity-based methods also remain sensitive to bulk sample motion as they require consecutive B-scans in the same location or at least with significant overlap. Overall, intensity-based methods have been preferred in endoscopic applications primarily for their sensitivity to transverse flow. Endoscopic OCTA has notably been demonstrated in the esophagus [99, 131] and the rectum [132].

Spectroscopic OCT

As explained in previous sections, OCT imaging is performed by collecting interference spectra spanning a certain wavelength range. These spectra are then Fourier transformed to reconstruct the depth-resolved reflectivity profile of the sample. However, these interference spectra also contain spectroscopic information about the sample. This information can be recovered through time-frequency analysis (TFA) of the OCT interferogram, resulting in a depth-resolved estimation of the optical properties of the sample [133, 134]. Briefly, it is possible to recover the wavelength-resolved reflectivity profile (i.e., a processed A-line) by windowing the interference signal around a certain wavelength and with a given window width. By sliding this window across the entire interference spectrum, the reflectivity profile for all wavelengths can be recovered. The choice of window type and width in this time-frequency analysis plays an important role in the extracted profiles' depth and spectral resolution. Several variants exist including the short-time Fourier transform (STFT), the wavelet transform, and the Wigner distribution [134–136]. After correction for various effects such as sensitivity roll-off and confocal point PSF, it is possible to extract depth-resolved optical properties from the power spectrum, such as the absorption coefficient, μ_a, and the scattering coefficient, μ_s, through fitting or calibration measurements.

As such, spectroscopic OCT (SOCT) enables the extraction of optical properties on a microstructural scale. This effectively circumvents many problems associated with diffuse techniques such as diffuse reflectance spectroscopy (DRS) or differential pathlength spectroscopy (DPS), which only provide optical properties averaged over larger volumes and without depth information. Moreover, SOCT differs from standard OCT only in the data processing algorithms. While it offers several advantages at little additional cost, the applicability of SOCT methods is limited by the utilized wavelength range. Indeed, the spectroscopic information can only be retrieved for wavelengths within the spectral range of the OCT system. Many chromophores of interest (blood in particular) have spectral features in the VIS region and fewer in the NIR. Moreover, these features are usually spectrally broad, requiring wide spectral ranges to capture them effectively. Applying SOCT methods to conventional OCT systems may, therefore, provide limited added value. On the other hand, VIS or ultra-broadband systems may provide more insight with SOCT but incur additional complexity regarding fiber systems, optics, laser sources, and detectors.

OCT attenuation coefficient

Beyond providing qualitative anatomical imaging, the OCT signal can also be analyzed to extract quantitative information. This includes parameters such as the OCT attenuation coefficient, μ_{OCT}, and the backscattering coefficient, $\mu_{b,NA}$. These parameters relate to the sample's optical properties, including the scattering and absorption (μ_s and μ_a, respectively) and the scattering phase function, $p(\theta)$, which describes the probability of scattering direction. While the exact relationship between the measured parameters and the tissue optical properties remains an unsolved problem, the parameters may provide additional contrast that is not directly visible in standard OCT images [137, 138]. Moreover, these parameters (μ_{OCT} in particular) have shown great promise in their ability to differentiate tissues with similar appearances in OCT images. The attenuation coefficient has notably been applied in pre-clinical studies in gynecology, urology, laryngology and cardiology both ex and in vivo [84, 139–142].

Quantitative OCT is advantageous because it provides an objective metric to detect or differentiate various tissue types without requiring changes to standard OCT systems. Moreover, it is compatible with endoscopic imaging, as demonstrated by several previous studies [84, 140, 142]. However, accurate system calibration is crucial to account for system-dependent signal variations such as sensitivity roll-off and confocal point-spread function [138, 143], which can add to the experimental load when several different endoscopic devices are used. The extracted parameters are also highly model-specific. There currently exist several models describing light propagation for OCT as well as competing methodologies for extracting μ_{OCT} [137, 138, 144], potentially leading to different threshold values and conflicting classifications. Therefore, consensus on the methodology will be necessary before establishing validated quantitative discrimination criteria.

2.1.7 Multimodal endoscopic OCT

Multimodal OCT refers to the combination of OCT with one or several other modalities. These added techniques usually aim to provide complementary information to OCT, enhancing the system's diagnostic capabilities. In the case of OCT, which provides exquisite morphological information, it is often combined with methods targeting specific biological or chemical components indicative of physiological state or certain pathologies. However, OCT has also been implemented in multimodal systems for its high imaging speed and ability to scan large regions of tissue in a short time. In such systems, OCT functions as a targeting system to identify regions of interest (ROI), which are then imaged with another technique with enhanced imaging performance, but slower imaging speed [76].

Providing a full review of all multimodal systems that utilize OCT in conjunction with other modalities is beyond the scope of this thesis. Indeed, many such devices, implemented in medicine or experimental biology, are bulk microscopy systems intended for studying biological systems rather than detecting pathologies. They are, therefore, less relevant to the proposed research objectives. In this section, we will focus on multimodal systems that are either already applied in an endoscopic setting or have the potential to be. An overview of such systems is provided in Table 2.1. In this table, all systems combine OCT with at least one other technique, which complements the imaging achievable with OCT alone.

Some of the core challenges in combining techniques lie in ensuring co-registration of the multiple modalities, achieving simultaneous or time-efficient sequential imaging, and minimizing cross-talk, all within the size constraints of an endoscopic probe. Another key challenge lies in developing diagnostic algorithms that effectively incorporate information from multiple modalities.

Table 2.1 List of multimodal OCT systems that have either already been implemented in endoscopic applications or have the potential to be.

Application (or intended application)	Added modalities	Endoscopic?	Year	Ref.
Cancer detection	pH sensing	yes	2021	[145]
	VIS autofluorescence + color imaging	yes	2019	[146]
	Fluorescence lifetime	yes	2022	[147]
	VIS fluorescence spectroscopy	no	2008	[148]
Colorectal cancer detection	NIR fluorescence	yes	2018	[149,150]
	NIR fluorescence	yes	2018	[151]
Esophageal imaging	VIS fluorescence	yes	2012	[152]
	VIS fluorescence	yes	2021	[153]
	Color imaging	yes	2021	[154]
Airway imaging	VIS fluorescence	yes	2013	[155]
	VIS fluorescence	yes	2015	[156]
	VIS autofluorescence	yes	2014	[157]
Intravascular atherosclerotic plaque imaging	Photoacoustic + ultrasound	yes	2015	[158,159]
	diffuse NIR spectroscopy	yes	2013	[160]
	VIS fluorescence	yes	2012	[161]
	NIR fluorescence	yes	2011	[162]
	NIR fluorescence	yes	2014	[163]
	NIR autofluorescence	yes	2016	[164]
	NIR autofluorescence	yes	2015	[165]
	Fluorescence lifetime	yes	2020	[166]
	Fluorescence lifetime	no	2018	[167]
	Fluorescence lifetime	yes	2018	[168]
	Multiphoton luminescence	yes	2015	[169]
Morpho-chemical tissue characterization	Multiphoton + reflectance	yes	2021	[170]
	Fluorescence lifetime	no	2017	[171]
Ovarian cancer detection	Photoacoustic + ultrasound	yes	2011	[172]
	VIS autofluorescence	yes	2022	[173]
Oocyte maturity evaluation in IVF model	pH sensing	yes	2022	[174]

Fluorescence-based techniques

As apparent in Table 2.1, the modality most often combined with OCT is some form of fluorescence imaging, including autofluorescence imaging (AFI), fluorescence imaging using exogenous fluorophores in the VIS and NIR spectral ranges, and fluorescence lifetime imaging (FLIM). In AFI, the fluorescent signal of endogenous molecules such as collagen, keratin, elastin, porphyrins, reduced nicotinamide adenine dinucleotide (NADH), and oxidized flavin adenine dinucleotide (FAD) is measured after excitation with short wavelengths (UV and blue VIS light typically — although NIR AFI has also been demonstrated) [175]. Variations in the relative intensities of the fluorescent emissions can reveal changes in metabolic activity or tissue remodeling, which can, in turn, indicate a pathological state [176]. The contributions from different fluorophores are usually separated into distinct detection channels through spectral filtering. Alternatively, the full spectrum can be measured as a function of wavelength (i.e., fluorescence spectroscopy). When the fluorophores of interest present significant overlap in their emission spectra, it becomes difficult to distinguish their contributions. FLIM solves this by differentiating fluorophores based on their fluorescence lifetime, defined as the average time an electron remains in the excited state prior to radiative decay and emission of a photon [176]. Moreover, FLIM signals are affected by chemical factors and can, therefore, be used to gain insight into the microenvironment of cells and tissues [177].

Fluorescence imaging can also be performed using exogenous contrast agents, which have both significant advantages and disadvantages over endogenous fluorophores. The primary limitation of using exogenous markers is that only a small number of substances are permitted for in vivo use. Those that are typically lack specificity to the target diseases [178]. However, these fluorophores and others may be conjugated with tracer molecules or antibodies that enable highly specific fluorescence imaging [179]. Moreover, the emission spectra of these exogenous dyes may be tailored to the application, allowing multiplexed imaging with multiple dyes and higher fluorescence efficiencies.

Ultrasound and photoacoustic imaging

OCT has also been combined with ultrasound (US) and photoacoustic imaging (PAI). While OCT and US share many similarities regarding cross-sectional imaging capabilities, their resolution and maximum imaging depth differ. OCT provides microscopic detail on tissue structure, but only up to a limited depth, while US provides significantly enhanced imaging depth at lower resolution. Compared with conventional OCT imaging, combining OCT with US enables imaging of deep tissue structures and improves the interpretability of OCT images by matching them with co-registered US images, a well-established technique with which clinicians are already familiar.

As depicted in Fig. 1.1, PAI allows deeper imaging than OCT while maintaining comparable resolution. The technique relies on pulsed optical illumination to generate thermal expansion through light absorption, creating acoustic waves in the tissue. Ultrasound transducers then detect these acoustic waves as they would be in conventional US [180]. Because PAI relies on the absorption of light to generate an acoustic wave, it is sensitive to the optical absorption coefficient. Using multispectral PAI, which performs measurements using multiple illumination wavelengths, it becomes possible to quantify the relative concentrations of the different chromophores present in tissue [181]. As such, the information provided by PAI is complementary to that obtained with OCT, which relies principally on scattering for contrast.

RGB imaging and reflectance spectroscopy

Color- or RGB-imaging refers to the reconstruction of color images as they would appear when obtained with a camera. This implies that each pixel is assigned a red/green/blue triplet that encodes the color appearance. Fundamentally, color appearance allows the separation between tissue types, as depicted in Fig. 2.9 , or physiological state [182, 183]. For example, a redder tissue may indicate increased perfusion or inflammation. It is also possible to enhance the contrast generated by certain chromophores by illuminating the sample with specific colors or wavelengths for which these chromophores absorb differently than others. For example, narrow-band imaging (NBI) illuminates the sample exclusively with blue and green light, absorbed significantly more by blood, appearing darker than the surrounding tissue. NBI has been used to highlight surface microvasculature and superficial mucosal patterns due to the shallow penetration depth of blue/green light [184, 185]. Aside from providing additional tissue contrast, combining OCT with RGB imaging has the advantage of facilitating the interpretation of OCT datasets by providing a familiar visualization. This is especially true in endoscopic applications where white light video endoscopy (WLE) is widespread, such as in esophageal and colorectal imaging.

Aside from direct visual interpretation, RGB images can also provide information on the optical properties of the studied sample. Indeed, each color channel can be interpreted as a spectral band collecting light reflected off the sample. In biological imaging, the reflected light depends on the illumination as well as the reflectance spectrum of the sample. This reflectance spectrum depends on the optical properties of the sample as well as the imaging geometry. The exact relationship between the reflectance and these parameters is highly relevant to endoscopic applications and is discussed further in Section 2.3. Because of this relationship between color, reflectance spectrum, optical properties, and molecular composition, RGB imaging can provide insight into the relative abundance of relevant chromophores in biological tissue.

In essence, RGB imaging is also a form of spectroscopic imaging. Indeed, the reflected light is separated into three (broadband) spectral channels. By extending this principle to more narrow-band channels, it is possible to directly assess the reflectance spectrum of the sample, which can be analyzed to extract optical properties and molecular content. These methods are usually referred to as *multi*- or *hyperspectral imaging* (MSI and HSI, respectively). Such spectroscopic imaging methods are central to this thesis and are explained in more detail in Section 2.3.

2.1.8 OCT endoscopes

The implementation of in vivo, endoscopic OCT is contingent on developing safe, robust, and reliable endoscopes. Fundamentally, all endoscopes must accomplish three core functions:

1. transport light to and from the sample;
2. focus the light onto the sample;
3. perform a stable scan of the laser beam on the sample to obtain B- and C-scans.

In the sections below, we briefly discuss each of these functions (in reverse order) and their impact on endoscope design.

Scanning and stabilization

The intended clinical application of the endoscope, or rather the organ in which it will be used, defines some of its key parameters: scan pattern, size, and shape. OCT endoscopes can be roughly separated into two categories by imaging direction: forward-viewing and side-viewing. In luminal (i.e., tube-shaped) organs, it is convenient to utilize a side-viewing probe with circular scanning. This allows imaging of circular cross-sections of the organ. Coupled with axial motion along the organ's axis, this results in a helical scan and comprehensive volumetric imaging. Such probes represent the majority of OCT endoscopes because of the abundance of luminal structures in the human body and the simplified engineering compared to forward-viewing probes. Forward-viewing probes are typically used in non-luminal organs for biopsy guidance, device placement, or treatment monitoring. They are, however, less suited for surveying larger areas of tissue for screening purposes [2]. Within the context of this thesis, we concentrate on side-viewing probes, as they are more adapted to the chosen clinical application. Several examples of different side-viewing endoscopes are presented in Fig. 2.10.

Size and shape obviously impact which organs the endoscope can reach and, therefore, image. However, these parameters may also influence imaging stability by controlling the distance between the endoscope and the sample surface. Maintaining this distance is necessary for proper imaging because of the limited depth of focus of the laser beam and the limited imaging range of OCT. Failure to do so will result in out-of-focus, blurry images. In luminal organs, if the endoscope is the same size as the lumen, it will naturally be held in place by the walls of the organ and maintain a constant distance from the tissue surface. In Fig. 2.10, the left column consists of smaller diameter devices, often called *catheter* probes, which have diameters ranging from a few millimeters down to several hundred microns [2, 146, 186]. Such endoscopes are used in applications in cardiology, pulmonology, urology, and gynecology in small lumens such as blood vessels, small airways, or biopsy [140, 186–191]. In the same figure, the right column presents two endoscopes designs for large lumen imaging, primarily applied in esophageal imaging. The top two (D & E) are rigid, pill-shaped devices called *tethered capsule endescopes* (TCE) [192–195], while the bottom one (F) is composed of a small diameter catheter (similar to those in the left column) surrounded by an inflatable balloon sheath [196]. For all endoscopes in Fig. 2.10, B-scans are acquired through the rotation of the laser beam and C-scans through the axial motion of the device, typically through the retraction or *pullback* of the device. By synchronizing the rate of retraction with the rotation of the probe, it is possible to image the sample entirely along the length of the pullback.

The endoscopes in Fig. 2.10 can be further subdivided based on how the rotational motion of the beam is generated. Endoscopes A, B, D, and F belong in the *proximal scanning* category, where the rotation is generated upstream of the endoscope and transmitted to the complete assembly by a torque coil. Proximal scanning has the advantage of strongly reducing the overall cost of the device, such that they become disposable. However, proximal scanning also causes distortions in the images due to stress-induced refractive index changes and non-uniform rotation speeds (typically referred to as *non-uniform rotation*

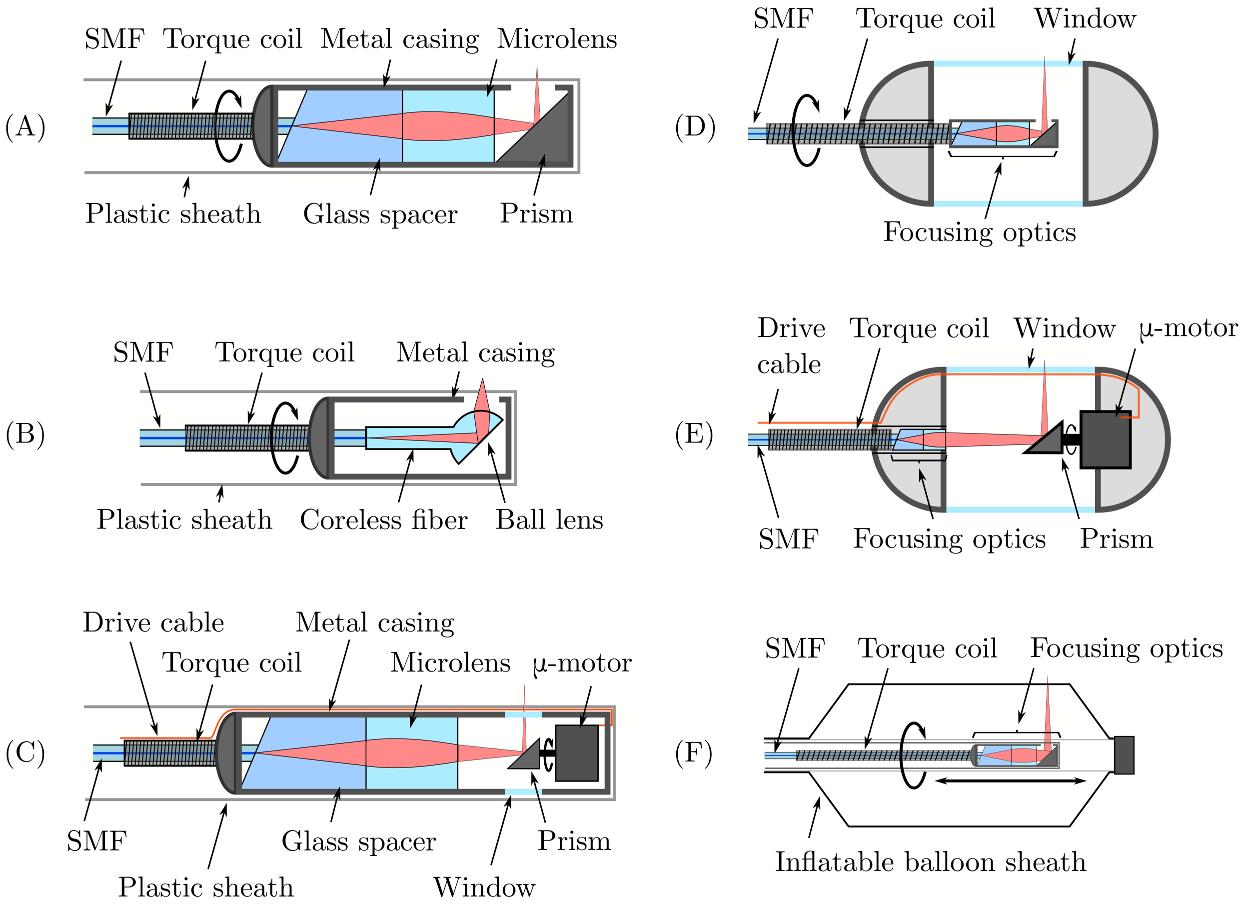

Figure 2.10 Various designs of side-viewing OCT endoscopes. The probes in the left column (A-C) are for small-diameter lumens, while those in the right column (D-F) are for large lumens. (A) Catheter probe using microlens and proximal scanning. (B) Catheter probe using ball lens and proximal scanning. (C) Catheter probe using ball lens and distal scanning. (D) Tethered capsule endoscope using proximal scanning. (E) Tethered capsule endoscope using distal scanning. (F) Inflatable balloon catheter with distal scanning. Figure partially adapted from [2].

distrortion or NURD). In proximal scanning, the device used to generate the fiber rotation is called a *fiber-optic rotary joint* (FORJ). In its simplest form, a FORJ transfers light from a static fiber to a rotating one, typically using a pair of lenses. The FORJ also usually handles the pullback using linear translation stages.

The second category is called *distal scanning* and uses a micromotor inside the endoscope to achieve beam scanning (e.g., endoscopes C and E in Fig. 2.10). Distal scanning has the advantage of enhanced stability (i.e., less NURD) and does not induce signal distortions. Distal scanning endoscopes have been reported as the favored solution for OCTA and PS-OCT applications [112,197,198], which are sensitive to the distortions induced by proximal scanning. Distal scanning also enables higher scanning speeds than proximal scanning. However, including the micromotor in the endoscope also has several downsides. Firstly, such micromotors often carry a high price tag ($>$ 1000 \$) which precludes using such endoscopes as disposable devices. Moreover, the micromotors can be fragile, making the endoscope more delicate to handle. Secondly, the endoscopes are subject to stricter clinical and fabrication requirements. Being non-disposable, they must undergo repeated cleaning or sterilization protocols which can degrade the optical performance over time. Furthermore, using an electrical device in vivo also carries additional safety requirements. Finally, although micromotors as small as 1 mm exist, the engineering complexity and costs associated with designing and fabricating submillimeter, distal-scanning endoscopes are significant.

Focusing

The second key function that the endoscope must perform is to focus the light into the sample with the correct working distance and numerical aperture. To achieve this, light from the single-mode fiber core is allowed to expand in a glass space or a coreless fiber before being focused onto the sample by a focusing element. Although most OCT endoscopes use gradient-index (GRIN) lenses, focusing has also been demonstrated using standard refractive lenses [199], ball-lenses [200], diffractive lenses [194, 201, 202], and ellipsoidal mirrors [203]. Each variant offers advantages and disadvantages in terms of size, robustness, cost, commercial availability, and optical performance. Within the context of multimodal imaging, it is imperative to consider the chromatic behavior of the focusing element if it is shared between two or more modalities that do not use the same spectral range. This includes both chromatic focal shifts and back-reflections from optical interfaces. The problem of chromatic behavior also appears in the FORJ used in conjunction with proximal scanning endoscopes. Indeed, backreflections may cause spurious background signals, while focal shifts may reduce the coupling efficiency between the static and rotating fibers.

Light transport

The last essential function of an endoscopic OCT probe is the transport of light to and from the sample. This is achieved using single-mode optical fibers (SMF). Single mode fibers have a small core diameters and a normalized frequency below 2.405, resulting in a unique possible propagation mode in the waveguide, i.e. single-mode operation. This is necessary for OCT imaging to preserve the temporal coherence and the phase of the signal. Without single-mode propagation, the signal from a reflector would accumulate different delays relative to the reference arm by traveling along the different available propagation modes, i.e. multimode propagation (not to be confused with multimodal imaging which refers to the combination of techniques). Multimode propagation would result in duplicate images after OCT data processing. Fibers operating in this regime are logically called multimode fibers (MMF). They typically have a larger core diameter and can accomodate much higher light throughput. For multimodal imaging, the same fiber may be used to transmit the optical signals from the other modalities aside from OCT. In this configuration, however, the collection efficiency for the other optical techniques (such as reflectance or fluorescence imaging) is often insufficient for in vivo imaging due to the small diameter of the SMF core. One solution is to use one or more additional fibers for the added modality. However, this can increase the complexity of the optical design and compromise the co-registration of the various modalities. Another approach, and the one adopted in this thesis, is the use of double-clad fiber (DCF), which is comprised of two co-centric channels in which light can be transported: a single-mode core and a multimode inner cladding. This technology is explained in detail in the following section.

2.2 Double-clad fiber technologies

A double-clad fiber (DCF) is a fiber comprised of three concentric layers, two of which are capable of guiding optical signals. These are a single-mode core, a multimode inner cladding, and an outer cladding, as depicted in Fig. 2.11. Optical signals may be transmitted through both the core and the inner cladding with little to no cross-talk. In imaging applications, this allows coherent imaging (e.g., OCT) through the core, while the larger diameter and numerical aperture of the inner cladding provide enhanced collection efficiency, useful in other imaging techniques such as reflectance or fluorescence imaging [204–206]. Moreover, the concentric geometry guarantees alignment-free co-registration of the two channels. As such, DCF represents an excellent tool for multimodal endoscopic imaging, particularly for systems aiming to combine OCT with other techniques. This has been widely recognized in the scientific community as the vast majority of the multimodal systems presented in Table 2.1 are, in fact, DCF-based systems. Beyond imaging and diagnostic systems, double-clad fibers have also been implemented in therapeutic applications, where the MM inner cladding is used to transmit high-power light for laser therapy while the core is used for concurrent imaging and guidance [207, 208].

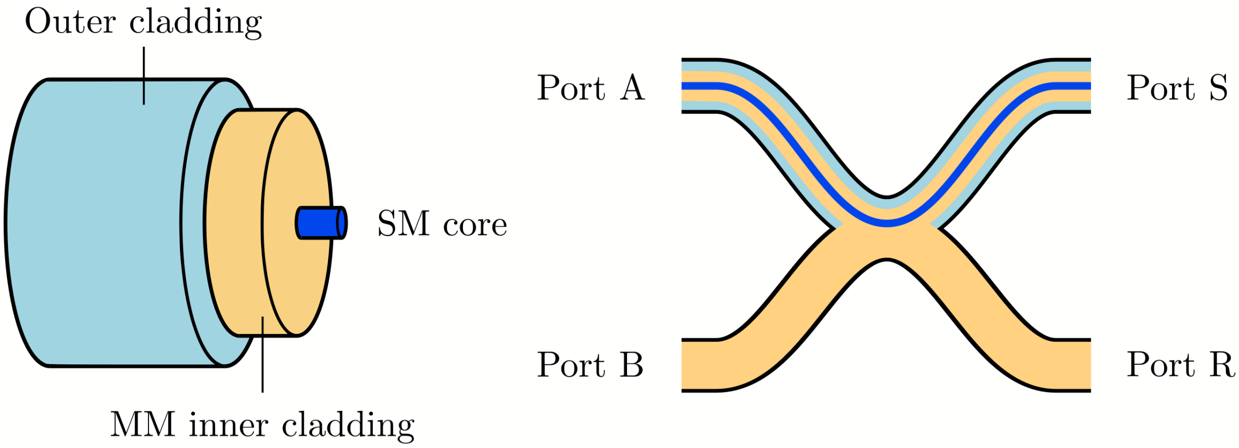

Figure 2.11 Schematic representation of a double-clad fiber (left) and a double-clad fiber coupler (right).

To maximize the utility of DCFs, it is necessary to be able to address the two channels (core and inner cladding) separately. Double-clad fiber couplers (DCFC) were developed to provide a fiber-based solution to this problem. In recent years, our group has proposed asymmetric double-clad fiber couplers that consist of a DCF fused to a MMF with higher etendue [209–211], as depicted in Fig. 2.11. Such couplers can be designed to operate in *extraction mode*, where the aim is to extract the light collected in the inner cladding of the DCF (i.e., high transfer from port S to port B), *injection mode*, where light is coupled from the MMF to the inner cladding of the DCF (i.e., high transfer from port B to port S), or *bi-directional mode*, where both injection and extraction occur, but at lower efficiencies [212]. In all cases, the SM operation in the DCF core is preserved (> 95% transfer between port A and port S, in both directions). Port R is typically not used and terminated with a beam dump to minimize return losses. This separation of channels into two output ports is particularly interesting because it enables independent filtering and detection. The appropriate detectors can then be used for each modality, and separate filtering may be performed to minimize cross-talk between the modalities. In this thesis, DCFCs are used in extraction mode in the systems presented in Chapters 3, 4 and 7, and in bi-directional mode in the system described in Chapter 5.

2.3 Imaging reflectance spectroscopy

In the broadest sense, spectroscopy is defined as the study of the interaction between matter and electromagnetic radiation as a function of wavelength or frequency [46]. This includes a wide variety of linear and non-linear interactions such as scattering, absorption, fluorescence, multiphoton fluorescence, Raman scattering, and many more. In this thesis, we concentrate on the study of absorption and scattering in the VIS and NIR spectral ranges (roughly 400–1700 nm) using reflectance spectroscopy methods. These techniques include point-scanning hyper- and multispectral imaging (HSI and MSI, respectively) and single-fiber reflectance spectroscopy (SFR).

2.3.1 Hyper- and multispectral imaging

Hyper- and multispectral imaging refers to imaging a scene or sample at several wavelengths across a certain spectral range [213, 214]. The distinction between the hyper- and multi- prefixes comes from the number of spectral bands acquired, where HSI usually has many (typically a continuum across a specific range) while MSI has a few distinct bands. In reflectance-mode HSI and MSI measurements, the stack of images is stored in a 3D data volume called *hypercube*, which has two spatial (x,y) and one spectral (λ) dimensions, as depicted in Fig. 2.12. More advanced HSI and MSI measurements can also have higher dimensionality and include the axial (z) or temporal (t) dimensions. Figure 2.12 also depicts several strategies to acquire the 3D hypercube. *Point scanning* implies that signal is only acquired from one spatial location at a time and that all spectral components are measured simultaneously by a spectrometer. *Pushbroom* HSI systems use a 2D detector with one dimension measuring a spatial dimension while tho other measures the spectral content. *Staring* HSI systems acquire the full 2D image (i.e., both spatial dimensions) for each spectral band one at a time. This can be achieved by filtering the reflected light or with band-by-band illumination. Finally, *snapshot* systems acquire the full hypercube at once but at the cost of resolution in either the spatial or spectral dimensions (often both). With recent development in spectral filter fabrication, a convenient way to perform snapshot HSI is with a 2D image camera where spectral filter arrays have been applied to the sensor [214–216]. Therefore, the number of spatial data points is divided by the number of different spectral filters, resulting in lower spatial resolution.

To extract meaningful spectroscopic information about the sample, the data acquired with

HSI/MSI must be corrected to account for several factors, such as illumination spectrum, system response, imaging geometry, and dark signal. The corrected spectral reflectance $R(\lambda)$ is calculated following:

$$R(\lambda) = \frac{I_{\text{raw}} - I_{\text{dark}}}{I_{\text{white}} - I_{\text{dark}}}, \tag{2.23}$$

where I_{raw} is the raw signal measured with the sample, I_{dark} is the dark signal measured with no illumination, and I_{white} is the signal from a reference sample with a known reflectance spectrum, usually a Spectralon diffuse reflectance target [213]. Once obtained, the corrected reflectance can be used in various clinically useful ways, such as extracting (approximate) maps of optical properties or chromophore concentrations [217], contrast enhancement between specific components [218] (e.g., blood with narrow-band imaging), or automatic tissue classification.

HSI and MSI have been implemented in a wide variety of medical applications for disease diagnosis and surgical guidance. In particular, the techniques have shown great promise in cancer detection. Most systems presented in literature analyze excised tissue or biopsy samples, however several endoscopic applications have emerged such as in the cervix [219], GI-tract (esophagus, stomach, intestines, and colon) [218, 220–226], and larynx [227]. Endoscopic systems mostly rely on snapshot and staring acquisition modes as they do not require moving parts in the distal part of the endoscope. However, Yoon et al. also demonstrated an endoscopic pushbroom system where the imaging plane is transferred out of the body via a fiber bundle and scanned externally [224, 225]. With ongoing advancements in camera miniaturization and filter technologies, it is expected that many more HSI/MSI endoscopy platforms will be implemented in the coming years.

While HSI/MSI systems have shown great potential in differentiating different tissues or identifying pathological tissue, the method is still lacking in its ability to connect the measured reflectance spectra to the true biochemical properties of the images sample as well as relating the spectral variations to the diseased state of tissue [228]. This can be attributed partly to the complexity of the widefield imaging geometry, where many parameters remain at least partially uncontrolled. Such parameters include the distance to the sample, the sample surface geometry, the illumination profile, the glare component, and the heterogeneity of the sample. Moreover, it is well known that, without significant approximations, extracting optical properties from reflectance measurements is an ill-posed, under-determined inverse problem that may have multiple different solutions [228, 229]. Despite this fundamental limitation, spectral imaging may still provide

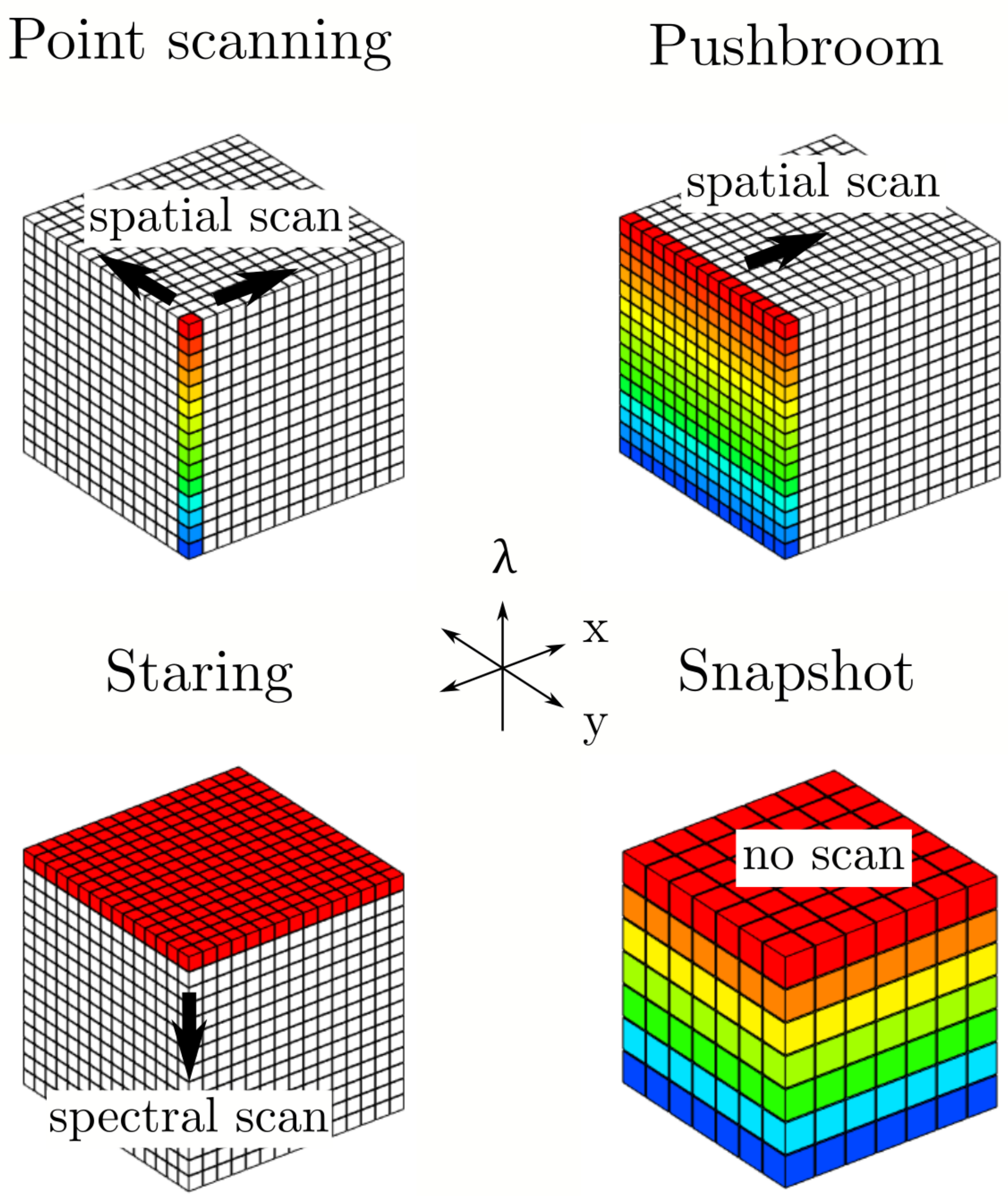

Figure 2.12 Schematic representation of HSI/MSI hypercubes for different acquisition strategies. In each figure, the black arrows indicate the "direction" of the scan necessary to acquire the full hypercube. The colored voxels indicate the data points acquired within a single measurement step.

valuable diagnostic information by applying the ever-expanding arsenal of advanced classification methods directly to reflectance spectra.

In the scope of this thesis, it is interesting to consider how such HSI/MSI may be combined with side-viewing OCT probes and the double-clad fiber technologies presented in the previous sections. Within this context, the point-scanning acquisition mode is favorable as it enables true co-registration between the OCT and spectral imaging without substantially complicating the endoscope design. Moreover, by utilizing internal illumination (i.e., using the same fiber for both illumination and collection), the imaging geometry is significantly simplified and approaches that of single fiber reflectance spectroscopy (SFR): a point spectroscopy method for which the recovery of optical properties has been extensively studied. Within this thesis, we investigate combined OCT and HSI with external illumination in Chapter 3, with internal illumination in Chapters 4 and 5.

2.3.2 Single fiber reflectance spectroscopy

Single fiber reflectance spectroscopy (SFR) is a point spectroscopy technique initially derived from diffuse reflectance spectroscopy (DRS). DRS uses a combination of two fibers, one for input and one for output, to probe the optical properties of the sample. SFR refers to the case where the source-detector separation is reduced to 0, such that the illumination and collection are performed through a single fiber. In this thesis, we also investigate an extension of SFR dubbed imaging single fiber reflectance spectroscopy (iSFR), where the fiber is not in direct contact with the sample but imaged onto the sample with some optical components. More specifically, we investigate iSFR in conjuction with double-clad fiber, which enables the combination with OCT. These configurations are illustrated in Fig. 2.13.

SFR offers several advantages that make it particularly appealing for endoscopic applications. Its small form factor (usually a few hundred microns in diameter) is generally beneficial as it can easily be integrated into small devices and even biopsy needles. Furthermore, SFR has a small sampling volume and shallow penetration depth, roughly proportional to the fiber diameter [230]. The small sampling volume allows SFR to be sensitive to tissue changes on a small spatial scale rather than averaging over a large volume. The shallow penetration depth is advantageous for detecting neoplastic lesions appearing in the superficial layers of epithelial tissue. As such, the technique has already been applied for cancer detection in various organs including the cervix [231, 232], breast [233], prostate [234], pancreas [235, 236], esophagus [37], and lungs [237].

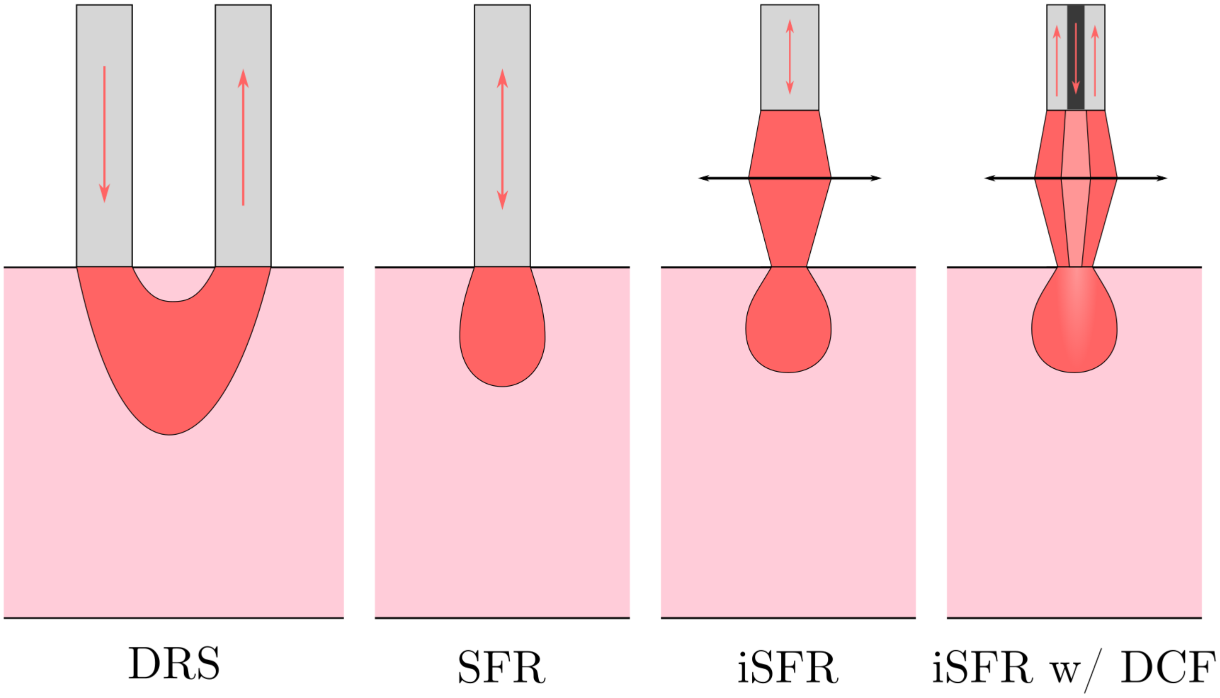

Figure 2.13 Schematic representation of the sensing configuration for diffuse reflectance spectroscopy, single fiber reflectance spectroscopy and imaging single fiber reflectance spectroscopy. The red zone in the sample represents the probed volume, through which most detected photons propagate before being collected by the detector fiber. The iSFR with DCF depicts core illumination and cladding collection although other modes are possible.

Unlike for DRS, the measured signals for SFR cannot be described using the diffusion approximation to the radiative transfer equation (RTE), as the average photon path length in the sample is on the same order of magnitude as the transport mean free path [238]. As such, photons are described as being in the *subdiffuse* regime rather than the diffuse regime. Subdiffuse photons only scatter a few times before being detected and are, therefore, much more sensitive to the scattering phase function, $p(\theta)$, which describes the probability distribution of scattering angles. While this sensitivity to the phase function complicates the modeling of the signal compared to the diffuse regime, it also provides an additional contrast mechanism for tissue differentiation [37]. No analytical solutions exist to describe subdiffuse propagation. However, several semi-empirical models have been proposed to relate the measured reflectance spectrum to the sample optical properties (μ_a,μ_s and $p(\theta)$) and the measurement geometry, including fiber diameter and numerical aperture [237–243]. To this day, the best model is the one developed by Post et al. [241], which boasts a median error of 5.6% when validated with Monte Carlo (MC) simulations across a wide range of optical properties. It is important to point out that the practical implementation of this model requires at least two measurements with fibers of different diameters (dubbed multi-diameter of MDSFR). The model relies on least-square fitting to extract the optical properties from the reflectance spectra. If only one fiber size is used, the equation system is underdetermined, leading to an unstable fitting process [244]. Experimentally, MDSFR may lead to errors as the signal collected from the two fibers does not originate from the same location on the sample.

Finally, it is critical to recognize the similarities between the (contact) SFR measurement geometry and that of non-contact iSFR. In their models, Post et al. describe reflectance as a function of the sample's optical properties and fiber properties (size and NA). In iSFR, the fiber size and NA are simply projected onto the sample by the optical components with some magnification. As such, the models should still apply, and SFR theory may be used to extract accurate optical properties. It is important to note that performing iSFR with DCF leads to a slightly different illumination/collection geometry, which will likely require adapting the standard SFR models, despite the dominant propagation regime still being subdiffuse. Combining iSFR with a scanning mechanism makes it possible to extend iSFR from a point measurement to an imaging application, similar to point-scanning HSI.

2.4 Concluding remarks

In conclusion, OCT has already made its mark in a wide variety of endoscopic applications. However, it has yet to establish itself as a standalone replacement for tissue biopsies, including in esophageal imaging. Beyond structural imaging, advanced OCT methods provide access to additional functional and morpho-chemical information. Aside from functional extensions, combining OCT with additional modalities to compensate for its shortcomings also shows great promise. However, this approach requires a careful selection of the added modality based on the target application and target structural, chemical, or biological markers. Moreover, designing multimodal systems and endoscopic probes requires considerable effort to ensure optimal operation of all integrated techniques. Double-clad fibers and associated technologies may provide an avenue for concurrent and co-registered by simultaneously using the SM core of the DCF for OCT imaging and the MM inner-cladding for the secondary method. Amongst the several candidate techniques, we selected VIS-NIR spectroscopic imaging as the second modality because it has already been applied in a wide variety of fields for the specific purpose of cancer detection. We investigate the various embodiments of spectroscopic imaging, including HSI, MSI, and imaging SFR, and identify each method's technical and theoretical aspects that may be incorporated into the final multimodal system to achieve maximum performance.

CHAPTER 3 COMBINED OPTICAL COHERENCE TOMOGRAPHY AND HYPERSPECTRAL IMAGING USING A DOUBLE-CLAD FIBER COUPLER

3.1 Introduction

Optical coherence tomography (OCT) is a high-speed, low-coherence interferometry technique that allows high-resolution, depth-resolved imaging in biological tissue [45]. In recent years, it has become a gold standard technique in ophthalmology [48,77,245] and an emerging tool in various other fields such as cardiology [82], gastroenterology [192, 246], laryngology [247], gynecology [248, 249], and dermatology [250]. OCT is particularly interesting for its ability to provide micron-scale, 3D imaging up to several millimeters deep into biological tissue. However, as detailed in Chapter 2, in its standard implementation OCT only provides limited information about the bio-molecular content of the studied sample [76]. While spectroscopic OCT (S-OCT), a functional extension of OCT, may provide depth-resolved spectroscopic information [135, 251–254], most relevant chromophores have few spectral features in OCT's NIR band, limiting the efficacy of the approach. S-OCT may be extended to the VIS spectral range where more relevant spectral features are located, but this comes with numerous additional technical difficulties. Such difficulties include (but are not limited to) the availability of coherent sources and associated high-speed detectors with sufficient bandwidth and spectral resolution for meaningful spectral analysis, the presence of significant dispersion, and the limited penetration depth of VIS light. As such, the access to molecular composition remains limited with OCT alone.

Hyperspectral imaging (HSI), on the other hand, provides 2D images (without depth resolution) of the sample in different spectral bands [213], as depicted in Fig. 2.12. A reflectance spectrum is acquired for each pixel in the field of view (FOV). These reflectance spectra carry information about the local optical properties, which can be analyzed to extract chemical and physiological information. The method has been implemented successfully in a variety of fields, such as surgical guidance [255–257], wound assessment [258], and diagnosis of cancer [259–261], retinal diseases [262–264], and circulatory diseases [265–267].

The combination of OCT and HSI enables a more complete analysis of the studied tissue because they provide complementary data. While other groups have previously demonstrated this combination in free-space [268, 269], we are the first to combine the two in a single all-fiber system, based on the use of double-clad fiber (DCF) and a double-clad fiber coupler (DCFC). As depicted in Fig. 2.11, a DCF possesses two independent channels, one multimode (MM) inner-cladding, and one single mode (SM) core, each of which can carry a signal independently. Through the use of a DCFC, it is possible to separate these two channels efficiently [270–272] to perform parallel imaging with two techniques. DCFC-based systems combining OCT with other techniques have been demonstrated previously, including combinations with fluorescence imaging [155,156], spectrally-encoded confocal microscopy [273], and laser marking [207]. This fiber-based approach provides enhanced robustness simplifying the implementation of such systems in a clinical setting and their potential miniaturization into endoscopic devices. We herein present the combination of OCT and HSI using a DCFC. OCT is performed through the SM core of the DCF, while HSI spectra are collected through the MM inner-cladding and measured with a spectrometer. We first characterize the performance of the proposed setup and then demonstrate combined imaging on biological tissue.

3.2 Methods

3.2.1 Experimental setup

The experimental setup is presented in 3.1. It consists of a commercial OCT system (OCM1300SS, Thorlabs, USA) with a DCFC (DC1300LE, Castor Optics, Canada) inserted in the sample arm. The commercial OCT system incorporates a wavelength-swept laser (SL1325-P16, Thorlabs) centered at 1325 ± 50 nm, with a sweep rate of 16 kHz and an integrated MZI-clock for k-linearization. OCT light is split into the sample and reference arm by a Michelson-type interferometer module (INT-MSI-1300). The sample arm port is connected to a segment of SMF28, which is fusion spliced to the DCF at port A of the DCFC, such that the SMF28 signal is coupled exclusively into the DCF core. The OCT light is transported in the DCF core from port A to port S, where it is collimated using a 16 mm collimation lens (C2: FC260APC-C, Thorlabs). The collimated beam is scanned on the sample using a two-axis galvanometer (G: GVS002, Thorlabs) and an uncoated 50 mm plano-convex lens (L: LA1131, Thorlabs). The galvanometer-based scanner and lens are placed exactly one focal length apart to achieve a telecentric scan. The OCT light backscattered from the sample and collected by the DCF core is transported back from port S to port A and to the interferometer module. It is important to note that DCF has the same dispersion properties as SMF28. As such, the fiber length in the reference arm is simply the sum of all fiber lengths in the sample arm. No additional hardware dispersion compensation methods were implemented. In the module, the interference signal with the reference arm is detected by a 15 MHz dual-balanced detector. The electrical signal is then digitized, processed, and displayed using the integrated digitizer and software.

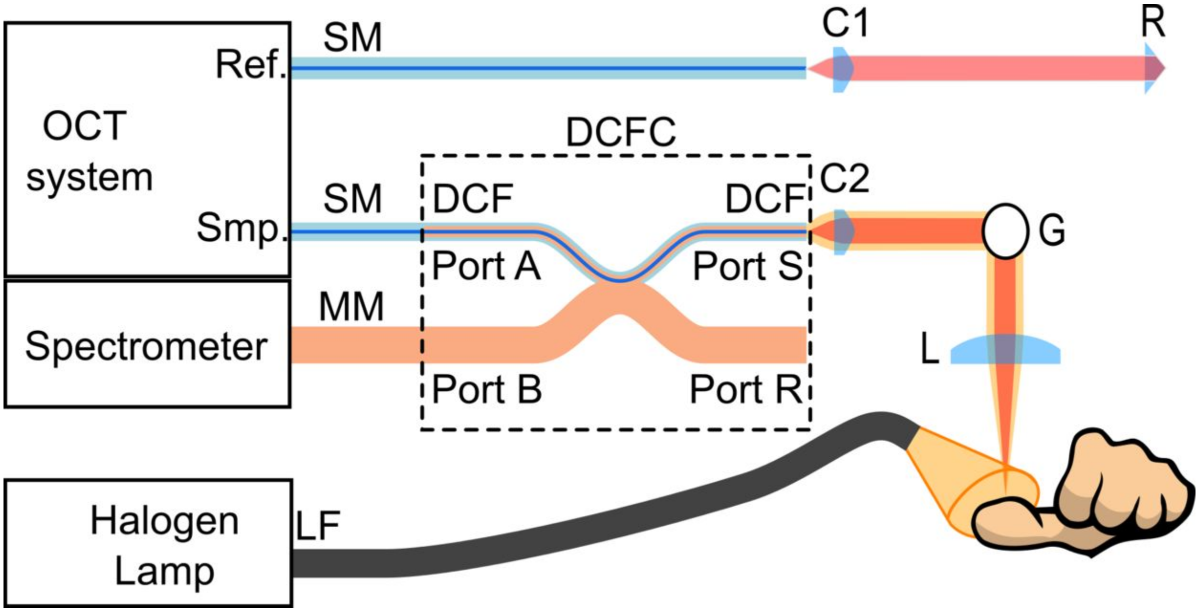

Figure 3.1 OCT-HSI optical setup: Ref, reference arm port; Smp, sample arm port; SM, single-mode fiber; MM, multimode fiber; DCF, double-clad fiber; DCFC, double-clad fiber coupler; C1 and C2, collimation lenses; G, dual-axis galvanometers; L, focalization lens; R, retroreflector prism; LF, light guide fiber. Figure reproduced from Guay-Lord, Attendu et al. [3] with permission from SPIE.

HSI illumination is carried out using an external halogen lamp (MKII fiber optic light, Nikon Inc., USA) coupled into a light guide (LF). For a given position of the galvanometers, light from a particular spot on the sample is collected by the DCF inner-cladding. This light is extracted from the inner cladding by the DCFC (port S to port B) with ≥60% efficiency and measured by a spectrometer (Maya2000, Ocean Optics, USA). Although the spectrometer can detect light from 200 to 1100 nm, the measurement range for our experiments was restricted to the range from 450 to 800 nm, primarily due to the spectrum of the HSI illumination source. It is important to note that some HSI light couples into the core of DCF and is transported to the OCT detector. However, no cross-talk was observed as the OCT detector is not sensitive to the VIS light from the halogen lamp. In the opposite scenario, where the OCT signal (centered at 1325 nm) couples into the inner cladding, there is also no cross-talk as this signal is outside the detection range of the spectrometer.

OCT and HSI acquisitions are currently carried out sequentially due to the difference in acquisition speeds: 16 kHz for OCT and 125 Hz for HSI. To minimize motion artifacts, the sample was firmly immobilized throughout both acquisitions. The shared FOV during imaging of biological tissue was $\sim 6 \times 6$ mm^2. During acquisitions, the illumination sources for both techniques were left on to evaluate potential cross-talk. OCT C-scans of $512 \times 512 \times 512$ pixels were acquired with the commercial software in about 20 s. HSI acquisitions were performed with in-house Labview software (Labview, National Instruments, USA). Due to the low acquisition speed, HSI images were limited to 75×75 pixels for a total measurement time of 45 s. We also perform spectral binning of 10 adjacent spectral pixels to enhance SNR, resulting in a 4.3 nm spectral resolution.

3.2.2 Signal and image processing

The spectral reflectance of each pixel, $R(\lambda)$, is determined using:

$$R(\lambda) = \frac{I_s(\lambda) - I_b(\lambda)}{I_r(\lambda) - I_b(\lambda)}, \tag{3.1}$$

where I_s, I_b, and I_r are the measured sample, background, and dark spectra, respectively. The background is measured with no sample, while the reference measurement is performed with a Spectralon reference target (SRS-99-020, Labsphere, USA), which has a uniform spectral reflectance from 250–2500 nm. Using the reflectance spectrum it is possible to predict the reflected power spectrum, $I(\lambda)$, for a given illumination, $S(\lambda)$, as described by:

$$I(\lambda) = R(\lambda) \cdot S(\lambda). \tag{3.2}$$

From the reflected signal, it is possible to determine the color appearance the sampled region would appear to a camera or the human eye. For the human eye, the spectrum can be converted into RGB coordinates using the well-established CIE1931 spectrum-to-color conversion methods [274] (more details on this in Chapter 4).

The spectral reflectance can also be used to extract molecular information about the sample. A simple but helpful approximation is the logarithm of the inverse reflectance (LIR), which is described in Eq. 3.3 and estimates the absorbance spectrum of the sample [275]:

$$LIR(\lambda) = -\log_{10}[R(\lambda)]. \tag{3.3}$$

The absorbance spectrum is of interest because it is a linear combination of the absorbance of the constituents, such as blood, water, fat, and melanin, in the case of biological tissue.

These components can then be emphasized in the images by selecting wavelength bands corresponding to specific absorption peaks. Moreover, the relative concentrations of the components, which is clinically relevant information, can be estimated using spectral unmixing methods [276].

3.2.3 Data fusion

During the OCT acquisition, the FOV was defined in the commercial OCT software, which internally generated a voltage ramp to drive the galvanometer-mounted steering mirrors in the scanner head. During the HSI acquisition, the user directly defined this voltage ramp. While the two resulting FOVs were matched visually, some minor differences remained. As such, image transformation was necessary to achieve true co-registration between both modalities. This was done by imaging a simple structure that could be visualized with both techniques. For this purpose, we used the crosshair pattern on a NIR viewing card (VRC2, Thorlabs). First, a maximum intensity projection of the superficial pixels of the OCT C-scan was taken to obtain a 2D image of the crosshair pattern. An HSI image at a wavelength with high contrast between the crosshair and the background was selected and resized to match the OCT data in pixel size. Both images are then converted to binary masks based on simple thresholding and used as input for a 2D affine image registration algorithm (*imregtform* in Matlab). This algorithm includes translation, rotation, scale, and shear transformations. The image registration algorithm outputs an affine transformation function that can be applied to all subsequent measurements sharing the same scanning parameters. The overlayed OCT and HSI images at different steps in the registration process are presented in Fig. 3.2. The overlay of the OCT image with the resized HSI image highlights the importance of image registration, as some features are separated by over 1 mm.

After registration, datasets from the two techniques are combined by overlaying the 2D images from the HSI channel onto the surface of the OCT 3D volumes. The surface topography of the OCT C-scan is obtained using a custom surface detection algorithm based on pixel intensity, vertical intensity gradient, and outlier analysis for neighboring pixels within a specific range. Once the surface is identified, color pixels from the 2D HSI image are applied to 7 pixels above the OCT surface. The number of pixels is selected to optimize color visibility while maintaining the surface topography. All image processing steps were performed in Matlab (Matlab, Mathworks, USA).

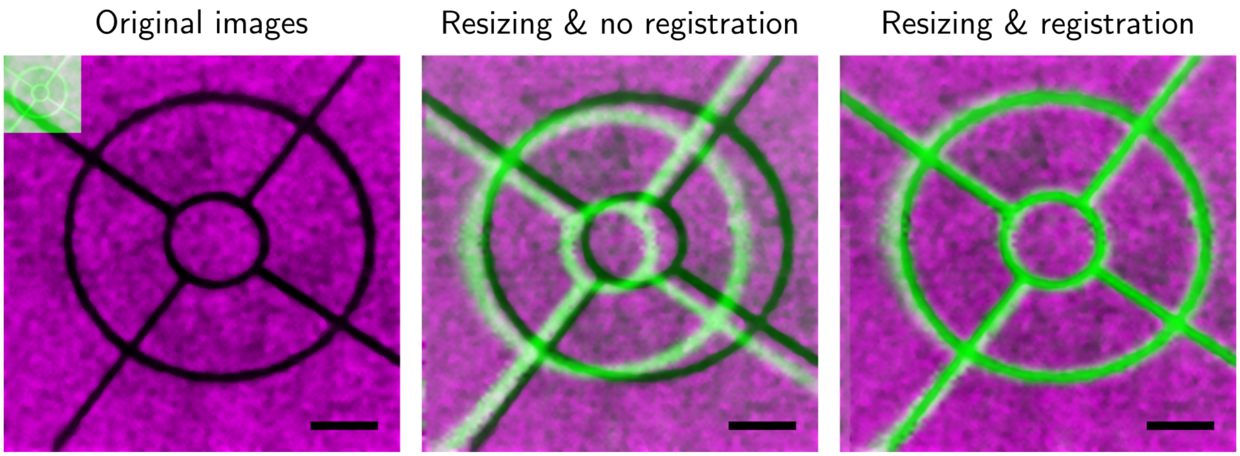

Figure 3.2 Overlayed OCT (purple & black) and HSI (green) images of the crosshair pattern on a NIR laser card at different steps in the image registration process. Scale bars are 2 mm.

3.3 Results

3.3.1 System characterization

The numerical aperture of the OCT beam in the image plane was estimated to be ∼ 0.04. This leads to a theoretical lateral resolution of 13 μm, using the 90/10 edge response criterion and assuming a gaussian point-spread function. The experimental lateral resolution was found to be 14.5 μm using a USAF1951 resolution target (R3L3S1P, Thorlabs) and the same edge response criterion. The theoretical axial resolution is assumed unchanged from the system specifications and equal to 12 μm in air. Experimentally, the axial resolution was found to be 17.4 μm by measuring the full width at half-maximum (FWHM) of the signal peak for a mirror. This loss in axial resolution can be attributed to an uncorrected dispersion mismatch due to fiber length differences. For HSI, the lateral resolution is determined by the size of the projection of the inner cladding onto the sample plane and the same 90/10 edge response criterion used for OCT. The theoretical value is ∼ 330 μm, and the experimental one was measured at 345 μm.

3.3.2 Combined imaging

A healing epithelial wound on the hand of a healthy volunteer was imaged with the multimodal system to demonstrate its performance when applied to biological tissue (approved by Ecole Polytechnique's Ethics Committee under project #BIO-08/09-01.). The imaged area was placed in OCT' focal plane and immobilized during the sequential acquisitions to minimize motion artifacts. The two light guides from the halogen lamp were placed at an angle on either side of the sample to avoid collecting strong specular reflections and to achieve approximately uniform illumination.

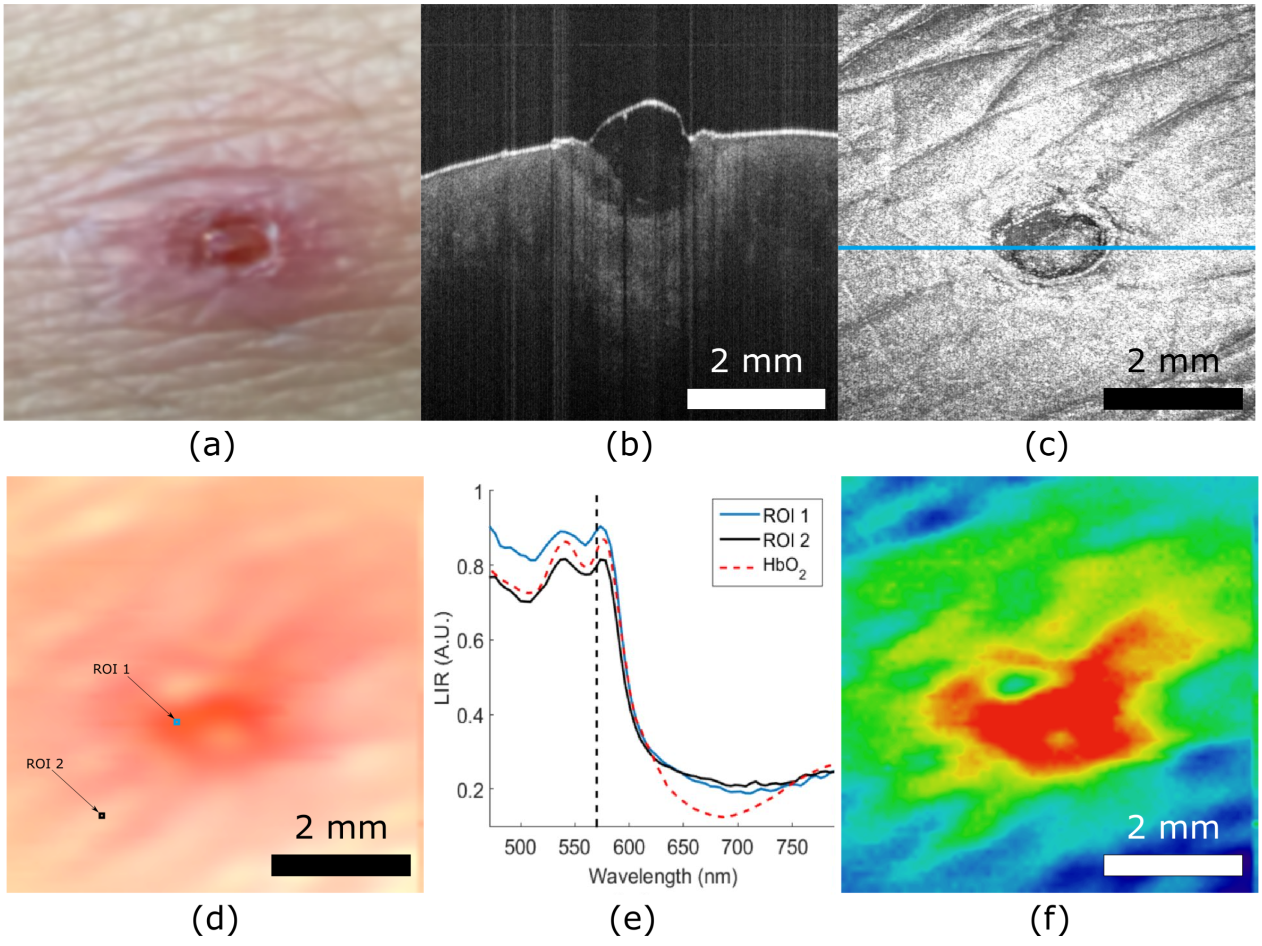

Figure 3.3 OCT and HSI images from a healing epithelial wound: (a) White-light CCD image. (b) Typical OCT B-scan. (c) En-face OCT reconstruction. The blue line indicates the position of the B-scan presented in (b). (d) En-face color image reconstructed from HSI data. (e) LIR representation as a function of wavelength for two regions of interest (ROIs) identified in Fig.2 (d). (f) En-face LIR image at 575 nm, identified as the dashed line in (e). Scale bars are 2mm. Figure reproduced from Guay-Lord, Attendu et al. [3] with permission from SPIE.

Figure 3.3(a) presents a photograph of the imaged area taken with a CCD camera under fluorescent lighting. Figure 3.3(b) presents a B-scan of the healing wound. This cross-sectional view allows the visualization of the depth of the damage, which extends below the surface of the tissue. Figure 3.3(c) an en-face view of the OCT C-scan computed using a maximum intensity projection along the depth axis. The en-face view highlights the high level of detail achievable with OCT. Figure 3.3(d) is the RGB image reconstructed from the HSI reflectance and demonstrates that approximate color reconstruction can be achieved with point scanning HSI. However, Fig. 3.3(d) also highlights the low lateral resolution of the HSI channel. The LIR spectra for the two regions of interest (ROI) identified in Fig. 3.3(d) are depicted in Fig. 3.3(e). The measured spectra closely follow the absorption spectrum of oxygenated hemoglobin, obtained from literature [277] and presented in the red dashed line. This correspondence indicates that the LIR may provide a qualitative estimate of the absorption properties of the sample. From the LIR, certain chromophores can be highlighted by displaying the HSI images at spectral bands corresponding to specific absorption peaks, as illustrated in Fig. 3.3(f). In this figure, the LIR image at 575 nm is presented, which corresponds to an absorption peak of hemoglobin, depicted in Fig. 3.3(e) with the vertical dashed line. The higher LIR in the vicinity of the wound in Fig. 3.3(f) could indicate a larger relative concentration of oxygenated hemoglobin in this area. However, great care should be taken in interpreting such LIR images. Firstly LIR remains an approximation that does not fully capture the relationship between the reflectance and the sample's optical properties. Secondly, the proposed analysis does not account for the specific illumination/collection geometry, illumination non-uniformities, and variations in the surface topology of the sample, all of which could influence the local reflectance from which LIR is derived.

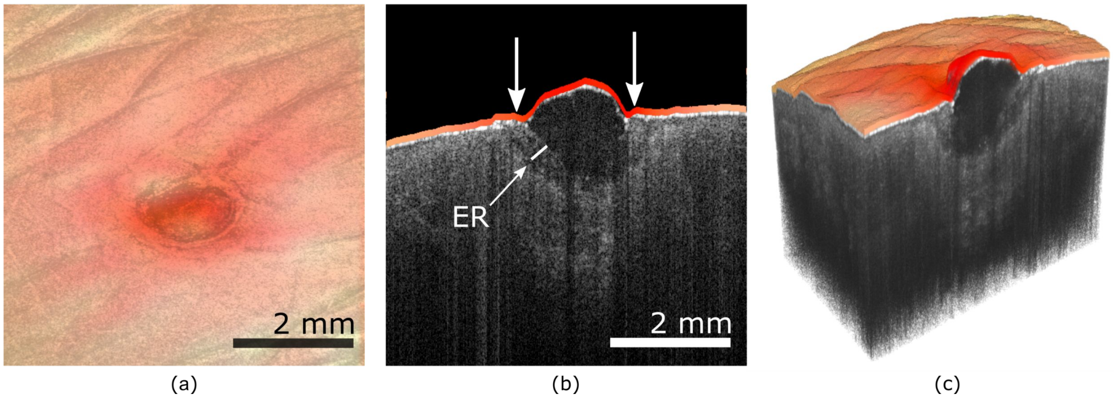

(a) (b) (c)

Figure 3.4 Combining OCT and HSI data. (a) OCT en-face projection overlaid with RGB image. (b) OCT B-scan with HSI extracted true-color overlay. An epithelial region is forming in the wounded area (ER). (c) Dual modality 3D rendering of the hand. Figure reproduced from Guay-Lord, Attendu et al. [3] with permission from SPIE.

Various combinations of OCT and HSI data are presented in Fig. 3.4. Figure 3.4(a) was generated by overlaying the reconstructed color image presented in Fig. 3.3(d) with the OCT en face view presented in Fig. 3.3(c). Such a combination allows imitating color imaging while retaining the high level of surface detail from the en face OCT image, resulting in a higher apparent lateral resolution than afforded by the HSI channel alone. Figure 3.4(b) presents a B-scan with the corresponding color pixels overlaid onto the surface. By repeating this process for all B-scans, the combined 3D volume can be constructed, as illustrated in Fig. 3.4(c). A similar volumetric representation could be generated using other colormaps extracted from the HSI data, such as reflectance or LIR images.

3.4 Discussion

The preliminary measurements presented in Figs. 3.3 and 3.4 demonstrate the potential of combining OCT and HSI. The general tissue architecture and subsurface structures, such as the extent of the wounded area or the epithelial regrowth, are visualized with OCT. Simultaneously, HSI provides complementary insight into the biochemical composition of the sample through color imaging and approximate absorbance. For example, the LIR image at the hemoglobin absorption peak, presented in Fig. 3.3(f), displays a zone of higher absorption surrounding the wound. This increase in absorption could indicate a higher concentration of hemoglobin associated with inflammation or increased tissue perfusion. Moreover, the HSI image reveals that this zone extends beyond the limits of the wound as visualized with OCT in Fig. 3.3(c). As such, each technique can access information invisible to the other, which further exemplifies the value of their combination.

However, several technical improvements are necessary for a successful implementation in a clinical setting. The current system implementation performs the OCT and HSI acquisitions sequentially and requires about 65 seconds for a full scan. Sequential acquisition is detrimental because it lengthens the imaging time and makes the system sensitive to motion artifacts. For clinical applications, it would be necessary to perform the acquisition of both techniques simultaneously and significantly reduce the total measurement time. Simultaneous acquisition would be feasible through software and hardware improvements to the setup. Currently, the HSI acquisition rate is limited by the spectrometer scan rate of 125 Hz. The spectrometer could be replaced with commercially available, high-speed devices with scan rates matching the OCT A-line frequency. Alternatively, existing line scan cameras with scan rates over 100 kHz could be used to develop custom high-speed spectrometers. Synchronized measurement would then require dedicated software for both acquisition and data processing. The current signal levels during HSI measurements indicate that the acquisition rate could be increased over an order of magnitude while maintaining sufficient signal strength. Increasing the acquisition rate (and decreasing the integration time correspondingly) further could require increasing the illumination intensity. This could be achieved by increasing the source power or using optics to concentrate the illumination to imaged area. However, maximum permissible exposure considerations may become relevant at this point. It is also interesting to note that the registration process presented in Fig. 3.2 would not be necessary with synchronous acquisition due to the shared scan pattern.

The illumination method for HSI may also be improved. Currently, the proposed system relies on external illumination. This geometry would be compatible with bench-top imaging systems and endoscopic applications that already utilize white light illumination [278–280]. However, these devices are typically forward viewing, complicating the miniaturization of the scanning mechanism necessary for OCT and point-scanning HSI. Moreover, the forward viewing geometry is not optimal for tubular organs, which are better imaged using side-viewing devices such as the ones presented in Fig. 2.10. An alternative would be to replace the external white light with a supercontinuum laser injected into the core of the DCF. This would significantly enhance the miniaturization potential of the distal part of the system and enable the fabrication of sub-millimeter endoscopes, as demonstrated by previous DCF-based multimodal endoscopes [156,281]. Internal illumination would also improve light throughput as the full power of the illumination would be concentrated in the imaged region, potentially enabling reduced integration times and faster HSI acquisition. Furthermore, this would improve the lateral resolution for HSI by reducing the spatial extent of the probed volume. Improved lateral resolution is also possible with external illumination by increasing the NA in the sample plane, reducing the size of the projection of the inner cladding on the sample. However, because OCT and HSI share the optics used for focusing, increasing the NA would also reduce the depth of field for OCT imaging, which may impede imaging deep in the sample.

Aside from technical developments, improvements are also necessary in signal processing and modeling. In this work, HSI data was used to present approximate absorbance maps and gain qualitative insight into the molecular composition of the sample. Several existing models allow more advanced quantitative analysis of HSI data through classification techniques, spectral unmixing, or inverse propagation models [276,282–284]. Such methods have been applied in clinical applications and have shown great promise by providing quantitative diagnostic information [260,285]. As such, it is relevant to determine if these methods apply to the proposed setup and how they should be adapted if necessary. A primary focus in future work will be on the adaptation and development of models to extract absolute optical properties from the measured reflectance spectra.

3.5 Conclusion

In conclusion, we have demonstrated the first combination of OCT and HSI using a double-clad fiber coupler. Combined OCT and HSI imaging may be of great clinical value as they provide information on the 3D sample morphology and its chemical makeup. In cancer, for example, tissue remodeling could be visualized with OCT, while changes in molecular composition, such as perfusion and blood oxygenation due to neovascularization, could be observed with HSI. The use of DCF and DCFC also provides the opportunity for miniaturization into an endoscopic device which could provide enhanced diagnostic capabilities compared to standard video-endoscopy.

Acknowledgements

This work was funded by the Canada Foundation for Innovation (CFI), the Natural Sciences and Engineering Research Council of Canada (NSERC), the Research Group in Biomedical Sciences and Technologies (GRSTB), and the National Science Foundation Graduate Research Fellowship (NSFGRF). This chapter was adapted from an article published in the Journal of Biomedical Optics [3], itself an expansion of a conference proceeding published at Photonics West 2016 [286].

CHAPTER 4 ARTICLE 1: CO-REGISTERED OPTICAL COHERENCE TOMOGRAPHY AND FREQUENCY-ENCODED MULTISPECTRAL IMAGING FOR SPECTRALLY-SPARSE COLOR IMAGING

This chapter was reproduced from:

Xavier Attendu, Marie-Hélène Bourget, Martin Poinsinet de Sivry-Houle, Caroline Boudoux, "Coregistered optical coherence tomography and frequency-encoded multispectral imaging for spectrally sparse color imaging," J. Biomed. Opt. 25(3) 032008 (21 November 2019) `https://doi.org/10.1117/1.JBO.25.3.032008`

Author contributions

The article presented in this chapter was submitted to the *Journal of Biomedical Optics* on 29/06/2019, accepted on 14/10/2019 and published on 21/11/2019. Xavier Attendu is the principal author and contributed ~70% of the work. Xavier Attendu contributed to the experimental design, development of the theoretical model, simulations, preparation of the experimental setup, data acquisition and analysis, and manuscript preparation and revision. Marie-Hélène Bourget and Martin Poinsinet de Sivry-Houle contirbuted to the preparation of the experimental setup, data acquisition and analysis, and manuscript revision. Caroline Boudoux was the senior investigator and provided assistance in the experimental design, data analysis and manuscript revision.

Chapter context

In this chapter we investigate multispectral imaging as a high-speed alternative to the full hyperspectral imaging approach presented in the previous chapter. While MSI reduces the number of spectral data points, it enables the implementation frequency-domain multiplexing (FDM) as an alternative to the conventional time-domain multiplexing or spectral division of the different wavelengths. Moreover, FDM allows concurrent and co-registered imaging at OCT acquisition rates, which is crucial for in-vivo applications, with reduced synchronization requirements. In the proposed system, the illumination for both techniques is internal, removing the external illumination utilized in the previous chapter. This significantly enhances the lateral resolution for the spectral imaging and the potential for miniaturization into endoscopic devices. However, the resulting illumination/collection geometry has a less well defined relationship between the measured reflectance and the optical properties of the sample, leading to complications in the analysis. Furthermore, we investigate frequency-domain multiplexing as an alternative to the conventional time-domain method.

Abstract

We present a system combining optical coherence tomography (OCT) and multispectral imaging (MSI) for co-registered structural imaging and surface color imaging. We first describe and numerically validate an optimization model to guide the selection of the MSI wavelengths and their relative intensities. We then demonstrate the integration of this model into an all-fiber bench-top system. We implement frequency domain multiplexing for the MSI to enable concurrent acquisition of both OCT and MSI at OCT acquisition rates. Such a system could be implemented in endoscopic practices to provide multimodal, high-resolution imaging of deep organ structures that are currently inaccessible to standard video endoscopes.

4.1 Introduction

Optical coherence tomography (OCT) is a powerful imaging modality which relies on interferometry to image subsurface structures [45]. It provides cross-sectional images of tissue morphology up to several millimeters deep, with axial resolutions ranging from 1 to 20 micrometers [287, 288]. Using optical fiber technology, OCT has been adapted to endoscopic imaging in various fields, which include cardiology [289], gastroenterology [2, 192, 246], laryngology [290], urology [291], and gynecology [191]. Furthermore, highly miniaturized OCT probes have enabled access to deep organ structures that are inaccessible to standard video endoscopes [292]. As such, OCT has the potential to expand current diagnostic capabilities in endoscopic practices.

Despite its great promises, OCT suffers from certain shortcomings. Firstly, OCT produces images that differ significantly from the color images obtained in standard white light video endoscopy (WLE), the standard of care for initial evaluation in many instances in gastrointestinal and pulmonary endoscopy [293, 294]. Differences such as the imaging scale, the perspective (cross-sectional vs. *en-face*) and the lack of color may potentially add to the challenges of interpretation and clinical translation for OCT. Secondly, in its standard implementation, OCT provides only limited information regarding the molecular composition of the sample. While some variants of OCT with enhanced molecular sensitivity exist, they typically present some performance trade-offs or limitations with respect to speed, sensitivity or experimental complexity [133, 292]. An alternative to enhancing the molecular sensitivity of OCT is the multimodal approach, whereby OCT is combined with other complementary techniques. For instance, OCT has previously been combined with fluorescence imaging [151, 156], multiphoton microsocopy [295], Raman spectroscopy [296], fluorescence lifetime imaging [168, 171] and hyperspectral imaging [3]. In each of these instances, the added modality provides molecular insight, complementary to the morphological imaging with OCT.

Another candidate for combination with OCT is multispectral reflectance imaging (MSI). This technique is similar to hyperspectral imaging (HSI), where images of a scene are captured at multiple spectral bands [213]. The difference between the two modalities lies in the number of spectral bands captured, where MSI has a few and HSI has many. In both cases, this results in a 3D dataset with two spatial dimensions and one spectral dimension. Each reflectance spectrum carries information on the attenuation properties of the studied sample, which can be used to infer molecular and/or physiological properties. While HSI may be better suited to detect subtle spectral differences, it also generates a significant amount of redundant data as well as additional experimental and computational complexity. In the case of MSI, a careful selection of the spectral bands allows the simplification of the setup without compromising molecular imaging capabilities, albeit for a selected set of molecular markers. Furthermore, the spectral reflectance information in the visible (VIS) range can be used to reconstruct the color of the sample. This can provide clinicians with a familiar perspective as well enable the continued use of current WLE evaluation protocols, where color is key in the identification of physiological features [182,183].

To this effect, we propose to combine OCT with a multispectral reflectance imaging system optimized to reproduce the sample's color as it would appear under white light endoscopy. Both modalities are combined in a single optical fiber through the use of a double-clad fiber coupler (DCFC) [209]. This allows for simultaneous OCT and MSI while conserving the potential for miniaturization. The miniaturization of the proposed system into a small diameter endoscopic probe could enable concurrent OCT, color imaging, and select spectral analyses of deep organ structures that are not accessible to standard WLE endoscopes. Both modalities are acquired concurrently and are intrinsically co-registered. We first present an optimization protocol for the selection of the MSI wavelengths and their relative intensities. We then demonstrate its implementation in a bench-top system where all MSI spectral bands are multiplexed in the frequency domain. Finally, we evaluate the system's performance for reflectance measurements, color reconstruction and high-resolution imaging.

4.2 Theory

4.2.1 Fundamentals of color reconstruction

The color appearance of an object can be reconstructed based on the spectral power distribution of the light reflected off the object that is then detected (using the eye or a camera). This reflected spectrum is defined as the multiplication of the illumination spectrum, $I(\lambda)$, and the spectral reflectance of the object, $R(\lambda)$. Using the standardized CIE 1931 color-matching functions $\bar{x}(\lambda)$, $\bar{y}(\lambda)$ and $\bar{z}(\lambda)$ (2° Standard Observer), this spectrum may be converted into a set of color coordinates in CIE XYZ color space [297]. The mathematical operations presented in Eqs. (4.1)-(4.4) can, therefore, be used to simulate the color appearance of a sample of known reflectance under any arbitrary illumination:

$$X = \frac{1}{N}\int_{\lambda} I(\lambda)R(\lambda)\bar{x}(\lambda)d\lambda; \tag{4.1}$$

$$Y = \frac{1}{N}\int_{\lambda} I(\lambda)R(\lambda)\bar{y}(\lambda)d\lambda; \tag{4.2}$$

$$Z = \frac{1}{N}\int_{\lambda} I(\lambda)R(\lambda)\bar{z}(\lambda)d\lambda; \tag{4.3}$$

$$N = \int_{\lambda} I(\lambda)\bar{y}(\lambda)d\lambda, \tag{4.4}$$

where X,Y and Z represent the color coordinates and N is a normalization factor. In Eqs. (4.1)-(4.4), the integration range covers the VIS spectral range, i.e. $\lambda = [380,780]$ nm. The color coordinates in the XYZ color space can then be transformed into RGB coordinates for display, or into other color spaces for further analyses [297, 298].

4.2.2 Optimizing spectrally-sparse color reconstruction

Equations (4.1)-(4.4) show that the XYZ coordinates, and therefore the color, of a sample differ when illuminated with a broadband (white) light source as opposed to several narrow-linewidth lasers. However, it is possible to select the number, the wavelengths and the relative intensities of such lasers in order for the color appearance to be as close as possible to that under a reference illuminant. In the case of such multi-laser scheme, the illumination spectrum, $I(\lambda)$, can be approximated as a sum of delta functions multiplied by relative intensity terms, as described in Eq. (4.5):

$$I(\lambda) = \sum_{i}^{n} I(\lambda_i)\delta(\lambda_i), \tag{4.5}$$

where the subscripts i and corresponding λ_i refer to the different laser lines used. This approximation is valid under the assumption that the reflectance spectrum and the color-matching function are almost constant over the spectral width of the laser line. By inserting (4.5) into Eqs. (4.1)-(4.4), the color coordinates can be expressed as sums rather than integrals:

$$CC = \frac{1}{N}\sum_{i}^{n} I(\lambda_i)R(\lambda_i)f_{\text{cm}}(\lambda_i); \tag{4.6}$$

$$N = \sum_{i}^{n} I(\lambda_i)\bar{y}(\lambda_i), \tag{4.7}$$

where CC are the color coordinates (X, Y and Z) and $f_{\text{cm}}(\lambda)$ are the corresponding color-matching functions. In Eq. (4.6) the constant factor that relates the integral of $I(\lambda)R(\lambda)f_{\text{cm}}(\lambda)$ over the narrow spectral width of a single laser line to the multiplication of single terms $I(\lambda_i)R(\lambda_i)f_{\text{cm}}(\lambda_i)$ will be factored out by the normalization by N.

Using Eqs. (4.1)-(4.4) for broadband illumination or Eqs. (4.5)-(4.7) for multi-laser illumination, it is possible to compute the color coordinates under any illumination for a sample of known reflectance. We can then optimize our choice of wavelengths and relative intensities to minimize the color difference between the color obtained under broadband illumination and the one obtained under multi-laser illumination. The color difference, typically denoted as ΔE, can be assessed quantitatively by comparing two sets of color coordinates. Associated with the characterization of color difference is the concept of *just noticeable difference* (JND). In color vision, the JND refers to the minimum ΔE that can be detected at least half of the time by a human observer [299]. In other words, it represents the limit of human perception. By definition, the JND is set to $\Delta E = 1$ [297, 300]. A common measure of color difference is obtained by computing the Euclidean norm of the difference between two color coordinate vectors in CIELAB, a color space derived from CIE XYZ [301]. However, this color difference metric is known to present perceptual non-uniformities meaning that a given ΔE is more noticeable for certain colors than for others [297, 298]. This may then lead to imbalanced optimization, favoring certain colors over others. We therefore selected the ΔE_{2000} color difference metric, as it was specifically developed to have improved perceptual uniformity [302, 303].

Mathematically, the optimization problem presented above can be expressed as:

$$\begin{aligned} \underset{\lambda_i, I(\lambda_i)}{\text{minimize}} \quad & \frac{1}{2} \|\boldsymbol{\Delta E}(\lambda_i, I(\lambda_i))\|^2 ; \\ \text{subject to} \quad & \lambda_i \in [380, 780] \text{ nm}; \\ & I(\lambda_i) \geq 0. \end{aligned} \tag{4.8}$$

In this system, $\boldsymbol{\Delta E}(\lambda_i, I(\lambda_i))$ is a vector containing the ΔE_{2000} color differences computed for multiple samples, λ_i are the n selected wavelengths and $I(\lambda_i)$ are the relative intensities associated with each wavelength. To achieve optimal reconstruction over a broad range of colors, it is not sufficient to perform this optimization on a single sample. Indeed, this may lead to a wavelength/intensity configuration that performs well for the selected sample, but very poorly for samples with different reflectance spectra and colors. Therefore, the process must be performed for multiple different output colors simultaneously, in order to optimize the overall color rendering ability of the multi-wavelength illumination.

It is interesting to note that this optimization can also be performed with fixed wavelengths. Such an optimization yields the relative intensities that result in optimal color reconstruction for the selected spectral lines. This scenario is useful as it is more representative of reality, where lasers are not available at any arbitrary wavelength or if non-optimal wavelengths are used (as is the case for the experimental system presented in this work) due to practical limitations such as cost, availability or other technical limitations. As such, the optimization over all wavelengths and intensities can be used to identify the optimum wavelengths ranges. The intensity-only optimization can then be performed using commercially available wavelengths that closely match the optimal ones, in order to realistically evaluate color rendering capabilities.

4.3 Materials and methods

4.3.1 Numerical optimization for color reconstruction

The color-rendering performance of a multi-wavelength laser source was simulated and optimized against that of a xenon white arc lamp (SLS401, Thorlabs, Newton, USA), as xenon illumination is commonly used in upper gastro-intestinal white light video endoscopy. However, the same analysis can be performed for other reference illuminants. The 24 reflectance spectra of a Macbeth ColorChecker, also know as a ColorChecker Classic (X-rite, Grand Rapids, USA), were used as the colored samples in the optimization process [304]. The color coordinates of each square under the reference illumination were computed using the corresponding reflectance spectra and Eqs. (4.1)-(4.4) (reflectance data available online [304]). The optimization problem described in Eq. (4.8) was solved using the *fmincon* solver from MATLAB (MathWorks, Natick, USA) to identify the n optimal wavelengths and their relative intensities. The optimization was carried out for 3 to 5 wavelengths, using the ΔE_{2000} color difference in the objective function (Eq. (4.8)). The initial point for the optimization was set to equally spaced wavelengths between 450 and 650 nm with equal initial intensity. We also performed several intensity-only simulations using commercially available wavelenghts that closely matched the optimal wavelengths identified through the optimization process.

To validate the accuracy of color reconstruction for biological samples, we simulated the appearance of the inner mucosa of a lip under multispectral illumination. For this purpose, we used a reflectance hyper-cube (i.e., an image with a full reflectance spectrum for each pixel) acquired using a hyperspectral camera (Specim IQ, Specim Spectral Imaging Ltd, Oulu, Finland). During the acquisition of hyperspectral images, a white reference reflector (SRS-99, Labsphere, North Sutton, USA) was included in the field of view (FOV) from which we determined the reflectance spectra.

4.3.2 System description

The experimental setup is presented in Fig. 4.1. In this setup, we use two distinct light sources. The first is a wavelength-swept laser scanning the range from 1260 to 1340 nm for OCT (OCS1300SS, Thorlabs, Newton, USA) with a sweep frequency of 16 kHz. The second source is a four-wavelength system which combines the output of four separate lasers (405, 488, 561 and 638 nm) into a single fiber (L4Cc, Oxxius, Lannion, France) for MSI. These wavelengths were not selected through the optimization process detailed above, but came pre-configured with the multi-laser system. In this multi-wavelength source, each laser can be controlled and modulated independently. The output of the OCT source is first split into a sample and reference arm using a 90/10 single-mode fiber coupler (TW1300R2A2, Thorlabs). The illumination signals of both modalities are then combined into a single SMF28 fiber using a home-built wavelength-division multiplexer (WDM). The output of the WDM is then spliced to a double-clad fiber coupler (DCFC, DC1300LEFA, Castor Optics, inc., St-Laurent, Canada). The illumination light is transported in the core of the double-clad fiber (DCF) from port A to port S, where it is collimated using a reflective collimator (RC, RC04APC-P01, Thorlabs). The collimated beam is scanned using a 2-axis galvanometer system (G, GVS002, Thorlabs) and a VIS-coated achromatic doublet lens (L, AC254-075-A, Thorlabs) in a telecentric configuration. Light backscattered from the sample is then collected in both the DCF core and inner cladding. Light in the inner cladding is extracted from port S to port B by the DCFC, where it is measured by a fast avalanche photodetector (APD, APD120A, Thorlabs). As the spectral range of the photodetector is from 400 to 1000 nm, it is not sensitive to OCT wavelengths and, therefore, only detects the MSI signal. Moreover, the frequency filtering used to extract the MSI signal (see section 4.3.3) further attenuates any potential noise from the OCT signal. Light collected into the fiber core is transported back to the WDM. As this component is reciprocal, VIS light is mostly extracted back to the VIS laser. In this configuration, it is not necessary to include any isolation to protect the laser source, as the intensity levels returning to the laser are minimal. The returning OCT signal is transported, via a fiber circulator (CR2, CIR-1310-50-APC, Thorlabs) to a 50/50 single-mode fiber coupler (TW1300R5A2, Thorlabs) where it interferes with the signal from the reference arm. The reference arm consists of a segment of SMF28 fiber length-matched to the total fiber length of the WDM and DCFC, a collimator (C1, CFS5-1310-APC, Thorlabs), a free-space segment matching the space between the fiber tip at port S and the sample and a mirror (R). It is important to note that the optical properties of the DCF used in the DCFC are matched to that of SMF28 fiber. As such, the component does not induce dispersion in the OCT signal and the fiber lengths in the reference arm can be matched one-to-one with those in the sample arm. Paddle polarization controllers (PC1 and PC2, FPC560, Thorlabs) are used in both interferometer arms to optimize the interference signal. The interference signal after the 50/50 coupler is detected using a balanced detector (DB Detection, PDB440C, Thorlabs). The OCT signal is unaffected by any residual VIS light as it lies outside of the spectral range of the DB detector. A custom A-line trigger (not shown) is used to trigger both OCT A-line and MSI acquisition. Custom LabView (National Instruments, Austin, USA) software is used to control the scan and synchronized acquisition of both modalities. The acquisition is performed using an AlazarTech ADC (ATS9440, AlazarTech, Pointe-Claire, Canada) with 20 MS/s sampling frequency. Scanning is synchronized and driven using a National Instruments DAC (PCI-6111, National Instruments).

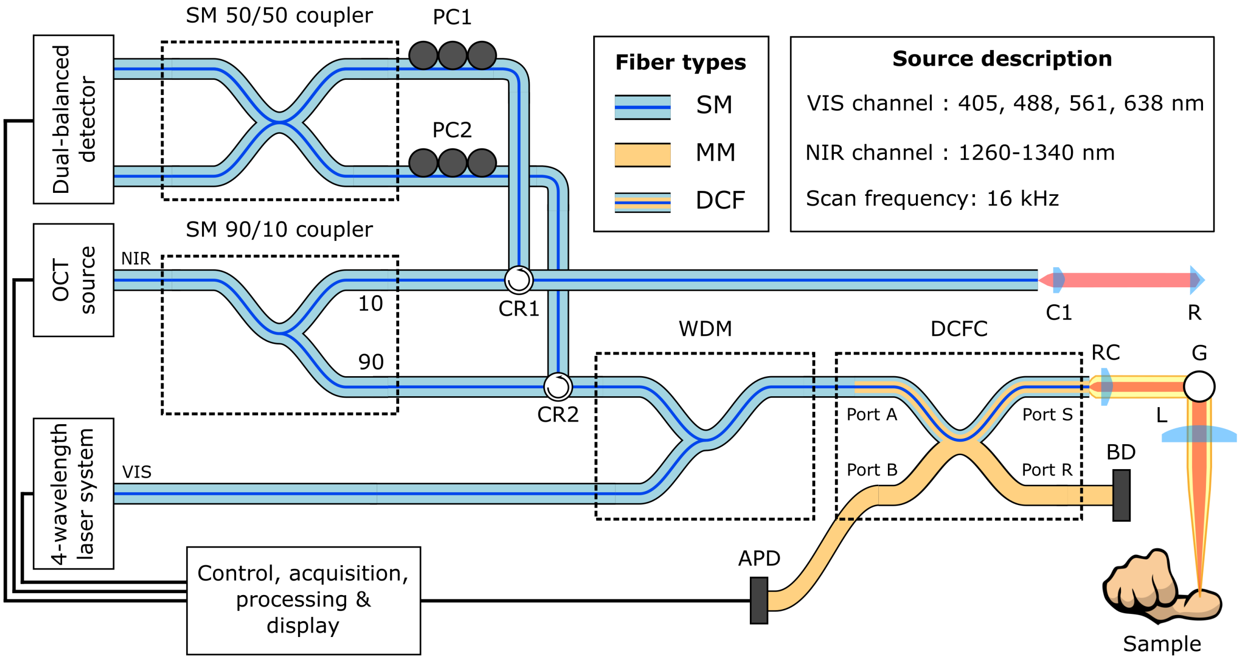

Figure 4.1 Experimental setup. **CR1, CR2**: fiber circulators; **WDM**: wavelength-division multiplexer; **DCFC**: double-clad fiber coupler; **SM, MM, DCF**: single mode, multi-mode and double-clad fiber respectively; **C1**: collimator; **RC**: reflective collimator **BD**: beam dump; **G**: 2D galvanometer scanning system; **L**: focusing lens; **R**: mirror/retroreflector; **PC1, PC2**: paddle polarisation controllers; **APD**: avalanche photodetector.

4.3.3 MSI signal acquisition and processing

All four spectral components of the MSI are acquired simultaneously and at the same pixel rate as the OCT A-line rate (16 kHz) through the use of frequency domain multiplexing. Each laser in the four wavelength source is modulated sinusoidally at a distinct frequency: 700, 800, 900 and 1000 kHz for 405, 488, 561 and 638 nm respectively. Using Fourier analysis, the collected intensity for each wavelength is identified and used to compute the reflectance as follows:

$$R(f_i) = \frac{I_{\text{sam}}(f_i) - I_{\text{dark}}(f_i)}{I_{\text{ref}}(f_i) - I_{\text{dark}}(f_i)}, \tag{4.9}$$

where each intensity measurement $I(f_i)$ corresponds to the height of the peak in the Fourier domain at the corresponding frequency, f_i. These values can be measured by performing a fast Fourier transform (FFT) on the signal after DC removal. A Hanning window is also applied prior to FFT to remove potential side lobes due to signal truncation. The *dark* measurement is performed without a sample, while the *reference* measurement is performed using a 99% white diffuse reflectance standard (SRS-99, Labsphere, North Sutton, USA). It is important to note that the reflectance measurements do not require the illumination intensities to match those determined in the optimization procedure. Indeed, once the reflectance is known at the selected wavelengths, the color appearance can be simulated in post-processing. During the reference measurements, the axial position of the reference sample is monitored with OCT and always positioned at the same location to avoid any variations in the illumination and collection areas. The axial position of the first surface of samples is likewise controlled.

Selecting the modulation frequencies for the multi-laser source requires considering certain properties of the FFT. For the MSI acquisition to run in parallel with the OCT acquisition, the longest sampling time corresponds to that of a single A-line. As such, the smallest resolvable frequency difference is given by $\Delta f_{\text{min}} = 1/\tau_{\text{A-line}} = f_{\text{A-line}}$. The MSI modulation frequencies must, therefore, be selected such that they are sufficiently far apart to be resolvable. The shape of the modulation must also be considered. Ideally, analog modulation with a sinusoidal waveform should be used as it results in a single peak in the Fourier domain. However, most commercial lasers only permit analog modulation up to several MHz, which might be restrictive for higher acquisition speeds. Digital (TTL) modulation typically allows much higher modulation frequencies, but with a square waveform. This results in multiple peaks in the Fourier domain at multiples of the fundamental modulation frequency. To avoid cross-talk between the different wavelengths, care should be taken that the fundamental frequency peaks do not overlap with secondary peaks from another laser. It is important to point out that not all lasers allow high-speed modulation. In particular, diode-pumped solid-state lasers (typical wavelength range from 530 to 600 nm) do not usually permit such high modulation frequencies. It is then necessary to combine these lasers with an external modulator. In our experimental setup, the 561 nm channel of the multi-laser system included an acousto-optic modulator with a 3 MHz bandwidth.

All of these criteria were respected when defining our acquisition parameters. All frequencies and their spacing are greater than $f_{\text{min}} = 16$ kHz, below the 3 MHz analog modulation limit, and below the maximum measurable frequency of 10 MHz defined by the 20 MS/s sampling rate.

4.3.4 OCT signal acquisition and processing

The OCT signal is sampled simultaneously with the MSI signal, using the same multichannel ADC. Sampling is carried out at 20 MS/s with 1312 samples per A-line. The k-clock output of the OCT swept-laser is not used as one of the two signals would inevitably have to be re-sampled. The OCT signal is first corrected for background and high-pass filtered to remove low-frequency components. It is then re-sampled using a cubic spline to achieve k-linear sampling and multiplied by a complex window for dispersion compensation. The re-sampling indices and the appropriate dispersion correction vector were identified using a calibration method based on two mirror measurements [305]. Dispersion compensation is particularly important in this scenario as the use of the WDM induces a significant dispersion mismatch between the two interferometer arms.

4.4 Results

4.4.1 Numerical optimization for color reconstruction

The results of the optimization protocol with 3 to 5 illumination wavelengths are presented in Table 4.1. All relative intensities are normalized to the intensity of the first wavelength. In this table, the $\langle \Delta E_{2000} \rangle$ column refers to the mean color difference across the 24 colored squares of the ColorChecker and $\langle \Delta E_{2000} \rangle_{\text{lip}}$ column to the mean color difference over all image pixels of the lip mucosa. Table 4.1 shows that color reconstruction below the JND threshold can be achieved with as few as 4 wavelengths for the ColorChecker. Figure 4.2 depicts the color appearance of the ColorChecker under the reference illumination (xenon) and under the multispectral illumination configurations described in Table 4.1. It should be noted that the color appearance of Fig. 4.2 may vary slightly depending on the color calibration of the monitor or the printer used by the reader. The ΔE_{2000} values for all 24 color squares of the ColorChecker and for all illumination configurations of Table 4.1 are also presented in Fig. 4.3 in bar chart format.

Table 4.1 Optimization results for simulations with free-running wavelengths.

N_λ	$\langle \Delta E_{2000} \rangle$	$\langle \Delta E_{2000} \rangle_{\text{lip}}$	Wavelengths [nm]	Relative intensities [A.U]
3	2.47	2.38	466, 537, 607	1, 1.07, 1.13
4	0.96	1.45	460, 518, 570, 619	1, 0.88, 0.92, 1.04
5	0.48	0.90	451, 497, 545, 589, 634	1, 1.12, 1.05, 0.93, 1.24

Table 4.2 Optimization results for intensity-only simulations. The first three rows used commercially available wavelengths closest to those presented in Table 4.1. The last row corresponds to the wavelengths from the 4λ laser source used in our experimental setup.

N_λ	$\langle \Delta E_{2000} \rangle$	$\langle \Delta E_{2000} \rangle_{\text{lip}}$	Wavelengths [nm]	Relative intensities [A.U.]
3	2.60	2.18	465, 540, 607	1, 1.09, 1.11
4	2.49	3.55	460, 520, 561, 630	1, 0.65, 1.02, 1.50
5	0.86	1.61	454, 491, 546, 589, 633	1, 1.26, 1.26, 0.89, 1.39
4	3.61	10.50	405, 488, 561, 638	1, 0.11, 0.12, 0.15

The optimization protocol was also performed with fixed wavelength values (see Table 4.2). All relative intensities are normalize to that of the first wavelength. The fixed wavelength values were selected from a list of commercially available lasers compiled from the catalogs of several suppliers (Oxxius, Coherent, Lasos, LaserGlow, and Cobolt). The wavelengths that were the closest to those identified in the free-running simulations were used in the intensity-only simulations. The last row of Table 4.2 describes the optimization results using the wavelengths from the multi-laser source used in our experimental setup. Fig. 4.4 consists of the images reconstructed from the lip reflectance hyper-cube, using the different illumination configurations presented in Table 4.2.

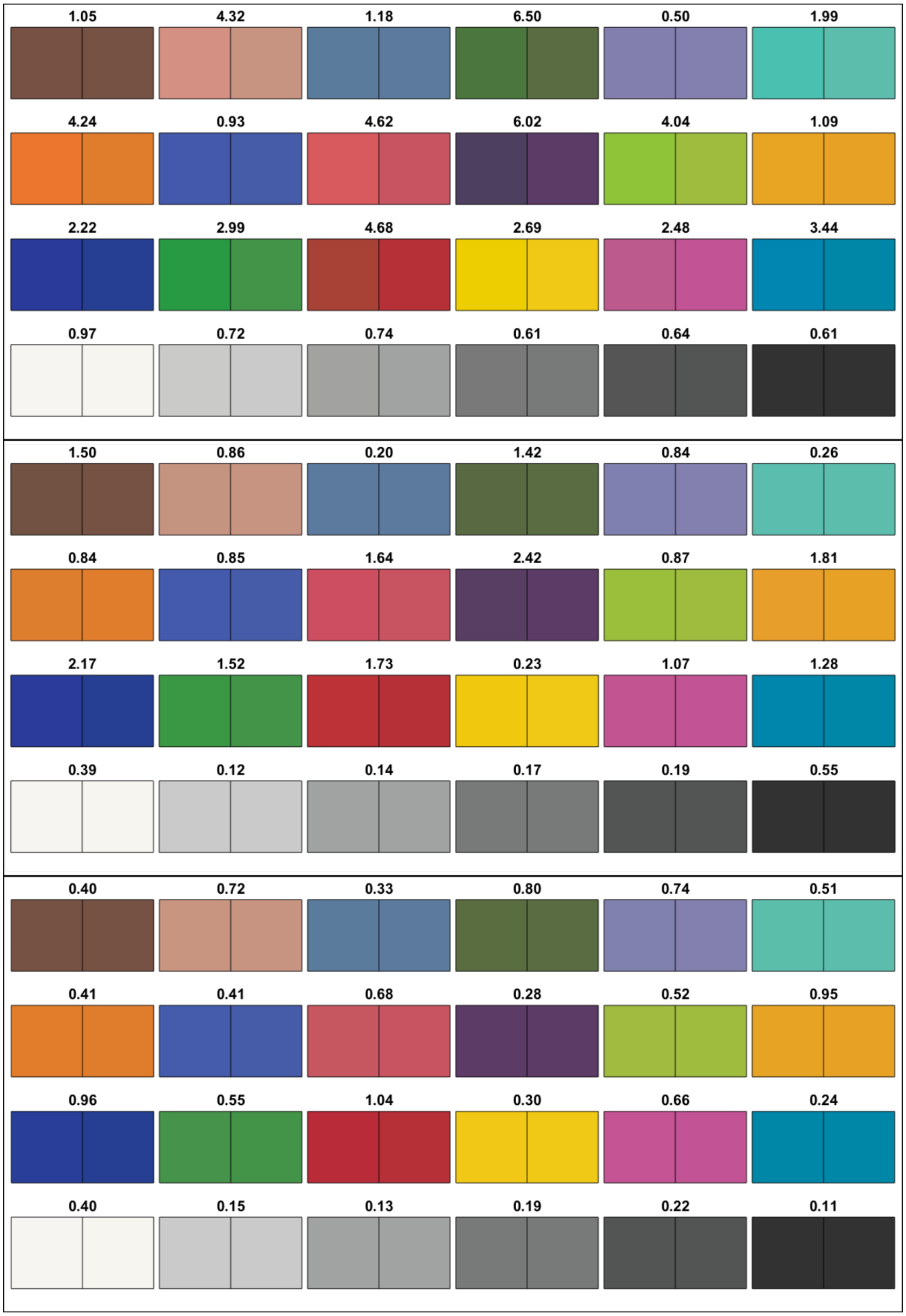

Figure 4.2 Reconstructed color appearance of the ColorChecker under the reference illuminant (right square) and multispectral illumination schemes presented in Table 4.1 (left square - from top to bottom 3, 4 and 5λ respectively). The ΔE_{2000} color difference is indicated above each sample.

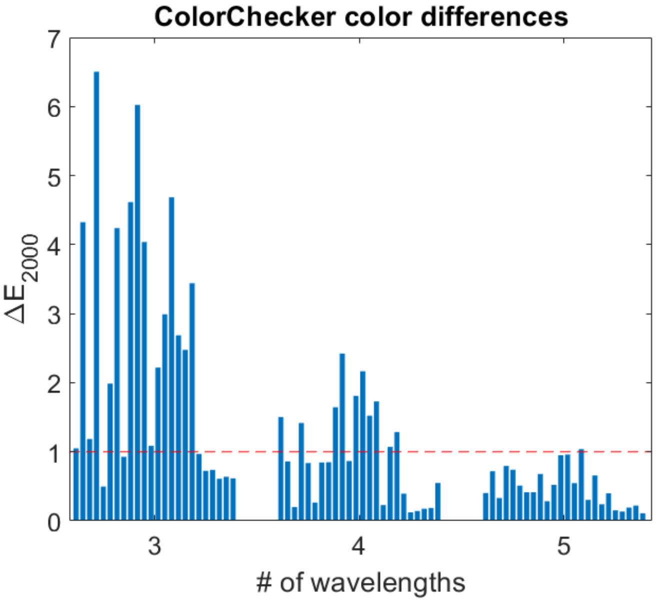

Figure 4.3 Color difference values for the different wavelength configurations listed in Table 4.1. Each bar represents one of the 24 colored squares (ordered from left to right and top to bottom in Fig. 4.2). The horizontal dashed line indicates the JND.

4.4.2 System characterization

We imaged a USAF 1951 resolution target to assess the lateral resolution of both modalities. We measured a lateral resolution of 28 μm for OCT and 22 μm for the overall MSI signal (total intensity projection). The individual wavelengths were found to have lateral resolutions of 23, 19, and 19 μm for 405, 561 and 638 nm, respectively. The resolution for 488 nm could not be measured due to the lack of contrast. The theoretical values, as defined for Gaussian beams using the Rayleigh criterion, are 27 μm for OCT and 9, 11, 12 and 14 μm for 405, 488, 561 and 638 nm, respectively (using NA = 0.027). Images of the test target are presented in Fig. 4.5, for both large and small FOVs. The low contrast in the 488 nm images and the contrast reversal in the 405 nm images are caused by the low reflectivity/higher absorption of the chrome patterns at those wavelengths. All images for a given FOV were acquired concurrently.

4.4.3 Experimental reflectance measurements

To test color reconstruction with MSI, reflectance measurements were carried out on blue, green, yellow and red Spectralon color standards (CSS-04-020 B/G/Y/R, Labsphere, USA), for which calibrated reflectance spectra are available. The reflectances at the four

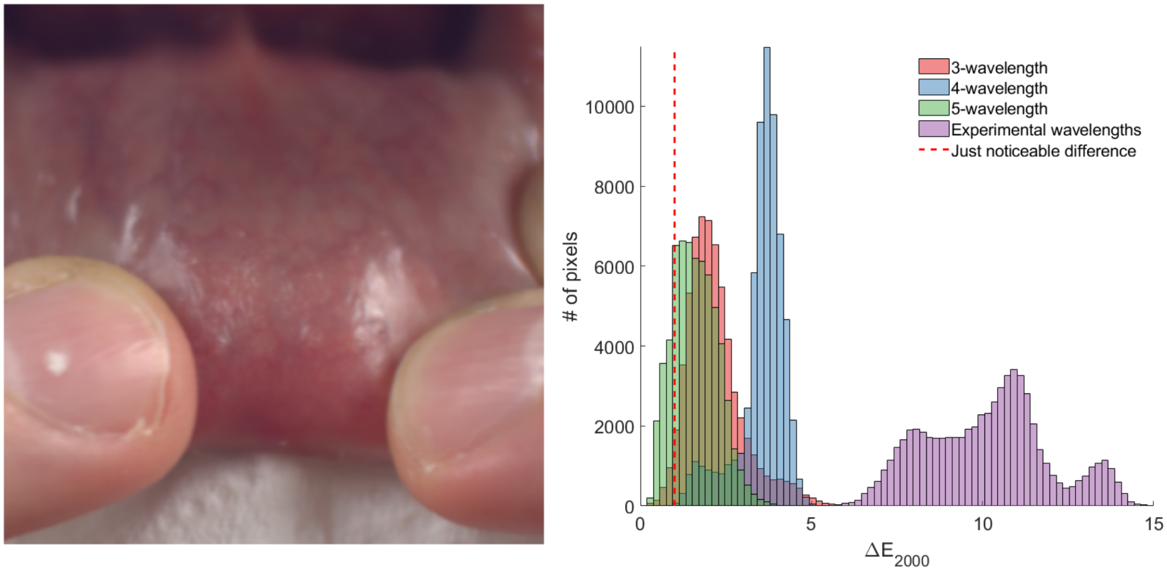
(a) Xenon reference

(b) Color difference histogram

(c) 3-wavelength

(d) 4-wavelength

(e) 5-wavelength

(f) Exp. wavelengths

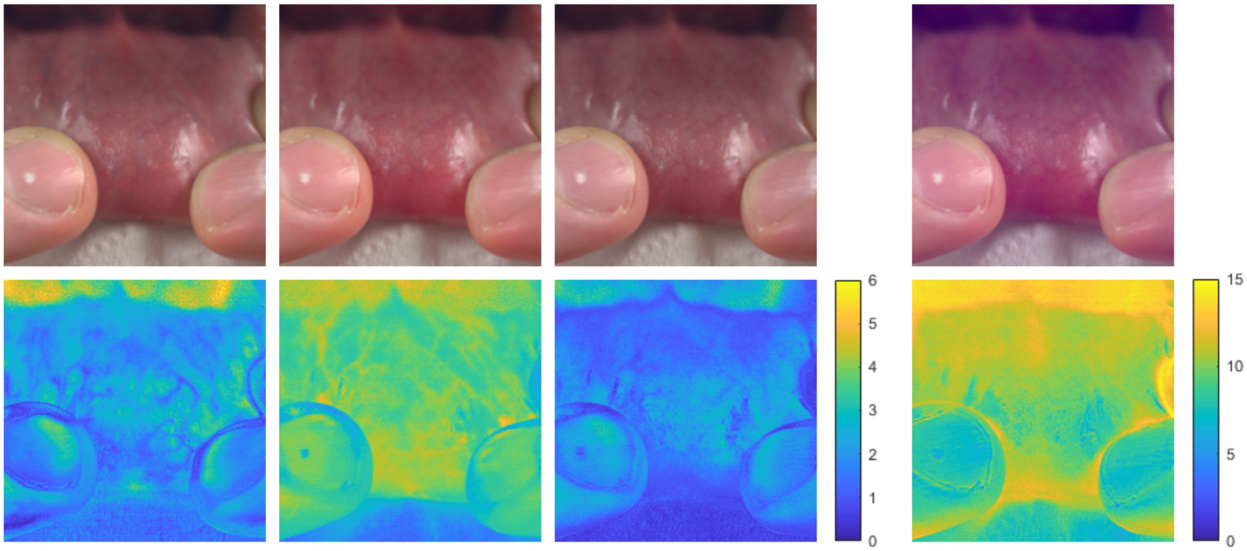

Figure 4.4 Reconstruction of true-color images of a lip from hyperspectral data. (a) Reference image under xenon illumination. (b) Color difference histograms of the ΔE_{2000} images (bottom images of subfigures (c)-(f)). (c)-(f) Reconstructed color images (top) using the wavelength/intensity configurations listed in Table 4.2 and the ΔE_{2000} image (bottom) when compared to the reference image.

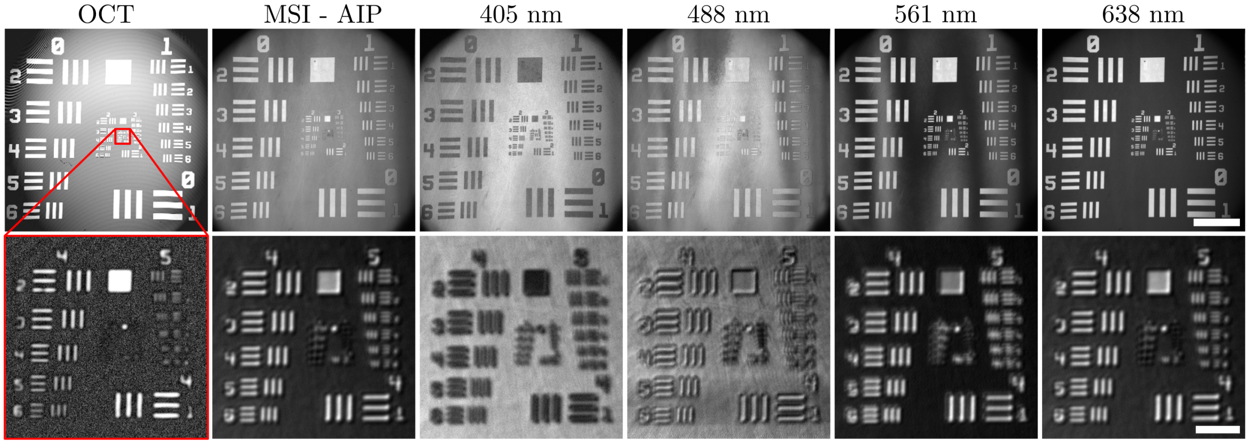

Figure 4.5 Multimodal imaging of a USAF resolution target. The top row is an 18x18 mm^2 FOV, and the scale bar is 4 mm. The bottom row is a zoomed-in, 1.2x1.2 mm^2 FOV, outlined in red in the top left image. The scale bar in the bottom images is 250 μm. The first column is OCT imaging, the second is an average intensity projection (AIP) with all four MSI wavelengths, and the last four are the individual MSI wavelengths extracted from a single acquisition.

experimental wavelengths were defined by comparing sample, reference, and dark measurements as described in Eq. 4.9. The sample, reference, and dark measurements are presented in bar plot format in Fig. 4.6, where the black bar is the dark, the colored is the sample, and the white bar is the reference. Each subplot presents the intensity measurements at the 4 wavelengths for one color target. The bar plots and left axis depict the height of the peak in the Fourier domain while the grey lines and the right axis show the experimental and theoretical reflectance values. These reflectance values were then used to reconstruct the color of each color target, as illustrated in Fig. 4.7. The three columns show the color under xenon illumination, the theoretical color under our 4λ illumination and the experimental color under the 4λ illumination.

4.4.4 Combined imaging

Co-registered OCT and MSI imaging was demonstrated on biological samples exhibiting a broad range of colors, namely: a mandarine peel, a lime peel and a strawberry, all placed on a blue piece of paper. The FOV was 7x7 mm^2 and is depicted in Fig. 4.8(a) in dashed lines. OCT and MSI signal were acquired simultaneously. The OCT volume was processed for surface detection using a home-built algorithm. As both modalities are intrinsically co-registered and equally sampled in the lateral dimensions, each pixel in the reconstructed color image 4.8(b) corresponds to a single A-line in the OCT volume. It

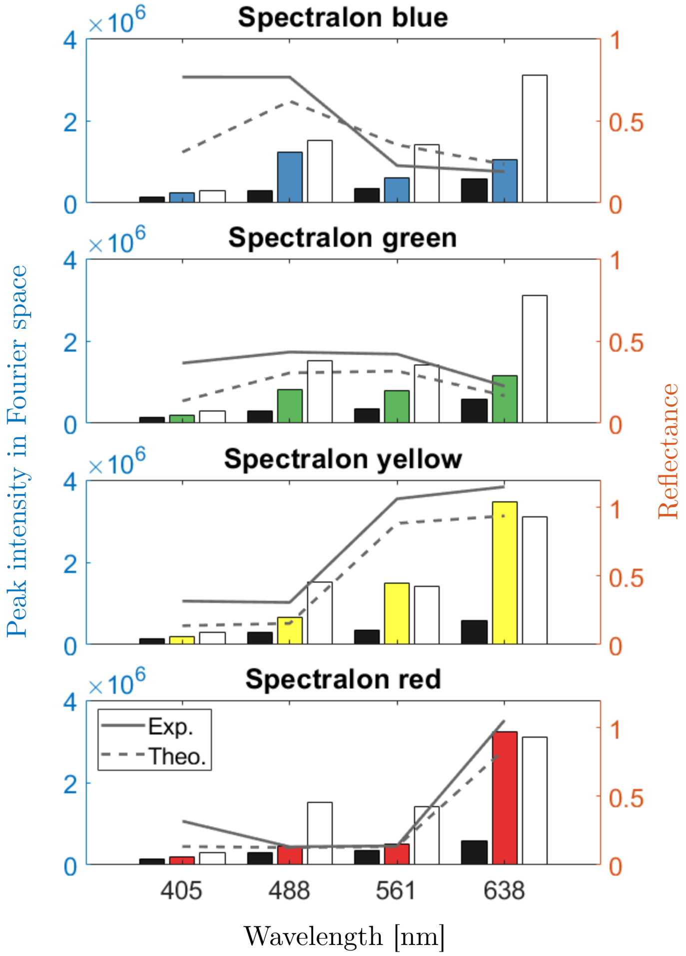

Figure 4.6 Experimental reflectance measurements on Spectralon color targets. (left axis) The bar plots depict the height of the peak in the frequency domain corresponding to each wavelength. For each wavelength, the dark (black bar), sample (colored bar), and reference (white bar) are shown. (right axis) The grey lines show the theoretical (dashed) an the experimental (solid) reflectance values, obtained from Eq. (4.9).

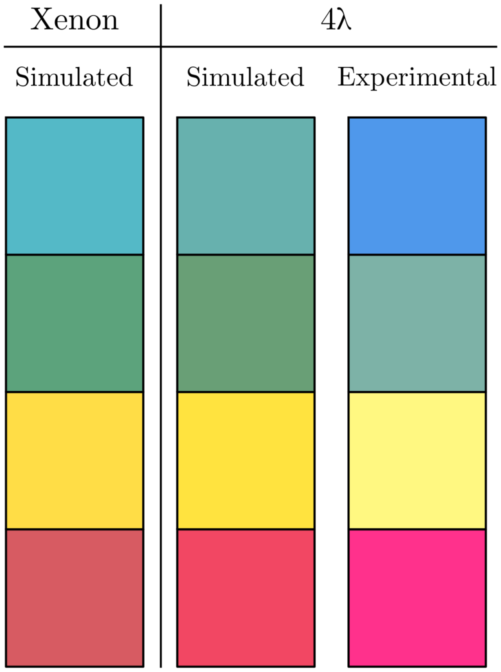

Figure 4.7 Reconstructed color of Spectralon color targets under 3 illumination schemes. From left to right: xenon illumination, theoretical color under 4λ illumination (using experimental wavelengths - see last row of Table 4.2) and experimental color under the same 4λ illumination. From top to bottom: blue, green, yellow and red Spectralon targets.

is, therefore, possible to apply one color pixel from the reconstructed color image to the surface of each A-line. This can be visualized in 2D (see Figs. 4.8(d) and (e)) or in 3D (see Fig. 4.8(c)). The reflectance values used to compute the color were obtained relative to a measurement of the white Spectralon standard. The blue vertical surface visible between the lime and mandarine peel in Fig. 4.8(c) is the blue paper visible in subfigures (a) and (b).

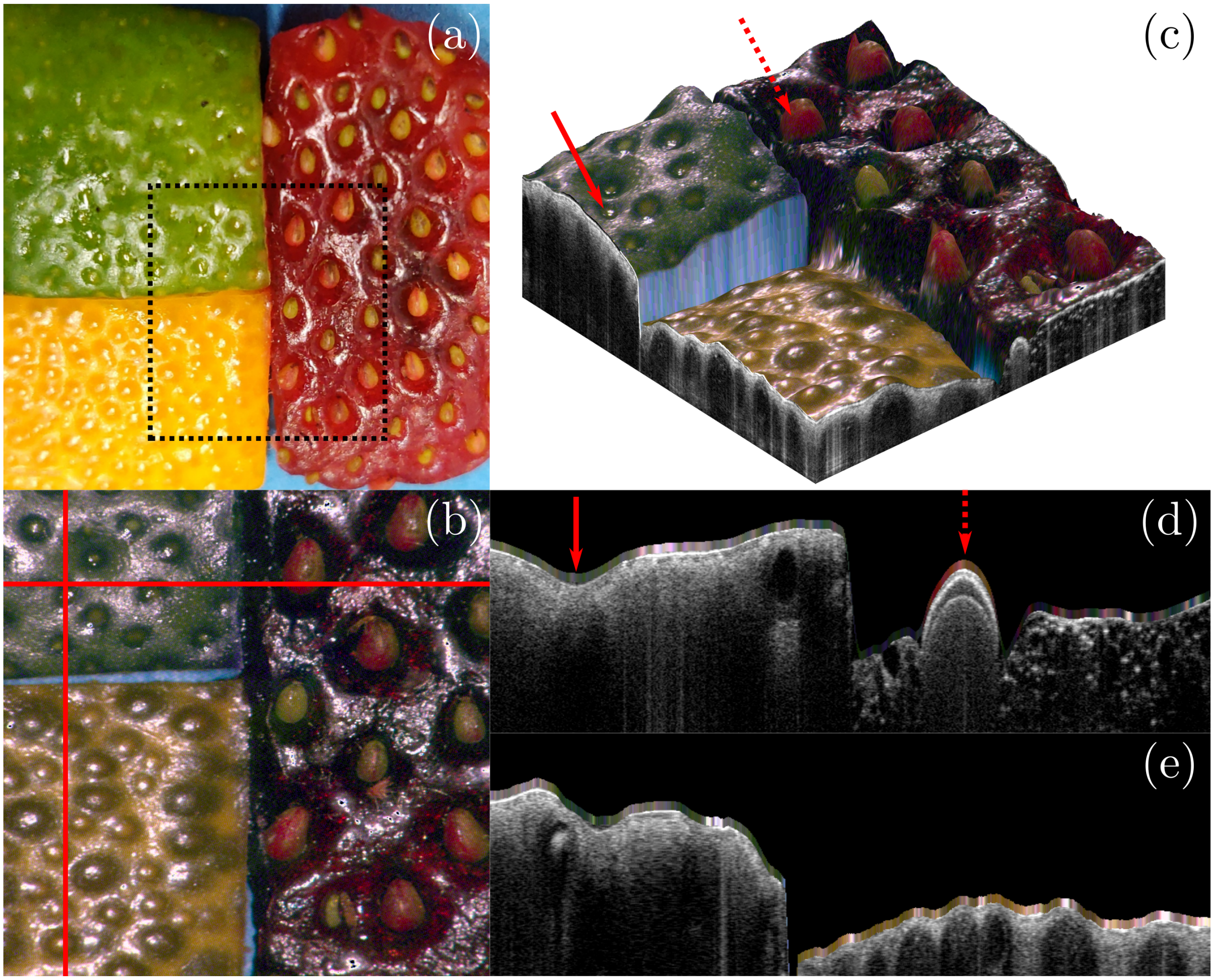

Figure 4.8 Combined OCT and MSI imaging of a fruit sample including mandarin peel, lime peel, and strawberry. (a) CCD picture of the sample. (b) True color image reconstructed from the MSI reflectance data. The red lines indicate the locations of the cross-sections presented in sub-figures (d) and (e). (c) 3D rendering of the fruit sample with color pixels super-imposed onto the sample surface. The red arrows identify features also visible in sub-figure (d). (d) & (e) OCT cross-sections with color pixels super-imposed onto the sample's surface.

4.5 Discussion

4.5.1 Numerical optimization for color reconstruction

The effectiveness of color reconstruction using multispectral illumination can be assessed qualitatively by considering Fig. 4.2, which shows that 4λ illumination enables near perfect color reconstruction. The color rendering capabilities of multi-laser illumination can also be evaluated quantitatively using the ΔE_{2000} and the JND. As illustrated in Fig. 4.3 and described in the $\langle \Delta E_{2000} \rangle$ column of Table 4.1, the 4λ illumination achieves a mean color difference just below the JND threshold, while 5λ illumination drops well below it.

In Table 4.1, we demonstrate that it is possible to accurately reproduce the color of a sample under a reference illumination, using only a few laser lines. The results of the optimization process with free-running wavelength values are, however, difficult to reproduce experimentally, as laser are not available at all arbitrary wavelengths. Table 4.2 presents the result of the optimization process when the wavelengths are set to commercially available values, and only their relative intensities are optimized. When comparing the optimization results ($\langle \Delta E_{2000} \rangle$ column) of Table 4.1 with the first three rows of Table 4.2, we see that the accuracy of the color reconstruction with commercially available wavelengths decreases slightly, but remains viable. The feasibility of accurate color reconstruction is further supported by Fig. 4.4, in which images of a human lip are reconstructed from hyperspectral data, using the wavelength configurations described in Table 4.2. A first observation, when comparing the Figs. 4.4(c)-(e) with the reference image (Fig. 4.4(a)), is that all images perform qualitatively well. In the case of Fig. 4.4(f), where the wavelengths deviate significantly from the optimal values outlined in Table 4.1, the color distortions are much more apparent. Typically, changing a wavelength by a couple of nanometers does not substantially degrade the color reconstruction. More significant deviations from the optimal wavelengths cause larger color differences, as observed in Figs. 4.4(d) and 4.4(f). In the context of this work, there is a significant mismatch between our experimental wavelengths and the optimal ones, as the multi-laser source came preconfigured.

Another interesting observation is that, for intensity-only optimization with commercial wavelengths, 3λ outperforms 4λ for the lip images. However, it is important to note that 4λ still performs better than 3λ for the ColorChecker ($\langle \Delta E_{2000} \rangle$ column). As such, 4λ performs better for general color reconstruction (ColorChecker), but poorer for this particular biological sample (lip). This can be explained by the fact that, for 4λ illumination, the optimization protocol leads to slightly poorer color rendering for red colors, which happen to be dominant in this particular scene. The color reconstruction was also tested over multiple other hyperspectral datasets (not shown, data available online [306]) and, on average, 4λ performed better than 3λ. The slightly decreased performance of the 4λ configuration could also be explained by the fact that the commercial wavelengths depart more significantly from the ideal values presented in Table 4.1 than for 3 or 5λ illumination. It is interesting to note that, in the context of *in vivo* use, where certain colors are predominant, better color reproduction can be achieved by weighting the optimization process in favor of these dominant colors. However, care should be taken to not over-emphasize the expected colors, as this may lead to a poorer reconstruction of the less frequent colors when they do appear in a scene, as might be the case when imaging pathological tissue (e.g. necrotic, inflammed or infected tissue).

In light of these results, it is feasible to achieve high fidelity color reconstruction with 3, 4, or 5 commercial laser sources. A larger number of wavelengths is preferable as it leads to increased color rendering performances across a broad range of colors, as well as a reduced sensitivity to the wavelength selection. The latter has important practical implications as lasers at more exotic wavelengths may come at a significantly higher cost. Finally, the use of more wavelengths is also interesting as it may enable additional spectroscopic analyses.

4.5.2 System performance

Our system was able to achieve concurrent and co-registered OCT and multispectral imaging, as illustrated in both Figs. 4.5 and 4.8. Figure 4.5 shows that it is possible to separate the different frequency components in the MSI signal to reconstruct images for each spectral band. However, the lateral resolution values for MSI were worsened compared to the theoretical values by factors ranging from 1.3 to 2.5. Two principal factors contribute to this effect. The first is the significant axial chromatic aberrations induced by the imaging lens (L in Fig. 4.1). Indeed, the focal shift between the MSI and OCT wavelengths is expected to be on the order of 1 mm. To not compromise the structural imaging with OCT, the system was optimized such that OCT was in focus while the MSI was slightly out of focus. This led to a broader point spread function (PSF) and thus poorer imaging resolution. These chromatic effects may be corrected through the use of more advanced color-correcting optical components or by replacing any refractive elements with reflective optics. The use of reflective optics is also interesting because it removes any problems associated with back-reflections, which contribute to background noise. In our experiments, back-reflections were apparent in the OCT images when the scanning beam had a normal incidence to the imaging lens leading to a localized decrease in SNR. The second effect is the multimodal nature of the VIS illumination. Indeed, the MSI illumination is carried out through the fiber core of the DCF, which has optical properties identical to an SMF28 fiber. All four MSI wavelengths are well below the cut-off wavelength for such a fiber (1250 nm), and the propagation in the DCF core is therefore multimodal. This causes distortions in the wavefront, which lead to an aberrated PSF and poorer lateral resolution. This effect could be addressed through the use of photonic crystal fibers, which are single mode at all wavelengths. However, this is not feasible in this setup as the DCFC technology is currently not compatible with such fibers. While these effects result in sub-optimal optical performance, the system's performance is adequate for practical intents and purposes. Indeed, if diffraction-limited resolution were achieved for the VIS wavelengths, a much denser sampling would be necessary to satisfy the Nyquist criterion. This would lead to much longer acquisition times and a significant oversampling for OCT.

It is also relevant to notice that through the combined use of the DCFC and the WDM, the system is entirely fiber-based. As such, it is highly robust to movement and vibrations and requires simplified laser safety considerations. These factors may facilitate future implementation in a clinical setting.

4.5.3 Reflectance measurements

The reflectance measurements depicted in Fig. 4.6 indicate significant differences between the theoretical and the experimental reflectance values for all four Spectralon samples. This is due to the difference in measurement geometry. The collected intensity for any given wavelength and imaging geometry can be described as a Beer-Lambert law that accounts for the different path lengths inside the sample, assuming a homogenous absorption coefficient. This expression can also be reformulated as the expected value of the attenuation for a given path length distribution:

$$I(\lambda) = I_0(\lambda) \int_0^{\infty} e^{-\mu_a(\lambda) l} \rho(l) dl = I_0(\lambda) \langle e^{-\mu_a(\lambda) l} \rangle, \tag{4.10}$$

where $I_0(\lambda)$ is the initial intensity of the collected light without attenuation, $\mu_a(\lambda)$ is the absorption coefficient, l is the photon path length and $\rho(l)$ is the photon path length distribution (PPLD) which is defined by the sample scattering properties and the illumination/collection geometry. Any reflectance measurement is then defined as the ratio of the measured intensity with and without attenuation, but with the same PPLD:

$R(\lambda) = I(\lambda)/I_0(\lambda) = \langle e^{-\mu_a(\lambda)l} \rangle$. Two reflectance measurements of the same sample (fixed μ_a) could then only be expected to return the same value if they also share the same PPLD. The theoretical reflectance values described in the specification of the Spectralon color standards are determined by illuminating the sample with a large diameter pencil beam and collecting all of the diffuse light with an integrating sphere. In the experiments presented in this work, both illumination and collection are carried out through a single fiber and the imaging optics (i.e. in a confocal geometry). As such, the collected photons have a significantly different propagation regime than in the widefield case. It can, therefore, be expected that the PPLD and the measured reflectance values will differ from the theoretical values.

It should be noted that some of the measured reflectances return values greater than 1 (see Fig. 4.6 for the yellow and red Spectralon targets). This effect may be attributed to the measurement uncertainty associated with the sample, reference, and dark measurements. The resulting relative uncertainty on the measured reflectance was on the order of 15%. All measured reflectances over unity were still within the range of 1 ± 0.15. It is also possible that the scattering properties of the white and colored Spectralon targets are not identical due to the presence of the additional chromophores. The PPLD would then be different, which may result in reflectance values greater than one.

The variation in measured reflectance caused by the imaging geometry also influences the reconstructed color, as illustrated in the third column of Fig. 4.7. It is, therefore, inevitable that color differences appear between acquisitions with video cameras and widefield illumination, and point scanning systems such as the one presented in this work. These differences may be accounted for by defining approximate correction factors which would consist of both system and sample specific components. Such correction factors require the study of the propagation of light in the sample as a function of the sample's optical properties and the system specific imaging geometry. The theoretical framework for this analysis has already been developed in a non-imaging technique called *single fiber reflectance spectroscopy* (SFR) where reflectance measurements are carried out with single-fiber probes in direct contact with the sample [239, 307–309]. These SFR models may be adapted for non-contact imaging with the DCFC setup to accurately determine the correction factors necessary to recover the reflectance as measured by a video camera. Furthermore, these models may be used to estimate both the optical and physiological properties of biological samples.

4.5.4 Multimodality, spectroscopic analyses and future work

The clinical utility of combined OCT and MSI lies in the simultaneous access to both depth-resolved structural information and surface color. OCT may reveal sub-surface structural pathological features, while color information provides a familiar perspective that may also be used for diagnostic purposes. Figure 4.8 illustrates such combined imaging. It demonstrates the feasibility of reconstructing high-resolution color images co-registered with OCT imaging. Furthermore, MSI is not limited to color reconstruction. Indeed, it would be relatively simple to change or add wavelengths that would allow other types of clinically valuable spectroscopic analyses. Such analyses may include oximetry or blood hematocrit measurements that may be indicative of abnormal/pathological conditions such as inflammation or neoplastic angiogenesis. Furthermore, the same optimization process presented here could be used to reproduce sample appearance under narrowband imaging illumination. The addition of wavelengths would not compromise color reconstruction as the signal from each wavelength can be addressed independently. The spectroscopic information could then be processed and overlayed onto the OCT data for simultaneous visualization. Such analyses would rely on accurate propagation models to infer optical properties from the measured reflectance values. Future efforts will, therefore, be concentrated on adapting the afore-mentioned SFR models to our imaging setup.

4.6 Conclusion

We have presented several key steps in the development of a combined optical coherence tomography and multispectral imaging system. This includes an optimization procedure to guide the selection process of MSI wavelengths and their relative intensities for optimal color reconstruction. Using this procedure, we demonstrate that it is theoretically possible to reproduce the color of a sample as it would appear under broadband illumination using only a few wavelengths. Furthermore, we developed a fiber-based system which allows concurrent and co-registered imaging with both modalities. MSI signals are multiplexed in the frequency domain, acquired using a single detector and separated in post-processing using Fourier analysis. We demonstrate the system's ability to carry out high-speed, high-resolution, and simultaneous imaging with both modalities. Future efforts will be centered around modeling of light transport in samples to extract optical properties as well as better reconstruction of color.

Disclosures

C. Boudoux is a founding partner of Castor Optics Inc.

Acknowledgements

This research was supported in part by the Natural Sciences and Engineering Research Council of Canada (NSERC), the Canada First Research Excellence Fund (CFREF) through the TransMedTech institute, and by the Fonds de Recherche du Quebec - Nature et Technologies (FRQNT). The authors would like to acknowledge and thank M. Leduc from Polytechnique Montréal's Laboratory of Optical Fibers for designing and making the custom fiber WDM, L. Majeau from Castor Optics for useful discussions regarding the DCFC and Oxxius for generously lending the L4Cc multi-wavelength source.

CHAPTER 5 COMBINED OPTICAL COHERENCE TOMOGRAPHY AND ULTRA-BROADBAND, IMAGING SINGLE-FIBER REFLECTANCE SPECTROSCOPY

5.1 Introduction

Optical coherence tomography is a powerful interferometric technique that provides high-speed, high-resolution, depth-resolved imaging [45]. Over the last three decades it has shown great promise as a diagnostic tool in various fields including ophthalmology [310, 311], gastroenterology [2, 292], cardiology [80, 289], pulmonology [112, 312], and urology [291, 313–315]. While OCT is an effective method to assess morphology and detect microstructural changes, its standard implementation lacks sensitivity to molecular content. Variants of the technique with enhanced chemical sensitivity have been developed; however, they still present limitations or performance tradeoffs compared to other optical modalities [76, 292]. An alternative to overcome these limitations is a multimodal approach, combining OCT with one or several other techniques with complementary contrast mechanisms. These include modalities such as fluorescence [155, 156, 273] and fluorescence lifetime imaging [171], multiphoton microscopy [316], Raman spectroscopy [296, 317], and hyper- or multispectral imaging [3, 318, 319]. Such combinations provide additional insight into the sample biology, which may lead to enhanced diagnostic and tissue differentiation capabilities.

Another potential candidate for combination with OCT is a spectroscopy technique called single-fiber reflectance spectroscopy (SFR). SFR evolved organically from diffuse reflectance spectroscopy (DRS) as researchers measured ever smaller source-detector separations until they perfectly overlapped. As its name indicates, SFR measures the reflectance spectrum of the sample and relies on the use of a single fiber for both illumination and collection. In its typical implementation, SFR is performed with a multimode fiber in contact with the sample; however, it may be carried out in a non-contact manner with optics projecting an image of the fiber tip onto the sample. This enables scanning of the sampling location, which leads to imaging SFR (iSFR) rather than the single-point approach. Analysis of the reflectance spectra provides information on the absorption and scattering properties of the sample, which can be correlated to molecular content and physiological parameters such as tissue perfusion or blood oxygenation [37,241,242,320,321]. A key advantage of SFR is that, due to the illumination/collection geometry, the signal is primarily composed of light propagating in a sub-diffuse regime resulting in a very superficial and spatially constrained sampling volume [241, 242, 320]. Moreover, the sub-diffuse regime renders the measurements susceptible to the scattering phase function [242], which can also provide insight into tissue microstructure. As such, by producing complementary information on the sample and having a compatible form, iSFR appears to be a viable modality for combination with OCT.

In this work, we present the combination of OCT with broadband, imaging single-fiber reflectance spectroscopy using double-clad fiber (DCF) and a double-clad fiber coupler (DCFC). This system performs OCT at 1300 nm through the core of the DCF and iSFR with core illumination and inner-cladding collection over the extended spectral range of 450–1650 nm. As such, this chapter combines the full spectral measurement from Chapter 3 with the internal illumination demonstrated in Chapter 4. In this configuration, OCT provides information on the sample morphology, while broadband spectroscopic imaging provides insight into the molecular composition. The extended spectral range of the spectroscopic channel covering both VIS and NIR allows sensing several important biological chromophores, including blood, water, and fat, as depicted in Fig. 5.1. As such, measurements of the full spectrum over this extended range may be used to identify key spectral features for tissue classification and develop diagnostic algorithms. Moreover, identifying important spectral features may guide the choice of spectral bands for multispectral illumination schemes, such as the one presented in Chapter 4. While broadband hyperspectral systems have been developed in the past, they do not investigate the specific imaging geometry (with point-scanning and overlapping illumination and collection) or the corresponding propagation regime. In this subdiffuse regime, the optical features differentiating between healthy and malignant tissue might differ from conventional widefield HSI. Beyond identifying characteristic spectral features, by removing all chromatic effects with the RSH, this system can also be used to develop non-contact SFR models, an ongoing project discussed briefly in Chapter 10.

There are several technical challenges associated with developing the proposed system. We first present and characterize an all-reflective scanner head (RSH), which allows achromatic and backreflection-free imaging at all wavelengths. We also detail the method for multiplexing and demultiplexing the optical signals and evaluate potential cross-talk between the modalities. Finally, we present preliminary imaging with OCT, iSFR, and both modalities simultaneously to demonstrate the capabilities of the multimodal system.

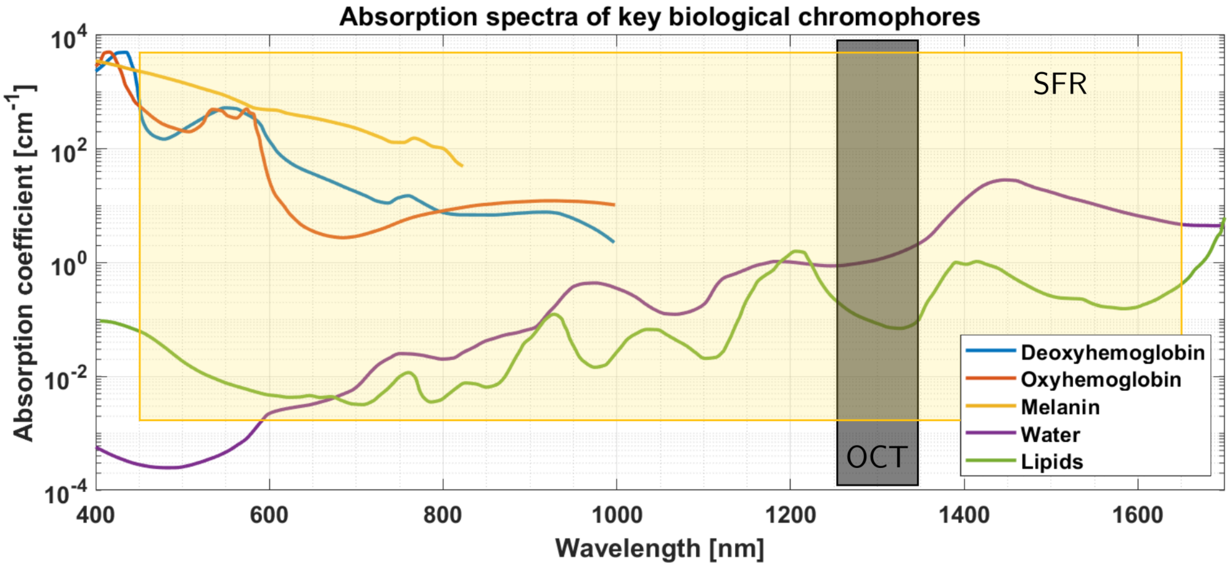

Figure 5.1 Absorption spectra of key biological chromophores. Colored boxes indicate the OCT and iSFR spectral ranges. Absorption coefficient data extracted from [4].

5.2 Methods

5.2.1 Experimental setup

Figure 5.2 presents a schematic of the experimental system. It consists of a standard 1300 nm SS-OCT fiber system with additional components added to the sample arm. These components include a broadband, free-space beam combiner (BC) and a double-clad fiber coupler (DCFC, DC1300LE2, Castor Optics, St-Laurent, Canada) inserted into the sample arm. The free-space BC allows the injection of the OCT laser (Axsun swept laser 1310, Excellitas Technologies, Mississauga, Canada) and a broadband supercontinuum laser (EXU-6, NKT, Birkerod, Denmark) into a single fiber for illumination. The broadband supercontinuum light is combined with the OCT light with a non-polarizing beamsplitter (NPBS, BS030, Thorlabs, Newton, NJ, USA) optimized for reflection (90%) across the OCT spectral range. This preserves the OCT signal power at the cost of the supercontinuum light, which is only transmitted with an average efficiency of ∼10%. Both signals are then coupled into the core of a 3 m segment of SMF-28, spliced to port A of the DCFC, using a reflective collimator (RC, RC04APC-P01, Thorlabs). It is important to note that several fold mirrors not depicted in Fig. 5.2 are used for alignment purposes. The SMF-28 segment spliced to port A of the DCFC prevents the injection of light into the cladding of the DCF. For OCT, this is important to avoid *ghost signal* resulting from light briefly propagating in the inner cladding of the DCF before coupling back into the core [207]. For iSFR, this is important to achieve core illumination without residual cladding illumination. All light exiting the DCF at port S of the DCFC is focused onto the sample using a custom reflective scanner head (RSH). The detail of the RSH is discussed in a sub-section below. After interaction with the sample, back-scattered light is collected in the DCF at port S. Detection is performed in the core of the DCF for OCT and through the inner cladding for iSFR. Light captured in the inner cladding is extracted to port B and routed to the spectral detection module, also discussed in a sub-section below. OCT light is returned to the OCT fiber system through the free-space beam combiner for detection and acquisition. A bandpass filter (BPF) composed of a 1400 nm shortpass and a 1200 nm longpass filter removes most of the iSFR signal collected in the DCF core that may generate cross-talk between the two modalities in the OCT channel.

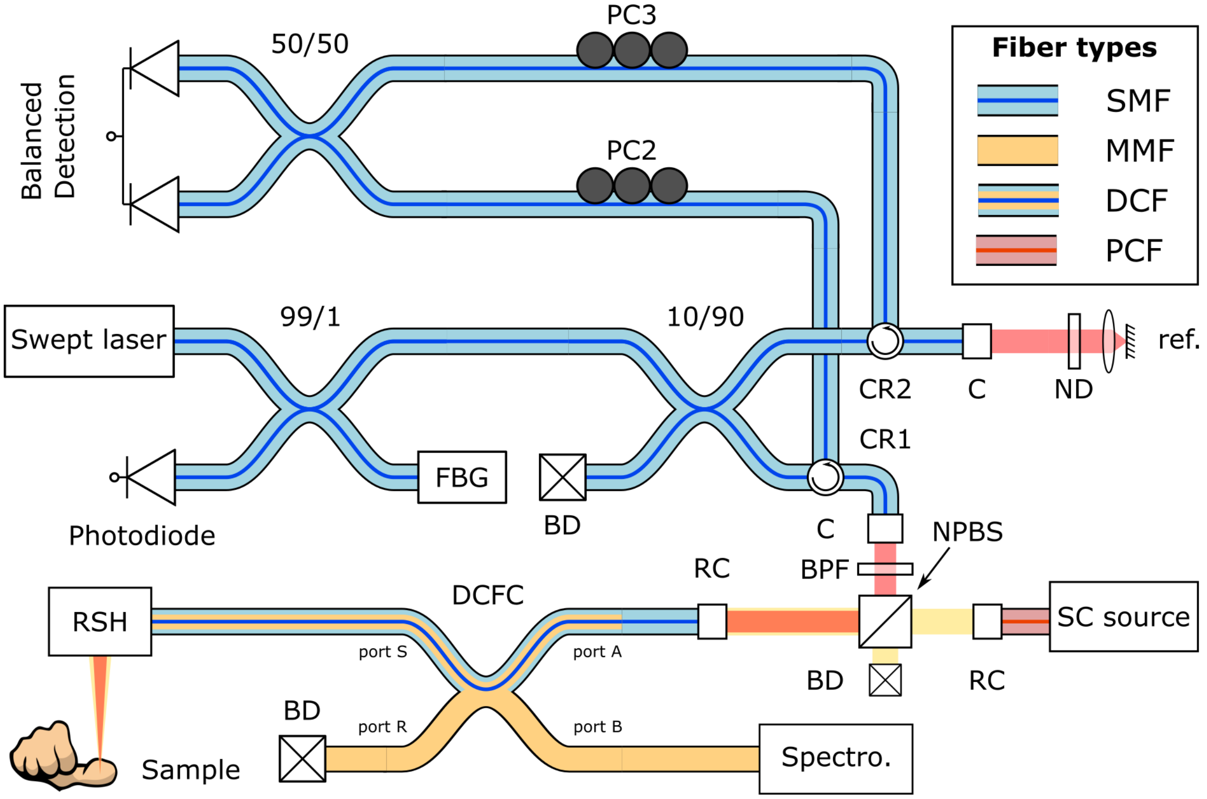

Figure 5.2 Experimental setup: (**PC**) polarization controller, (**FBG**) fiber Bragg grating, (**CR**) broadband circulator, (**C**) collimator, (**ND**) variable neutral density filter, (**BD**) beam dump, (**BPF**) bandpass filter, (**NPBS**) non-polarizing beamsplitter, (**RC**) reflective collimator, (**DCFC**) double-clad fiber coupler, (**RSH**) reflective scanner head, (**SMF**) single mode fiber, (**MMF**) multimode fiber, (**PCF**) photonic crystal mode fiber, (**DCF**) double-clad fiber.

AO reflective scanner head

The use of broadband light proposed in this paper produces technical difficulties for standard refractive optics, such as significant chromatic aberrations and back-reflections. Indeed, refractive optics are not designed with such a broad wavelength range in mind and present significant chromatic focal shifts, which can considerably degrade image quality and reduce fiber coupling efficiencies. Furthermore, anti-reflection coatings are not commonly available over the entire spectral bandwidth, leading to significant back-reflections and background signals, potentially drowning out the useful signal. Fortunately, these undesirable chromatic effects can be addressed through reflective optics. To this effect, we designed an imaging head comprised exclusively of reflective components, presented in Fig. 5.3. This scanner head consists of a parabolic reflective collimator (RC04APC-P01, Thorlabs, Newton, NJ, USA), a deformable mirror with a tunable focal length (DM, Revibro, Revibro Optics, Bozeman, MT, USA), a flat mirror (PF10-03-P01, Thorlabs) mounted on a high-stability kinematic mount (Polaris, Thorlabs) for beam folding, a fixed spherical mirror (CM254-250-P01, Thorlabs), a 75 mm focal length off-axis parabolic mirror (OAP, MPD139-P01, Thorlabs) and either a flat mirror on a gimbal mount (GMB1, Thorlabs) for manual scanning or a dual-axis scanning mirror system (MR-15-30, Optotune, Dietikon, Switzerland). The RC first collimates the output of the DCF fiber. The deformable mirror and the spherical mirror are arranged in a slightly off-axis $2f$ configuration to provide beam expansion. The focal length of the deformable mirror can be tuned between 70 mm and infinity (flat mirror) by an analog voltage input. The enlarged, collimated beam is then focused by the OAP and scanned with the 2D beam-steering mirror. It is important to note that, in contrast with typical scanner heads, focusing is performed before scanning, as the parabolic mirror does not permit telecentric scanning. In this configuration, the focal plane will inevitably be spherical, affecting image quality for larger fields-of-views (FOV). This can be corrected dynamically by inducing minor variations of the focal length of the DM, thereby making the beam incident on the OAP slightly convergent or divergent and causing small axial shifts of the focal point. By synchronizing the DM with the scanning mirror, it becomes possible to achieve a flat focal plane over the entire FOV. The maximum FOV size, over which a flat imaging field can be achieved, is determined by the maximum axial focal shift, limited to a few mm by increasing optical aberrations as the system deviates from the ideal $2f$ configuration.

It is important to recognize that the $2f$ beam expander is an essential part of the proposed optical design. Firstly, it provides beam expansion necessary to achieve an adequate numerical aperture at the imaging plane, which would otherwise be limited by the 4 mm

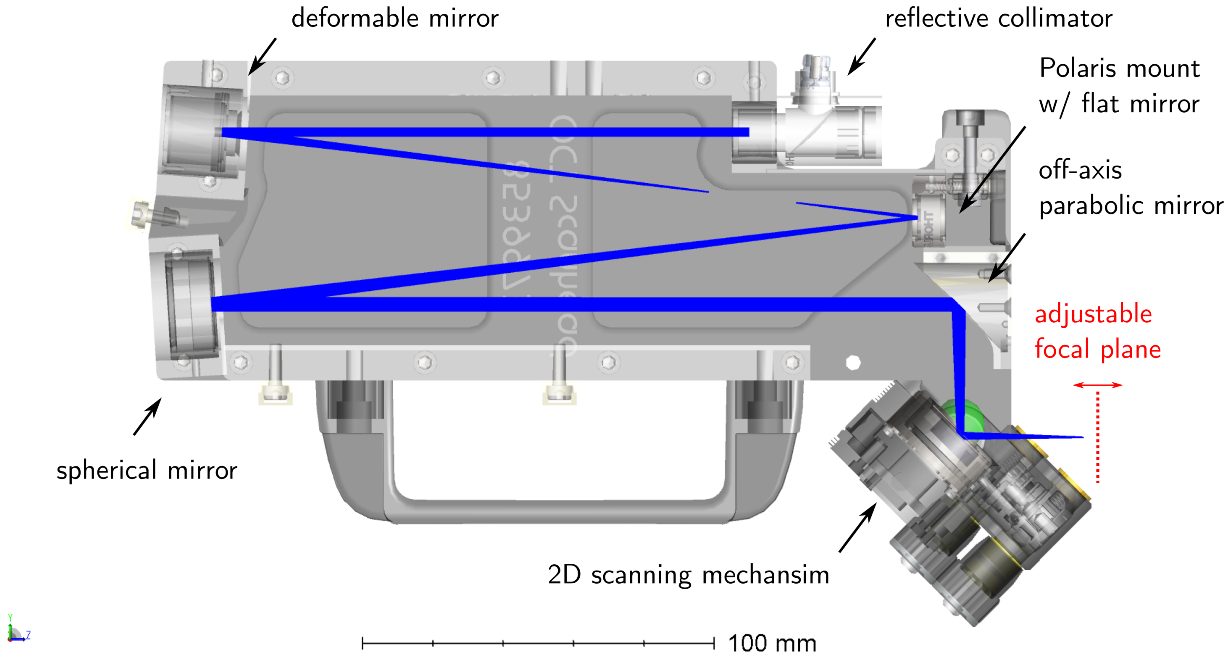

Figure 5.3 Cross-section of the reflective scanner head with beam path overlay (in blue). This schematic depicts beam scanning with a flat mirror and a gimbal mount for manual adjustments.

clear aperture of the DM. Secondly, it allows an axial shift of the focal distance, which requires the beam incident on the OAP to be convergent or divergent. As the DM is limited to positive focal lengths (i.e., limited to concave shapes), obtaining a divergent beam at the OAP would not be possible without the $2f$ setup.

The RSH was designed with all components positioned relative to the base plate, ensuring high fabrication tolerances. All non-optical components were milled out of aluminum, which was anodized to reduce the potential for the transport of contaminants. It is important to note that while manufacturing tolerances were very tight, precision alignment was still necessary to achieve optimal optical performance. We, therefore, added precision tip and tilt screws to the DM and spherical mirror. A second aluminum plate encloses the optical components for laser safety purposes.

Spectral detection

The detection module in the setup, indicated as *Spectro.* in Fig. 5.2, consists of a free-space spectral splitter realized with a 950 nm dichroic beamsplitter (DMLP950, Thorlabs). All input and output fiber ports are collimated or injected using reflective collimators (RC08SMA-P01, Thorlabs) to maximize collection efficiency and minimize chromatic effects. VIS and NIR signals are then routed to two spectrometers with wavelength ranges 400–1000 nm and 900–1650 nm, respectively (AvaSpec-ULS2048CL-EVO & AvaSpec-NIR256-1.7-EVO, Avantes, The Netherlands). These spectrometers represent the limiting factor in the system's overall acquisition speed, with a maximum acquisition rate of about 300 spectra/s. Images were mostly acquired with a corresponding integration time of 3 ms.

5.2.2 Operation & measurement protocol

Deformable mirror focus calibration

The DM used here has four actuator rings that can be controlled independently to achieve various mirror shapes, including parabolic. However, all four rings were driven using the same voltage signal in this instance, resulting in a spherical mirror shape. We established through ray-tracing simulations that the improvement in optical performance achieved by using a parabolic shape was not significant. Furthermore, this considerably simplified the mirror calibration and control. Indeed, the device used in this setup is a prototype unit without a feedback loop. Accurate calibration of the voltage to focal length relationship is necessary to adjust the overall focal length of the RSH properly. We performed this calibration through 3D beam profiling for different driving voltages and axial positions. A challenging aspect of the DM calibration is its temperature and humidity sensitivity. We observed significant daily variations in the calibration curve, although these variations could be accounted for relatively simply with an offset in the driving voltage ramp. It should be noted that the DM supplier (Revibro Optics) now offers the same device with a feedback loop that automatically compensates for day-to-day variations. Due to the low acquisition rates of the spectrometers, most imaging was constrained to a smaller number of points and, to maintain adequate spatial sampling, smaller FOVs of only a few mm^2. In these smaller FOVs, the focal plane remains almost flat across the imaging field, and no DM synchronization was implemented. In this case, the DM control voltage was set to a constant value, identified through visual inspection of OCT images.

System control & synchronization

Proper synchronization is essential between the scanning mirror and the DM for in-focus imaging across the entire FOV, and between the OCT and spectroscopy acquisition hardware, for truly co-registered imaging. As mentioned above, the acquisition of spectral data represents the system's bottleneck in terms of speed. The spectrometers were therefore used as the master clock for the complete system. A single hardware trigger signal generated by a digital to analog converter card (PCIe-6323, National Instruments, USA) was used to drive both spectrometers, the OCT acquisition board, the 2D beam scanning system, and the DM. For every galvanometer angular position, a single spectrum was acquired in each spectroscopy channel and multiple OCT A-lines (depending on the selected spectrometer integration times), which were then averaged in the spectral domain (i.e., before FFT) for an enhanced SNR. All components were controlled through an in-house Labview (National Instruments) interface, which also handled the acquisition, processing, and display.

Data processing

OCT data was processed following a conventional OCT processing pipeline. K-linearization of the data was achieved using the k-clock integrated into the swept-laser source. Multiple interference spectra were acquired and directly averaged together for each scan position in the spectral domain. Care was taken to avoid fringe washout from averaging too many spectra or due to phase instabilities between subsequent acquisitions. The averaged signal was then corrected for the background signal and highpass filtered to remove the DC and low-frequency signals further. Numerical k-linearization and dispersion compensation were applied when necessary, following the method presented in [305]. The signal was then windowed, and Fourier transformed to obtain the processed A-lines.

Spectral data was processed according to Eq. 5.1:

$$R(\lambda) = \frac{S_{\text{sample}}(\lambda) - S_{\text{dark}}(\lambda)}{S_{\text{ref}}(\lambda) - S_{\text{dark}}(\lambda)}, \tag{5.1}$$

where S_{sample}, S_{ref}, and S_{dark} are the signals acquired from the sample, reference, and dark measurements, respectively. The reference sample used here was a 99% Spectralon white diffuse reflectance target (SRS-99-010, Labsphere, USA) which has a spectrally flat response over the 250–2500 nm range. The dark signal is the signal measured in the absence of a sample. It is important to note that the reflectance of the Spectralon target is only 99% in the diffuse sense, where all the scattered light is collected. Here, illumination and collection are carried out over a limited solid angle due to the low NA. As such, the reference signal measured with the Spectralon target accounts for the spectral shape of the illumination but does not constitute the maximum possible reflectance. Values calculated with Eq. 5.1 can, therefore, exceed unity.

5.3 Results

5.3.1 RSH field curvature correction with focus shifting

The spherical focal plane of the system is depicted in Fig. 5.4. For a given curvature of the DM, the focal plane is located at a distance $f_0 + \Delta f$ from the 2D scanning mirror's center of rotation, indicated by the red dot at the top of the figure. To achieve a flat imaging field, the distance Δf has to be adjusted as a function of θ, the angle between the undeviated beam and the measurement point. The maximum achievable radial position, $r_{\max}$, is determined by the maximum focal shift, $\Delta f_{\max}$, for which high-quality focusing can be achieved. Here we define, albeit arbitrarily, high quality focusing as producing a diffraction-limited spot in the sample plane. The maximum angle and corresponding maximum radial imaging range can be computed by solving Eqs. 5.2 and 5.3:

$$\cos\theta_{\max} = \frac{f_0 - \Delta f_{\max}}{f_0 + \Delta f_{\max}}; \tag{5.2}$$

$$r_{\max} = (f_0 + \Delta f_{\max}) \cdot \tan\theta_{\max}. \tag{5.3}$$

To achieve the flat imaging field as presented in Fig. 5.4, the system must be able to shift the focal plane by $\pm\Delta f_{\max}$ and not only in the positive direction. However, we may define f_0 freely provided acceptable focusing can be achieved in the $f_0 \pm \Delta f$ range. Using $f_0 =$ 38 mm, as is the case in the actual setup, the maximum radial range and corresponding square FOV are presented in Tab. 5.1 for different $\Delta f_{\max}$ values. It is interesting to note that the FOVs presented in Tab. 5.1 are large relative to comparable refractive scan lenses.

Table 5.1 Theoretical imaging ranges with focal plane adjustments.

$\Delta f_{\max}$ [mm]	$r_{\max}$ [mm]	FOV [mm^2]
0.5	9.0	12.7×12.7
1.0	13.0	18.4×18.4
1.5	16.3	23.1×23.1
2.0	19.4	27.4×27.4
3.0	25.0	35.4×35.4
4.0	30.5	43.1×43.1

The RSH's ability to generate diffraction-limited spots in the focal plane was evaluated for different focal shifts using Zemax. We found that the focal plane could be shifted from -4 mm to +50 mm, limited by the DM's focal length range [70 mm;∞]. However, the upper limits of the focal shift range are less relevant for imaging applications as they result in

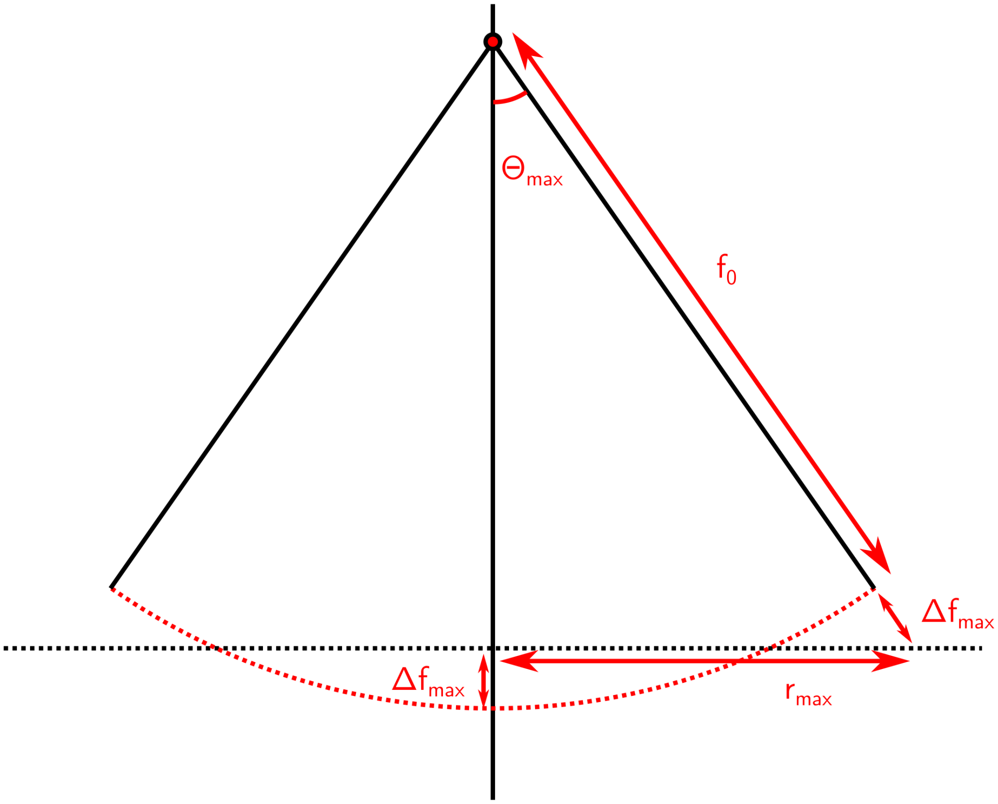

Figure 5.4 Geometrical representation of the focal length adjustment performed with the RSH. The red dashed line is the focal plane without DM adjustments, and the black dashed line is the target flat focal plane with DM adjustments.

very low NA and large spot sizes. Figure 5.5 presents the spot diagrams for the focal shift range of [-4;+20] mm. In such a spot diagram, the beam is considered diffraction limited if all rays (blue spots) fall well within the Airy disk, depicted in black in each diagram. As such, $\Delta f = -5$ mm is the extreme value at which the beam will no longer achieve the ideal spot (at 1300 nm — this limit is wavelength-dependent).

Figure 5.5 also highlights another relevant behavior of the RSH: a variation in the Airy disk size corresponding to a variation in NA in sample space. This effect is caused by changes in the overall focal length and beam size variations at the off-axis parabolic mirror. By changing the focal length of the DM, the beam expands more or less before reaching the OAP. Moreover, these two effects build upon each other, resulting in a non-negligible variation of NA of [0.047;0.017] across the $\Delta f = [-4;+8]$ mm range. It is important to consider this effect, as using both extremes within one image would result in significant variations in lateral resolution. For example, using $\Delta f = \pm 4$ mm and $f_0 = 38$ mm as presented in Tab. 5.1, the spot size would vary from 8.9 μm to 19.0 μm within the image (at 1300 nm). Too many parameter combinations (wavelength, spot size, Rayleigh range, choice of f_0 and Δf) influence this effect to discuss all scenarios, but the effect should be evaluated for the intended implementation. Indeed, it may represent a limiting factor that could prevent us from achieving the large theoretical FOVs listed in Tab. 5.1.

We characterized the experimental performance of the RSH by performing beam profiling at different axial positions and DM deformations. To preserve the DM, the driving voltage was limited to 80% of its maximum range resulting in the focal shift range of [0;+8] mm. Figure 5.6 presents the theoretical and experimental performance of the RSH. For the evaluated Δf range, the experimental data points are close to the theoretical values indicating that we achieve focusing close to the diffraction limit. The spot size variation with focal shift also follows the expected trend closely. The X and Y waist sizes overlap almost perfectly, indicating minimal astigmatism. However, for distances far away from the focus (i.e., at multiple Rayleigh lengths), we observed some non-ideal behavior in the beam's divergence (not shown), indicating the presence of some degree of aberration. While this is unlikely to affect imaging performance, we will investigate this in the future.

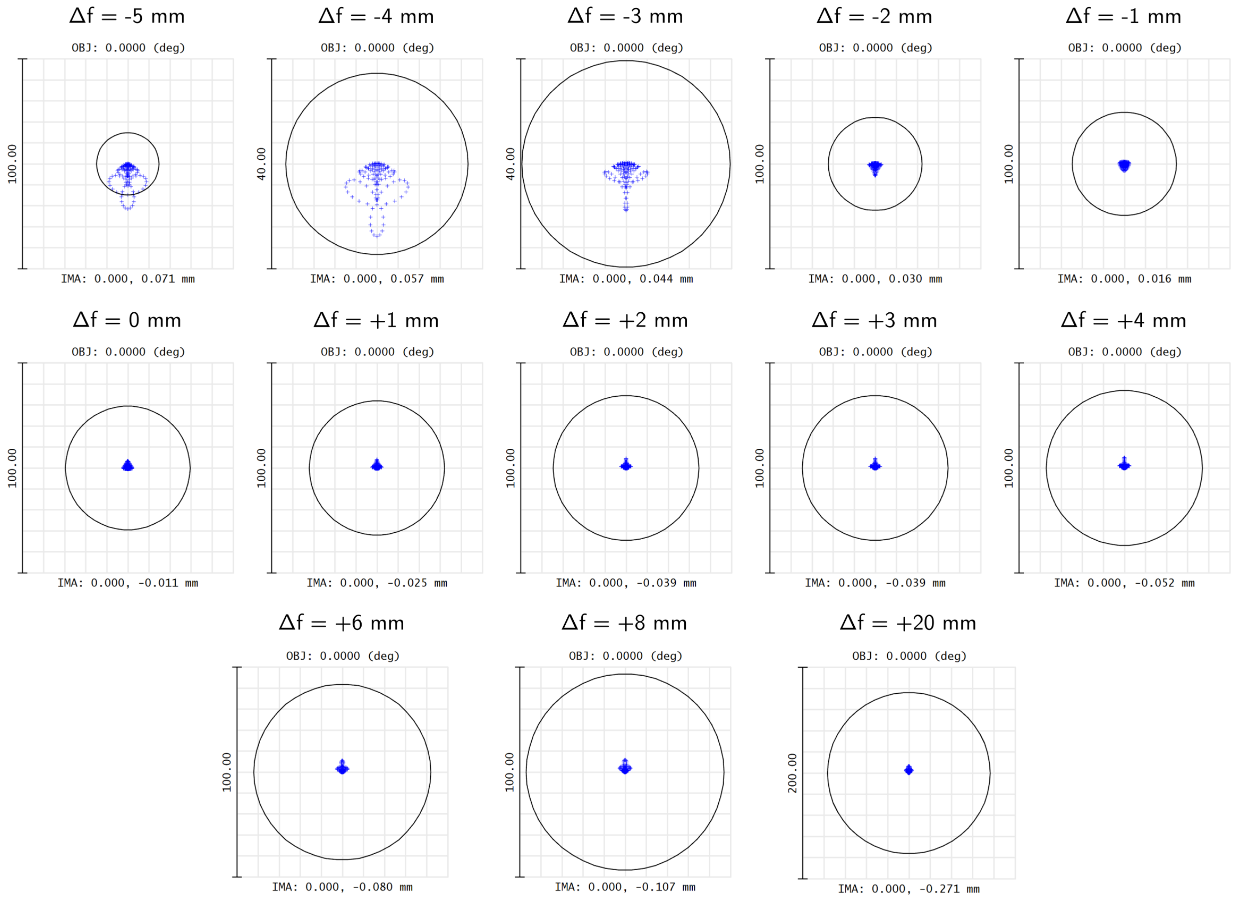

Figure 5.5 Zemax spot diagrams for focal shifts ranging from [-5;+20] mm. Diffraction-limited focusing occurs when the blue rays fall well within the black Airy disk.

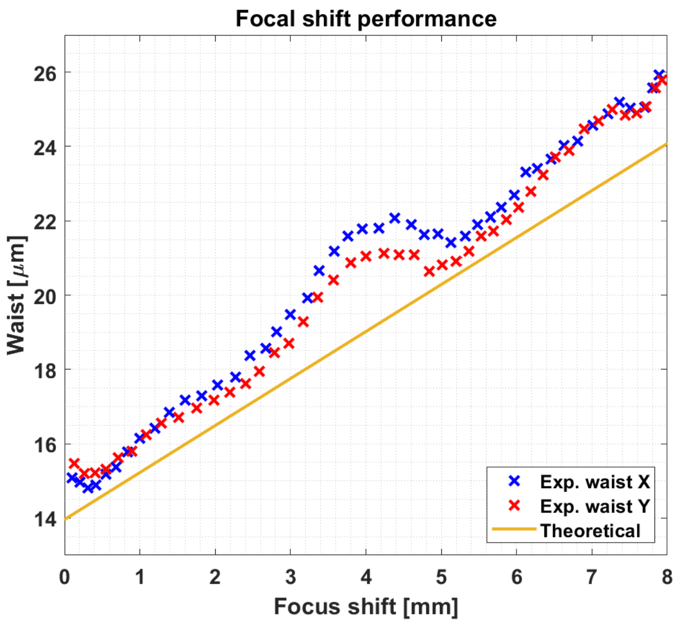

Figure 5.6 Experimental spot sizes for different focal shifts. The waist value corresponds to the $1/e^2$ radius determined through beam profiling at 1300 nm.

Extended depth-of-field OCT with focus scanning

Aside from flattening the focal plane, the DM also allows us to perform focus scanning. By acquiring multiple B-scans and shifting the focal plane to different depths within the sample, we can avoid blurring at depths that are out of focus [322]. This is particularly interesting for OCT imaging with a higher NA, where the depth-of-focus is strongly reduced ($\propto 1/\mathrm{NA}^2$). In Fig. 5.7, four B-scans were acquired with the focal plane shifted to different depths in the sample. The combined image (bottom) is a maximum intensity projection (MIP) of the four B-scans, which has sharp features across the entire ~ 5 mm imaging depth, although the beam only had a Rayleigh length of about 1 mm. The bottom image does present some slight blur in certain locations, which can be attributed to the MIP, small sample motion, or lack of repeatability from the scanning device. An alternative to using a MIP would be to select an in-focus, horizontal slice of each B-scan and stitch these slices together vertically.

5.3.2 Preliminary imaging

By imaging a printed ColorChecker target, we demonstrate our ability to perform spectroscopic imaging or iSFR over the wavelength range of 450–1650 nm. As visible in Fig. 5.8,

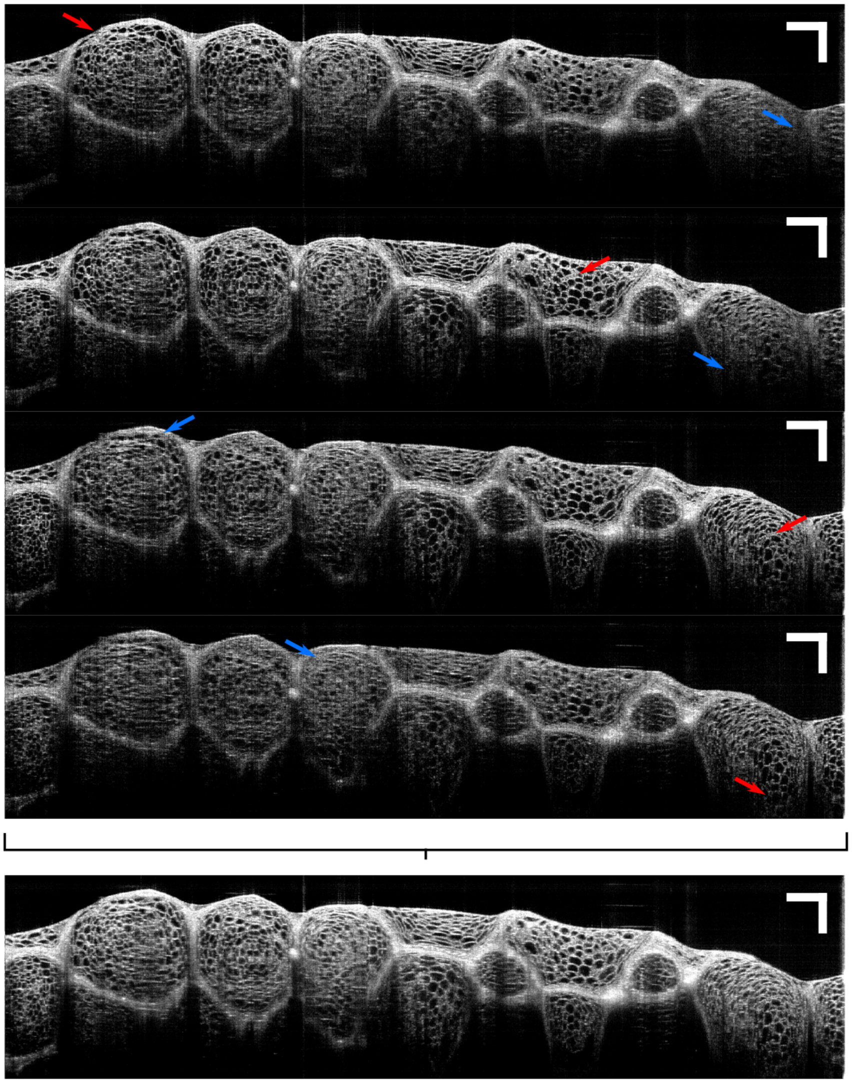

Figure 5.7 OCT imaging of a mandarine slice with focus scanning. The bottom image is generated by performing a maximum intensity projection of the top images, each acquired with the focal plane located at a different depth. The red arrows highlight in-focus features, while the blue arrows highlight out-of-focus features. Scale bars are 1 mm.

we can obtain continuous spectra over the entire wavelength range for each pixel in the image. Figures 5.8(A)–(J) present spectral images at several wavelengths. From these images, we can observe that all wavelengths are in focus and produce sharp images, thanks to the achromatic nature of the RSH. It is interesting to notice the variation in the relative brightness of the squares at different wavelengths indicative of the different reflectance spectra for each color square in the target. The system also provides sufficient lateral resolution to distinguish the different cyan/magenta/yellow/black (CMYK) ink dots from the printer used to print the sample. The CMYK ink used in printers has almost no contrast in the NIR, resulting in near-identical images across the entire NIR band, as illustrated by Figs. 5.8(G)–(J). Figure 5.8(H) presents the RGB reconstruction from the spectral data (main image) and a CCD photograph of the sample (inset). The close match between the two demonstrates the ability of iSFR to reproduce high-resolution, photo-realistic images through point-scanning measurements. However, it is important to note that this photo-realism is only achievable for highly scattering samples (paper in this instance) where the propagation volume of the collected photons is near-identical for widefield and point illumination. Figure 5.9(B) illustrates a scenario where this condition is not satisfied.

The dip in reflectance between 1300 and 1400 nm, and the slight degradation in the image quality in Fig. 5.8(H), is caused by saturation of the NIR spectrometer by the high intensity of the OCT laser at these wavelengths. The swept-laser used for OCT is approximately two orders of magnitude more powerful in terms of spectral power density (W/nm) than the broadband illumination used for iSFR. While the OCT signal can be and is used for iSFR, this mismatch in power leads to inefficient use of the dynamic range of the NIR spectrometer. A tradeoff between signal quality outside the OCT range and saturation within the range is often necessary. As such, it may be preferable to acquire the two modalities sequentially rather than concurrently. While the OCT signal may negatively impact the quality of the iSFR signal, the broadband illumination for iSFR has no impact on the OCT images. This can be attributed to the bandpass filter in the sample arm of the OCT system, the lack of interference effects between the OCT and SFR light, and to lower spectral power density of the SFR illumination.

We also performed combined OCT and iSFR measurements on biological samples. Fig. 5.9 presents combined imaging of a piece of porcine liver. In biological tissue with lower scattering, the propagation regime of the photons collected with the system differs significantly from the diffuse photons collected by our eyes. As such, the color appearance can no longer be directly reconstructed by applying color conversions to the reflectance spectrum, as illustrated in Fig. 5.9(B), where the color differs significantly from the pho-

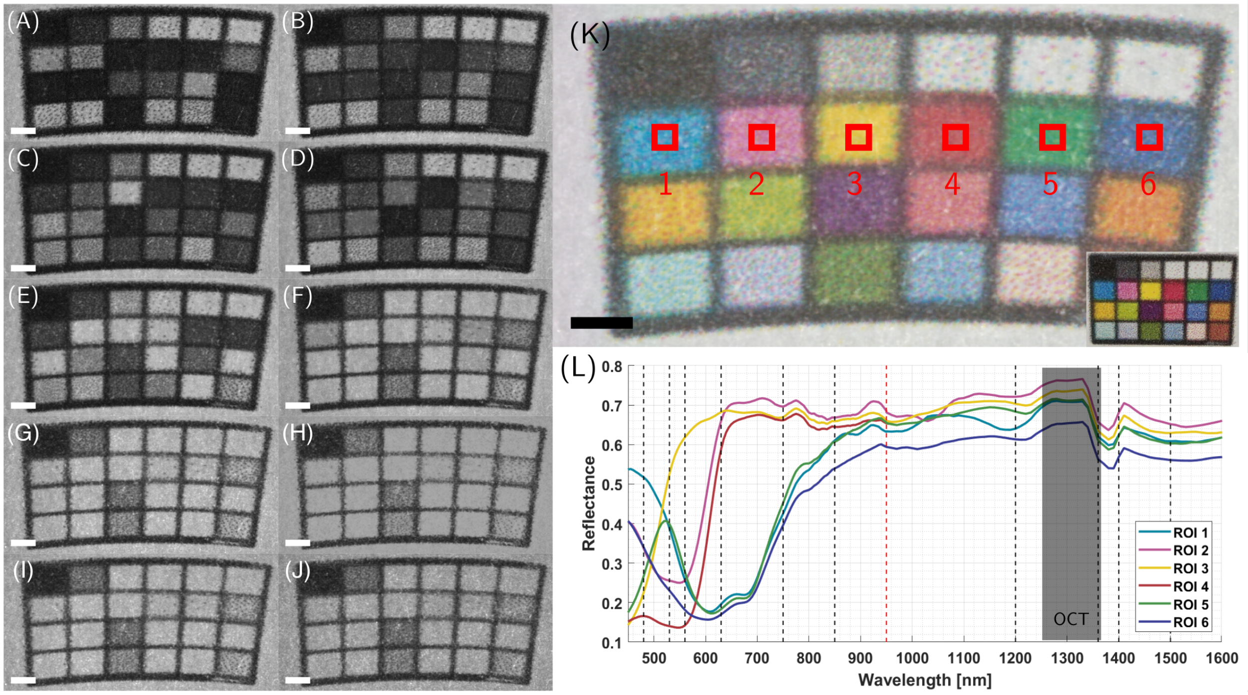

Figure 5.8 Broadband spectroscopic imaging of a printed ColorChecker target. (A)–(J) Reflectance images at various wavelengths: 480, 530, 560, 630, 750, 850, 1200, 1360, 1400 & 1500 nm. (K) Reconstructed color image of the target. The inset in the bottom left is a photograph of the sample (L) Reflectance spectra of ROIs indicated in (K). The curve color matches the color of the ROI. The black dashed lines indicate the spectral bands used in the images in (A)–(J). The red dashed line indicates the wavelength at which the spectra were merged ($\lambda = 950$ nm). The dark band labeled OCT indicates the approximate spectral range of the OCT illumination. All scale bars are 1 mm.

tograph in (A). More advanced analysis of the propagation of the collected photons is necessary to extract absolute values of optical properties and potentially reconstruct color-accurate images. Nonetheless, the reflectance signal can still highlight spectral differences and reveal hidden features. The logarithm inverse reflectance (LIR), an approximation of the sample absorbance, of the two ROIs in Fig. 5.9(B) are plotted in (D). This plot highlights several relevant absorption peaks highlighted by black arrows. The first two, in the VIS range, are absorption peaks of HBO_2, while the third, in the NIR range, is an absorption peak of water. Figure 5.9(D) highlights the spectral differences between the two ROIs. Figure 5.9(C) presents the reflectance at the water absorption peak. At this spectral band, previously invisible features of the lobule are revealed, as highlighted by the red arrows. Simultaneous OCT measurements also reveal complementary information about the sub-surface structure of the sample. In Figs. 5.9(E) & (F), we can observe structural features that are not visible in the superficial iSFR images. Notably, the connective tissue outlining the individual lobules can be traced, and individual blood vessels can be identified. Overall, Fig. 5.9 illustrates the wide variety of approaches that can be adopted to study the sample with the proposed setup. Structural information can be gathered with OCT, while iSFR can be leveraged to reveal hidden features or differentiate between different tissue types. Combined quantitative analysis to extract absolute optical properties is also possible, but it is left to future work.

5.4 Discussion

5.4.1 RSH & system design

The proposed RSH offers several advantages over conventional, lens-based scanner heads. First and foremost, it allows achromatic imaging across an ultra-wide spectral bandwidth of 450–1650 nm. Second, it allows very large FOVs by flattening the image field. Finally, because it relies exclusively on reflective optics, it does not contain any optical interfaces that can generate unwanted backreflections. This feature is vital for reflectance mode spectral imaging. However, the design also presents some shortcomings. The first is a distortion of the imaging field called the *keystone effect*. This distortion is associated with the scanning mechanism and is visible in the images of the ColorChecker target in Fig. 5.8. In these images, the target appears slightly rounded and trapezoidal when in reality, it is perfectly rectangular. Numerical compensation of this effect, through resampling or non-linear corrections of the scan pattern, is possible but has not been implemented yet. A second shortcoming is the radial nature of the beam scanning. Even with a flattened focal plane, the direction of the light rays will be radial from the center of rotation of the

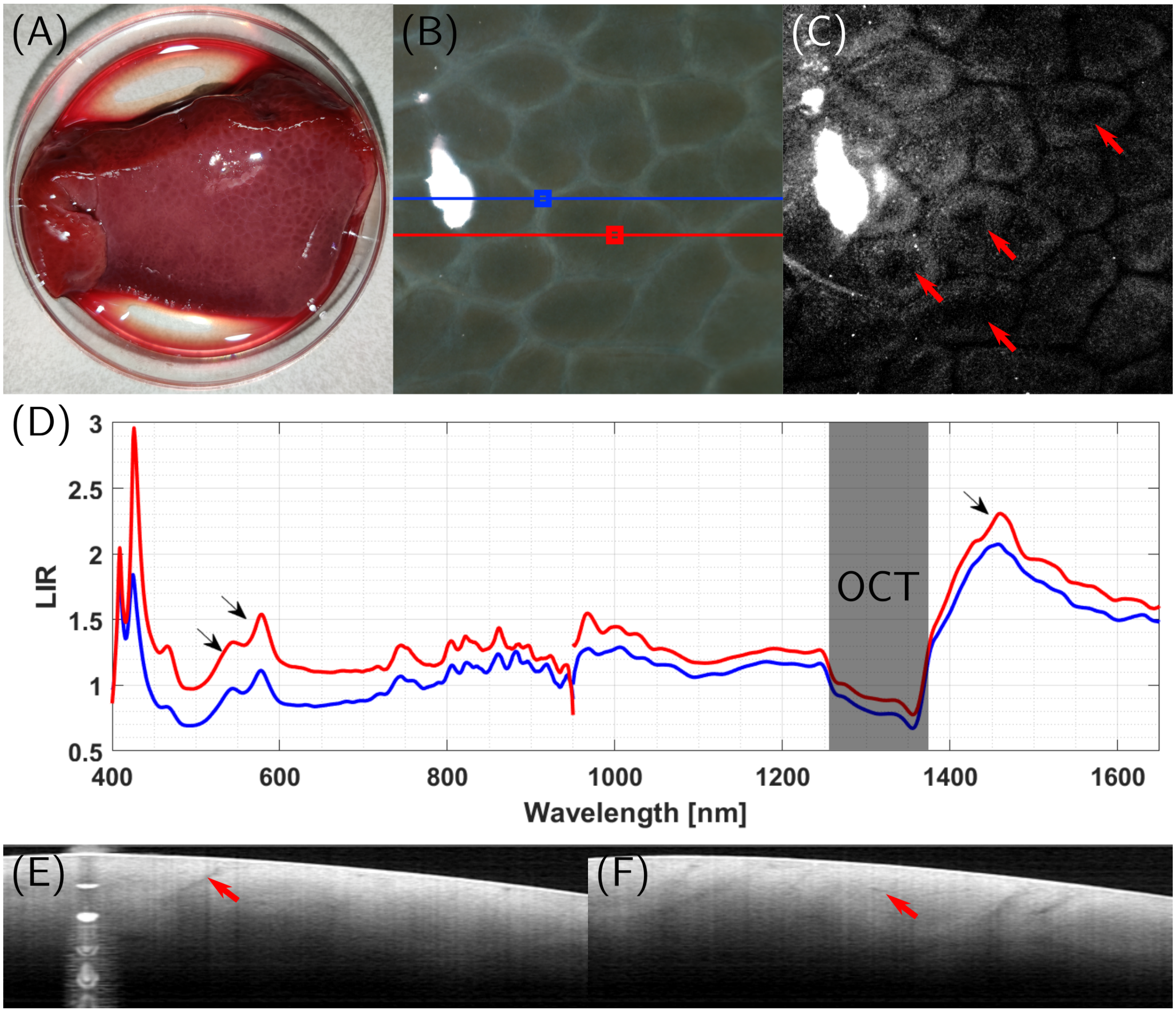

Figure 5.9 Combined OCT and iSFR imaging of porcine liver. (A) Photograph of the sample. (B) Color reconstruction from VIS reflectance spectra. The two ROIs are connective tissue (blue) and the center of a lobule (red). The horizontal lines passing through the ROIs indicate the location of the cross-sectional views presented in (E) and (F). (C) Reflectance image at $\lambda = 1462$ nm corresponding to an absorption peak of water. The red arrows highlight lobule features not visible in the color reconstruction. (D) Logarithm inverse reflectance of the ROIs in (B). The black arrows indicate spectral features of biological relevance. From left to right: 542 & 579 nm, two absorption peaks of HbO_2 and 1462 nm, an absorption peak of water. The dark band labeled OCT indicates invalid data due to signal artifacts. (E) OCT B-scan through the blue ROI. The red arrow highlights the continuation of the connective tissue below the sample's surface. (F) OCT B-scan through the red ROI. The red arrow indicates a vessel passing through the center of the lobule.

2D scanner. As such, the spacing between neighboring A-lines will not be constant as a function of depth. A final consideration is the efficiency of the RSH. Indeed, a double pass through the device requires twelve mirror reflections. Assuming an average R=97.5% efficiency per reflection for all wavelengths (with protected silver mirrors), $R^{12} = 0.74$, implying that 26% of the total signal is lost. Care should be taken during alignment to minimize further losses and maintain maximal efficiency.

The optical system presented in Fig. 5.2 enables the combination of OCT and broadband supercontinuum light for iSFR. However, the coupling efficiency of the supercontinuum light is extremely low. Because of the spectral overlap between the two sources, it is not possible to use dichroic filters to combine them. As such, the two sources are combined using a 90/10 (R/T) non-polarizing beamsplitter which has an average efficiency of 5–10% for the supercontinuum channel. Combined with fiber coupling losses and those from the various other optics in the beam path, it is estimated that the total transfer rate of the supercontinuum is <5%. These high losses are compensated by the high power of the laser source but need to be addressed if higher speed imaging is to be attempted. Current imaging speeds are typically around 300 Hz, limited by the spectrometers, but signal levels suggest that imaging at 1 kHz or 1 ms integration time would be feasible. However, higher signal levels are necessary to hope to match OCT acquisition speeds and shorten the overall measurement time. Combined with the demonstrated problems for acquiring spectral data in the OCT range, this would encourage reducing the wavelength range to remove the spectral overlap and enable the use of dichroic filters. Alternatively, the two modalities could be acquired sequentially with direct coupling of the OCT light or the supercontinuum light into the DCFC. However, sequential acquisition has the downside that image registration would rely on the repeatability of the scanning mechanism, which would not achieve true co-registration as with concurrent imaging.

5.4.2 Combined OCT and SFR analysis

A key aspect of utilizing iSFR for biomedical applications is the adaptation of current SFR models to this new DCFC-based, non-contact geometry. The development of such models would allow the processing of spectral data into absolute values of optical properties, which could, in turn, be correlated to the physiological state of the tissue. However, there remain several significant challenges in the way of achieving this. One of these challenges is the management of glare. Glare refers to the signal returning from the Fresnel reflection at the first sample interface. Because of the unknown surface roughness, the portion of this Fresnel reflection which scatters back into the collection cone of the system is currently not controlled. In the extreme cases, strong specular signals are generated, which drown out the remainder of the returning light, as seen in Fig. 5.9(B) and (C). However, every other pixel also comprises some small amount of glare, which must be accounted for in the signal analysis. OCT may be the solution to this problem as it already provides a depth-resolved map of the sample reflectivity. Analyzing glare would therefore imply evaluating the signal in the first few pixels of the sample in the OCT image.

Another challenge in SFR signal analysis is the underdefined nature of the problem when using a single fiber [241]. Indeed, current models use a number of variables that exceed the number of measurement points provided by a single fiber. To overcome this, two fibers with different diameters are used to acquire more data and to obtain an over-defined problem. This variation of the technique is called multi-diameter SFR or MDSFR. Least-square optimization is then applied to find the best fitting solution. For iSFR with the system presented here, there are two possibilities to reproduce MDSFR measurements. The first is by using focus shifting to change the spot size and NA in the sample plane to emulate the use of different fibers. The second possibility is using both available channels of the DCF for illumination. Indeed, by using a bi-directional DCFC, it is possible to simultaneously inject and extract light from the inner cladding of the DCF. Moreover, a wideband multimode circulator could be implemented between the DCFC and spectrometers to ensure robust coupling of light into the multimode branch of the DCFC. However, it remains to be determined if switching between core and cladding illumination will sufficiently change the imaging geometry to be equivalent to MDSFR measurements.

5.5 Conclusion

In conclusion, we have demonstrated a system capable of performing co-registered and concurrent OCT at 1300 nm and iSFR over the extended spectral range of 450–1650 nm. We demonstrated using an all-reflective scanner head with focus shifting capabilities to perform achromatic imaging across large FOVs. This system provides a large amount of data which allows the analysis of the imaged sample from a variety of different morpho-chemical perspectives that may be used to identify features of interest or abnormalities. More research is necessary into adapting SFR models to the non-contact imaging geometry to obtain robust and quantitative information on the sample's optical properties. The combination of OCT with iSFR data may contribute to this objective. The system presented in this work will likely serve as a platform for developing and validating such data analysis methods.

Acknowledgements

This chapter was the subject of oral presentations at Photonics West 2020 and 2021. I would like to acknowledge the contirbutions of Paul R. Bloemen, Niels H. Kind, Dirk J. Faber, Caroline Boudoux and Ton van Leeuwen for helping in the experimental design, design and fabrication of the reflective scanner head, and data analysis.

CHAPTER 6 PRELIMINARY GRIN-BASED TETHERED CAPSULE ENDOSCOPE DESIGN FOR ESOPHAGEAL OPTICAL COHERENCE TOMOGRAPHY

6.1 Introduction

This research project's overarching goal is to develop multimodal imaging systems and, ultimately, their application to esophageal cancer detection. To this effect, we first investigated existing endoscope designs that may be used for multimodal optical coherence tomography in the esophagus. Such designs include tethered capsule endoscopes (TCE) [192,195,323] and inflatable balloon catheters [196,197,324]. These designs can be implemented using either proximal or distal scanning mechanisms. In the context of this project, we favored distal over proximal scanning to avoid the added complexity of developing our own wideband fiber-optic rotary joint (FORJ). Indeed, commercially available FORJs have a limited spectral bandwidth and may generate unwanted effects such as poor coupling, strong backreflections, and loss of modal integrity when used in conjunction with double-clad fibers (DCF) [325]. Such effects are detrimental to multimodal imaging and may be bypassed through distal scanning. We selected the TCE format for its larger size and the associated simplification in the fabrication process. Furthermore, the larger size allows more flexibility in optical design. Finally, OCT-based TCEs have been shown to be usable in unsedated patients [192, 326], which would favor their use in potential screening applications. We selected gradient-index (GRIN) optics for focusing because of their low cost and the fact that it was possible to perform focal length adjustments. It is worth noting that several other possibilities exist for focusing, such as microlenses [199], ball-lenses [153], and diffractive lenses [194, 201]. However, these solutions require significant expertise and advanced equipment, which was not available at the time.

In this chapter, we present a preliminary design for a tethered capsule endoscope using gradient-index (GRIN) optics and micromotor-based distal scanning. We demonstrate preliminary OCT images but highlight the significant shortcomings of this design for use in multimodal imaging, particularly in the case of reflectance mode imaging. We encountered many difficulties during the development and fabrication process because we attempted to perform adjustments to the GRIN elements ourselves. Moreover, it quickly became apparent that using GRIN elements would necessarily lead to performance compromises in terms of chromatic focal shift and background signal due to backreflections. It is important to note that despite these significant performance reductions, this design remains viable in specific scenarios. For example, the backreflections can be filtered out spectrally for combined OCT and fluorescence imaging. However, in the context of an expensive and re-usable distal scanning endoscope, we ultimately opted to abandon this more straightforward design to favor the no-compromise, all-reflective design presented in Chapter 7.

6.2 Methods

6.2.1 Tethered capsule endoscope design & fabrication

The endoscope design, depicted in Fig. 6.1, is inspired from existing designs presented in literature [192, 199]. The capsule comprises three parts: an aluminum top cap containing the micro-optics, a transparent PETG plastic tube (9245K21, McMaster, US), and an aluminum bottom cap that holds the micromotor assembly for distal scanning. The optical assembly consists of a connectorized pigtailed SMF (SMPF0115-FC, Thorlabs, USA) or DCF (DCF13, Thorlabs), a glass mating sleeve (51-2800-1800, Thorlabs), and a GRIN lens (GRIN2913, Thorlabs). The GRIN lens was ground down and re-polished to achieve the desired pitch, and a gap filled with high-transmission UV-curing glue (OP-4-20641, Dymax, USA) was left between the glass ferrule and the GRIN lens for manual adjustment of the final focal length prior to fixation. The UV-curing glue also acted as an index-matching medium. The micromotor (SBL04-08, Adamant Namiki, Japan) was held in place using screws (visible in the schematic in Fig. 6.1). A 1 mm diameter 45° rod mirror (47-628, Edmund Optics, UK) was glued on the axle of the micromotor to deviate the beam by $\sim 90°$ towards the outer surface of the capsule. During the gluing process, care was taken to *not* fixate the rod mirror perfectly perpendicular to the vertical axis, such that the incidence angle on the plastic tube would not be normal and hard specular reflections would not be collected. The overall outer diameter of the capsule was 1/2" or 12.7 mm. The total length could be tuned slightly by adjusting the length of the plastic tube. A proper working distance (WD, distance from the outer surface to the focal plane) could be maintained by sliding the optical assembly in or out of the capsule. For the prototype presented in Fig. 6.1, the total length came out to 32 mm, excluding the protruding glass ferrule and pigtailed fiber.

6.2.2 ABCD model for GRIN-based focusing

Figure 6.2 depicts a standard optical configuration for GRIN-based focusing. This assembly contains a single-mode fiber (SMF), a spacer that allows the beam to expand (usually glass or air), and the GRIN lens for focusing. As its name indicates, a GRIN lens has an

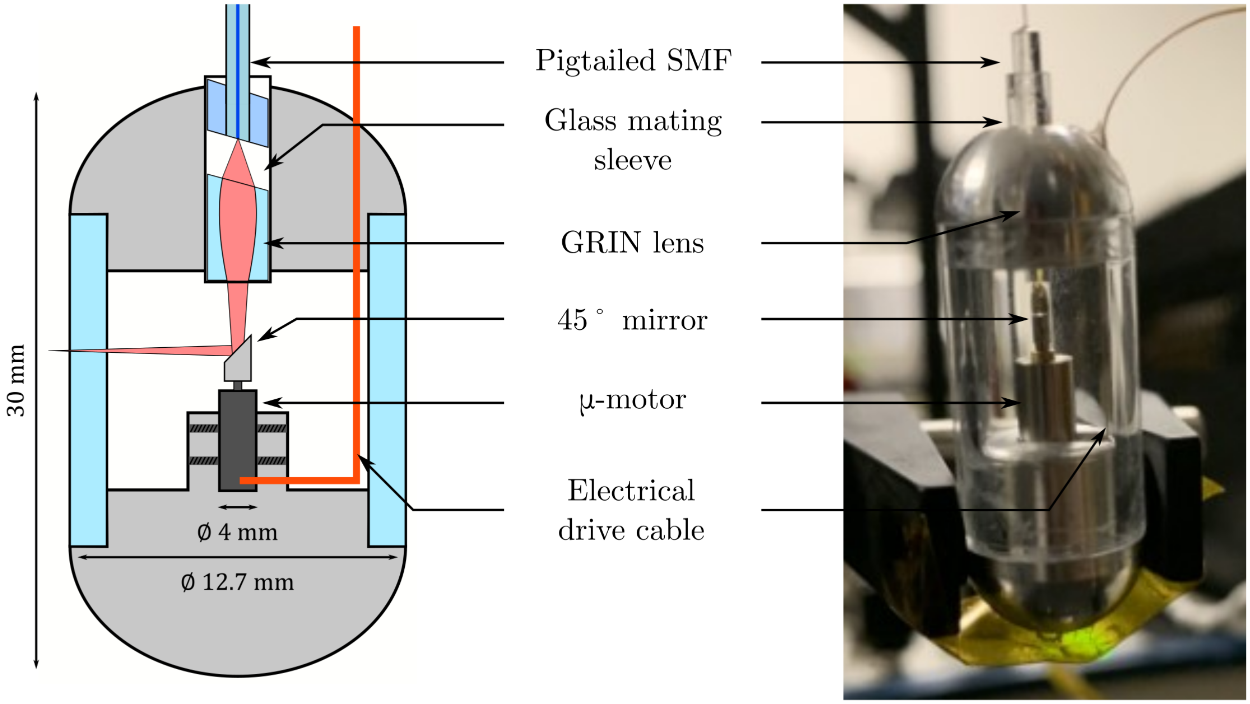

Figure 6.1 Tethered capsule endoscope. (left) Schematic representation of the device. Drawing not to scale (right) Assembled device.

index profile that varies along the radial direction, given by:

$$n(r) = n_0\left(1 - \frac{\alpha^2 r^2}{2}\right), \tag{6.1}$$

where $n(r)$ is the radial index profile, n_0 is the index at the center of the GRIN lens (i.e., at $r = 0$), and α is the gradient constant. The propagation of a gaussian beam through the system presented in Fig. 6.2 can be modeled using ABCD matrices [2, 327, 328]. This matrix is constructed as follows:

$$\begin{pmatrix} A & B \\ C & D \end{pmatrix} = \underbrace{\begin{pmatrix} 1 & z_{WD} \\ 0 & 1 \end{pmatrix}}_{(6)} \underbrace{\begin{pmatrix} 1 & 0 \\ 0 & n_0 \end{pmatrix}}_{(5)} \underbrace{\begin{pmatrix} \cos(\alpha z_G) & \frac{1}{\alpha}\sin(\alpha z_G) \\ -\alpha\sin(\alpha z_G) & \cos(\alpha z_G) \end{pmatrix}}_{(4)} \underbrace{\begin{pmatrix} 1 & 0 \\ 0 & \frac{n_S}{n_0} \end{pmatrix}}_{(3)} \underbrace{\begin{pmatrix} 1 & z_S \\ 0 & 1 \end{pmatrix}}_{(2)} \underbrace{\begin{pmatrix} 1 & 0 \\ 0 & \frac{n_F}{n_S} \end{pmatrix}}_{(1)}. \tag{6.2}$$

In Eq. 6.2, the numbers below each matrix correspond to the interactions of the laser beam with the elements of the optical system in Fig. 6.2. These are: (1) the refraction at the fiber–spacer interface where n_F and n_S are the fiber and spacer refractive indices, respectively; (2) the propagation through the spacer where z_S is the length of the spacer;

(3) the refraction at the spacer–GRIN interface where n_0 is the center refractive index of the GRIN lens; (4) the propagation through the GRIN lens where α is the gradient constant and z_G is the length of the lens [329]; (5) the refraction at the GRIN–air interface; (6) the propagation from the edge of the GRIN lens to the sample plane where z_{WD} is the working distance.

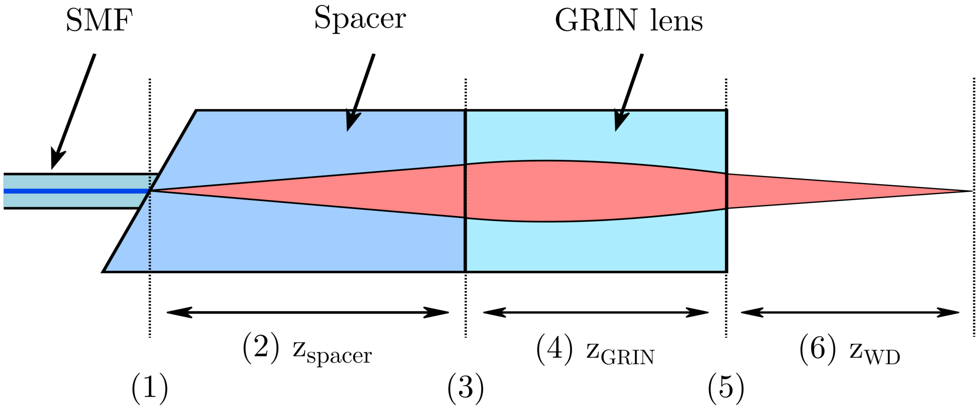

Figure 6.2 Schematic representation of GRIN-based focusing optics for endoscopic imaging. The numbered elements correspond to the ABCD matrices in Eq. 6.2 in reverse order (i.e., from right to left).

For a given ABCD matrix, the output Gaussian beam can be determined following:

$$\begin{pmatrix} q_2 \\ 1 \end{pmatrix} = k \begin{pmatrix} A & B \\ C & D \end{pmatrix} \begin{pmatrix} q_1 \\ 1 \end{pmatrix}, \tag{6.3}$$

where q_1 and q_2 are the input and output complex beam parameters, respectively, and k is a constant meant to maintain the second component of the output vector equal to 1. In single mode operation, a gaussian beam with waist w_0 = MFD/2, where MFD is the mode field diameter, is used to set the input complex beam parameter [330]. The relation between the complex beam parameter and the gaussian beam is given by:

$$\frac{1}{q(z)} = \frac{1}{R(z)} - \frac{i\lambda_0}{\pi n w(z)^2}, \tag{6.4}$$

where $R(z)$ is the radius of curvature of the wavefront and $w(z)$ is the waist radius. By isolating the real and complex components in Eq. 6.4, it is possible to recover the beam characteristics from the complex beam parameter. The imaging performance, including the expected lateral resolution and depth-of-focus, can be derived from these characteristics. It is important to note that this approach is only valid to model single-mode output from the fiber core [330], as is the case for OCT. For multimode operation at wavelengths below the fiber cut-off wavelength (~1260 nm in the case of SMF28), the gaussian beam model no longer applies, and it is better to use the ray approximation and model the fiber core as a point source with divergence described by the NA. In this case, the ABCD matrix remains identical, but the beam vector becomes:

$$\begin{pmatrix} y_2 \\ \theta_1 \end{pmatrix} = \begin{pmatrix} A & B \\ C & D \end{pmatrix} \begin{pmatrix} 0 \\ \theta_2 \end{pmatrix}, \tag{6.5}$$

where y_i and θ_i are the beam height and angle relative to the optical axis, respectively (initial beam height $y_1 = 0$ for a point source). This geometrical optics approximation does not inform us about diffraction effects to precisely predict beam size in focus but may be used to predict the axial location of the focal plane.

Chromatic effects

In the context of multimodal OCT, which may use different spectral bands, it is crucial to consider the chromatic effects of each optical component. In the ABCD matrix, each of the refractive indices intrinsically has a wavelength dependence. For the fiber core and spacer (if a glass spacer is used), these can be accounted for using the appropriate Sellmeier equations [331] as described by:

$$n^2(\lambda) = 1 + \sum_i \frac{A_i \lambda^2}{\lambda^2 - C_i^2}, \tag{6.6}$$

using the coefficient presented in Table 6.1. It should be noted that the exact core index of most fibers is proprietary information and that the values used here are approximations that aim at modeling the chromatic variations. Because no information is known about the wavelength dependence of the optical glue, we assumed a constant value of 1.50, as provided by the specifications.

Table 6.1 Sellmeier coefficient for SMF28 components. The cladding is pure silica, while the core is approximated to be doped with 4.7 % GeO_2, based on the NA specification at 1310 nm. All wavelength values (λ and C_i) are in μm.

Description	A_1	A_2	A_3	C_1	C_2	C_3
Pure silica (SiO_2)	0.6961	0.4079	0.8975	0.0684	0.1162	9.896
Pure Germania (GeO_2)	0.8069	0.7182	0.8542	0.0690	0.1540	11.84

For the GRIN lens, we used empirical equations provided by the manufacturer and extracted from Zemax (Zemax OpticStudio, US) [332, 333], which describe the wavelength dependence of the refractive index at the center of the GRIN, n_0, and the gradient constant, α (see Eqs. 6.7, 6.8, and Table 6.1):

$$n_0(\lambda) = B + \frac{C}{\lambda^2}, \tag{6.7}$$

$$\alpha(\lambda) = K_0 + \frac{K_1}{\lambda^2} + \frac{K_2}{\lambda^4}. \tag{6.8}$$

Table 6.2 Coefficients for wavelength-dependent parameters of GRIN lens.

Description	Zemax material	B	C	K_0	K_1	K_2
GRIN2913	SLW-1.8	1.5868	8.14e-3	0.3238	5.364e-3	2.626e-4

Optimization of variables

In the proposed design, several parameters can be altered within certain constraints to produce various image space NAs, defining spot sizes and Rayleigh ranges for a given WD. Assuming unchanged materials, the design presented in Fig.6.2 has three variables: the length of the spacer (z_S), the length of the GRIN lens (z_G), and the working distance (z_{WD}). There are, however, several constraints on these variables. The first are the maximum and minimum lengths permitted. The spacer length can range from 0 to 12 mm, corresponding to the length for which the beam size is too large for the GRIN lens. The GRIN elements used here are 1.8 mm in diameter. However, it is recommended that rays traveling through the element not exceed 80% of this value to avoid aberrations and vignetting. We, therefore, validated the beam size at the GRIN input and the maximum radial height of the rays traveling through it. The length of the GRIN lens can be between 0 and 5.57 mm, corresponding to the initial length as purchased. For values in between these extremes, the GRIN lens was polished down. It should be noted that it is possible to order custom GRIN elements with arbitrary lengths, which would expand the range of possible lengths. This was not explored during the fabrication of this prototype. Finally, the WD must be at least larger than the outer radius of the capsule, such that the focal plane is located outside the last glass surface. For large WDs, the complete optical assembly can be translated backward to position the focal plane in the desired location. This ideal location was defined as 0.5 mm from the outer surface. The NA of the system should also be considered as it defines the spot size, which is related to lateral resolution, and the Rayleigh length, which affects the depth-of-focus and, therefore, the OCT imaging range. We imposed the constraint that the full, two-sided depth-of-focus ($2z_R$) be larger than

1 mm in air at 1300 nm. This implies a maximum NA of 0.029 in image space. We also imposed the constraint that the spot size (ω_0) be smaller than 30 μm to maintain adequate lateral resolution ($\Delta x \sim 1.16\omega_0$). This resulted in a minimum NA of 0.0138.

Simulations and parameter optimization were performed in Matlab (Mathworks, US) with the ABCD matrix model and Zemax (Zemax OpticsStudio, USA) with ray-tracing. The optimization was performed for λ_{ref} = 1300 nm to avoid compromising the imaging quality for OCT, but chromatic effects were also considered for the wavelength range 400–1500 nm.

6.2.3 Backreflections

Backreflections (BR) are an issue for most reflectance-based imaging techniques as they preclude spectrally separating remitted light from the illumination. In the context of the proposed TCE design, the primary sources of backreflections are material interfaces that generate a Fresnel reflection due to the index difference. For uncoated glass-air interfaces, the reflected signal can be up to 4%. For surfaces treated with antireflective (AR) coatings, these backreflections can be minimized down to values below 0.5%. These spurious signals can be further attenuated by reducing the efficiency with which they couple back into the system. While these values may appear low, the signal re-emitted in reflectance mode imaging may be much lower, which results in a very poor signal-to-background ratio (SBR) or, in the worst case, the useful signal being completely drowned out by the background. Another issue is that all AR coatings are intended to operate within a limited spectral range. Outside of this range, they generate BRs worse than uncoated surfaces. Since no AR coatings exist that operate across the full VIS and NIR regions, they do not represent a viable solution for multimodal systems that wish to combine VIS and NIR imaging.

As such, we investigated how the design variables affected the coupling efficiency of the backreflections. The coupling efficiency was quantified by evaluating the overlap between the back-reflected beam and the inner cladding of a DCF ($\varnothing_{clad}$ = 105 μm). To simulate this, the optical system was mirrored at the last interface, and the surface area of the output beam was evaluated, as depicted in Fig. 6.3. In this Figure, the last interface generates the strongest backreflections due to the significant index difference. The reflection at the surface circled in red in Fig. 6.3 produces a ray with the exact same properties (position and angle) as a ray that would continue within the GRIN element. As such, it will behave identically and can be used to predict the path of the real backreflection.

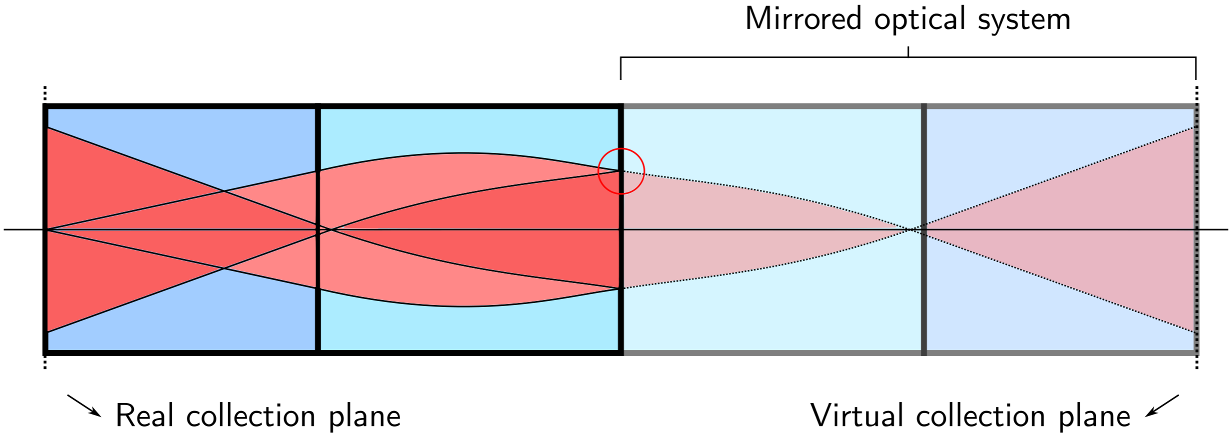

Figure 6.3 Schematic representation of the mirrored optical system used to quantify the coupling efficiency of the backreflections at the last interface.

6.3 Results

6.3.1 Optimal focusing

First, we considered the scenario without a spacer, where the GRIN lens length is altered to achieve the desired WD. In practice, the index-matching optical glue would still be inserted to guarantee a good optical contact between the fiber tip and the GRIN lens. However, the distance between the two is sufficiently small to be considered negligible. Furthermore, this has no impact on the validity of the matrix model. Solutions were identified for working distances ranging from 7.5 mm to 12 mm in steps of 0.5 mm. These solutions are presented in Table 6.3. Viable configurations (i.e., with a Rayleigh length $z_R > 0.5$ mm) were found for all WDs. It is interesting to note that $z_{WD} = 7.5$ mm represents the shortest achievable WD as z_G is approximately equal to the initial length at purchase of the GRIN element. The values presented in Tab. 6.3 match closely for both Zemax and Matlab simulations, indicating that both models are equivalent. This equivalence is further supported by the near identical results for the chromatic behavior of the optical assembly, presented in Fig. 6.4. The graphs presented in this figure highlight the poor chromatic performance of GRIN lenses as the focal plane for VIS wavelengths would be shifted several millimeters back into the capsule. Despite the relatively long Rayleigh lengths achieved in these low-NA configurations, the wavelengths below 1300 nm would, for the most part, be largely out of focus. This would result in blurred and low-quality imaging for modalities operating at those wavelengths.

The second scenario considered was a fixed GRIN lens length. By varying the spacer length it is possible to achieve different WDs, as presented in Fig. 6.5 and Tab. 6.4. In this scenario, the GRIN length was set to $z_G = 5.285$ mm, corresponding to the GRIN length with no spacer and a WD of 12 mm (see the last row of Tab. 6.3). It is apparent both from Fig. 6.5(A) and the numerical data in Tab. 6.4 that increasing the spacer length strictly reduces the WD. As such, $z_G = 5.285$ mm is the maximum GRIN length with which all z_{WD} up to 12 mm can be obtained. The fact that the WD can be simply tuned by adjusting the spacer length is practical as it simplifies the alignment procedure. By placing an infrared laser viewing card (VRC2, Thorlabs) at the desired focal distance, the spacer length can be manually tuned until the laser is in focus. It is also interesting to note that using a spacer does not influence the chromatic focal shifts of the optical assembly, as depicted in Fig. 6.5(B).

The final scenario considered was that of a fixed WD, with different combinations of spacer and GRIN lengths. The analyses were performed for $z_{WD} = 8.5$ mm, but the variables' behavior was similar for other WDs. Table 6.5 and Fig. 6.6(A) show that it is possible to tune the image space NA while maintaining a constant WD. This is particularly interesting because it provides a measure of control over the lateral resolution and Rayleigh length of the system without altering the position of the last surface of the GRIN lens, which would allow the design of a pre-aligned housing for the optical components. Finally, Fig. 6.6(B) highlights that the chromatic effects are practically independent of the $[z_S, z_G]$ combinations. While this does not solve the problem of chromatic focal shifts, it does confer some predictability to the design once a WD is selected.

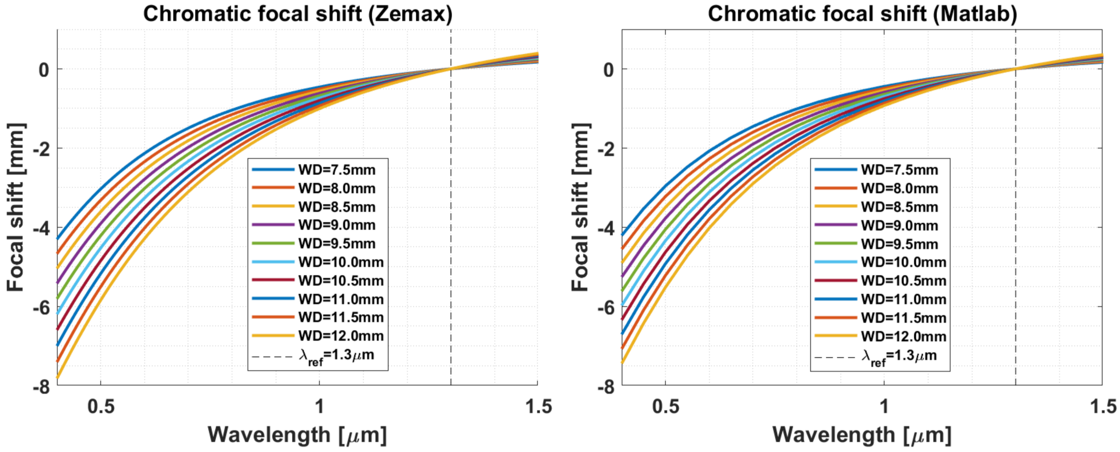

Figure 6.4 Chromatic focal shift for configuration with no spacer and variable GRIN lens length. Results from Zemax (left) and Matlab (right) optimizations.

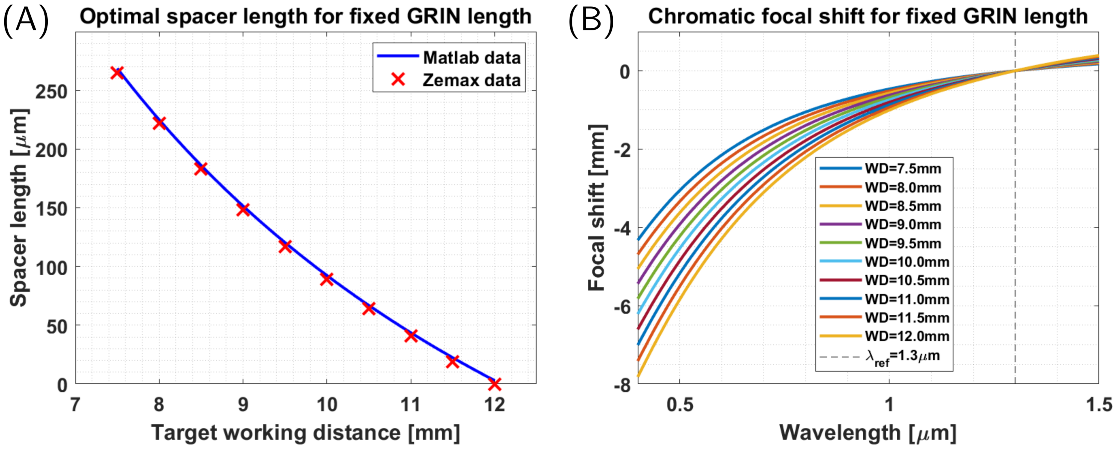

Figure 6.5 Optimization results for a fixed GRIN length and variable working distance. (left) Calculated spacer length from Zemax and Matlab. (right) Resulting chromatic focal shifts for different working distances.

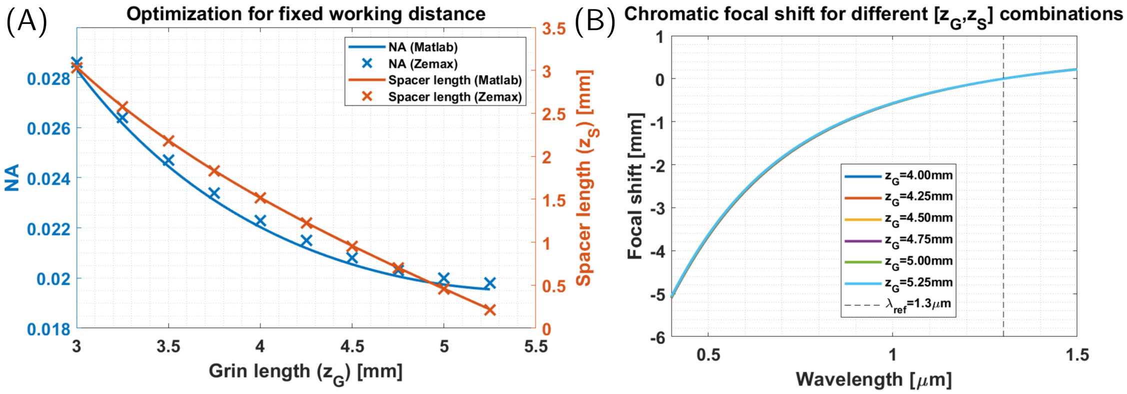

Figure 6.6 Optimization results for a fixed working distance (z_{WD} = 8.5 mm). (left) Calculated spacer length and corresponding NA from Zemax and Matlab. (right) Resulting chromatic focal shifts for different combinations of spacer and GRIN lens lengths.

Table 6.3 Optimization results with no spacer. All values were evaluated at $\lambda = 1300$ nm. For each evaluated parameter (GRIN length, NA, waist size, and Rayleigh length), the left and right columns contain the Zemax and Matlab results, respectively.

z_{WD} [mm]	z_G [mm]		NA		ω_0 [μm]		z_R [mm]	
7.5	5.566	5.569	0.0223	0.0219	18.6	18.9	0.832	0.860
8.0	5.520	5.523	0.0210	0.0206	19.7	20.0	0.938	0.971
8.5	5.479	5.482	0.0198	0.0195	20.9	21.2	1.056	1.089
9.0	5.442	5.445	0.0188	0.0185	22.0	22.4	1.171	1.214
9.5	5.409	5.412	0.0178	0.0175	23.2	23.6	1.306	1.347
10.0	5.380	5.382	0.0170	0.0167	24.3	24.8	1.432	1.487
10.5	5.353	5.355	0.0162	0.0159	25.5	26.0	1.577	1.634
11.0	5.328	5.331	0.0155	0.0152	26.6	27.2	1.714	1.788
11.5	5.305	5.308	0.0148	0.0146	28.0	28.4	1.889	1.949
12.0	5.285	5.287	0.0142	0.0140	29.1	29.6	2.052	2.118

Table 6.4 Optimization results with fixed GRIN lens length ($z_G = 5.285$ mm). All values were evaluated at $\lambda = 1300$ nm. For each evaluated parameter (spacer length, NA, waist size, and Rayleigh length), the left and right columns contain the Zemax and Matlab results, respectively.

z_{WD} [mm]	z_S [mm]		NA		ω_0 [μm]		z_R [mm]	
7.5	0.265	0.269	0.0224	0.0220	18.5	18.8	0.825	0.852
8.0	0.222	0.225	0.0211	0.0207	19.6	20.0	0.929	0.965
8.5	0.183	0.186	0.0198	0.0195	20.9	21.2	1.056	1.084
9.0	0.148	0.152	0.0187	0.0185	22.1	22.4	1.183	1.211
9.5	0.117	0.120	0.0178	0.0175	23.3	23.6	1.309	1.344
10.0	0.089	0.092	0.0169	0.0167	24.5	24.8	1.449	1.485
10.5	0.064	0.067	0.0161	0.0159	25.7	26.0	1.596	1.633
11.0	0.041	0.044	0.0154	0.0152	26.9	27.2	1.745	1.787
11.5	0.019	0.022	0.0148	0.0146	28.0	28.4	1.889	1.949
12.0	0.000	0.003	0.0141	0.0140	29.3	29.6	2.081	2.117

Table 6.5 Optimization results with fixed working distance ($z_{WD} = 8.5$ mm). All values were evaluated at $\lambda = 1300$ nm. For each evaluated parameter (spacer length, NA, waist size, and Rayleigh length), the left and right columns contain the Zemax and Matlab results, respectively.

z_G [mm]	z_S [mm]		NA		ω_0 [μm]		z_R [mm]	
3.00	3.031	3.038	0.0286	0.0283	14.5	14.6	0.506	0.516
3.25	2.573	2.579	0.0264	0.0262	15.7	15.8	0.594	0.605
3.50	2.177	2.183	0.0247	0.0245	16.8	16.9	0.678	0.692
3.75	1.828	1.833	0.0234	0.0231	17.7	17.9	0.756	0.775
4.00	1.513	1.518	0.0223	0.0220	18.6	18.8	0.832	0.852
4.25	1.224	1.229	0.0215	0.0212	19.2	19.5	0.895	0.921
4.50	0.955	0.959	0.0208	0.0205	19.9	20.1	0.956	0.980
4.75	0.700	0.704	0.0203	0.0201	20.4	20.6	1.004	1.027
5.00	0.455	0.458	0.0200	0.0197	20.7	21.0	1.035	1.062
5.25	0.216	0.219	0.0198	0.0196	20.9	21.2	1.056	1.082

6.3.2 Backreflections

Simulations with the mirrored optical systems were carried out for all configurations presented in Tables 6.3–6.5 and for several wavelengths in the 400–1500 nm range. The individual results are depicted in Fig. 6.7, where the coupling coefficient was approximated as the ratio of the DCF inner-cladding area over the beam area. It is apparent from Fig. 6.7 that the optimal configuration appears to be those with a shorter GRIN length and a longer spacer from the third scenario outlined in the previous section. Nonetheless, the average coupling ratio across all wavelengths, denoted by the dashed red line in Fig. 6.7, is at least on the order of 10%, which is more than an order of magnitude larger than the expected signal level from the sample, assuming a 4% reflection at GRIN-air interface. It is important to point out that the GRIN lenses used in this setup were AR-coated for the 1100–1700 nm range (C-coating, Thorlabs), potentially resulting in much stronger specular reflections (upwards of 10%) for VIS wavelengths. As such, none of the configurations evaluated here offer a significant reduction in the back-coupling of the BR.

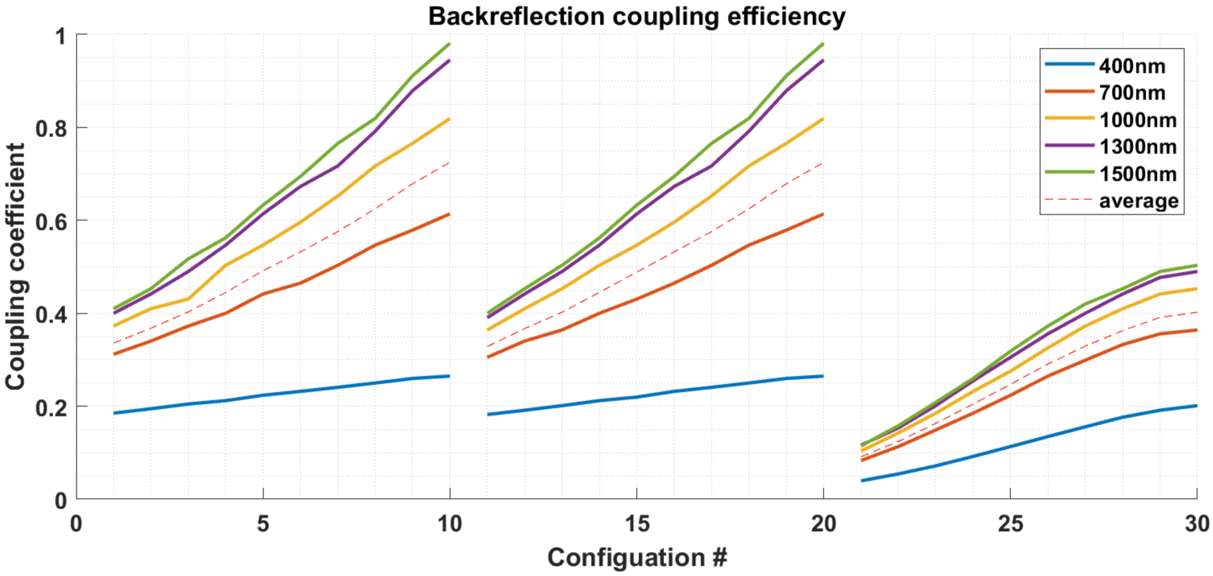

Figure 6.7 Backreflection coupling efficiency as a function of configuration and wavelength. The configuration number corresponds to the order in which they are presented in Tables 6.3,6.4 and 6.5.

6.3.3 Preliminary imaging

After performing the analyses presented in the previous sections, it quickly became apparent that a GRIN-based design would not yield good multimodal imaging. As such, we focused on fabricating an SMF-based GRIN assembly to demonstrate the functionality of the OCT system alone. After polishing the GRIN lens, we obtained $z_G = 5.35 \pm 0.05$ mm and a spacer length close to 0. The theoretical and experimental values for the NA, spot size, and Rayleigh range are presented in Tab. 6.6. By comparing these values, we see that we are underperforming slightly compared to the theoretical lateral resolution. This may be caused by imperfections at the surface of the polished GRIN or inhomogeneities in the optical glue, which can cause aberrations in the wavefront and prevent us from achieving diffraction-limited operation. However, the performance is sufficient for TCE-based OCT imaging for all practical intents and purposes. A preliminary image of fingers wrapped around the device is presented in Fig. 6.8. In this image, several layers of the skin on the finger are recognizable. However, several possible improvements remain, including better dispersion compensation and synchronization of the acquisition speed with the motor rotations. The lack thereof is highlighted by the sharp truncation in the image indicated by the blue arrow in Fig. 6.8. Finally, the electrical drive wire, indicated by the red arrow in Fig.6.8, obstructed a small portion of the field of view. While this is inevitable in this proposed design, others have proposed alternatives that allow shadow-free OCT imaging [334].

Table 6.6 Theoretical and experimental results of the optical assembly. Experimental results were obtained using a custom knife-edge beam profiling system.

	Theoretical	Experimental
NA	0.016	0.017
ω_0 [μm]	25.6	28.7
z_R [mm]	1.43	1.34

6.4 Discussion

Through the simulations presented in this work, we have conclusively demonstrated that single GRIN-based optical assemblies deliver poor performance for systems combining OCT with other techniques, particularly those operating in spectral ranges different from OCT. For future research, it would be interesting to assess more advanced builds, which could include other optical elements such as microlenses or ball lenses. It would also be interesting to investigate the use of negative GRIN lenses (i.e., with an inverted index profile) to realize a color-corrected multi-GRIN assembly similar to modern achromatic lenses. However, negative GRINs are challenging to find and are not currently sold as off-the-shelf components to the best of our knowledge. GRIN lenses were selected for this

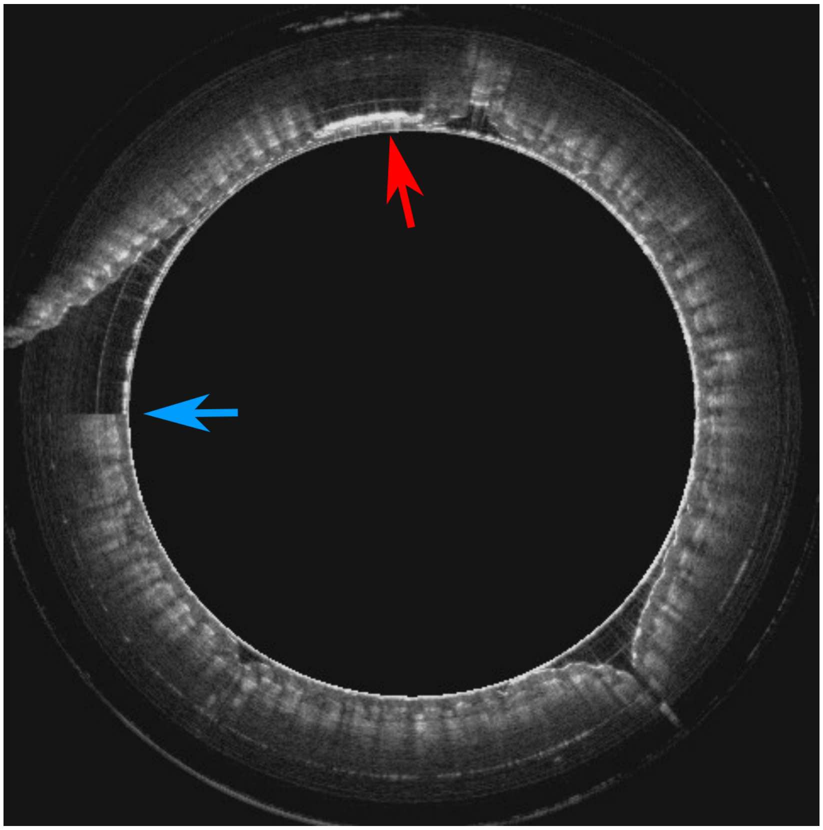

Figure 6.8 Preliminary image with TCE device. The red arrow indicates the electrical drive wires used to power the micromotor and the blue arrow shows a truncation in the image due to a mismatch between the acquisition speed and the motor rotation speed.

preliminary model for their relative simplicity, low cost, and availability of equipment for polishing.

Another interesting avenue to explore is the use of tilted surfaces to reduce or remove backreflections. Similarly to fibers terminated with APC connectors, there might be some benefit to polishing the last GRIN surface at an angle. This analysis will likely need to account for the size of the DCF inner cladding and its NA. Furthermore, the backreflections that couple directly from the core to the cladding of DCF fibers can also be an issue if not properly managed.

6.5 Conclusion

In conclusion, we demonstrated that neither GRIN lenses nor the selected design for the TCE device provided optimal performance. While the fabricated optical assembly performed admirably for imaging, it is unlikely that it would do so in a multimodal system. For these reasons, this project was abandoned in favor of the all-reflective approach presented in the next chapter.

Acknowledgements

I would like to acknowledge the contributions of Gabriel Charland-Gagné, Gianmarco Concilia, Mikael Leduc, Mathias Strupler, and Caroline Boudoux in the design, fabrication, and characterization of the capsule..

CHAPTER 7 ALL-REFLECTIVE TETHERED CAPSULE ENDOSCOPE FOR MULTIMODAL OPTICAL COHERENCE TOMOGRAPHY IN THE ESOPHAGUS

7.1 Introduction

Esophageal cancer (EC) is a growing concern in Western countries due to rapidly rising incidence rates [14]. It is amongst the deadliest cancers due to its asymptomatic nature in the early stages of development. This results in most diagnoses occurring at advanced stages, leading, in turn, to an average 5-year survival rate on the order of 20% [6]. Currently, surveillance and diagnosis of EC rely on white light video-endoscopy (WLE) and random biopsies. However, this approach is poorly suited for early diagnosis as WLE cannot detect the subtle changes associated with pre-cancerous lesions, and random biopsies only sample small amounts of the organ [22]. In addition to low sensitivity for early stage detection, screening or surveillance in risk groups is further inhibited by the high cost of endoscopic procedures, which generally require sedation, specialized personnel, and equipment [192].

Optical coherence tomography (OCT) has shown great potential as an alternate method for early detection of EC. It overcomes many current limitations by providing non-invasive, depth-resolved, sub-surface, microscopic imaging of the esophagus. Moreover, its non-invasive nature and high imaging speed allow comprehensive imaging of the organ, increasing the odds of detecting localized (pre-)cancerous lesions. Previous studies have shown that OCT may be implemented to detect or differentiate various tissue types and conditions such as Barrett's Esophagus (BE), low– and high-grade dysplasia (LGD and HGD, respectively), and specialized intestinal metaplasia (SIM) [1,41,42,44].

Despite promising results, to this day, OCT alone has not demonstrated sufficient performance to replace the standard practice of WLE and random biopsies. One approach to enhance the diagnostic capabilities of standard OCT is to combine it with other modalities that provide complementary information. Previously, systems for esophageal imaging have combined OCT with autofluorescence imaging [152], fluorescence imaging with an exogenous dye [153], and color imaging [154]. Other modalities have also been combined with OCT in endoscopic systems developed for other organs and pathologies. Such combinations include fluorescence lifetime imaging [166–168], NIR fluorescence [151], diffuse reflectance spectroscopy [160], multispectral reflectance imaging [146], and photoacoustic imaging [159]. The technical feasibility of such multimodal endoscopic systems has been demonstrated and could, in principle, be adapted for esophageal imaging. However, a key question remains: which combination provides optimal sensitivity and specificity for the early detection of EC?

This work presents the first-ever all-reflective tethered capsule endoscope (TCE) designed to enable multimodal optical coherence tomography in the esophagus. It was designed to be used in conjunction with all the DCF- and DCFC-based bench-top systems presented in the previous chapters of this thesis. Adapting the concept of the all-reflective scanner head presented in Chapter 5, the device relies on a single ellipsoidal mirror and several beam-folding mirrors to focus light from a double-clad fiber onto the sample plane. The exclusive use of reflective optics enables achromatic and backreflection-free imaging at all wavelengths, bypassing all the issues highlighted in Chapter 6. Furthermore, it allows the co-registered combination of OCT with various other modalities without needing to re-engineer the optical design of the endoscopic probe. This will lead to more efficient clinical translation of multimodal OCT systems and enable a platform approach to identifying which combination of techniques is best suited for the early detection of esophageal cancer. Here, we demonstrate combined OCT and VIS reflectance spectroscopy over the 500–700 nm range. We first present the key design, fabrication, and assembly steps necessary to realize the tethered capsule and the tools developed for fine-tuning the internal alignment. We then characterize the optical performance of the complete device and present preliminary multimodal images. Finally, we discuss the limitations of the proposed design and future improvements.

7.2 Methods

Figure 7.1 presents the proposed all-reflective design and a photograph of the assembled device. In line with previously published TCE designs implemented in vivo [153,192,195, 199, 335], we designed to capsule to have an outer diameter of 13 mm. In the prototype presented here, the total length was 35 mm (stiff length excluding the tether comprised of the optical fiber and the electrical drive cable). Light delivery is performed using a DCF for various forms of multimodal imaging. The key component differentiating this design from others is the ellipsoidal mirror (EM) used to achieve finite conjugation between the fiber tip and the focal plane. Precise design and alignment of the EM combined with beam folding allow the positioning of the focal plane just outside the capsule, as illustrated in Fig. 7.1(A). The use of the EM, in particular, and reflective optics, in general, makes the assembly extremely sensitive to alignment errors [336]. As such, the tolerances applied to the mechanical design were extremely high to ensure the proper positioning of all components. Moreover, the optical alignment was carried out in steps to ensure optimal operation after adding each sub-assembly. Finally, beam scanning is performed using an inverted micromotor to avoid a shadow associated with the electrical drive wire, inspired by a previous design by Lopez-Marín et al. [334].

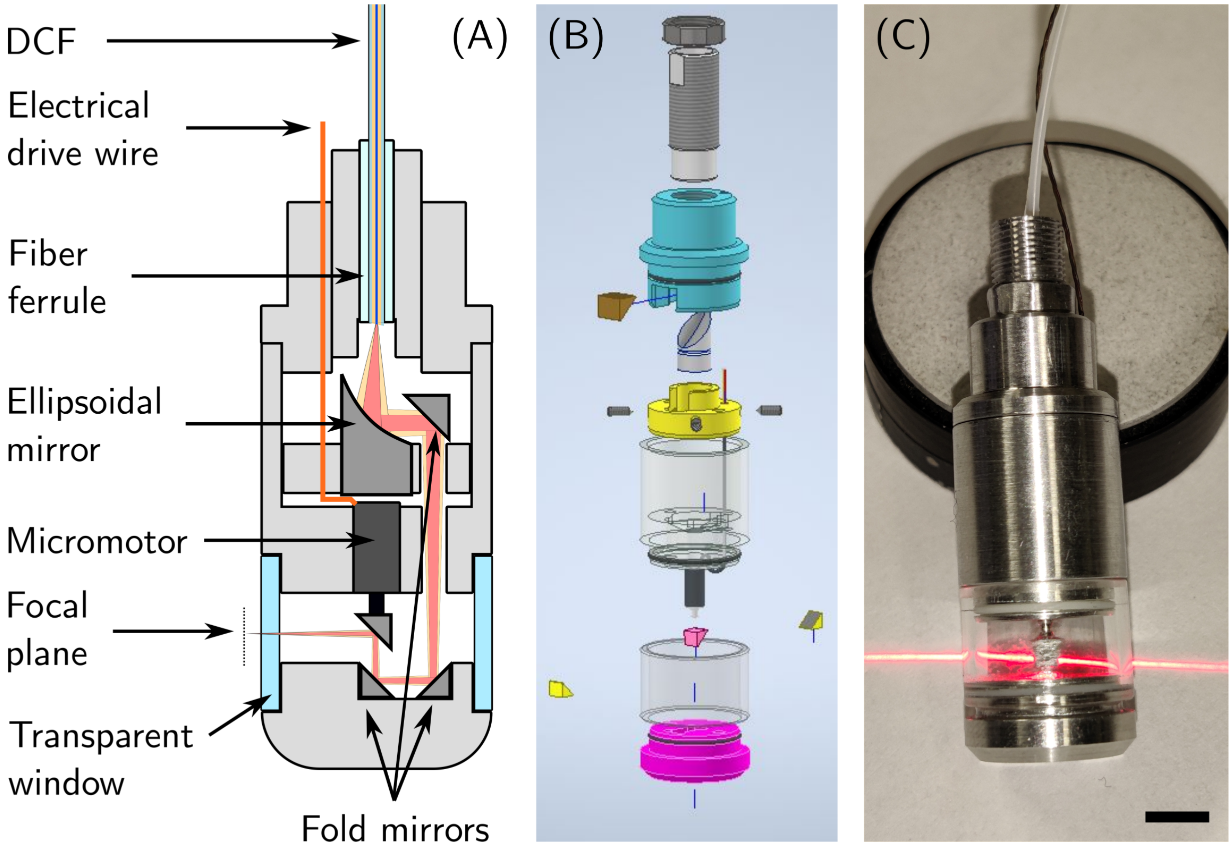

Figure 7.1 All-reflective tethered capsule endoscope. (A) Schematic representation of the reflective TCE. The red and yellow light beams represent the illumination from the core and inner cladding of the DCF, respectively. (B) Exploded view of the 3D CAD model. (C) Photograph of the assembled tethered capsule endoscope with a red guide laser. The scale bar is 5 mm.

7.2.1 Optical design

The optical design of the proposed capsule is centered around a single, off-axis ellipsoidal mirror to achieve finite conjugation between the fiber tip and the measurement point located 0.5 mm outside of the capsule surface. The EM surface is an ellipsoid of revolution, also called a spheroid. It can be described by Eq. 7.1 in Cartesian coordinates:

$$\frac{x^2}{a^2} + \frac{y^2}{b^2} + \frac{z^2}{b^2} = 1, \tag{7.1}$$

where a and b are the semi-axes of the elliptical cross-section along the XZ or the YZ plane. This cross-section, depicted in Fig. 7.2, can be rotated along the semi-axis of length a to form the full ellipsoidal surface. Spheroids have the property of having two foci, and that any ray emitted from one focal point will be reflected to the other one, thereby achieving finite conjugation. In practice, this implies positioning the fiber at one focal point such that all emitted rays are imaged onto the second one, located at the sample plane.

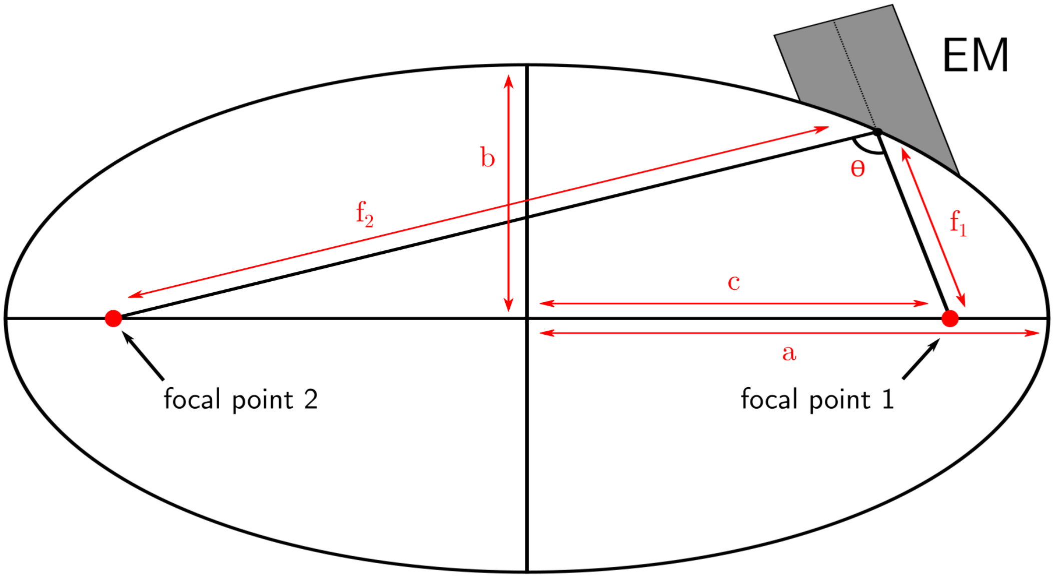

Figure 7.2 Geometrical representation of the elliptical section of the ellipsoidal surface. Variables f_1 and f_2 represent the two focal lengths, a and b are the lengths of the semi-axes, c is the distance from the origin to the foci, and θ is the deviation angle of the center ray.

Ellipses have the additional property that the lengths of the segments connecting the foci to any point on the ellipse must add to $2a$, as described in Eq. 7.2:

$$f_1 + f_2 = 2a. \tag{7.2}$$

Based on Eqs. 7.1 and 7.2, it is possible to fully define the ellipsoidal surface for a target pair of focal lengths and center deviation angle. In the case of the TCE, these focal lengths were selected to satisfy three requirements. The first is a given value for the numerical aperture (NA) in image space, roughly equal to the fiber core output NA multiplied by the angular magnification, M_α, of the ellipsoidal mirror: $M_\alpha = f_1/f_2$. The image space NA was chosen to achieve a sufficient depth-of-focus, characterized by the Rayleigh length (z_R) of a gaussian beam, and a target spot size, characterized by the beam waist (w_0). It is important to note that the SM output divergence and corresponding NA of the DCF core are not well characterized by the specified fiber NA but rather by assuming a gaussian beam propagation with waist equal to the mode-field diameter. As such, for single mode operation of the DCF core, as is the case for OCT imaging, the fiber output NA is equal to 0.09 and not 0.12 (DCF13, Thorlabs, USA). The second constraint is that the second focal length (f_2) be sufficiently long to enable the beam folding presented in Fig. 7.1(A), such that the focal plane is located approximately 0.5 mm outside the outer surface of the capsule. This constraint arises from the size of the individual components, such as the ellipsoidal mirror, the micromotor, and the right-angle reflective prisms. The mechanical constraints are discussed further in the following section. Interestingly, f_2 may be adjusted by scaling f_1 accordingly to maintain the desired angular magnification. However, extending f_1 increases the distance between the fiber tip and the EM, which results in a longer total stiff length of the device. Finally, the third constraint is on the beam size at various positions along the beam path. Beyond a certain diameter, the beam will begin to clip on the housing, resulting in reduced beam quality and transmission efficiency. The limiting factor here is the beam size of the multimode output of the inner cladding of the DCF, which has a larger NA than that of the core: 0.2 for DCF13. This constraint applies both when the inner cladding is used for illumination and collection.

For esophageal imaging, we selected an image space NA of 0.02, resulting in a theoretical spot size of $w_0 = 21\ \mu$m and a Rayleigh length of $z_R = 1.04$ mm at 1300 nm. For a SM core output NA of 0.09, we used the combination of $f_1 = 6.5$ mm and $f_2 = 30$ mm to achieve 0.0195 image space NA with a 90° deviation. This resulted in a maximum beam diameter at the EM of 2.6 mm from the DCF inner cladding. All parameters of the ellipsoidal surface were derived from the target values of f_1 and f_2, and Eqs. 7.1 and 7.2. These parameters were then used to diamond-turn 4 mm diameter custom EMs out of aluminum (B-Con Engineering, Canada).

All other optical components are off-the-shelf 1 or 2 mm right angle prisms (Sumipro, The Netherlands) used for beam folding. Finally, the DCF fiber was mounted into a 0.9 mm ceramic ferrule with a standard FC/APC 8° angle polished tip (Diamond SA, Switzerland). The DCF patch cord was terminated with an E2000 connector compatible with clinical sterilization protocols.

7.2.2 Mechanical design

The TCE is composed of a number of parts, as illustrated in the exploded view of the TCE in Fig. 7.1(B). The first, colored in grey and located at the top of the image, houses the fiber ferrule. The outside is threaded to enable fine adjustment of the fiber holder's axial position relative to EM by screwing it in and out of the second housing, in light blue in the diagram. A nut is used to lock the ferrule holder in place once the optimal position is found. The yellow component is the EM holder. The EM is held in the central slot and can be locked in place using the screws visible next to the holder in the exploded view. A positioning groove was milled along the circumference of the EM at a known distance from the mirror base. This allows the EM to position itself axially as the screws are tightened. These screws are also used to perform fine adjustments of the EM position and orientation (tip & tilt), as described in the section on the alignment of the ellipsoidal mirror. The semi-transparent grey part below the yellow EM holder is the housing for the 2.4 mm diameter, hollow shaft micromotor (DBL024-05XX, Namiki Adamant, Japan). Care was taken to leave several hundred microns between the bottom faces of the motor and the EM to allow the motor electrical drive wire to be bent without being crushed. The final 1 mm prism reflecting the light towards the outside of the capsule (pink in the diagram) is first mounted on a 600 μm diameter rod, which is then inserted and glued into the hollow shaft of the micromotor. A high-strength, transparent glass window (DURAN®, Technoglas, The Netherlands) allows the laser light through to reach the sample. Two V-grooves were milled into the top and bottom notches over which the glass window is slotted. These grooves are filled with polymer O-rings, visible in white Fig. 7.1(C), to add resistance and keep the components from sliding apart prior to the final fixation with glue (LOCTITE®AA-3921, Henkel Corporation, USA). The final part, located at the bottom of the exploded view, is the capsule cap, which holds two 2 mm fold prisms/mirrors to reflect the laser beam up towards the prism fixated on the micromotor. All structural parts of the TCE aside from the glass window were milled from aluminum. Two through-holes were drilled into all structural parts in the plane perpendicular to the one containing the laser path to ensure the proper rotational alignment of all parts relative to each other by sliding straight rods through them (not shown in the diagram).

7.2.3 Assembly

Because of the off-axis nature of the optical assembly and the resulting sensitivity to proper alignment, it was necessary to develop several intermediate assembly and verification steps to ensure the proper operation of the optical system.

Ellipsoidal mirror alignment

The alignment of the EM and the fiber tip is critical to obtaining a diffraction-limited spot in the sample plane. Despite the precision manufacturing of the mirror, the mirror housing, and the fiber ferrule, some fine-tuning of the alignment remains necessary. To obtain real-time feedback, the fiber & EM subassembly were mounted onto a custom alignment tool presented in Fig. 7.3. This subassembly includes all parts at or above the yellow EM housing in Fig. 7.1(B) except for the first beam folding prism (in brown). This tool is mounted onto a scanning-slit beam profiler (BP209IR1, Thorlabs) such that the theoretical focal plane (f_2 = 30 mm here) is located precisely in the measurement plane of the beam profiler. This measurement plane is not the surface of the device but rather a few millimeters lower. The alignment tool is marked with centering lines that can be aligned with the beam profiler to ensure the proper orientation of the device. A small extension is inserted in the back of the EM and can be used for gross rotational alignment. Once completed, a clamp is fixed onto the extension, which can then be rotated using the adjustment screws at the extremity of the rotation lever. The fine adjustment screws for XY translation, tip, and tilt of the EM can be accessed via the diagonal groves in the alignment tool. The EM slot in the housing is 200 μm wider than the outer diameter of the EM to allow lateral translations and tip and tilt. The four fine alignment screws are positioned in two pairs facing each other and can be controlled individually for tip and tilt or in pairs for translation. Additionally, the threaded housing of the fiber ferrule can be translated axially to adjust the distance between the fiber tip and the EM. All adjustment mechanisms were used iteratively to achieve the expected diffraction-limited spot size measured with the beam profiler. All optimization was performed at 1300 nm with the single mode output of the DCF core. It is important to note that while it is possible to achieve optimal alignment, the rudimentary nature of the alignment mechanisms does not guarantee a quick convergence nor the reversibility of the fine adjustment. As such, this process had to be repeated from the beginning several times to achieve the desired result. Once the assembly is in its final position, the tightened adjustment screws fixate the EM in place. The components' positions are further stabilized by gluing the screws and the mirror to the housing.

Motor shaft assembly

Another essential alignment is the orientation of the last prism, which deviates the laser beam towards the outside. The laser beam should not reach the transparent window under a normal incidence. Indeed, the air-glass and subsequent glass-air interfaces gener-

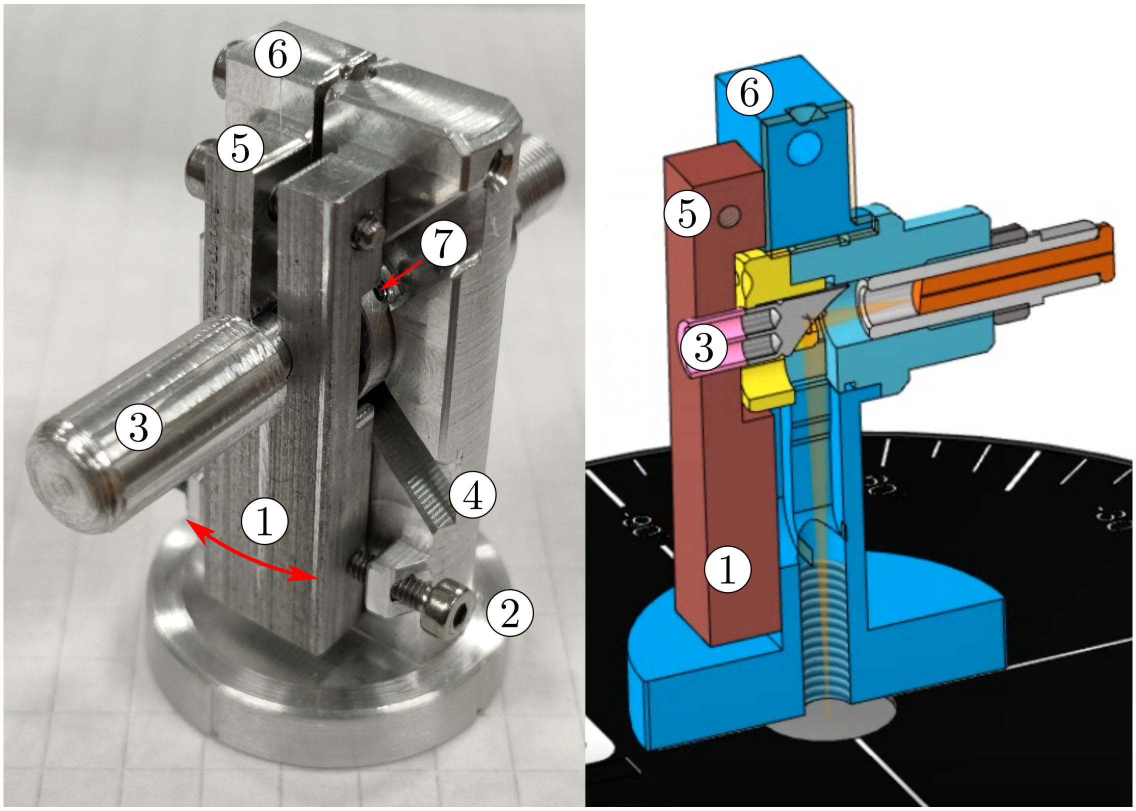

Figure 7.3 Alignment tool for the fine alignment of the ellipsoidal mirror. (Left) Photograph of the tool. (Right) Cross-section of the 3D CAD model. (1) Clamp for fine rotational adjustments. (2) Adjustment screws to apply controlled rotation to the clamp. (3) Extension inserted into the EM for rotational adjustments. (4) Grooves to access tip & tilt screws. (5) Clamping mechanism for rotational adjustments. (6) Clamping mechanism for fiber and EM housings. (7) One of four tip & tilt adjustment screws.

ate strong specular reflections that would decrease the signal-to-background ratio (SBR). A simple geometrical analysis shows that these specular reflections can be avoided if the incidence angle is greater than the half angle of the cone of the focused beam, i.e., $\theta_{\text{inc}} > \sin^{-1}(\text{NA})$. In this case, the largest collection NA is that of the inner cladding or NA=0.04, so the angle of incidence must be greater than 2.5°. Assuming a perfectly vertical beam before the last prism, the incidence angle on the transparent window is equal to twice the tilt angle of the prism compared to it being perfectly aligned with the capsule's vertical axis. As such, the prism must be titled at least 1.25°. For good measure, we applied a 2° tilt to the prism resulting in a 4° angle of incidence on the glass surface. This tilt was achieved by using the mount presented in Fig. 7.4. An alignment groove was milled into a holder to guide a hollow rod to the back surface of a 2 mm reflective prism. Polymer clamps were 3D printed to secure the components in place without damaging the optical surface of the prism. Before placement, the hollow rod was filled with UV-curing glue (LOCTITE®AA-3921, Henkel Corporation, USA). Once in place and secured, a UV-compatible multimode fiber was inserted into the rod until some glue could be observed flowing out from the rod/prism junction. The UV source injected into the fiber was then activated for several minutes until the curing was complete. Particular care was taken to avoid excessive overflow between the rod and prism, as this would hinder the proper insertion of the rod into the hollow shaft of the micromotor. The tool was designed to align the rod with the center of mass of the prism to minimize vibrations and radial shifts during rotations. The rod and prism assembly were then inserted into the motor's hollow shaft and glued in place.

Focal plane adjustment

The distance between the focal plane and the EM is fixed and defined by the surface parameters. However, the position of the focal plane relative to the outer surface of the TCE can be adjusted by extending the vertical beam path after the first fold prism (see Fig. 7.1(A)). This can be achieved by slightly pulling the motor housing and cap apart, so long as the glass window remains securely on the notches. A final alignment tool was developed to this effect, depicted in Fig. 7.5. This tool is placed flat on the beam profiler and measures the beam diameter as the cap is moved closer or further away from the capsule body. By comparing the measured beam size to prior beam profiling, it is possible to extrapolate the exact position of the focus relative to the measurement plane and the capsule surface. Once the desired focus position is achieved, the glass window and cap can be fixed into place by curing the glue applied prior to assembly. The O-rings also have

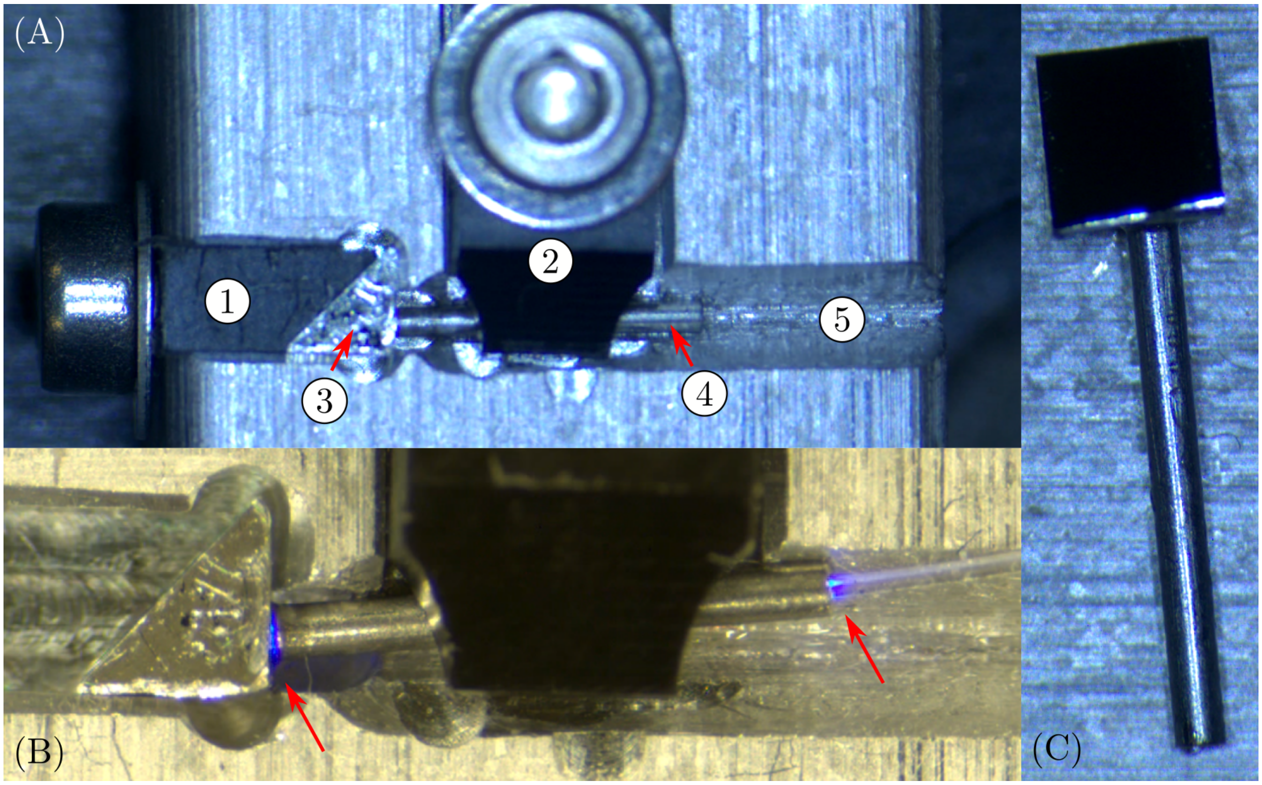

Figure 7.4 Motor shaft alignment tool & assembled prism and rod. (A) Loaded alignment tool with prism clamp (1), rod clamp (2), prism (3), hollow rod (4), and rod alignment groove (5). (B) Glued prism and rod assembly. Red arrows highlight the blue fluorescence of the UV-curing glue. (C) Final assembly to be inserted into the micromotor. All scale bars are 1 mm.

the additional function of preventing glue overflow into the TCE.

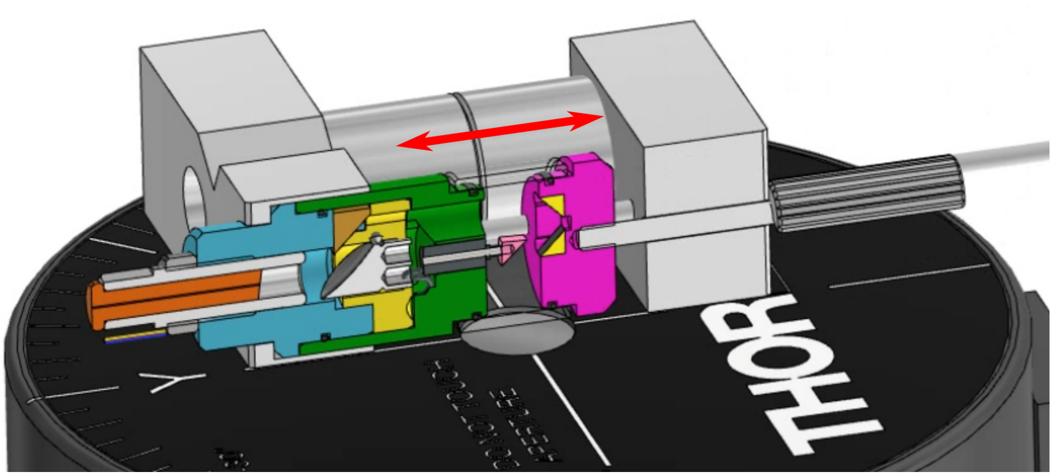

Figure 7.5 Focal plane alignment tool. The capsule cap is translated towards or away from the capsule body using the screw on the right.

7.2.4 Complete system

For imaging, we used the fiber system presented in Fig. 7.6. This system comprises a standard SS-OCT system at 1300 nm, with a free space wavelength combiner and a double-clad fiber coupler inserted in the sample arm. The wavelength combiner allows the combination of OCT and VIS light in the core of an SMF28 fiber, which is then spliced to the DCF. The VIS light covers 450–950 nm from a filtered supercontinuum laser (EXU6, NKT Photonics Ltd., UK). Core illumination is carried out for both modalities, while collection is performed with the core for OCT and the clad for reflectance imaging. The high-speed spectrometer (Cobra VIS CS550-600/200, Wasatch Photonics, USA) is used to collect spectroscopic information over the 500–700 nm spectral range.

7.3 Results

We characterized the capsule's performance regarding OCT imaging, beam quality, and overall transmission efficiency over a broad spectrum. Beam characterization was performed with the aligned EM before assembling the full capsule to maintain access to positions before and after the focal plane. As such, the characterization does not incorporate the effect of all optical components after the EM. However, the flat prism mirrors should

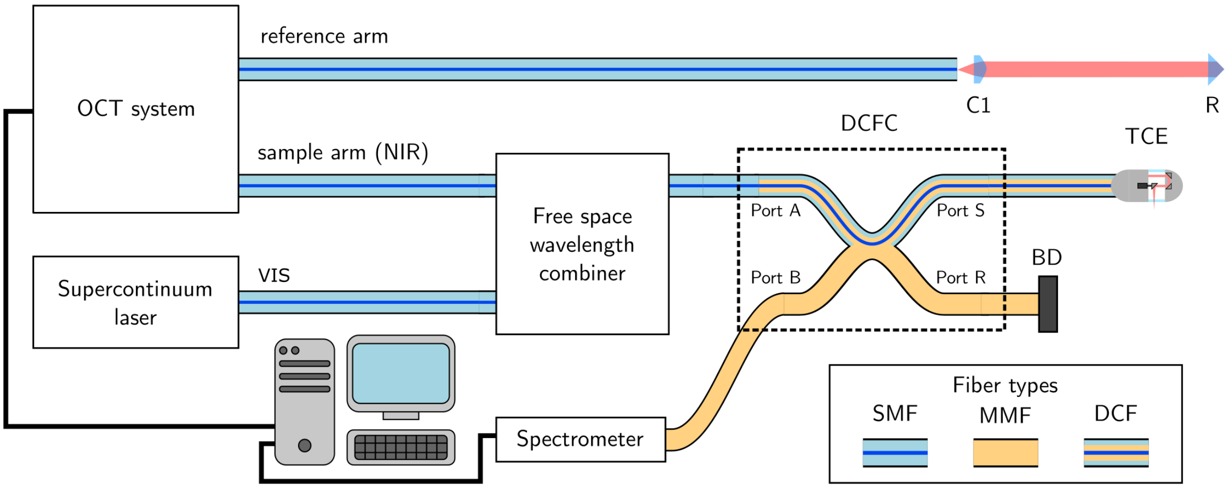

Figure 7.6 Complete experimental setup. **C1**: collimator, **R**: retroreflector, **DCFC**: double-clad fiber coupler, **TCE**: tethered capsule endoscope, **BD**: beam dump, **SMF**: single mode fiber, **MMF**: multimode fiber and **DCF**: double-clad fiber.

not induce any aberrations, and the influence of the glass window was found to be minor in Zemax simulations (Zemax OpticsStudio, USA). This influence includes the spot size being altered by $< 10\%$, the focal plane being shifted back by ~ 500 μm, and inducing minimal astigmatism. As such, the measured beam profiles should be representative of the beam at the output of the TCE. The output beam profiles, presented in Fig. 7.7, were measured from the core at 635 nm and 1300 nm and from the inner cladding using the broadband spectrum of the supercontinuum source. The extracted beam parameters, including the beam waist (w_0), the axial position of the waist (z_f), and the Rayleigh length (z_R), are summarized in Table 7.1. These parameters were determined from fitting experimental data points, where w_0 and z_R were fitted independently. The theoretical values were calculated assuming NA=0.0195. The difference in waist size and slight astigmatism makes it apparent that the final assembly is close to but not quite at the optimal alignment. However, the 15% increase in spot size compared to the theoretical value will not significantly degrade imaging quality, and the ~ 400 μm shift between the X and Y focus should not be noticeable given the long Rayleigh range. As such, these values were considered adequate for practical applications. The significant shift in the position of the focal plane for cladding illumination is expected as described by Beaudette et al. [337]. The spot size obtained with cladding illumination also represents the collection area when the cladding is used to capture light. While the collection area varies with depth at the focal plane from core illumination, it is important to recognize that this variation is small across the Rayleigh range of the core illumination: $< 7\%$ across the [5,7] mm range. As such, the collection area and corresponding collection efficiency should remain approximately constant during imaging.

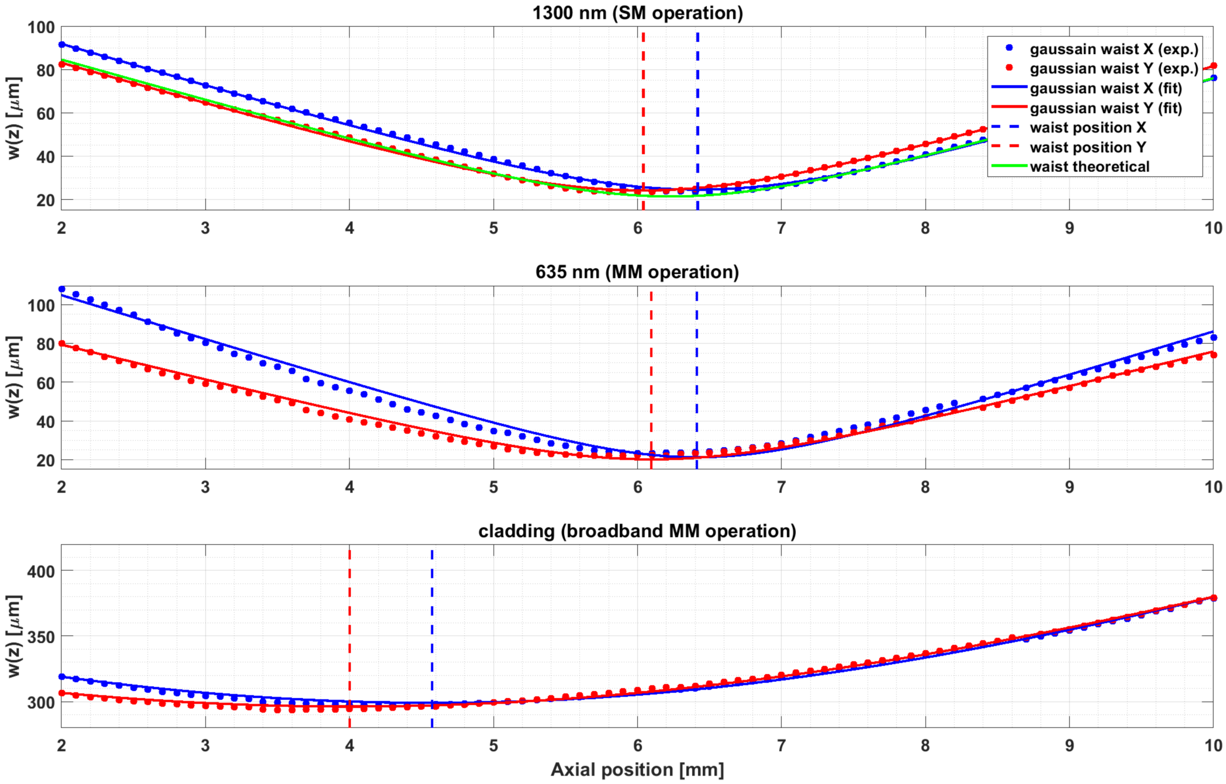

Figure 7.7 Beam profiling results for different illumination schemes.

Table 7.1 Beam parameters for different illumination schemes obtained from fitting. Theoretical values calculated for NA=0.0195.

Illumination mode	$w_{0,x}$ [μm]	$w_{0,y}$ [μm]	$z_{f,x}$ [mm]	$z_{f,y}$ [mm]	$z_{R,x}$ [mm]	$z_{R,y}$ [mm]
Core 1300 nm (SM operation) theoretical	21.4		N/A		1.097	
Core 1300 nm (SM operation)	24.5	24.2	6.418	6.041	1.226	1.230
Core 635 nm (MM operation)	21.2	20.2	6.412	6.097	0.912	1.077
Cladding broadband (MM operation)	299.1	296.3	4.573	4.002	6.934	7.470

Figure 7.8 presents the transmission efficiency of the device across the VIS and NIR spectra, defined as the ratio of the input and output spectra. To account for the NA-dependent transmission efficiency of the spectrometers, the spectra were normalized to absolute power measurements at 635 nm and 1300 nm for the VIS and NIR bands, respectively. The theoretical transmission curve was defined as the reflectance curve of protected aluminum (G01, Thorlabs) to the fifth power to account for all reflective elements in the

beam path. It is apparent in Fig. 7.8 that the reflectance is the principal source of loss and that this results in very low efficiencies for specific wavelengths, which calls into question the choice of aluminum as a mirror surface. The problem is even further exacerbated by the fact that the presented curves must be squared to account for the double-pass occurring during imaging. A more appropriate choice would be to use protected silver mirrors, as they offer significantly better performance across all VIS/NIR wavelengths. For reference, the theoretical curve for protected silver (P01, Thorlabs) mirrors is also presented in Fig. 7.8. It should be noted that the theoretical values from Thorlabs may not be perfectly representative of mirror coatings from other manufacturers.

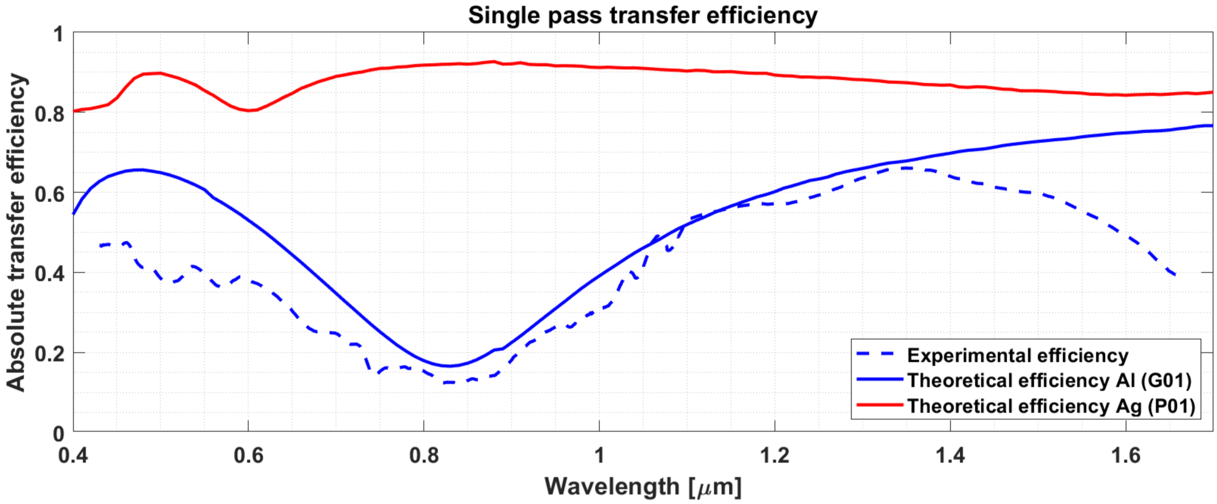

Figure 7.8 Single pass transfer efficiency. The theoretical efficiency curves were computed as $R^5(\lambda)$ where R is the reflectance of the different types of mirrors. Aluminum mirrors were used in this version of the TCE.

7.3.1 Preliminary imaging

During preliminary OCT imaging, it quickly became apparent that the system had a significant dispersion mismatch. This imbalance was primarily associated with the refractive optics used for the reference arm, which had no counterpart in the all-reflective TCE. Moreover, the small amount of free-space propagation in the capsule (35 mm total) was initially vastly exceeded in the initial reference arm. The reference arm was therefore adjusted to minimize the free-space propagation. The remaining dispersion mismatch was corrected numerically following the method outlined in [305]. Figure 7.9(A) presents an OCT B-scan of fingers wrapped around the capsule. Figure 7.9(B) present the axial PSF and gaussian fit in linear scale, while (C) illustrates the impact of dispersion compensation in logarithmic scale. The axial resolution after k-linearization and numerical dispersion compensation (shown in Fig.7.9(B)) was measured to be 12 μm.

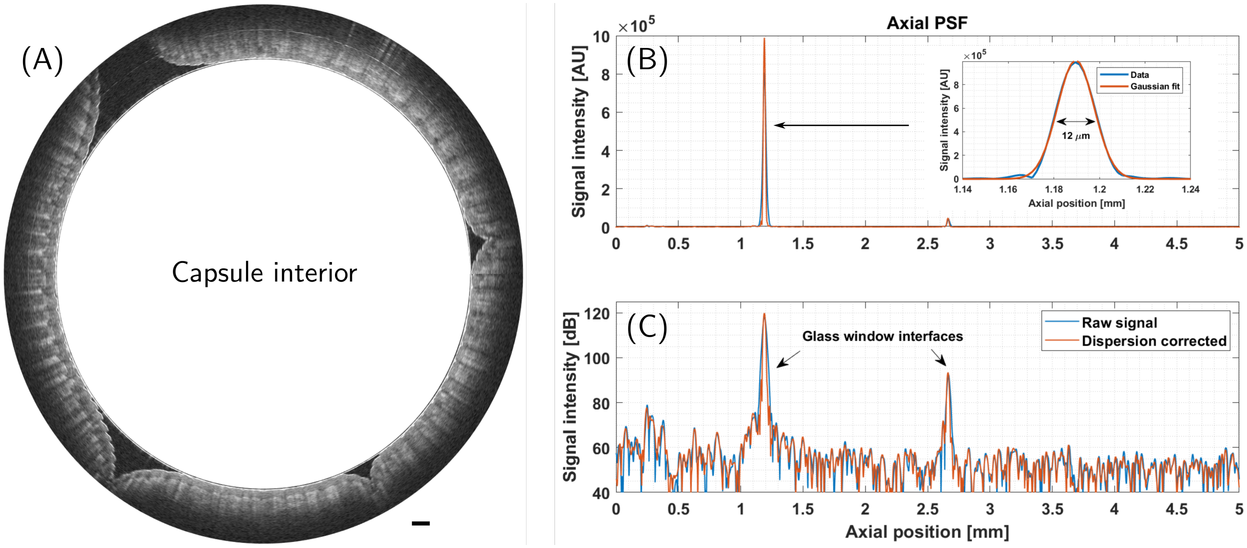

Figure 7.9 Preliminary OCT imaging. (A) B-scan of fingers wrapped around the capsule. Total image width equal to 2.8 mm and scale bar equal to 1 mm. (B) Axial PSF obtained from reflections of the glass-air interfaces of the transparent window. The inset shows the gaussian fit of the PSF. (C) Same as (B) but in a logarithmic scale.

We also performed combined imaging with both OCT and reflectance spectroscopy. We imaged a simple printed ColorChecker target to demonstrate the reflectance mode imaging capabilities. The capsule was first fixed in place, and the ColorChecker was wrapped around it. The ColorChecker was then pulled back slowly using a motorized translation stage. The raw spectral image (i.e. the detected signal) at $\lambda = 520$ nm is presented in Fig. 7.10(A). This image shows a white area where the signal is saturated (indicated by the red arrow) due to a strong specular reflection at one of the glass-air interfaces. The alignment of the beam and the non-perpendicular reflection occurring at the prism mounted on the micromotor should prevent this; however, the alignment of the final prism is likely incorrect. This can also be seen in the slight tilt in the red beam from the guide laser in Fig. 7.1(C). This saturation results in negative and invalid reflectance values, observable in Fig. 7.10(D). For each pixel, the reflectance was computed by dividing the dark-corrected signal from the sample by the dark-corrected signal from the reference. Here, a white section of paper was used as the reference, and the section with no sample as the dark signal, as indicated by the blue and red boxes in Fig. 7.10(A). Figure 7.10(B) and (C) present an en-face OCT image and a B-scan located at the red line in (B). While no saturation occurs in these images, the strong reflection can be observed slightly in the en face image and more clearly in (C), as indicated by the red arrow. Figure 7.10(D) presents the spectral reflectance image at $\lambda = 520$ nm. The normalized reflectance spectra (solid lines) for each ROI highlighted in (D) are presented in Fig. 7.10(E) and compared to the theoretical values (dashed lines). It is apparent in Fig. 7.10(E) that the spectral trends are similar but not identical between the experimental and theoretical values. This mismatch may be attributed to differences in the reflectance spectrum of a printed Colorchecker compared to a real one. Nonetheless, Fig. 7.10 demonstrates the ability of the RTCE to perform co-registered imaging with both modalities, with all wavelengths in focus and most of the imaging range free of backreflections.

7.4 Discussion

7.4.1 Advantages and limitations of the proposed design

The all-reflective design offers a variety of advantages over conventional designs relying on other focusing optics. First and foremost, it provides achromatic beam focusing, as demonstrated in Fig. 7.7. Perfectly achromatic beam focusing is valuable for multimodal imaging, as proposed in this thesis, but also for high-resolution OCT (typically referred to as μOCT), where axial variations of the illumination spectrum due to chromatic focal shifts can induce depth-dependent variations in the axial PSF and corresponding resolution [194,200]. Previously proposed solutions have successfully corrected chromatic focal shifts for broadband and/or multimodal systems; however, these solutions often require advanced optical engineering and are specifically tailored to the utilized spectral ranges. In comparison, the proposed reflective design represents a one-size-fits-all solution. This design also removes optical interfaces producing unwanted backreflections as reported by other groups [146] and discussed in the previous chapter.

The proposed design also presents certain limitations. The first is the achievable numerical aperture in image space. Indeed, the image space NA is directly related to the fiber NA through the angular magnification of the EM. However, the angular magnification is strongly constrained by the device's size. For example, the first focal length cannot be indefinitely extended to increase the magnification because it will extend the stiff length of the TCE. Moreover, extending f_1 will result in a larger beam size at the EM, which will, in turn, need to be larger. However, for a fixed capsule diameter, there is a maximum beam and mirror size for which the beam is not clipped at the mirror or after the first fold prism. As such, the proposed design is ill-suited for techniques requiring higher numerical aperture, such as multiphoton fluorescence microscopy or confocal microscopy.

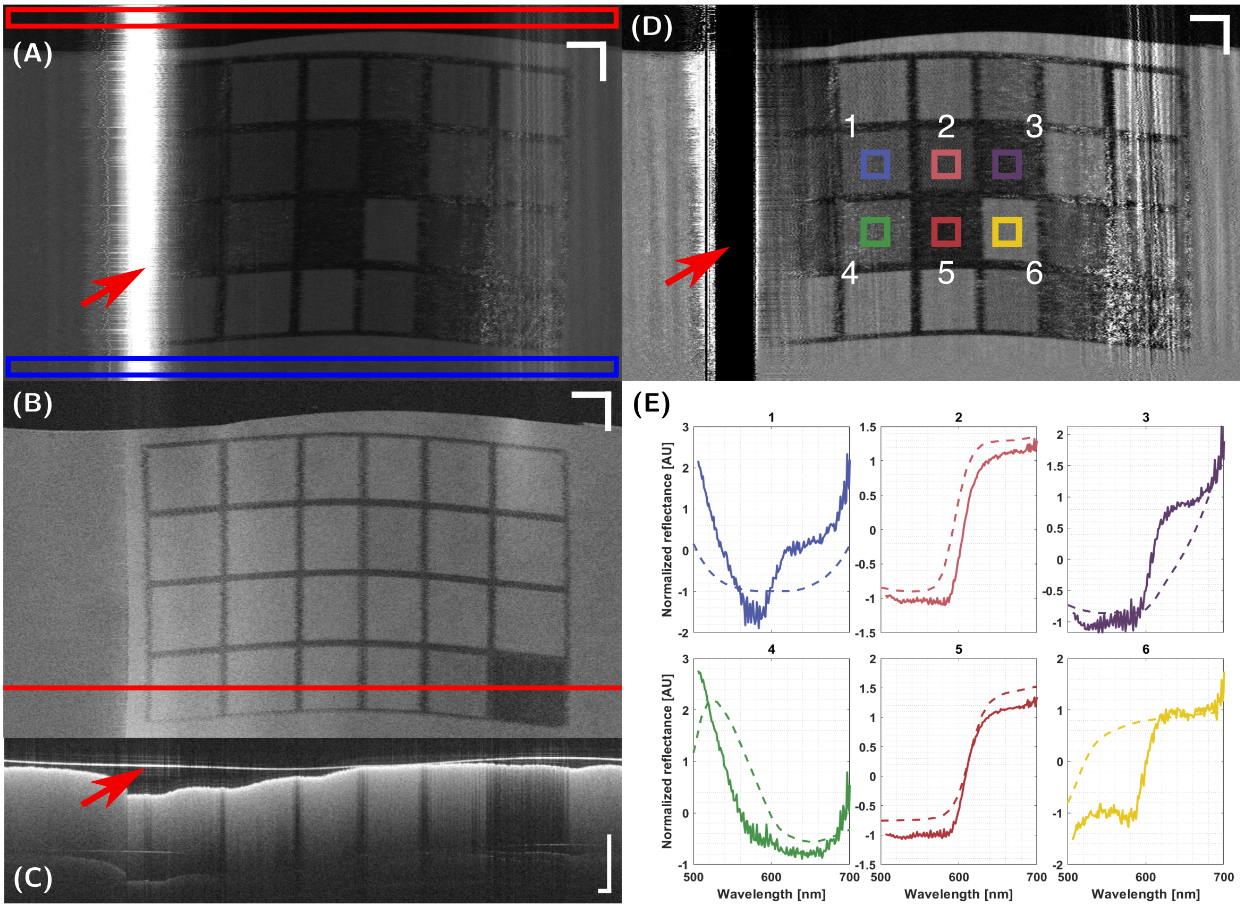

Figure 7.10 Combined imaging of a printed ColorChecker. (A) Raw image of the ColorChecker at 520 nm. The red box indicated the area of the image used as the dark measurement, where there was no sample around the capsule. The blue box indicates the part of the image used as the reference for calculating the reflectance spectrum. The red arrow highlights an area where strong specular reflections occur, and the signal is saturated. (B) Matching en face OCT view. The red line shows the location of the cross-sectional view presented below. (C) OCT cross-section. The red arrow highlights the strong signal from the capsule's external glass-air interface. (D) Reflectance image at 520 nm. The red arrow highlights the undesirable effect caused by the strong specular reflection resulting in unrealistic reflectance values (below 0 or above 1). The intensity range was set to [0;2] to avoid saturation from pixels with glare. The colored squares numbered 1–6 are the ROIs used in the graphs below. (E) Spectral data averaged over the ROIs in (D). The solid lines are the experimental values, and the dashed lines are the theoretical values from literature. All data was normalized by subtracting the mean and dividing by the standard deviation to compare spectral shapes effectively. Scale bars in A, B, and D are 3 mm and 1 mm in C.

A second shortcoming of the proposed design is the strict size constraint applied to the micromotor. Indeed, the motor must be as short as possible to minimize the overall length of the device. However, this leads to a very limited choice regarding suppliers and motor performance. Moreover, such miniature micromotors often lack feedback loops to inform of the angular position of the beam. Since there is no electrical wire crossing the OCT field of view or other angular markers, it is difficult to assess any potential variations in rotation speed or other non-uniform rotational distortions (NURD). While NURD is typically less significant with micromotor probes than with proximal scanning probes [338], some form of NURD correction is still necessary to optimize image quality or implement OCT angiography methods [197, 339]. Numerical methods using the correlation between overlapping A-lines could be used to this effect. However, such methods are computationally expensive and would not be implemented in real-time. Alternatively, markers could be added to the field of view at the expense of obscuring parts of the image. A second difficulty associated with the smaller motors is that they tend to operate at high minimum speeds, which increases the required A-line/pixel rate necessary to achieve Nyquist sampling along the circumference of the esophagus. While modern OCT systems can reach MHz A-line rates, the additional modalities may require a lower imaging speed.

7.4.2 Future work

Future efforts will be centered around enhancing the device's efficiency, improving the assembly process's repeatability, and moving towards clinical certification for human use. Aside from replacing the aluminum mirrors with silver ones, the assembly process is also critical in the overall transfer efficiency. Indeed, misalignments may lead to minor beam clipping and potential specular reflections off the glass window. These specular reflections and transfer losses significantly reduce the SBR and degrade the overall image quality. Moreover, the improper manipulation of the fold mirrors during assembly and alignment sometimes results in minor scratches on the optical surface, which can cause losses and reduce the overall beam quality. The last objective will include validating all materials' toxicology, stress testing the TCE to establish failure mechanisms, and converting the optical system to a mobile clinical cart. Further testing with various optical modalities will also be performed to validate their operation and identify the first candidate for in vivo imaging.

7.5 Conclusion

In conclusion, we have presented an all-reflective tethered capsule endoscope for esophageal imaging. The all-reflective design allows for achromatic and backreflection-free imaging across VIS and NIR wavelengths and could be utilized for combining various modalities with OCT through a double-clad fiber. Such a device could accelerate the clinical translation of multimodal OCT in the esophagus by avoiding iterative optical design and potential re-certification.

Acknowledgements

This chapter was presented as a poster at the Gordon Research Conference 2022. I would like to acknowledge the contribution of Paul R. Bloemen, Niels H. Kind, Dirk J. Faber, Daniel M. de Bruin, Caroline Boudoux, and Ton van Leeuwen in the experimental design, capsule design and fabrication, and data analysis.

CHAPTER 8 ARTICLE 2: SIMPLE AND ROBUST CALIBRATION PROCEDURE FOR K-LINEARIZATION AND DISPERSION COMPENSATION IN OPTICAL COHERENCE TOMOGRAPHY

This chapter was reproduced from:

Xavier Attendu, Roosje M. Ruis, Caroline Boudoux, Ton van Leeuwen, Dirk J. Faber, "Simple and robust calibration procedure for k-linearization and dispersion compensation in optical coherence tomography," J. Biomed. Opt. 24(5) 056001 (13 May 2019) `https://doi.org/10.1117/1.JBO.24.5.056001`

Author contributions

The article presented in this chapter was submitted to the *Journal of Biomedical Optics* on 13/12/2018, accepted on 19/03/2019 and published on 13/05/2019. Xavier Attendu is the principal author and contributed ~70% of the work. Xavier Attendu contributed to the experimental design, development of the theoretical model, preparation of the experimental setup, data acquisition and analysis, and manuscript preparation and revision. Roosje M. Ruis contributed to the development of the theoretical model, preparation of the experimental setup, data acquisition and analysis, and manuscript revision. Caroline Boudoux, Ton G. van Leeuwen and Dirk J. Faber were senior investigators and assisted in the experimental design, data analysis and manuscript revision. Dirk J. Faber additionally contributed to the development of the theoretical model.

Chapter context

Dispersion compensation and k-linearization are essential steps in the data processing pipeline of FD-OCT systems. During the development of the various benchtop systems presented in the previous chapters, performing these calibration protocols efficiently and robustly was important as the systems were frequently altered and required components which induced non-negligible dispersion mismatches. The underlying theory for the calibration procedures was also essential to validating optimal system operation. Current methods for system calibration usually account for dispersion compensation and k-linearization separately requiring complicated measurement protocols or iterative optimization routines. By contrast, the proposed method requires only two quick and simple mirror measurements to extract the calibration vectors for both processing steps.

Abstract

In Fourier domain optical coherence tomography (FD-OCT), proper signal sampling and dispersion compensation are essential steps to achieve optimal axial resolution. These calibration steps can be performed through numerical signal processing, but require calibration information about the system that may require lengthy and complex measurement protocols. In this work, we report a novel, highly robust calibration procedure that can simultaneously determine correction vectors for non-linear wavenumber sampling and dispersion compensation. The proposed method requires only two simple mirror measurements and no prior knowledge about the system's illumination source or detection scheme. This method applies to both spectral domain and swept-source OCT systems. Furthermore, it may be implemented as a low-cost fail-safe to validate the proper function of calibration hardware such as k-clocks. We demonstrate the method's simple implementation, effectiveness, and robustness on both types of OCT systems.

8.1 Introduction

Optical coherence tomography (OCT) is an interferometric imaging technique, which provides depth-resolved images up to several millimeters deep with a typical resolution in the order of micrometers [45]. In order to attain the theoretical axial resolution over the entire imaging depth, however, several conditions must be met. Firstly, in Fourier-domain OCT (FD-OCT) systems, the interference signal must be sampled linearly in wavenumber (k) prior to performing each Fast Fourier transform (FFT) in order to reconstruct the depth reflectivity profile with bandwidth-limited axial resolution [340, 341]. Furthermore, dispersion must be matched in both interferometer arms, as dispersion imbalance leads to an unequal, wavelength-dependent phase delay of the light. A dispersion mismatch will induce broadening of the reconstructed OCT peaks, therefore reducing SNR and resolution [342]. Various solutions have been developed to address both these requirements. However, many of these imply expensive and/or complicated additional hardware, computationally intensive algorithms or time-consuming calibration procedures.

K-linear sampling can be achieved directly during signal acquisition with specialized hardware or re-created in post-processing with interpolation of the acquired signal. For spectral-domain OCT (SD-OCT), hardware-driven k-linear acquisition can be achieved with k-linear spectrometers [343]. In swept-source OCT (SS-OCT) systems, linear k-sampling relies mostly on external sampling clocks, called k-clocks, coupled with high-end acquisition electronics capable of non-uniform sampling frequencies [344]. If the interference signal is not directly sampled linearly in wavenumber, the most common approach is to perform numerical re-sampling using interpolation [345]. Interpolation requires a re-mapping function which relates sample index to actual wavenumber or fractional indices for interpolation. This re-mapping function is typically determined through an independent calibration procedure and may require further hardware. In SD-OCT for example, the spectrometer can be wavelength-calibrated using narrow spectral lines from reference sources, such as a krypton lamp [346]. Methods to identify the re-mapping function directly from OCT measurements have also been proposed [347]; however, such methods can be experimentally and computationally tedious [348,349]. A more straightforward and more common method involves linearizing the unwrapped phase of the interference spectrum measured when imaging a mirror. However, this method does not decouple the effects of non-linear sampling and dispersion mismatch and is only valid in the complete absence of dispersion, which is difficult to achieve in real systems. If applied to systems presenting a dispersion mismatch, simple phase linearization leads to re-mapping functions valid only for one specific depth position [350]. In a recent publication, Uribe-Patarroyo et al. proposed an optimization algorithm based on mirror measurements at multiple depth locations, which successfully decouples and corrects non-linearity in wavenumber and dispersion mismatch [351]. While this method provides a "true" re-mapping function, independent of dispersion and therefore valid across the entire imaging depth, the associated measurement protocol and algorithm deployment present additional experimental complexity. By comparison, Wang et al. and Makita et al. demonstrated a method which also extracts the true re-mapping function which relies only on two measurements and very simple algorithmic steps [352, 353]. In this method, a mirror is imaged at two different axial positions, and the unwrapped phase signals are subtracted from one another to remove the component due to dispersion. As the resulting phase signal must be linear with wavenumber, any non-linearity in the subtracted signal can be attributed to non-linear k-sampling. The re-mapping function can then directly be evaluated by linearizing this differential phase signal.

Dispersion compensation is a widely researched subject in the field of OCT. Many different methods to correct dispersion mismatch between the sample and reference arms have been proposed, both hardware- and software-based. Furthermore, it is important to distinguish between methods that only correct system dispersion and those that also correct for sample dispersion. The latter are particularly important when imaging structures through thick dispersive media as is often the case in ophthalmic OCT [354]. Hardware-based dispersion compensation can correct for both system and sample depending on the implementation. Solutions include physically matching dispersion in both arms by adding compensating material [355], dispersive prisms [356], gratings [291] or fiber-stretchers [357] in one of the interferometer arms. However, all these methods typically only compensate up to second order dispersion. Higher orders can be minimized by adding comparable components to both interferometer arms or through more complex setups that include several of the components mentioned above [358]. Such systems have been shown to correct dispersion up to the third order [359,360]. On top of the limitations regarding correction order, physical dispersion compensation shares the same pitfalls as hardware-based k-linearization: increased complexity and cost. Various software methods have also been developed to address the problem of dispersion compensation. Such techniques often allow to correct dispersion mismatches to higher orders than what is possible through physical compensation and can, in some cases, simultaneously correct system and sample dispersion. Amongst these, some rely on an iterative adjustment of a phase correction signal to optimize image sharpness [342, 361, 362]. This approach is particularly useful for correcting sample induced dispersion which cannot be corrected prior to measurements. However, such optimization techniques are computationally intensive and, for the most part, impractical for real-time processing. Another method, presented by Uribe-Patarroyo et al., relies on iterative optimization to extract the phase component due to system dispersion, which can then be corrected in future measurements at low computational cost [351]. Recently, Singh et al. reported a novel dispersion compensation scheme which uses differential phase measurements, much like those in Wang's k-linearization method, to exactly extract the phase component generated by system dispersion [363]. Similarly to Uribe-Patarroyo's process, this phase component can then be used to correct dispersion in all future measurements. Singh's method requires only two mirror measurements, which must be positioned at precisely symmetrical locations about the zero-delay plane. When the phase signals from these measurements are subtracted from one another, the (linear) depth-dependent phase is removed, leaving only the dispersion-related terms.

As such, numerous methods exist for k-linearization and dispersion compensation for FD-OCT systems. However, these methods imply varying levels of technical, algorithmic and experimental complexity as well as varying accuracy and robustness. Ideally, implementation complexity should be minimized without sacrificing robustness and effectiveness. To this effect, we herein present and validate a novel, simple and complete calibration procedure, which simultaneously extracts calibration information for k-linearization and dispersion compensation. Thorough descriptions of all experimental and algorithmic steps are provided to facilitate the method's implementation. The proposed method requires no additional hardware or *a priori* information, is highly robust, and relies only on two mirror measurements, obtained on either side of the zero-delay plane. Furthermore, we introduce a novel numerical phase shifting step allowing for the mirror measurements to be performed at arbitrary positions, as long as they are on either side of the zero-delay plane. We demonstrate that the method is equivalently applicable to SD- and SS-OCT systems, both with and without k-clock. Finally, we demonstrate that this procedure may still be applied in the case of improper configuration of the k-clock.

8.2 Theory

Our method, expanded in Appendix 8.7 and summarized in Fig. 8.1, is based on the manipulation of the phase of the complex spectral interference signal obtained from mirror measurements, using a standard FD-OCT system. We assume that there is a certain degree of dispersion mismatch due to the presence of a segment of dispersive material in one of the interferometer arms. All steps of the proposed method rely on the expression of the spectral phase signal ($\Delta\phi$), obtained experimentally, as the sum of a k-linear, depth-dependent component (ϕ_{lin}) and a k-nonlinear, depth-independent component (ϕ_{disp}):

$$\Delta\phi = \phi_{\text{lin}}(\delta z, k) + \phi_{\text{disp}}(k) = \underbrace{2(k-k_0)\,\delta z}_{\phi_{\text{lin}}} + \underbrace{(k-k_0)^2 n_g'(k_0) D + \ldots}_{\phi_{\text{disp}}} \tag{8.1}$$

In this equation, δz is depth, k_0 represents the central wavenumber, n_g' represents the first derivative of the group index with respect to k of the segment causing the dispersion mismatch between the two interferometer arms, and D is its thickness. A detailed mathematical derivation of Eq. (8.1) is given in Appendix A. Experimentally, the phase signal is determined by computing the phase of the analytical complex interference signal, obtained from the real measured signal using the Hilbert transform ($\mathcal{H}$), as described by:

$$\begin{aligned} \tilde{I}(k) &= I(k) + i\mathcal{H}(I(k)), & (8.2)\\ \Delta\phi &= \tan^{-1}\left(\frac{\text{Im}(\tilde{I}(k))}{\text{Re}(\tilde{I}(k))}\right). & (8.3) \end{aligned}$$

From Eq. (8.1) and the properties of the Fourier transform, it is apparent that the linear term will determine the position of the peak in the processed A-line, while non-linear, dispersion-induced terms will be responsible for peak broadening and distortion [342]. It is important to note that all the following steps assume that the phase signal has been unwrapped. From Eq. (8.1), we define the two calibration measurements, where $\Delta\phi_+$

refers to the measurement with the mirror physically located on one (positive) side of the zero-delay plane, at δz_+, and $\Delta\phi_-$ refers to the measurement with the mirror located on the opposite (negative) side, at δz_-:

$$\Delta\phi_+ = \phi_{\text{lin}}(|\delta z_+|) + \phi_{\text{disp}}, \tag{8.4}$$

$$\Delta\phi_- = \phi_{\text{lin}}(|\delta z_-|) - \phi_{\text{disp}}. \tag{8.5}$$

The sign reversal of the dispersion component (ϕ_{disp}) observed in Eq. (8.5) is due to the experimental retrieval of the (real) interferometric signal, discussed in Appendix section A3. We will refer to a set of two such measurements as a calibration pair throughout this manuscript.

8.2.1 k-linearization

Using Eq. (8.4) and (8.5), and following Wang et al., we can cancel out dispersion-related terms and isolate a linear term [10]:

$$\Delta\phi_{\text{lin}} = \frac{\Delta\phi_+ + \Delta\phi_-}{2} = \frac{\phi_{\text{lin}}(|\delta z_+|) + \phi_{\text{lin}}(|\delta z_-|)}{2} = 2(k - k_0)\left(\frac{|\delta z_+| + |\delta z_-|}{2}\right). \tag{8.6}$$

Equation (8.6) describes the phase term of a dispersion-free signal corresponding to a mirror located at the average absolute position of the two individual peaks. Any non-linearity in the unwrapped phase can, therefore, be attributed to improper sampling. Fractional indices for re-sampling can be obtained by linearizing $\Delta\phi_{\text{lin}}$. Linearization of the phase signal implies generating a linear vector of the same length as the vector $\Delta\phi_{\text{lin}}$ spanning from $\Delta\phi_{\text{lin},0}$ to $\Delta\phi_{\text{lin},N-1}$ where the subscripts refer to first and last samples respectively. For each element of this newly-generated, linear vector, we can identify a fractional index through interpolation corresponding to its position in the original phase vector. Thereafter, these fractional indices can be used to re-sample all subsequent measurements to obtain k-linear sampling. This process should be carried out on both measurements of the calibration pair before dispersion compensation can be performed.

8.2.2 Dispersion compensation with numerical phase shifting

Once k-linearized, the interference spectra are processed to obtain A-lines. The values of $\delta z_\pm$ are then evaluated by finding the axial position of the peak corresponding to the mirror. The peak axial positions can be evaluated in several ways such as applying a fit (e.g. Gaussian) or directly identifying the index corresponding to the position of the peak maximum. In both cases, the interference spectra should be extensively zero-padded prior to FFT to increase the number of data points available for the measurement. Measurements based on identifying the position of the maximum are particularly sensitive to this as insufficient padding may lead to errors due to the discrete nature of the signal. If proper k-linearization has been performed, the shape of the axial PSF should be completely independent of depth. Therefore, if measured in the same way, the peak positions relative to the axial profile will be identical for both mirrors, regardless of the goodness of fit. The numerical shift computed from the peak positions (Eqs. 7-9 or 11) will then always be valid, independently of how the peak positions were identified. As such, Gaussian fitting will be adequate even if the PSF deviates from a Gaussian profile due to a non-Gaussian illumination spectrum or due to the presence of significant high-order dispersion. Once the peak positions have been identified, we can numerically apply a linear phase correction, equivalent to translating both mirrors in air, which brings the two measurements ($\Delta\phi_+^*$ and $\Delta\phi_-^*$) back to perfectly symmetrical positions:

$$\begin{aligned}
\Delta\phi_{\text{shift}\pm} &= 2(k-k_0)\left(-|\delta z_\pm| + \frac{|\delta z_+|+|\delta z_-|}{2}\right), && (8.7)\\
\Delta\phi_+^* = \Delta\phi_+ + \Delta\phi_{\text{shift}+} &= 2(k-k_0)\left(\frac{|\delta z_+|+|\delta z_-|}{2}\right) + \phi_{\text{disp}}, && (8.8)\\
\Delta\phi_-^* = \Delta\phi_- + \Delta\phi_{\text{shift}-} &= 2(k-k_0)\left(\frac{|\delta z_+|+|\delta z_-|}{2}\right) - \phi_{\text{disp}}. && (8.9)
\end{aligned}$$

It is interesting to note that the applied phase shift and equivalent translation are arbitrary so long as the final positions of the peaks are symmetrical. The dispersion-induced phase term can then be isolated by finding the difference as proposed by Singh et al. [363]:

$$\phi_{\text{disp}} = \frac{\Delta\phi_+^* - \Delta\phi_-^*}{2}. \qquad (8.10)$$

This phase signal can then be fitted relative to sample index using Nth-order polynomial fitting. Thereafter, dispersion can be corrected by multiplying the complex signal by $\exp\left(\mp i\phi_{\text{disp}}^{\text{fit}}\right)$ for peaks on the positive side and the negative side of zero-delay respectively. It is important to notice that it is not necessary to have any knowledge of the real values of k or $\delta z_\pm$. Indeed, if the interference signal is defined in index space ($j = [0, 1, 2, \ldots N-1]$), then the processed A-lines will be located in a space defined from $-\pi$ to π corresponding to the optical path length difference. The peak positions ($\theta_{\text{peak}\pm}$) determined previously can then directly be used to compute the phase shift vector and shifted phase signals, expressed as:

$$\Delta\phi_{\text{shift}\pm}(j) = j\left(-|\theta_{\text{peak}\pm}| + \frac{|\theta_{\text{peak}+}| + |\theta_{\text{peak}-}|}{2}\right), \tag{8.11}$$

$$\Delta\phi^{*}_{\pm}(j) = \Delta\phi_{\pm}(j) + \Delta\phi_{\text{shift}\pm}(j). \tag{8.12}$$

The shifted phase signals determined in Eq. (8.12) can then be used to compute the dispersion phase component described in Eq. (8.10).

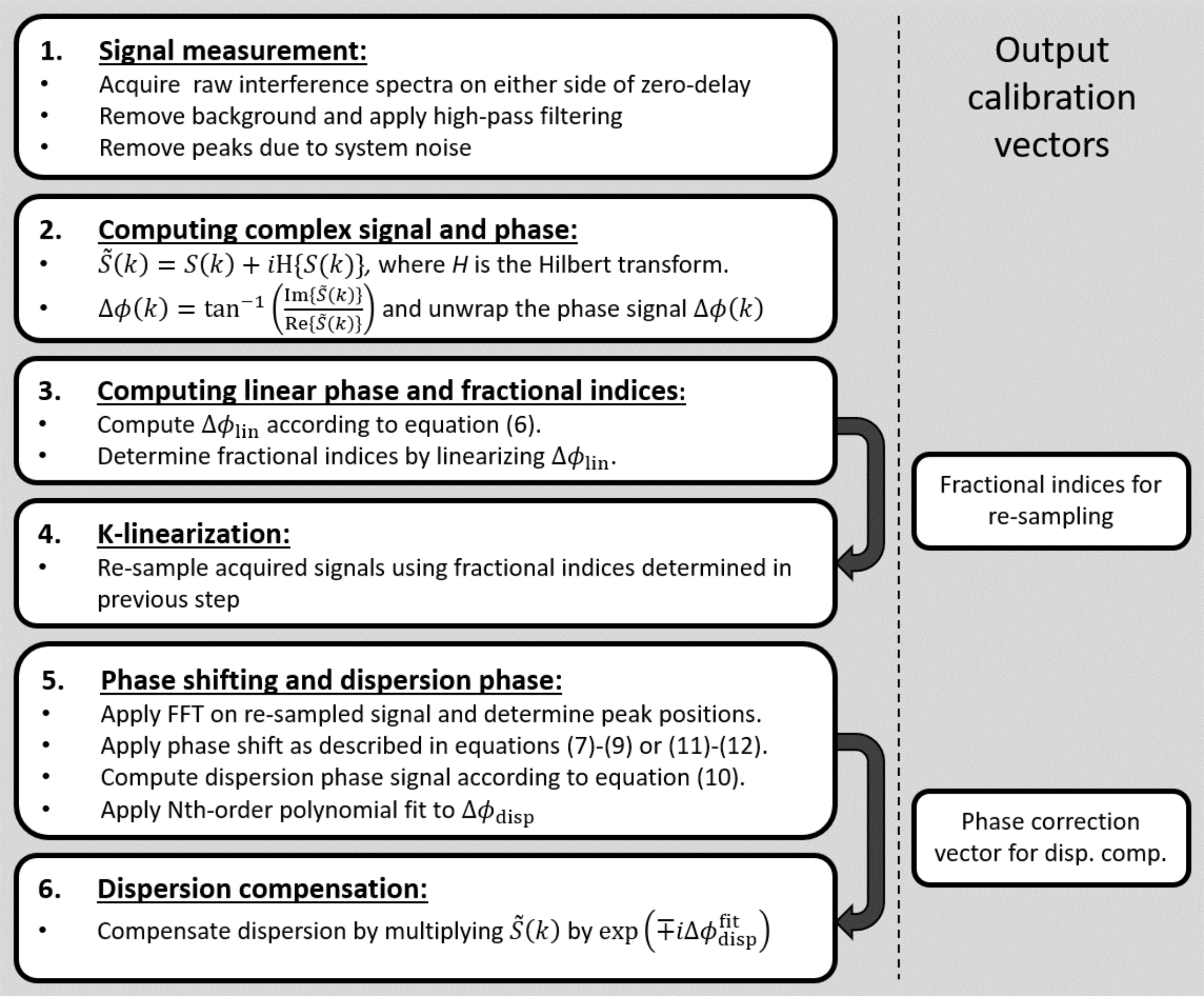

Figure 8.1 Flowchart of the calibration procedure. The calibration's output variables are identified in the boxes on the right

8.3 Materials and methods

8.3.1 System description

The calibration procedure was tested on two separate FD-OCT systems: one SD-OCT and one SS-OCT, shown in Fig. 8.2. The SD-OCT system (OCP840SR-NP, Thorlabs, USA) utilizes a superluminescent diode source (SLD-371, Superlum, Ireland) and a 1024-pixel spectrometer with a spectral resolution of 0.06 nm. A-lines were acquired at a 5 kHz rate. The SLD spectrum was measured using a USB4000 spectrometer (Ocean Optics, USA) and found to be centered at 850 nm with a full-width half maximum (FWHM) spectral bandwidth of 26 nm. The system also includes a 50/50 broadband fiber coupler as well as collimation and focusing optics. Through physical length measurements of the interferometer arms, we found a 1±0.1 cm mismatch in fiber length between the sample and reference arms. The SS-OCT is a custom system using a 50 kHz commercial swept-source (Swept laser 1310, Axsun, USA) with an integrated k-clock. The source spectrum was measured using a NIRQuest512 spectrometer (Ocean Optics, USA), and found to be centered at 1313 nm with a FWHM bandwidth of 95 nm. The interference signal was detected using a balanced photodetector (PDB450C, Thorlabs, USA) and filtered with an 80 MHz low-pass filter (VLF-80+, Mini-Circuits, USA) prior to digitization. Signal sampling was carried out with a high-speed acquisition card (ATS9350, AlazarTech, Canada) capable of both uniform and non-uniform sampling speeds. For measurements with the k-clock, 1088 samples were recorded per acquisition at a mean acquisition rate of 130 MS/s. Measurements without k-clock contained 3855 samples acquired at 500 MS/s. The number of samples in measurements without the k-clock was selected to match the spectral range obtained with the k-clock based on recognizable features in the spectra. Data acquisition was controlled using custom LabView software (National Instruments, USA) and synchronized with the swept-source laser using a custom fiber Bragg grating (FBG) sweep trigger. For the purpose of this experiment, a dispersion mismatch was induced by adding approximately 1 cm of distilled water in a petri dish to the sample arm of the SS-OCT system.

8.3.2 Measurement protocol

Single A-line measurements were carried out on a mirror for axial positions (δz) ranging over ±1 mm around the zero-delay plane, at 100-micron intervals. A manual micrometric stage was used to translate both the focusing lens and the sample mirror in order to avoid signal variation due to confocal gating. Raw interference signals (i.e., without

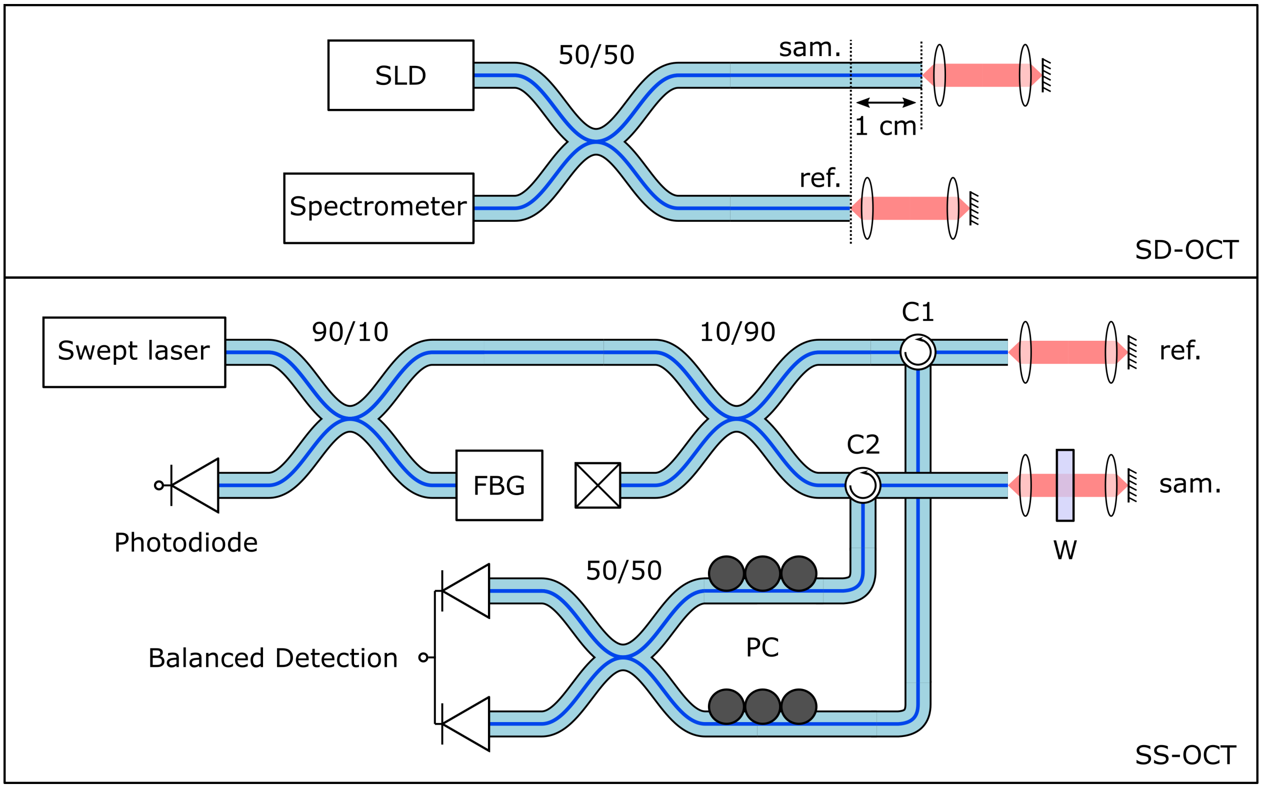

Figure 8.2 Schematic representation of both OCT systems: an SD-OCT (top) and a SS-OCT (bottom). (**FBG**) Fiber Bragg grating, (**SLD**) superluminescent diode, (**C1 & C2**) fiber circulators, (**PC**) polarisation controllers, (**W**) water.

any processing) were recorded from both systems using custom LabView software. All signals used for calibration were computed from the average of 64 consecutive A-line measurements. Background removal was achieved by subtracting the background spectrum from the mirror measurements as well as numerical high-pass filtering. The background was measured by successively blocking the sample arm, the reference arm, and both arms. The background signal subtracted from the other measurements was computed as $I_{\text{back}} = I_{\text{sam}} + I_{\text{ref}} - I_{\text{both}}$. The calibration described in Section 8.2 and in Fig. 8.1 was carried out for all possible combinations of negative and positive mirror locations. In the calibration, signals were zero-padded to 10 times their original length prior to FFT, and a fifth order polynomial fit was used to compute the dispersion correction vector (step 5 in Fig. 8.1). For each combination, the extracted calibration vectors were applied to all individual measurements, and their peak position and FWHM were measured. Finally, for each mirror location, the peak position and FWHM were averaged over all calibration pairs. The negative and positive peaks located at ±100 μm were not included during the calibration as these peaks had reduced SNR due to the high-pass filtering applied previously. This combined with their position close to the edge of the A-line led to instabilities when applying fits to the data and inaccurate calibration. For the SS-OCT system, data was acquired both with and without the k-clock. Measurements were also carried out on the SS-OCT system without the added dispersion (i.e., without the 1 cm water in the sample arm) and with varying k-clock delays. K-clock delay refers to the delay between the optical trigger in the swept laser source and the electronic trigger signal at the acquisition card. Improper adjustment of this parameter may lead to incorrect sampling as discussed further below. For both systems, the spatial pixel increment (μm/pixel) was determined from the two outermost mirror position (known separation of 2 mm).

8.3.3 Practical considerations

For optimal implementation of the proposed method, it is essential to consider certain practical aspects. Firstly, proper background removal is crucial to the method as the presence of background will strongly influence the phase signal quality. The presence of strong DC or low-frequency noise components will prevent proper phase retrieval with the Hilbert transform, hence the necessity for proper background subtraction and high-pass filtering. Furthermore, the signal of the calibration measurements should be processed to reduce random noise or contributions from system interference. Random noise can easily be attenuated by averaging multiple interference spectra. However, in systems with low phase stability, care should be taken not to wash out fringes by averaging over too many A-lines. Non-random system noise due to interference between various components in the optical path will appear as additional peaks in the processed A-line. The mirror peaks used for the proposed calibration procedure must be distinct from these background peaks. This background signal can be eliminated by applying spatial band-pass filtering (i.e., filtering out additional peaks in the signal after FFT and then transforming back). Finally, "null" data points, i.e., data points without any signal, should be omitted from this analysis as they will produce unstable phase values. Such points are easily identifiable by their non-smooth appearance when plotting the unwrapped phase of the acquired signal. They are usually located at the beginning or end of data acquisitions and correspond to the extremities of the broadband illumination spectrum (dark pixels for SD-OCT systems and time-points outside of the duty cycle of the wavelength-swept laser for SS-OCTs).

8.4 Results

The results of the calibration procedure on 1D measurements for both the SD and SS-OCT systems are illustrated in Fig. 8.3. The figure plots the axial resolution as a function of depth (physical mirror position) for the SD-OCT system (Fig. 8.3A), for the SS-OCT system with k-clock (Fig. 8.3B) and without k-clock (Fig. 8.3C) acquisition. Fig. 8.3D reproduces the curves of Fig. 8.3C using the same scale as 8.3B for simplified comparison. The error bars in Fig. 8.3 are obtained by calculating the standard deviation (STD) of the peak FWHM computed with all possible calibration pairs (n=81). For each case, the resolution is plotted as a function of depth for raw (blue dashed curve), k-linearized (red dashed curve), and fully corrected data (k-linearized and dispersion compensated - yellow dashed curve). The solid green line represents the optimal attainable value, often overlapping with the yellow dashed curve. It is important to note that this method corrects peak broadening due to improper sampling and dispersion mismatch. Other effects, including the spectral shape of the illumination, spectral transmission of the optical system, detector spectral efficiency, and alignment of polarization states, may lead to a poorer axial resolution compared to the expected value based only on the source spectral bandwidth. In order to properly assess the method's performance, the recovered axial resolution was compared to the bandwidth-limited, optimal value obtained by directly linearizing the phase of each peak (mean value over all acquired peaks). All numerical values are summarized in Table 8.1, by calculating the mean and standard deviation of the resolution over all measured axial positions. The *relative variation* row refers to the STD divided by the mean expressed in percent.

The results of the calibration procedure applied to the SS-OCT system without any artificially added dispersion and with varying k-clock delays are presented in Fig. 8.4 and in Table 8.2. Figure 8.4 plots the axial resolution as a function of depth for three different k-clock delays relative to the optimal value (calculated from system fiber length): -32.7 ns (minimum - Fig. 8.4A), -16.8 ns (Fig. 8.4B) and 3.6 ns (maximum - Fig. 8.4C). The color scheme and the calculation of error bars and theoretical resolution limit are all identical to that for Fig. 8.3 and Table 8.1. The values in Table 8.2 are calculated as mean and standard deviation of the resolution over all measured axial positions.

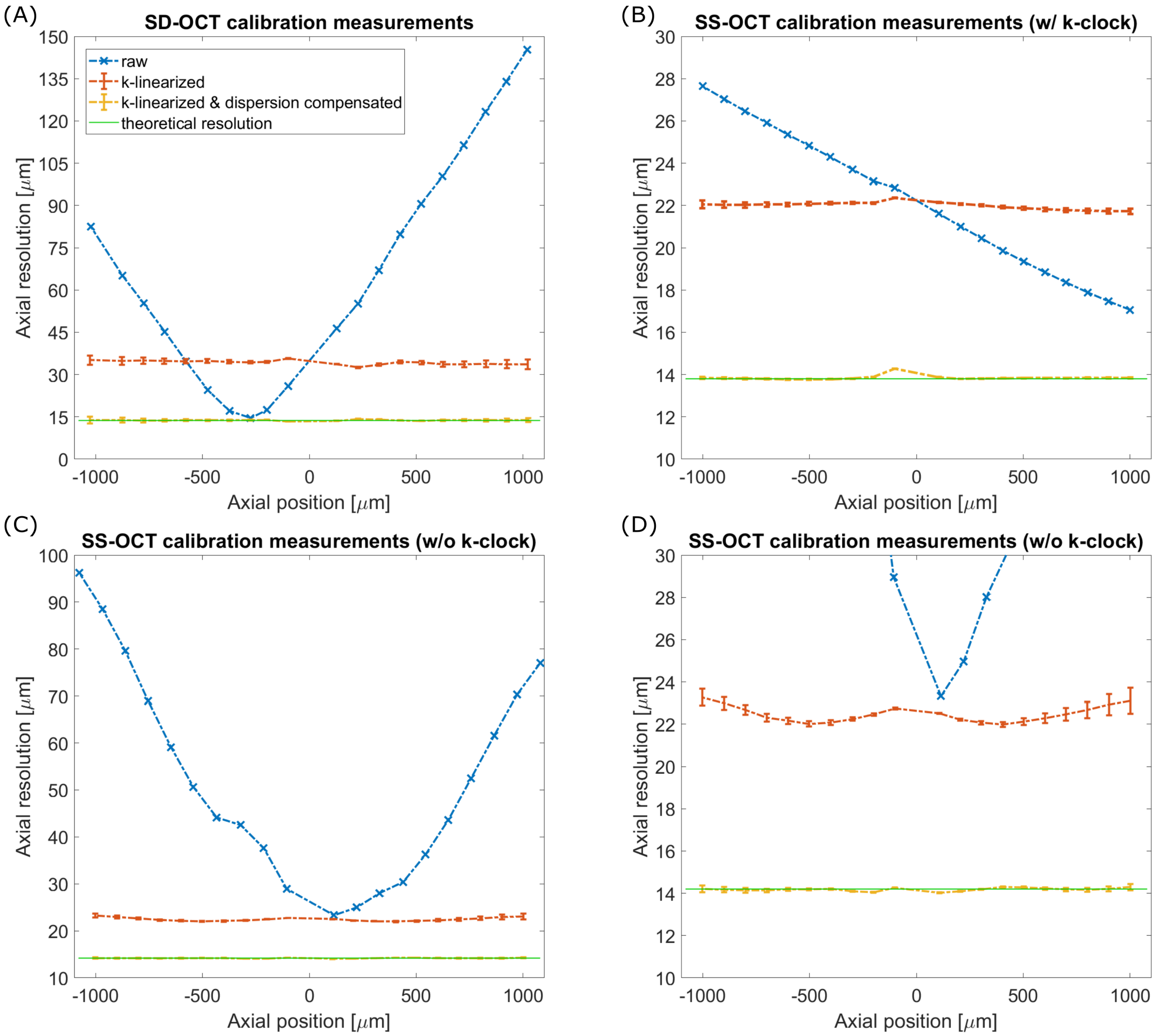

Figure 8.3 Measured axial resolution at different steps in the calibration procedure & recovery of optimal axial resolution with both systems. (A) SD-OCT measurements. (B) SS-OCT measurements with a k-clock (C) SS-OCT measurements without a k-clock. (D) Same SS-OCT measurements as in (C) but with vertical axis matched to sub-figure B.

Table 8.1 Statistics of the calibration procedure averaged over all axial positions. Dispersion in the SD-OCT system is due to fiber length mismatch; dispersion is artificially added in the SS-OCT measurements.

	SD-OCT			SS-OCT (w/ k-clock)			SS-OCT (w/o k-clock)		
	Raw	K-lin.	Full	Raw	K-lin.	Full	Raw	K-lin.	Full
Optimal (μm)	13.8±0.4			13.8±0.1			14.2±0.2		
Mean (μm)	66.9	34.3	13.8	22.1	21.9	13.8	52.2	22.5	14.2
STD (μm)	39.6	1.2	0.5	3.3	0.2	0.1	21.5	0.5	0.1
Rel. variation (%)	59.2	3.5	3.6	15.0	0.9	0.7	41.2	2.2	0.7

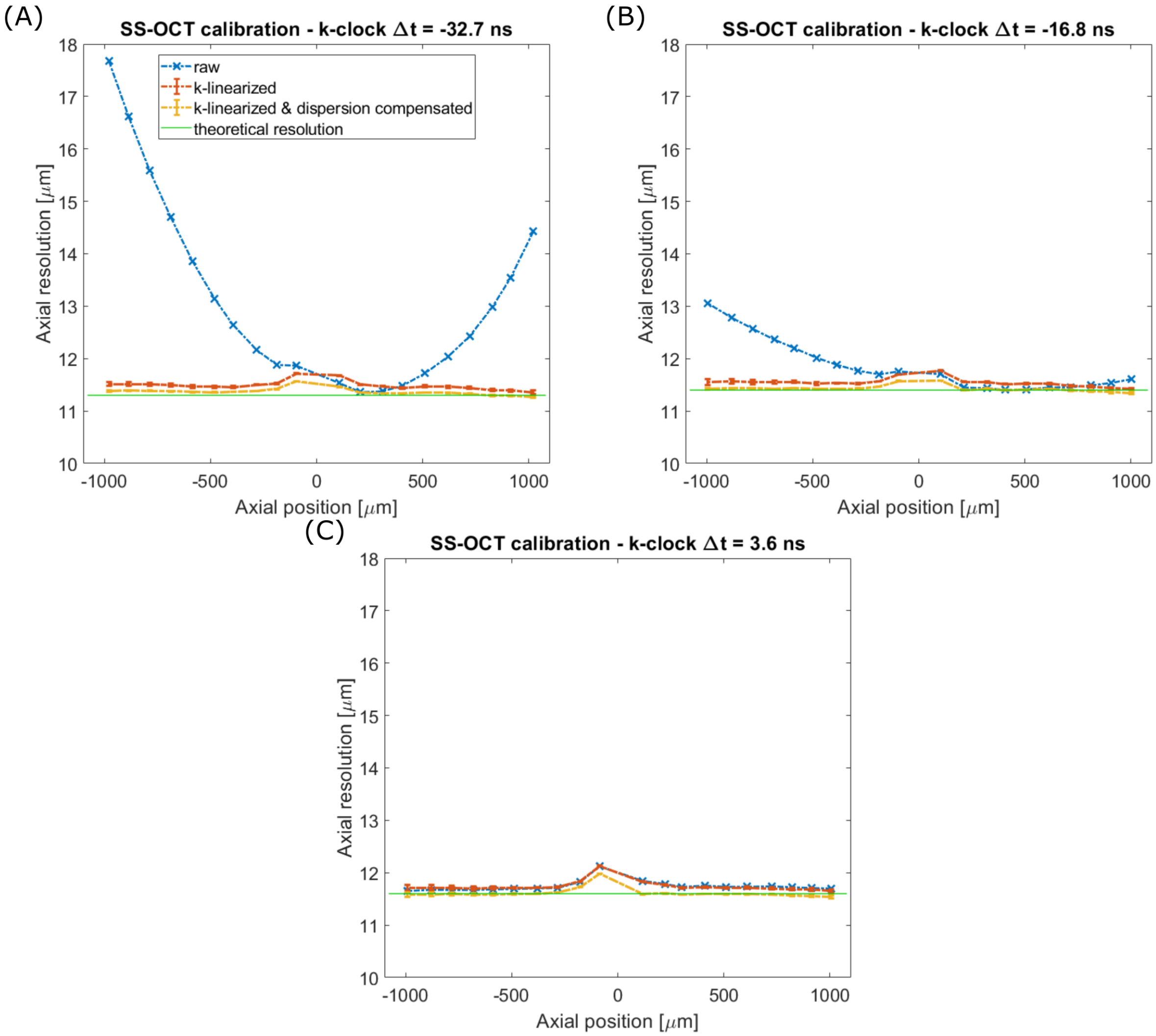

Figure 8.4 Measured axial resolution & recovery of optimal axial resolution with SS-OCT for different k-clock delays. (A) Δt=-32.7 ns (B) Δt=-16.8 ns (C) Δt=3.6 ns.

Table 8.2 Statistics of the calibration procedure for different k-clock delays, averaged over all axial positions. No artificially added dispersion.

	Δt = -32.7 ns			Δt = -16.8 ns			Δt = 3.6 ns		
	Raw	K-lin.	Full	Raw	K-lin.	Full	Raw	K-lin.	Full
Optimal (μm)	11.3±0.1			11.4±0.1			11.6±0.3		
Mean (μm)	13.2	11.5	11.4	11.9	11.5	11.4	11.7	11.7	11.6
STD (μm)	1.8	0.1	0.1	0.5	0.1	0.1	0.1	0.1	0.1
Rel. variation (%)	13.6	0.9	0.9	4.2	0.9	0.9	0.9	0.9	0.9

8.5 Discussion

8.5.1 Performance of the proposed method

Fig. 8.3 shows the recovery of k-linear sampling as well as the successful compensation of any dispersion mismatch present in the systems. In all instances, raw data curves are strongly dependent on depth, while k-linearized curves are flat, demonstrating that indeed, k-linearization of the OCT signal removes the depth-dependency of the measured axial resolution, as predicted by the theoretical framework. The subsequent dispersion compensation step improves the axial resolution down to the theoretical value, allowing for the recovery of the optimal axial resolution over the entire imaging range. Table 8.1 shows that, after application of the calibration, the theoretical axial resolution is recovered to within less than 1% over the entire imaging range for all systems and configurations. The method's insensitivity to the position of the calibration pair is demonstrated by the very narrow error bars in Fig. 8.3 as well by the low standard deviations reported in Table 8.1. As such, these results indicate that the optimal axial resolution is recovered, no matter which combination of mirror positions was used.

Furthermore, Fig. 8.3B and 8.3D as well as Table 8.1 show small differences in the recovered axial resolution for the SS-OCT system depending on whether the swept-source k-clock is used or not (13.8 μm and 14.2 μm, respectively). As both these measurement sets were acquired concurrently and on the same system, it would be expected that the recovered axial resolutions be identical. We propose three potential sources that may contribute to this discrepancy. Firstly, there may have been minute differences in the spectral bandwidth between the two sets of acquisition parameters. While in both cases the acquisitions were initiated by the spectral sweep trigger, the end of the acquisitions may have varied slightly in time and therefore in their spectral positions. Precautions were taken to minimize this issue; however, it may still account for a portion of the 400 nm difference in axial resolution. A second contributing factor might be the slightly lower SNR observed in the SS-OCT data acquired without the use of the k-clock. Indeed, the average sampling speed without the k-clock was roughly four times higher than when the k-clock was active, which would induce a higher noise equivalent power. Finally, it is possible that the discrepancy is associated with fitting instabilities due to the low number of data points contained within the reconstructed peaks in both cases. As such, the difference might be generated by a slight underestimation of the k-clocked peak width or an overestimation of the non-k-clocked one. However, it is important to note that whatever the cause of this effect, its magnitude is sufficiently small to be considered negligible for all practical intents and purposes.

Finally, it is particularly interesting to note that this method requires no a priori knowledge regarding the optical system, the acquisition hardware and parameters, or the illumination source. Indeed, it relies strictly on the information acquired during the two measurements. This allows for a very simple implementation, valid across all OCT platforms. Two afore-mentioned methods to obtain the k-linearization vector [352] and to determine the dispersion correction [363] also only require two mirror measurements. Our method maintains that advantage while generalizing to allow for mirror measurements on opposite sides of zero delay and removing the requirement of exactly symmetrical mirror positions with respect to zero-delay by numerical phase shifting.

8.5.2 k-clock sampling issues

Another crucial point highlighted by this work is the potentially imperfect k-linearization of k-clocks. As observed in Fig. 8.3B, 8.4A and 8.4B, the axial resolution of the raw signal acquired with a k-clock still varies with depth, which indicates non-linear k-sampling. This was caused by an improper clock-delay in the k-clock output. As is the case in many wavelength-swept lasers used for OCT, the k-clock signal in our setup is obtained from the zero-crossings of the interference signal of a fiber Mach-Zehnder interferometer (MZI) built into the light source. These zero-crossings are equally spaced in k-space thus producing a k-linear clock signal. However, if the total travel time of the light in the OCT system is not equivalent to the travel time in the MZI plus the electronic delay of the clock pulse, there is an offset between the clock pulse and the intended sampling point, which re-introduces non-linearities in sampling. Such effects may, therefore, appear when the total fiber length of the OCT system is altered. While some wavelength-swept lasers offer adjustable clock-delay, the range of the delay is often limited which implies inevitable axial resolution degradation when operating outside of this range. Such situations may arise in clinical systems operating with long endoscopic probes or, inversely, in systems using photonic integrated circuits (PICs) with very short total optical paths. OCT systems based on PICs are doubly advantaged by the proposed method as they also present significant peak broadening due to dispersion mismatch [364–366]. The effect of an incorrect k-clock delay can be quite significant as illustrated in Fig. 8.3B, where the axial resolution varies by 5-6 μm over a 1 mm imaging range. Fig. 8.4 shows that the calibration procedure successfully recovers optimal resolution over the entire imaging range, regardless of the k-clock delay. Furthermore, our method remains stable and robust even when the signal is already linearly sampled in k-space as is the case in Fig. 8.4C. In this scenario, the fractional indices for re-sampling are almost identical to the initial indices and do not alter the measured signal. The root-mean-square difference between the original indices and the re-sampling indices was found to be 0.01%, and the mean axial resolution over the imaging range was identical. As such, this method can be implemented as a low-cost fail-safe to ensure correct sampling even when a k-clock is used. Alternatively, it could be used as a validation method to ensure that the proper k-clock delay is being used. Indeed, improper delay settings would be noticeable through differences between the original indices and the fractional indices for re-sampling.

8.5.3 Calibration using measurements on the same side of zero-delay

It is possible to deploy an approximation of the procedure outlined in this paper using two mirror measurements located on the same side of zero-delay. In such a case, the phase from both measurements would be given by Eq. (8.4) or (8.5). The linear component can then be extracted by subtracting one from the other. The fractional indices can then be computed from this differential signal [352]. Once k-linearized, the dispersion component of a single measurement can be determined performing a polynomial fit on the full unwrapped phase ($\Delta\phi_{\pm}$) and keeping only the non-linear terms [367]. However, it was demonstrated that this method for dispersion compensation was less effective than the differential approach, particularly when higher order dispersion terms become significant [363]. This is particularly relevant for ultra-broadband or visible-light OCT systems. The use of a single measurement for dispersion compensation does not account for the presence of residual secondary peaks due to system noise, whereas in the differential approach, such additional peaks would be canceled out. As such, while this approximation remains viable, it did lead to a small degradation in axial resolution and a wider distribution for our data. It can be expected that this effect will become more significant for systems with more or higher-order dispersion.

8.6 Conclusion

In conclusion, we present a method which corrects non-linear k-sampling and system-induced dispersion mismatch, using only two mirror measurements. Two calibration vectors are extracted which allow numerical re-sampling for k-linearization as well as a phase correction to account for dispersion compensation. We demonstrate the procedure's simplicity, its robustness to the position of the mirror peaks and its applicability to both SD- and SS-OCT systems. We anticipate that this method may be extended to calibrate systems which also contain sample-induced dispersion mismatches such as in ophthalmologic imaging through the dispersive medium of the eye. In such a scenario, a strong sample reflection could be used instead of a mirror to perform the calibration.

8.7 Appendix

8.7.1 Propagation constant

In this section, we provide the theoretical background of the proposed calibration method. Our method relies on the manipulation of the spectral interference signal obtained during OCT measurements of a single reflector, which can be expressed as

$$I_{\mathrm{int}}(k) = I_{\mathrm{DC}}(k) + 2\sqrt{I_s(k)I_r(k)} \cdot \mathbb{R}e[\exp(i\Delta\phi(k))], \tag{8.13}$$

where $I_{\mathrm{int}}(k)$ is the intensity measured at the detector, $I_{\mathrm{DC}}(k)$ is the sum of $I_r(k)$ and $I_s(k)$, the intensities in the reference and sample arms respectively, and $\Delta\phi(k)$ is the phase difference between the fields from the reference and sample arms. The phase in each arm is given by

$$\phi_r = 2\sum_p \beta_p(k) l_p, \tag{8.14}$$

$$\phi_s = 2\sum_q \beta_q(k) l_q. \tag{8.15}$$

In Eq. (8.14) and (8.15), the variables $\beta_{p,q}(k)$ denotes the material specific propagation constants and $l_{p,q}$ is the physical length of the corresponding medium. The factor 2 accounts for the light traversing this distance twice. In a dispersive material, the propagation constant depends on wavenumber such that,

$$\beta(k) = kn(k), \tag{8.16}$$

where $n(k)$ is the wavenumber-dependent complex index of refraction specific to each material. The imaginary part of $\beta(k)$ determines the material absorption coefficient. Throughout this report, we consider only the real part of $n(k)$ and therefore $\beta(k)$. The propagation constant can be expanded into a Taylor series around an arbitrary wavenumber, k_0 (typically the central wavenumber), as follows:

$$\beta(k) = \beta(k_0) + \beta'(k_0)(k-k_0) + \frac{1}{2}\beta''(k_0)(k-k_0)^2 + ..., \tag{8.17}$$

Where the $'$ prime denotes differentiation with respect to wavenumber. Using Eq. (8.16) and applying the rules for chain derivation, we obtain

$$\beta(k) = k_0 n(k_0) + \frac{d}{dk}[kn(k)]\bigg|_{k=k_0}(k-k_0) + \frac{1}{2}\frac{d^2}{dk^2}[kn(k)]\bigg|_{k=k_0}(k-k_0)^2 + ..., \tag{8.18}$$

$$\beta(k) = k_0 n(k_0) + [n(k_0) + k_0 n'(k_0)](k-k_0) + \frac{1}{2}\frac{d}{dk}[n(k) + kn'(k)]\bigg|_{k=k_0}(k-k_0)^2 + ..., \tag{8.19}$$

To simplify the notation, we introduce the group refractive index

$$n_g(k) = n(k) + kn'(k), \tag{8.20}$$

which we substitute into Eq. (8.19) to obtain

$$\beta(k) = k_0 n(k_0) + n_g(k_0)(k-k_0) + \frac{1}{2}n_g'(k_0)(k-k_0)^2 + ..., \tag{8.21}$$

The propagation constant, Eq. (8.21), can then be summarized as the infinite series

$$\beta(k) = k_0 n(k_0) + \sum_{m=1}^{\infty} \frac{n_g^{(m-1)}(k_0)}{m!}(k-k_0)^m. \tag{8.22}$$

The first term is a constant phase term that may be neglected in subsequent analysis. First order dispersion (m=1) accounts for group delay of the spatial interferometric signal, whereas the higher order terms lead to broadening and chirping of the OCT signal.

8.7.2 Interferometer with dispersion mismatch

First, consider a perfectly dispersion balanced OCT interferometer. We introduce a segment of glass of thickness D at z=0, and determine the phase of the interference spectrum Eq. (8.13), corresponding to the back surface of the glass segment. From Eq. (8.14) and (8.15), $\phi_r = 2kl_0$ and $\phi_s = 2kl_0 + 2\beta_{\text{glass}}(k)D$. Following the steps leading up to Eq. (8.22), we find that Fourier transform of Eq. (8.13) yields the spatial OCT signal, consisting of a peaked signal determined by the source spectrum, shifted to depth position $z = n_g(k_0)D$ and possibly widened, chirped or otherwise distorted by the higher orders $m \geq 2$ of the propagation constant $\beta_{\text{glass}}(k)$.

To resemble a realistic OCT system with a mismatch in fiber lengths between both arms of the interferometer, we shift the reference mirror over a distance $z = n_{\text{g}}(k_0)D$ so that the position of zero group delay difference coincides with the back surface of the glass. We then add a further offset, δz, to the sample arm such that

$$\begin{aligned} \phi_r &= 2kl_0 + 2kn_g(k_0)D, && (8.23)\\ \phi_s &= 2kl_0 + 2\beta_{\text{glass}}(k)D + 2k\delta z, && (8.24)\\ \Delta\phi(k) &= 2k\delta z + 2D[\beta_{\text{glass}}(k) - kn_g(k_0)]. && (8.25) \end{aligned}$$

Re-arranging, and expanding the propagation constant following Eq.(8.21) gives:

$$\Delta\phi(k) = 2k\delta z - 2Dkn_g(k_0) + 2D\left(n_g(k_0)(k-k_0) + \frac{1}{2}n_g'(k_0)(k-k_0)^2 + \ldots\right) + 2Dk_0 n(k_0), \quad (8.26)$$

where the last, constant term does not have any k-dependence. Changing the k-dependence of the first 2 terms to $(k - k_0)$ dependence, so that the second term in the equation and the first term within the brackets cancel, will add constant terms:

$$\Delta\phi(k) = 2(k-k_0)\delta z + 2D\left(\frac{1}{2}n_g'(k_0)(k-k_0)^2 + \ldots\right) + \text{constant terms}. \quad (8.27)$$

The constant terms will have no impact on the processed A-line as they will be factored out of the Fourier transform and removed when we compute the absolute value. As such, we can simply ignore them in subsequent steps. We therefore obtain the simplified expression for the spectral phase of a single reflector:

$$\Delta\phi(k) = 2(k-k_0)\delta z + (k-k_0)^2 n_g'(k_0)D + \ldots = \phi_{\text{lin}}(\delta z) + \phi_{\text{disp}}. \quad (8.28)$$

8.7.3 Experimental retrieval of the interferometric phase

Despite the complex notation of Eq.(8.13), the detected signal is a real-valued modulated spectrum. In a non-dispersed interferometer, signals from exact opposite locations with respect to zero-delay cannot be distinguished (the so-called complex ambiguity) unless special measures are taken: the Fourier transform on the spectral interferogram will yield an A-line with mirror-peaks at $-\delta z$ and $+\delta z$. If the mirror is located at $+\delta z$, the spectral interferogram following Eq.(8.13) and (8.28) is

$$I_{\text{int}}(k)_{+} \propto \cos\Bigl(\phi_{\text{lin}}(\delta z) + \phi_{\text{disp}}\Bigr). \tag{8.29}$$

If the mirror is located at $-\delta z$, the spectral interferogram following Eq.(8.13) and (8.28) is

$$\begin{aligned} I_{\text{int}}(k)_{-} &\propto \cos\Bigl(-\phi_{\text{lin}}(\delta z) + \phi_{\text{disp}}\Bigr) \\ = \cos\Bigl(-\bigl[\phi_{\text{lin}}(\delta z) - \phi_{\text{disp}}\bigr]\Bigr) &= \cos\Bigl(\phi_{\text{lin}}(\delta z) - \phi_{\text{disp}}\Bigr). \end{aligned} \tag{8.30}$$

We therefore adopt the following notation of the spectral phase corresponding to peaks at positive and negative delays, respectively:

$$\Delta\phi_{+} = \Bigl|\phi_{\text{lin}}(\delta z_{+}) + \phi_{\text{disp}}\Bigr| = \phi_{\text{lin}}(|\delta z_{+}|) + \phi_{\text{disp}} \tag{8.31}$$

$$\Delta\phi_{-} = \Bigl|\phi_{\text{lin}}(\delta z_{-}) + \phi_{\text{disp}}\Bigr| = \phi_{\text{lin}}(|\delta z_{-}|) - \phi_{\text{disp}} \tag{8.32}$$

Disclosures

The authors have no relevant financial interests in this article and no potential conflicts of interest to disclose.

Acknowledgements

This work was supported in part by the Netherlands Organization for Scientific Research (Applied and Engineering Sciences), iMIT- OBAMA (Grant No. 12708). XA is additionally supported by the Natural Sciences and Engineering Research Council of Canada (NSERC), a fellowship from TransMedTech, Canada First Research Excellence Fund (CFREF), and a travel grant from the Fonds de Recherche du Quebec - Nature et Technologies (FRQNT).

CHAPTER 9 ARTICLE 3: CALIBRATION PROCEDURE FOR ENHANCED MIRROR ARTIFACT REMOVAL IN FULL-RANGE OPTICAL COHERENCE TOMOGRAPHY USING PASSIVE QUADRATURE DEMULTIPLEXING

This chapter was reproduced from:

Xavier Attendu, Dirk J. Faber, Guy Lamouche, Ton van Leeuwen, Caroline Boudoux, Maxime Rivard, "Calibration procedure for enhanced mirror artifact removal in full-range optical coherence tomography using passive quadrature demultiplexing," submitted to J. Biomed. Opt. (2022).

Author contributions

The article presented in this chapter was submitted to the *Journal of Biomedical Optics* on 23/05/2022. Xavier Attendu is the principal author and contributed ~70% of the work. Xavier Attendu contributed to the experimental design, development of the theoretical model, preparation of the experimental setup, data acquisition and analysis, and manuscript preparation and revision. Dirk J. Faber contributed to the development of the theoretical model and the data analysis. Guy Lamouche, Ton G. van Leeuwen, Caroline Boudoux, and Maxime Rivard were senior investigators and assisted in the experimental design, data analysis and manuscript revision. Maxime Rivard also contributed to the preparation of the experimental setup, development of the model and data acquisition.

Chapter context

Full-range optical coherence tomography (FR-OCT) enables imaging on both sides of zero-delay by removing the mirror artifact, which effectively doubles the imaging range. This mirror artifact can be problematic in the context of endoscopic OCT because optical interfaces inside the endoscope, such as the glass windows in Chapters 6 and 7, may be folded back into the useful imaging range and degrade the overall imaging quality. To avoid this in conventional OCT systems, the image is shifted until the overlap is removed (if that is even possible), which usually results in a reduced imaging range. As such, the proposed methods for implementing FR-OCT may help extend the useful imaging range and avoid image degradation due to overlapping mirror artifacts. Moreover, this method allows the use of imperfect quadrature demultiplexing circuits that would otherwise only provide limited extinction of the mirror artifact.

Abstract

Passive optical demodulation enables real-time reconstruction of the complex interference signal, removing mirror artifacts in optical coherence tomography. However, this requires extremely high precision while measuring the real and imaginary components of the complex signal. Standard optical designs typically do not satisfy the requirements and post-processing is necessary to correct the measured signals. We propose a framework describing the signal produced by an imperfect quadrature demodulation circuit as well as a protocol allowing the precise measurement and correction of the associated errors directly from mirror measurements. We demonstrate the method's simple implementation, effectiveness in attenuating the mirror artifact and evaluate its robustness to time and experimental conditions.

9.1 Introduction

In its standard implementation, Fourier-domain optical coherence tomography (FD-OCT) suffers from the *complex conjugate* or *mirror artifact*, which prevents simultaneous imaging on both sides of the zero-delay plane [287]. In addition to reducing the overall imaging range, this configuration requires the sample to be located at a certain distance from the zero-delay plane, which may lead to a reduction in sensitivity due to spectral roll-off [368]. Several methods have been proposed to overcome these limitations and enable *full-range* optical coherence tomography (FR-OCT), which allows artifact-free imaging on both sides of the zero-delay plane. These methods can be sub-divided into three categories: frequency modulation techniques, phase-shifting interferometry, and passive quadrature demultiplexing methods. The advantages and limitations of each option are briefly discussed below.

The frequency modulation approach relies on the use of active optical components such as acousto- and electro-optic modulators (AOM and EOM, respectively) to superimpose a modulation on top of interference signal in optical frequency-domain imaging [368, 369]. This modulation causes the interference signal associated with a null spatial offset to be shifted to a non-zero frequency, allowing imaging with both positive and negative spatial offsets. Frequency modulation provides excellent extinction of the complex conjugate (≥ 60 dB) [368] as well as improved signal-to-noise ratio (SNR) due to the elimination of low-frequency noise [369]. It is worth noting that 60 dB is considered excellent as OCT imaging of biological tissue rarely presents such a broad dynamic range. Indeed, if the extinction exceeds the intensity of the signal, the mirror artifact will be lowered below the noise floor and effectively removed. While the frequency modulation approach provides excellent performance, it presents certain drawbacks, including experimental complexity, increased costs, and enhanced bandwidth requirement for the detectors and high-speed digitizers. Furthermore, such methods are limited to swept-source OCT (SS-OCT) systems and are incompatible with (spectrometer-based) spectral-domain systems (SD-OCT).

Another approach for full-range OCT consists of using phase-shifting interferometry to reconstruct the complex interference signal (i.e., both the phase and amplitude of the interference fringes) from two or more interference spectra acquired sequentially [287, 370, 371]. Options to obtain a phase shift between the acquisitions include piezoelectric transducers (PZT) mounted on the reference mirror [371–373] and electro-optic phase modulators [374, 375]. Such methods, however, require multiple acquisitions per A-line, thereby reducing the overall acquisition speed and increasing their sensitivity to sample motion and the system's overall phase stability. A variant of the phase-stepping approach, called *BM-scanning*, removes the requirement for multiple acquisitions by introducing the phase shift across A-lines within a B-scan. The complex signal can then be recovered by performing a Hilbert transform (HT) across the spatial dimension prior to applying the usual Fourier Transform (FT) [376–381]. Phase-shifting methods, in general, have the added benefit that they can be implemented in both types of Fourier domain OCT (FD-OCT) systems . However, to the best of our knowledge, none of the phase-shifting approaches have achieved extinction of the complex conjugate equivalent to that obtained with frequency modulation, and are usually limited to $\leq$ 40 dB [371, 372, 375, 381].

The last group of FR-OCT methods uses optical systems to passively separate and simultaneously measure the complex interference signal's real and imaginary components. This can be accomplished using polarization optics [382,383] or alternative interferometer configurations with N×N fiber couplers, with $N \geq 3$ [74,384,385]. In both instances, however, the separation of the signal components must be stable, uniform across the complete spectral bandwidth, and precisely known. This typically requires highly accurate and time-consuming calibrations or sophisticated and expensive optical components. Given these complex specifications, passive demultiplexing commonly does not achieve high extinction ratios. It is usually also limited to extinction ratios $\leq$ 40 dB [74, 382–385]. Like phase-shifting methods, passive demultiplexing is compatible with both FD-OCT techniques. However, the passive approach is usually only applied to SS-OCT systems as it requires two detection channels. In the case of SD-OCT, two spectrometers would be required, significantly increasing the system's cost. Finally, the simultaneous measurement of both the real and imaginary signal components allows maintaining high acquisition speeds and makes passive demultiplexing insensitive to sample motion.

As such, no method is dominant: each has drawbacks in terms of cost, complexity, stability, or overall performance. In this paper, we propose a calibration protocol for passive demultiplexing, which may address some shortcomings mentioned in the previous paragraph. We propose a simple and straightforward procedure to experimentally assess and correct the relative differences in the two measurement channels, including the chromatic or spectral effects as well as the *RF-errors* associated with detection and acquisition electronics [386]. The proposed method relies only on measuring the interference signal from a mirror at different depth locations and can be performed directly on the system without any modifications other than adding the optical quadrature demultiplexing circuit. We first describe the underlying theoretical framework, then demonstrate the proposed method on an SS-OCT system with a polarization-based demultiplexing scheme. However, it is important to note that the method may be generalized to other passive quadrature demultiplexing schemes in FD-OCT.

9.2 Theory — complex signal reconstruction

The aim of passive quadrature demultiplexing is the reconstruction of the complex interference signal, $\tilde{S}$, which lifts the ambiguity between the positive and negative delays after FT or, in other words, removes the mirror artifact. This reconstruction requires the simultaneous measurement of the real and imaginary parts of the interference signal, also called the real (S_R) and quadrature (S_Q) signals. In principle, these two signals are identical except for a $\pi/2$ phase shift at all wavelengths and axial positions. An ideal demodulation circuit allows the direct measurement of these signals in two output channels, which can then be used to reconstruct the complex signal following:

$$\tilde{S} = S_R + i \cdot S_Q. \tag{9.1}$$

In real applications, however, there exist minor deviations in the phase and amplitude of the two measured signals, which results in residual mirror peaks (see Appendix 9.6.1 for more details). The accuracy in amplitude- and phase-matching required to achieve mirror artifact extinction ≥ 60 dB cannot be achieved with physical components and necessitates the measured signals to be corrected in post-processing. This work outlines a method to perform the necessary adjustments to the measured signals to achieve high mirror peak extinction. We begin by deriving expressions for the OCT signal, which encompasses the effects of the demodulation circuit. We show that, for each channel, the combined effect of all components in the passive demodulation scheme can be simplified down to two phasors: one wavelength-dependent and one depth-dependent. Finally, we propose a method to measure these phasors and correct the measured signals accordingly.

In Eq.9.1 and throughout this manuscript, we use variables with a tilde symbol to denote complex-valued vectors. Variables without the tilde symbol refer to the real component of their complex counterpart (e.g., $S = \mathcal{R}\{\tilde{S}\}$). While the mathematical derivations presented here utilize complex signals, all measurement data consists of real values. The *measured* complex signals are the analytic representation of the real-valued signals, obtained via an adaptation of the Hilbert Transform (HT), as discussed in Section 9.3.2. These measured complex signals should not be confused with the *reconstructed* complex signal.

9.2.1 Chromatic errors

The complex signal measured at the n^{th} output of the demodulation circuit can be described by:

$$\tilde{S}_n(k) = \underbrace{I_R T_{Rn} + \sum_m T_{Sn} R_m I_S}_{\text{DC terms}} + \underbrace{\sum_m 2\sqrt{T_{Rn} T_{Sn} R_m I_R I_S}\, e^{i(\theta_m + \phi_n)}}_{\text{interference term}}, \tag{9.2}$$

where I_S and I_R are the intensities in the sample and reference arms, respectively, T_{Sn} and T_{Rn} are the transmission efficiencies from the sample and reference arms, respectively, R_m is the intensity reflectivity of the m^{th} reflector in the sample arm, θ_m is the phase ramp associated to the position of the reflector, Δz_m, and is equal to $2k\Delta z_m$, and ϕ_n is the phase offset attributed to the n^{th} output port. All the above variables (with the exception of Δz_m) are functions of the wavenumber, k. Assuming that the DC components are removed through balanced detection and background removal, the balanced interference signals, $\tilde{S}_{I,\text{int.}}(k)$ and $\tilde{S}_{II,\text{int.}}(k)$, can be isolated, as:

$$\begin{aligned} \tilde{S}_{I,\text{int.}}(k) &= \sum_m 2\sqrt{R_m} e^{i\theta_m} \cdot \left[\sqrt{T_{R1} T_{S1} I_R I_S}\, e^{i\phi_1} - \sqrt{T_{R3} T_{S3} I_R I_S}\, e^{i\phi_3}\right] \\ \tilde{S}_{II,\text{int.}}(k) &= \sum_m 2\sqrt{R_m} e^{i\theta_m} \cdot \left[\sqrt{T_{R2} T_{S2} I_R I_S}\, e^{i\phi_2} - \sqrt{T_{R4} T_{S4} I_R I_S}\, e^{i\phi_4}\right] \end{aligned} . \tag{9.3}$$

Here, we assume that the autocorrelation terms, suppressed through balanced detection, are negligible. The validity of this assumption is particularly important in the context of FR-OCT as autocorrelation artifacts usually occur close to zero-delay, an area now part of the useful imaging range. While autocorrelation artifacts from biological tissue tend to be negligible, multiple specular reflections from optical components in the interferometer arms can lead to more significant ones. Fortunately, such specular reflections can be mitigated through the proper choice of optics and anti-reflection coatings. To lighten the mathematical notation, the subscript *int.* is dropped from Eq. 9.3, and the measured signals $\tilde{S}_I$ and $\tilde{S}_{II}$ will refer solely to the interference signal. Equation 9.3 is simplified by grouping the transmission and intensity variables, extracting from the summation the terms that are not depth-dependent, and using the fact that the sum of two phasors can be rewritten as a single one. This results in a condensed expression for the complex, balanced signals:

$$\begin{aligned} \tilde{S}_I(k) &= A_I(k)e^{i\Omega_I(k)}\sum_m C_m e^{i\theta_m} \\ \tilde{S}_{II}(k) &= A_{II}(k)e^{i\Omega_{II}(k)}\sum_m C_m e^{i\theta_m} \end{aligned} \quad , \tag{9.4}$$

where the $A_{I/II}$ and $\Omega_{I/II}$ are wavelength-dependent terms describing the amplitude and phase of the term in square brackets in Eq. 9.3, and C_m is proportional to the amplitude reflectivity ($r_m = \sqrt{R_m}$) of the reflector at depth Δz_m. The terms in the summation represent the interference signal unaltered by the demodulation circuit, which is identical in both channels. The two complex signals $\tilde{S}_I$ and $\tilde{S}_{II}$ will only differ from system contributions allowing for a definition of an amplitude ratio $\beta(k) = A_I/A_{II}$ and an overall phase offset $\Delta\phi(k) = \Omega_{II} - \Omega_I$.

For an ideal demodulation system with perfectly balanced power separation (all T_{Sn} and T_{Rn} being equal) as well as perfect phase characteristics ($\phi_n = (n-1)\cdot\pi/2$), the amplitudes of $\tilde{S}_I$ and $\tilde{S}_{II}$ are equal and the phase offset exactly equal to $\pi/2$. As such, the measured signals are in perfect quadrature, such that $S_R = \mathfrak{Re}\{\tilde{S}_I\} = S_I$ and $S_Q = \mathfrak{Re}\{\tilde{S}_{II}\} = S_{II}$. The measured signals can therefore directly be used in Eq. 9.1 to reconstruct the complex signal. However, in the non-ideal case, the perfect quadrature must first be reconstructed following Eq. 9.5 [74, 384]:

$$S_Q(k) = \frac{\beta(k)\cdot S_{II}(k) - \cos\Delta\phi(k)\cdot S_I(k)}{\sin\Delta\phi(k)}, \tag{9.5}$$

while still using $S_R = S_I$. A complete derivation of this equation is provided in Appendix 9.6.2. When computing the values of β and $\Delta\phi$, it is crucial to avoid flipping the terms in the amplitude ratio and the phase difference. While the definition of channel I and II is arbitrary, it is important to remain consistent once the each detection channel has been assigned a label.

Equation 9.5 requires that $\beta(k)$ and $\Delta\phi(k)$ be known. In the past, these values have been evaluated by measuring the transmission and phase properties of the demodulation circuit separately [74, 384] or through optimization routines that converge on the values producing the highest extinction of the mirror artifact [386]. Given Eq. 9.4, we propose that $\beta(k)$ and $\Delta\phi(k)$ can be determined directly from a simple mirror measurement. Indeed, the phase and amplitude of the two real measured signals can be recovered using a Hilbert transform. Amplitude vectors can then be divided by one another to obtain β, while phase vectors can be subtracted to get $\Delta\phi$. It is worth mentioning that computing the amplitude and phase of the measured signals does not allow the extraction of the absolute transmission and phase characteristics of the demodulation circuit (i.e., variables T_{Rn}, T_{Sn}, and ϕ_n in Eq. 9.2). Fortunately, the absolute values are not necessary for the proposed method.

9.2.2 RF-errors

In 2015, Siddiqui et al. [386] identified *RF-errors*: a second source of errors in the reconstruction of the quadrature signal. These errors are specific to swept-source OCT as they originate in the temporal encoding of the spectral information and all associated distortions. Such RF-errors include fiber or electrical cable length differences between the two channels,causing one signal to be delayed relative to the other. Other variations include the frequency response of all electronic components in the detection circuit, such as the detectors, filters, and the data acquisition card. Each of these effects will generate frequency and, therefore, depth-dependent amplitude and phase variations, which will affect the computed values for β and $\Delta\phi$. It is therefore necessary to expand Eqs. 9.2–9.5 to incorporate the axial dependence. Failing to account for these variations will result in calibration vectors only valid at the specific depth at which they were computed. It is important to note that the terms *RF-errors* and *spatial errors variations* are used interchangeably throughout this manuscript. In the time-domain (or equivalently, in k-space), the impact of the various electronic components can be described as a series of convolutions of the original signal by the impulse responses, $h_i(t)$, of each element:

$$\tilde{S}_I'(t) = \left(\left(\left(\tilde{S}_I(t)\right) * h_1(t)\right) * h_2(t)\right) * \ldots \tag{9.6}$$

Using the convolution theorem, it is convenient to describe the signal in Fourier domain (i.e., in frequency- or z-space), where the chain of convolutions becomes a simple multiplication of the elements transfer functions, $\mathcal{F}\{h_i(t)\} = H_i(f)$ and $H_i(f) \leftrightarrow H_i(z)$. All the transfer functions can then be grouped into a single phasor accounting for both amplitude and phase variations:

$$\mathcal{F}\{\tilde{S}_I'\} = \mathcal{F}\{\tilde{S}_I\} \cdot H_1(z) \cdot H_2(z) \cdot ... = \mathcal{F}\{\tilde{S}_I\} \cdot \alpha_I(z) e^{i\omega_I(z)}, \tag{9.7}$$

where $\alpha_I(z)$ and $\omega_I(z)$ are the depth-dependent amplitude and phase variations, respectively. A similar expression can be derived for the second channel. Now let us consider the case of a single perfect reflector in the sample arm (i.e., a mirror). In this case, the summation in the expression of the complex, balanced signals (Eq. 9.4) can be removed, and a single complex exponential remains. The FT of this signal becomes a complex peak, $\tilde{\gamma}(z-\Delta z)$, centered around the position of the reflector, Δz. Inserting this expression of the peak into Eq. 9.7, we obtain:

$$\mathcal{F}\{\tilde{S}_I'\} = \tilde{\gamma}(z-\Delta z) \cdot \alpha_I(z) e^{i\omega_I(z)}, \tag{9.8}$$

which is simply the interference signal multiplied by the system's transfer function. Due to the Dirac-like nature of the axial point-spread function (PSF), the primary contribution of the transfer function will be at the depth corresponding to the center of the interference peak. Operating under this assumption that the signal peak is Dirac-like (i.e. very narrow and negligible everywhere except at the center of the peak), we can approximate the signal in each channel as:

$$\begin{aligned} \tilde{S}_I'(k) &= A_I(k) e^{i\Omega_I(k)} C e^{i\theta} \cdot \alpha_I(\Delta z) e^{i\omega_I(\Delta z)} \\ \tilde{S}_{II}'(k) &= A_{II}(k) e^{i\Omega_{II}(k)} C e^{i\theta} \cdot \alpha_{II}(\Delta z) e^{i\omega_{II}(\Delta z)} \end{aligned} . \tag{9.9}$$

Qualitatively, we can understand this approximation as the fact that the interference signal of a single reflector is a pure (single-frequency) sinusoid. Therefore, it will only experience a constant amplitude modulation and phase delay due to the system's frequency response. This approximation is crucial to the proposed method as it enables the direct measurement of the depth-dependence of both β and $\Delta\phi$. The initial expressions for the amplitude ratio and the phase offset between the two channels can now be adapted to incorporate the z-dependence:

$$\beta(k,z) = \frac{\|\tilde{S}_I'\|}{\|\tilde{S}_{II}'\|} = \underbrace{\frac{A_I(k)}{A_{II}(k)}}_{\beta_k} \cdot \underbrace{\frac{\alpha_I(z)}{\alpha_{II}(z)}}_{\beta_z}; \tag{9.10}$$

$$\Delta\phi(k,z) = \measuredangle\tilde{S}'_{II} - \measuredangle\tilde{S}'_{I} = \underbrace{[\Omega_{II}(k) - \Omega_{I}(k)]}_{\Delta\phi_k} + \underbrace{[\omega_{II}(z) - \omega_{I}(z)]}_{\Delta\phi_z}. \tag{9.11}$$

Obtaining the parameters β and $\Delta\phi$ from multiple mirror measurements located at different axial positions can simultaneously inform us on the chromatic and spatial (RF) variations of the demodulation circuit. The spatial variations between the two signals can then be corrected by simply multiplying $\tilde{S}''_{II}$ by the phasor describing the relative difference between the transfer functions:

$$\tilde{S}''_{II} = \mathcal{F}^{-1}\left\{\mathcal{F}\{\tilde{S}'_{II}\} \cdot \beta_z \cdot e^{-i\Delta\phi_z}\right\}. \tag{9.12}$$

The corrected signal, $\tilde{S}''_{II}$, shares its axial dependence with $\tilde{S}'_{I}$. As such, the spatial dependence will be removed from β and $\Delta\phi$, and a unique set of chromatic correction vectors can be defined for all axial positions (β_k and $\Delta\phi_k$). Finally, the perfect quadrature component, S'_Q, which accounts for both spatial and chromatic effects, can be reconstructed using Eq. 9.5, with S_I and S_{II} replaced with S'_I and S''_{II}:

$$S'_Q = \frac{\beta_k \cdot S''_{II} - \cos\Delta\phi_k \cdot S'_I}{\sin\Delta\phi_k}. \tag{9.13}$$

Here, S'_I corresponds to the real-valued, *unaltered* signal in channel I, while S''_{II} is the real, *corrected* signal in channel II, derived from the measured signal S'_{II} using Eq. 9.12. This corrected quadrature signal can then be, in turn, used in Eq 9.1 to reconstruct the corrected complex interference signal following:

$$\tilde{S} = S'_I + i \cdot S'_Q. \tag{9.14}$$

Finally, it should be noted that the calibration vectors extracted by this protocol will only be valid for a given set of acquisition parameters, such as the A-line rate, number of samples per A-line, sampling rate, spectral bandwidth etc. Varying any of these parameters affects the pixel to wavelength correspondence within an A-line as well as characteristics of the imaging range such as physical pixel size and total imaging range. As such, previously obtained correction vectors will not be compatible with the signal obtained in the new configuration.

9.3 Methods

9.3.1 FR-OCT system description

The proposed calibration method was experimentally validated on the setup depicted in Fig. 9.1, a swept-source OCT system centered at 1550 nm. We utilize a linear-in-wavenumber swept laser source (Insight Akinetic Swept Laser, Insight Photonic Solutions, USA) with a spectral bandwidth of 80 nm, variable-sweep rate and an average output power of 10 mW. The source output was further increased by an amplifier (BOA, Thorlabs, USA) to 75 mW. Laser light is separated into the sample and reference arms using a 90/10 fiber optic coupler. Light backscattered in both arms is re-directed towards an interferometer using fiber circulators. In this work, the selected interferometer design is a Mach-Zehnder terminated with a 2×4 optical hybrid (COH24, Kylia, France). The component performs both the interferometric re-combination of the sample and reference signals, as well as the quadrature demultiplexing. Demultiplexing is performed using an internal, free-space, polarization-based scheme to generate four output signals with $\pi/2$ offsets. The $\pi/2$ increments in phase offset are practical as signals of opposite sign (π phase shift) can be measured with balanced detection, thereby removing DC signals and common noise. While we demonstrate the method on this setup, the theoretical framework may be extended to other polarization-based methods as well as N×N fused or integrated optical hybrids, provided $N > 2$. The output signals of the two balanced detectors (BDP-1, Insight Photonic Solutions) are connected to a dual-channel, high-speed digitizer for acquisition of the measurement data (ATS9360, Alazar Technologies, Canada). Measurements were performed using in-house LabView software (LabView, National Instruments, USA), and data analysis was carried out in MATLAB (MATLAB, Mathworks, USA). All experimental data and processing scripts are available in the supplementary materials, in Code 1 and Dataset 1 specifically (see Refs. [387, 388]).

9.3.2 Complex signal reconstruction — practical implementation

The theory outlined in the previous section predicts that it is possible to reconstruct the perfect quadrature signal, thereby achieving complete extinction of the mirror artifact. In practice, however, several factors such as system noise, mechanical or thermal instabilities, numerical errors or approximations, and measurement errors affect the end result. As such, given the extremely high precision requirements necessary to achieve extinctions ≥ 60 dB, enhanced attention to detail is necessary during data acquisition and processing. Figure 9.2 presents the practical steps that should be performed in order to correctly im-

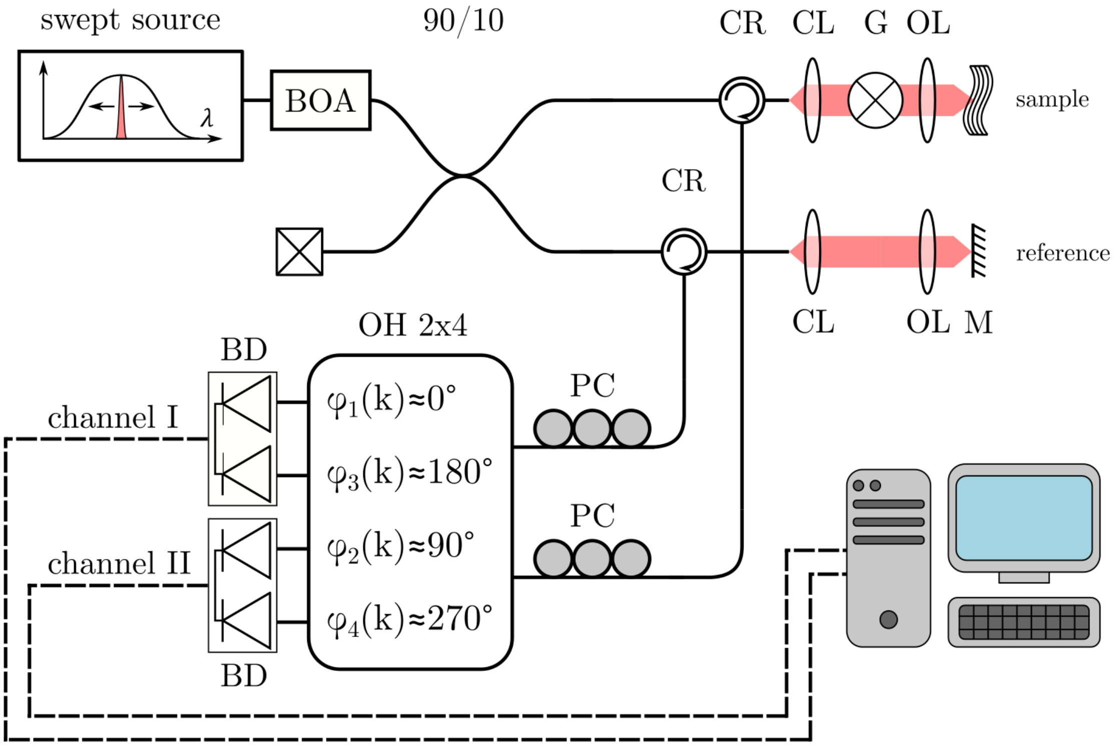

Figure 9.1 Experimental setup: **CR** fiber circulator, **CL** collimator lens, **G** galvo-scanner, **OL** objective lens, **M** mirror, **PC** polarization controller, **OH** optical hybrid, **BD** dual balanced detector, **BOA** booster optical amplifier. Solid lines are optical fibers and dashed lines are electrical cables.

plement the proposed method and achieve optimal mirror artifact extinction.

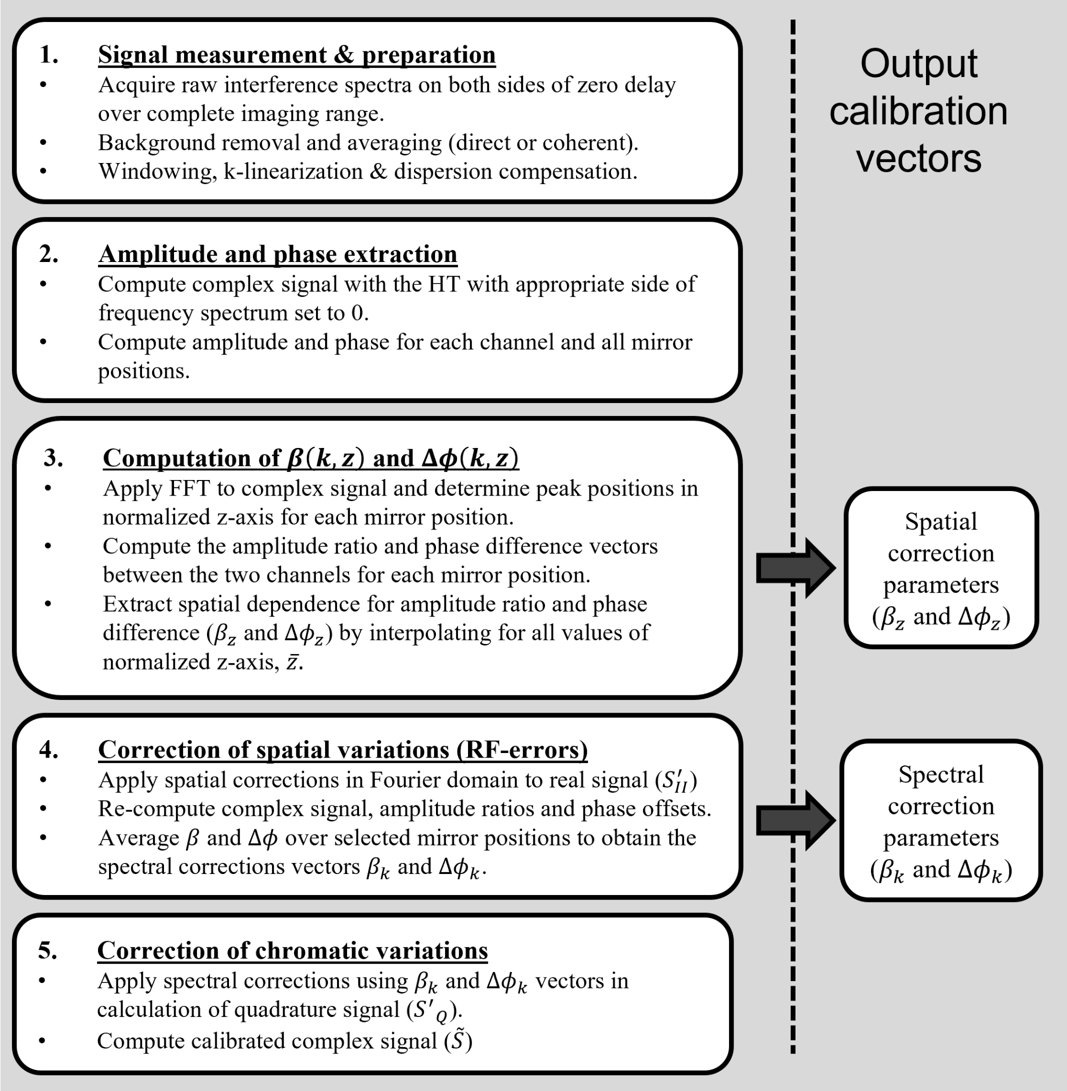

1. **Signal measurement & preparation**
- Acquire raw interference spectra on both sides of zero delay over complete imaging range.
- Background removal and averaging (direct or coherent).
- Windowing, k-linearization & dispersion compensation.

2. **Amplitude and phase extraction**
- Compute complex signal with the HT with appropriate side of frequency spectrum set to 0.
- Compute amplitude and phase for each channel and all mirror positions.

3. **Computation of $\boldsymbol{\beta(k,z)}$ and $\boldsymbol{\Delta\phi(k,z)}$**
- Apply FFT to complex signal and determine peak positions in normalized z-axis for each mirror position.
- Compute the amplitude ratio and phase difference vectors between the two channels for each mirror position.
- Extract spatial dependence for amplitude ratio and phase difference (β_z and $\Delta\phi_z$) by interpolating for all values of normalized z-axis, $\bar{z}$.

Spatial correction parameters (β_z and $\Delta\phi_z$)

4. **Correction of spatial variations (RF-errors)**
- Apply spatial corrections in Fourier domain to real signal (S'_{II})
- Re-compute complex signal, amplitude ratios and phase offsets.
- Average β and $\Delta\phi$ over selected mirror positions to obtain the spectral corrections vectors β_k and $\Delta\phi_k$.

Spectral correction parameters (β_k and $\Delta\phi_k$)

5. **Correction of chromatic variations**
- Apply spectral corrections using β_k and $\Delta\phi_k$ vectors in calculation of quadrature signal (S'_Q).
- Compute calibrated complex signal ($\tilde{S}$)

Figure 9.2 Flowchart of the calibration process. The box numbers correspond to the subsection numbers in Section 9.3.2 of this manuscript.

Signal measurement and preparation

All measurements for the calibration procedure are performed using a mirror as the reflector in the sample arm. As explained in Section 9.2.2, each mirror position provides only the relative difference in the frequency response of the two channels at the position at which the measurement is performed. As such, it is necessary to perform measurements across the entire intended imaging range (i.e., on both sides of zero-delay). Additionally, these measurements couple well with calibration measurements necessary for k-linearization and dispersion compensation [305]. The total number of measurements at different axial positions should be sufficient to capture oscillations in the transfer function. A larger number of measurement points will also enhance the robustness of the numerical fits performed in this process. The frequency response of the various electronic components (detectors, filters, or data acquisition cards), usually specified in datasheets, may provide insight into the expected behavior of the overall transfer function. Finally, the exact spacing between measurements is not critical, as the method does not require knowledge of the absolute axial position, only the normalized one, which can be obtained by fitting the processed peak. Non-uniform sampling in depth (e.g., denser around depths with expected oscillations in the transfer function) is also acceptable and even beneficial as it allows for a more accurate interpolation.

While measurements can be performed by adjusting the length of either arm of the interferometer, it is usually simpler to alter the length of the reference arm. Extending the collimated segment of the reference arm rather than moving the sample mirror leaves the sample mirror in the focal plane of the objective lens. This will ensure a higher and more stable signal intensity for all measured positions. It is interesting to note that the protocol can function when moving the sample mirror, as both channels will experience the same signal fluctuations due to the confocal beam parameter. However, measurements far outside the Rayleigh range will have a lower SNR, which may induce errors in calculating the correction vectors.

The proposed method relies on using the HT to compute the complex analytical signal, from which phase and amplitude information can be extracted. This transform is highly sensitive to DC offsets. Proper background removal should be performed on all measurements, where the background signal should be measured once for each mirror position. Further DC removal can be achieved by subtracting the mean from the signal. In standard OCT systems, high-pass filtering may be performed to remove the residual low-frequency signal. This is not advised in FR-OCT as it will result in an attenuated band around zero-delay (i.e., in the middle of the measurement range).

In this work, phase and amplitude information is extracted directly from calibration measurements. The SNRs associated with these values are, therefore, directly proportional to that of the measurements. As such, the proposed method cannot result in extinction ratios exceeding the SNR of the calibration measurement (see Appendix 9.6.1 for more detail). Consequently, performing coherent averaging of multiple A-lines is highly recommended to maintain peak amplitude while lowering the noise floor. Coherent averaging is achieved by correcting the phase drift and jitter that may occur between A-lines in

SS-OCT prior to computing the mean intereference signal. In this work, we followed the averaging method outlined in Ref. [389]. A crucial point is that, for each A-line, the same phase correction must be applied to both channels of the demodulation circuit to preserve their relative phase [386]. The proposed method will fail if coherent averaging is applied to the two channels independently of one another. Coherent averaging is also necessary in this instance to enable visualization of attenuation greater than 60 dB, else the mirror artifact is hidden below the noise floor.

Finally, the calibration measurements must be properly k-linearized, either through hardware methods or through numerical resampling, prior to their use in the quadrature correction. Non-linear k-sampling may introduce phase and amplitude variations comprising mixed terms that depend on both wavenumber and depth. In such a scenario, it would no longer be possible to separate the chromatic and axial contributions, as depicted in Eqs. 9.10 and 9.11. This would also undermine the approximation in Eq. 9.9 as non k-linear sampling results in broader and, more importantly, a depth-dependent axial point-spread function. However, numerical re-sampling may be performed prior to implementing the proposed method, without any impact on overall performance. It is not mandatory to compensate for dispersion on the calibration measurement prior to using them in the quadrature correction as the dispersion mismatch will result in a depth-independent, non-linear phase term in the interference signal [305] that is identical in both arms of the demodulation circuit. However, performing dispersion compensation is recommended as it will yield calibration measurements with higher SNR. Furthermore, dispersion-compensated peaks will be narrower, supporting the approximation required for the validity of Eq. 9.9. It is also interesting to note that phase-stability is not a prerequisite for the successful implementation of this method. Indeed, phase instabilities in the system will be equally represented in both detection channels and, therefore, will not affect the corrections.

Computing analytical signal & extracting amplitude and phase

We compute the complex analytical signal for each mirror position and channel, typically using the HT. Many different numerical implementations of the HT exist, which perform a different number of operations. Strictly speaking, the HT should return an identical signal phase-shifted by $\pi/2$. The analytical signal can then be reconstructed using the input signal as the real component and the HT as the imaginary part. However, many implementations of the HT (e.g., in Matlab) directly return the analytic representation of the input signal by applying an FT on the input signal, setting all negative frequency components to 0, and then performing the inverse FT. This approach, therefore, assumes that the true signal peak is always located on the positive side of zero-delay. For the calibration, this should be inverted for peaks measured on the negative side of zero-delay, such that the analytical signal has all positive frequency components set to zero. This manipulation is required during the calibration only, when the position of the mirror is known, and not during subsequent imaging. Once the complex analytical signal is obtained, the amplitude and phase at each sample point can be obtained using standard identities. Care should be taken to employ the appropriate inverse tangent for phase extraction (typically called *atan2*) as well as proper angle unwrapping to avoid discontinuities in the phase vector. Such discontinuities will cause significant errors in subsequent fitting and cause the method to fail.

Computing $\beta(k,z)$ and $\Delta\phi(k,z)$

The correction vectors $\beta(k,z)$ and $\Delta\phi(k,z)$ are defined as a function of wavenumber, k, and axial position, z. In the spatial dimension, however, they are only sampled at the positions at which mirror measurements are performed, Δz_m. Interpolation is therefore necessary to reconstruct the correction vectors at all axial positions. First, to establish the positions at which measurements were obtained, it is necessary to evaluate the magnitude of the FFT of the interference signal for each channel. This can be performed on the complex analytical signals computed in the previous step. When the analytical signals are properly generated, peaks should appear only on the correct side of zero-delay. Gaussian fitting (or a simple search for the maximum value) may be used to extract the exact position of the peak. Rather than the absolute axial position in millimeters, it is convenient to use a normalized z-axis, defined relative to the number of samples, N, in the spectral interferogram as follows:

$$\bar{z} = \left\{ \begin{array}{ll} \left[-\frac{\pi}{2}; \frac{\pi}{2} - \frac{\pi}{N}\right] & \text{for } N \text{ even} \\ \left[-\frac{\pi}{2}; \frac{\pi}{2}\right] & \text{for } N \text{ odd} \end{array} \right\} . \tag{9.15}$$

Once the peak position is determined, the values of β and $\Delta\phi$ can be obtained for all k-values by simply computing the ratio of amplitudes and the difference of phases as described in Eqs. 9.10 and 9.11. A simple mistake to avoid is the inversion of the channels when computing these values. Furthermore, we recommend fitting the extracted values of β and $\Delta\phi$ with respect to wavenumber and/or smoothing with a low-pass filter to reduce noise. Polynomial and smoothing spline fitting were tested and found appropriate provided adequate selection of number of terms or smoothing parameter. Centering and scaling data prior to polynomial fitting may be helpful to increase fit stability and reduce extreme oscillations towards the edges of the vectors. For both fitting methods, we also padded the signal with mirror copies of itself to further stabilize the behavior of the fits towards the edges. Extreme values very close to the edges, such as the one indicated by a red arrow in Fig. 9.3(b), should also be excluded from the fitting process.

Once the β and $\Delta\phi$ vectors have been extracted for all mirror positions, the spatial correction vectors β_z and $\Delta\phi_z$ can be obtained by fitting across all $\bar{z}$. From these fits, β_z and $\Delta\phi_z$ values can be defined for all points of the normalized z-axis, $\bar{z}$. Similar to previous fits, both polynomial and spline interpolation may be used provided they adequately capture the oscillations of the RF correction parameters. In order to perform the z-dependent fitting procedure, it is necessary to select a single wavelength component. In theory, the choice of this wavelength does not influence the performance of the calibration method. However, selecting edge values such as the first or last wavelength points may lead to erroneous results due to fit instabilities in the previous steps. As such, we recommend using the central wavelength. Furthermore, to account for the constant chromatic contribution present in each parameter (β_k and $\Delta\phi_k$ is Eqs. 9.10 and 9.11, respectively), it is necessary to normalize β_z and $\Delta\phi_z$. We therefore normalize the amplitude to 1 and the phase difference to 0 at $z = 0$. The phase normalization, in particular, is essential as the spatial correction (Eq. 9.12) will otherwise remove the $\pi/2$ phase offset between the two channels leading to numerical instabilities when evaluating Eq. 9.13. Finally, it is important to exclude mirror measurements located at zero-delay. Such measurements may yield unstable phase and amplitudes values, such as the one indicated by a blue arrow in Fig. 9.3(b), which can disrupt fitting.

Correcting spatial variations

Once the normalized values of β_z and $\Delta\phi_z$ are known for all $\bar{z}$, we apply the correction to the second channel described in Eq. 9.12. This correction removes the spatial variations between the two channels leaving only chromatic variations. Following the same process as outlined above, the $\beta(k,z)$ and $\Delta\phi(k,z)$ can be determined for each mirror position. Again, we recommend fitting or low-pass filtering of some kind along the wavelength dimension to reduce noise. The resulting curves should be near-identical for all mirror positions and can be averaged to produce the chromatic corrections vectors β_k and $\Delta\phi_k$. Errors may occur during the various fitting steps or in the computation of the complex signals for positions very close to zero-delay or towards the edges of the imaging range.

As such, it is sometimes necessary to exclude these points from the averaging procedure used to calculate the final chromatic correction vector.

Correcting chromatic variations

By applying the chromatic correction, the ideal quadrature signal, S'_Q, can be obtained following Eq. 9.13. In this equation, the β_k and $\Delta\phi_k$ vectors used should be those obtained in the previous step (i.e., after spatial correction) and not the ones obtained in step 3 of the method (see Fig. 9.2 and Section 9.3.2). Finally, with the measured signal in channel I, S'_I, and the ideal quadrature signal, S'_Q, the complex interference signal can be reconstructed, as described in Eq. 9.14.

9.4 Results

9.4.1 Calibration of demodulation circuit

To validate the calibration procedure, mirror measurements were performed across the entire imaging range (on both sides of zero-delay: ± 30 mm). Different path lengths were obtained by mounting the reference arm on a motorized stage and measuring in regular increments of 200 μm, for a total of 311 measurements. For each position, 512 A-scans were coherently averaged to increase SNR. The above protocol was then applied to extract spatial and chromatic correction vectors, presented in Fig. 9.3. Figures 9.3(a) and (b) depict the spatial parameters β_z and $\Delta\phi_z$, while (c) and (d) depict the chromatic parameters, β_k and $\Delta\phi_k$, before (in blue) and after (in red) correcting for the spatial dependence. The final chromatic correction vectors correspond to those obtained after spatial corrections. In sub-figures (a) and (b) the offset between the raw and fitted data is caused by the normalization. The blue and red arrows in Fig. 9.3(b) highlight erroneous extreme values at zero-delay and at the edge, respectively. These artifacts were excluded from fitting as reflected by the smooth red curve. It is visible in sub-figures (c) and (d) that all extracted values of β_k and $\Delta\phi_k$ are near-identical after correction of spatial dependence. The full calibration procedure to extract the correction parameters as well as figures illustrating the intermediate steps are presented in a MATLAB script, available in the supplementary materials [387].

The graphs presented in Fig. 9.3 demonstrate the necessity of the proposed method. The correction curves obtained after correction of spatial errors (green line) in sub-figures 9.3(c) and (d) show the chromatic difference between the two channels of the system. These differences can be associated with the chromatic behavior of the optical hybrid as well as differences in the spectral response of the two supposedly identical detectors. As neither of these chromatic effects can be easily adjusted, numerical post-processing appears to be the most viable solution. Sub-figures 9.3(a) and (b) highlight the residual spatial/RF-errors despite extensive optimization during system construction. Indeed, the output fiber lengths of the optical hybrid were matched to within path length differences smaller than 25 μm by the device manufacturer. The electrical cable lengths were matched to within a few millimeters and identical detectors were used. While parameters such as fiber- or electrical cable length can be adjusted, this can be very impractical, especially for millimeter-scale changes. Other parameters such as the overall frequency response of the detectors, electrical cables and data acquisition card cannot be adjusted. Again, numerical adjustments in post-processing are advantageous.

Using the calibration vectors presented in Fig. 9.3, the corrected complex signal was then reconstructed for each position. Figure 9.4 illustrates the resulting real and residual peaks for a few peaks and compares the result of (a) standard processing (no complex reconstruction), (b) direct reconstruction of the complex signal, $\tilde{S} = S_I' + i \cdot S_{II}'$, (c) calibrated reconstruction of the complex signal (this method), $\tilde{S} = S_I' + i \cdot S_Q'$. Figures 9.4(a-c) depict mirror peaks obtained with coherent averaging, while (d) shows the calibrated complex reconstruction applied to measurements without coherent averaging. Visualization 1 in the supplementary materials (see Ref. [390]) presents an animated version of Fig. 9.4, with the results at all 311 measured positions (at both positive and negative positions).

After complex signal reconstruction, the mirror artifact extinction coefficient was computed as the ratio of the peak height of the real peak over that of the residual mirror artifact. The comparison of Figs. 9.4(b) and (c) highlights the improvement obtained from performing a proper calibration of the passive demodulation circuit. Indeed, only approximately 20 dB of mirror artifact reduction is achieved without it. With our method, extinction exceeding 60 dB is achieved up to over 15 mm away from zero-delay. Beyond this range, performance gradually levels off to slightly below 50 dB. It is also interesting to observe that the proposed method fully preserves the peak shapes across the entire imaging range. In Fig. 9.4(d), we can observe that the achieved performance is sufficient to completely suppress the mirror artifact for standard operation of the system, where coherent averaging is not utilized. Finally, it is interesting to note that the complex signal reconstruction results in a signal gain of 6 dB. This gain is observable in Figs. 9.4(b) and (c) compared to Fig. 9.4(a) and can be explained by the fact that all the energy of the mirror peak is returned to the real peak. However, this gain is partially offset by an increase in the noise floor level of 3 dB, due to the incoherent addition of the noise in the

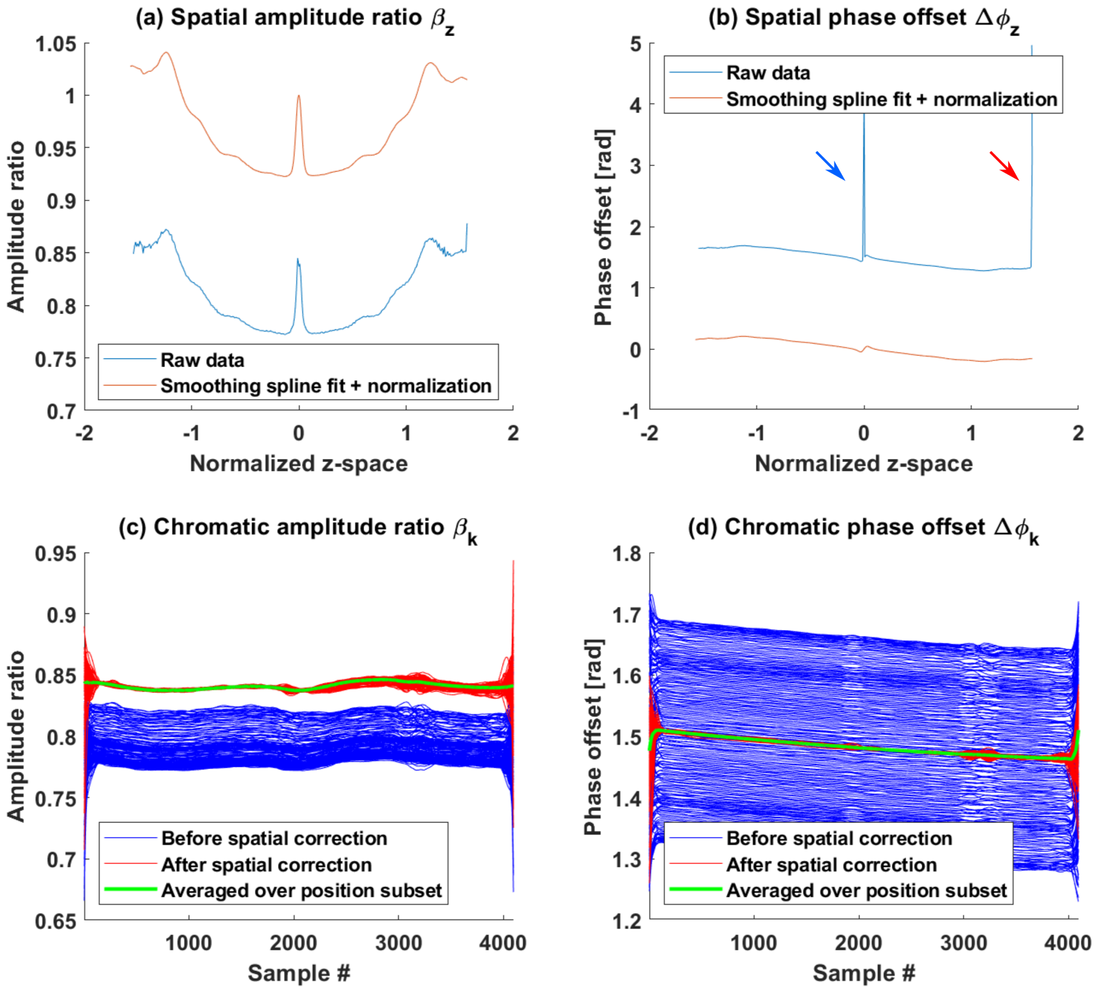

Figure 9.3 Correction vectors extracted using the proposed method. (a) Spatial amplitude ratio, (b) spatial phase offset, (c) chromatic amplitude ratio and (d) chromatic phase offset. Blue and red arrows in (b) indicate erroneous values at zero-delay and at the edge of the vector respectively.

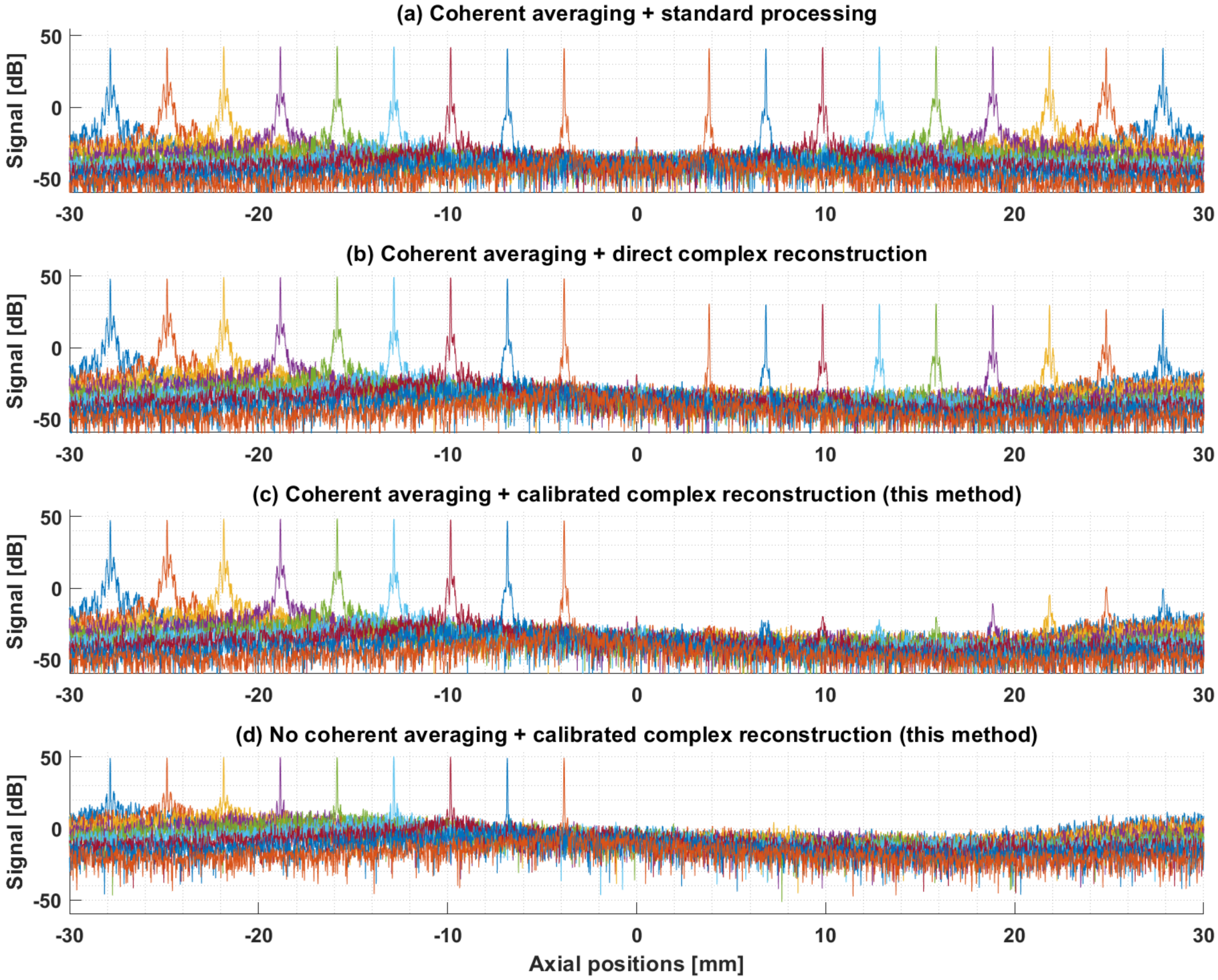

Figure 9.4 Validation of the calibration protocol using mirror peaks a various locations across the imaging range. (a) Baseline with no complex signal reconstruction. (b) Direct reconstruction of complex signal from measured signals with no correction to signals. (c) Reconstruction of complex signal with proposed method. (d) Reconstruction of complex signal with proposed method applied to a single A-line (i.e., the signal without coherent averaging as it would be acquired in standard operation of the OCT system).

two channels. Again, this increase in the noise floor is observable in Figs. 9.4(b) and (c) compared to Fig. 9.4(a). This effect is more noticeable in Fig. 9.8, where the background of the images processed with standard OCT processing (left column) is darker than those processed with some form of complex reconstruction (middle and right columns).

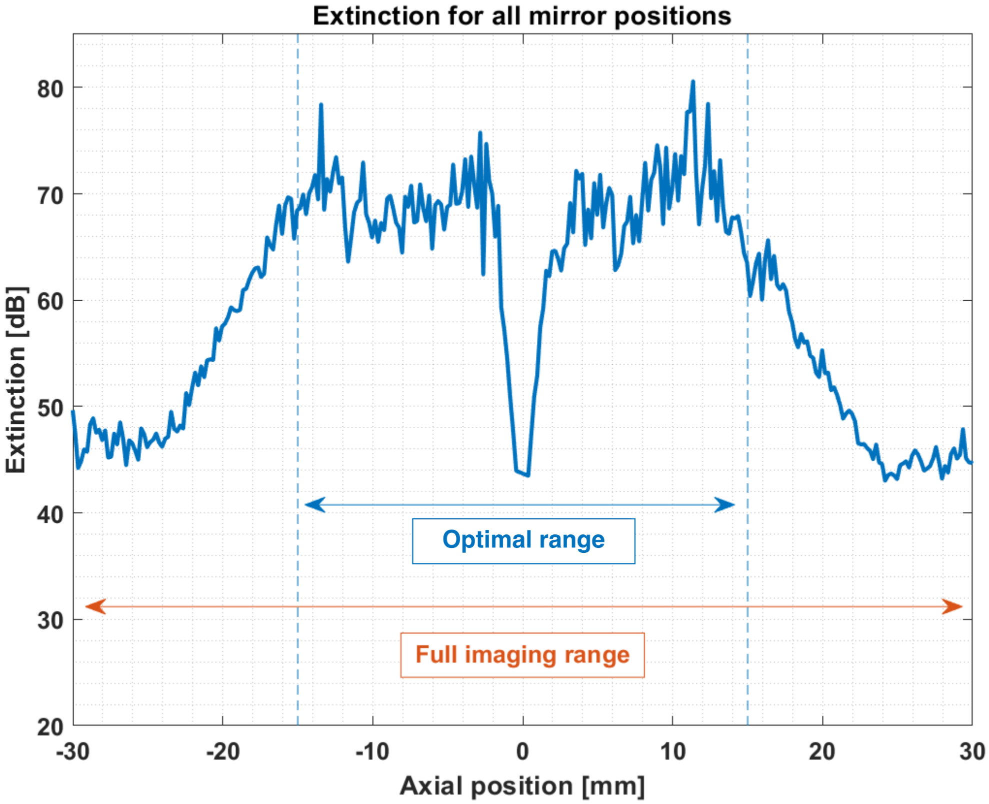

Figure 9.5 Extinction ratio at all 311 mirror positions. Optimal imaging range defined as ± 15. Data corresponds to day 1 in the time series presented in Fig. 9.7. The data points corresponding to zero-delay and one point on either side were omitted.

The exact extinction ratio achieved at each position is presented in Fig. 9.5. In this figure, we distinguish between the ± 15 mm range, where high performance is achieved, and the full imaging range. Two factors can explain the dip in performance around zero-delay. The first effect is an actual loss in performance very close to zero-delay. This can be attributed to the fact that the depth-dependent correction parameters cannot be measured directly at zero delay due to the fitting instabilities described in the previous section. Therefore, the values close to zero-delay are obtained through interpolation, potentially resulting in minor inaccuracies. The second effect is the overlap between the region's real and residual mirror peaks. In this scenario, the side lobes of the PSF of the real peak will contribute to raising the residual peak, thereby reducing the extinction ratio. The drop in extinction performance on the sides of the imaging range (i.e., in the zone outside of the optimal imaging range) can be explained in a similar manner. It can be observed in Fig. 9.4 that the noise floor is not constant for all peak positions. The sides of the sub-figures show that the noise floor level varies by up to 25 dB, both in the averaged and non-averaged cases. For a constant residual peak height *relative to the noise floor*, raising the latter will effectively reduce the extinction ratio by the same amount. This observation suggests that the dips outside of the optimal range in Fig. 9.5 are artificial and that the proposed method works almost equally well across the entire imaging range. This position-dependent noise floor is not caused by either the proposed method or the coherent averaging. Indeed it is visible in Fig. 9.4(a) that the effect also appears in A-lines processed without our method. Furthermore, the effect is also apparent in Fig. 9.4(d), where no coherent average was applied. Finally, we note that, for all practical intents and purposes, the achieved extinction is suitable for standard imaging because even the reduced performance on the edges effectively removes the mirror artifact for standard operation of the OCT system (see Fig. 9.4(d)).

9.4.2 Fit stability analysis

We also investigated the stability of the proposed method against the density of the axial sampling (i.e., the number of measurements used in the calibration). Figure 9.6 presents the achieved extinction ratios for different numbers of measurements in the form of a swarm chart, in which each point corresponds to the extinction ratio at one mirror position. In this figure, the data points included in the optimal range are blue, while those outside are orange. The full imaging range includes both types of points. Finally, for each cluster, the relative occurrence of extinction ratios is encoded into the width of the point cloud. As such, a wider cluster indicates a higher number of data points close to a certain extinction ratio. The x-axis denotes the axial spacing between mirror positions used to perform the calibration. Increasing this spacing leads to a reduction in the number of measurements used in the calibration. All 311 positions were evaluated to assess the resulting performance. It is apparent that increasing the sampling density (smaller sampling interval) leads to higher extinction ratios, particularly for the optimal range. However, the gain associated with very dense sampling may not be worth the increase in measurement time and complexity, especially if the calibration protocol needs to be repeated over time. Another visible effect is that, as the number of data points decreases, more data points from the optimal range (blue points) appear far below the main cluster. In this instance, these points correspond to the central dip seen in Fig. 9.5. The experimental system used in this work presented a significant feature close to zero-delay in the depth-dependent amplitude and phase parameters (β_z and $\Delta\phi_z$), which was not adequately captured when sampling density was too low. To address this, it is possible to use non-uniform sampling and acquire additional measurements at axial positions where features are present. The method's robustness to non-uniform axial sampling is advantageous as it simplifies the measurement protocol, especially if performed manually rather than with a motorized translation stage.

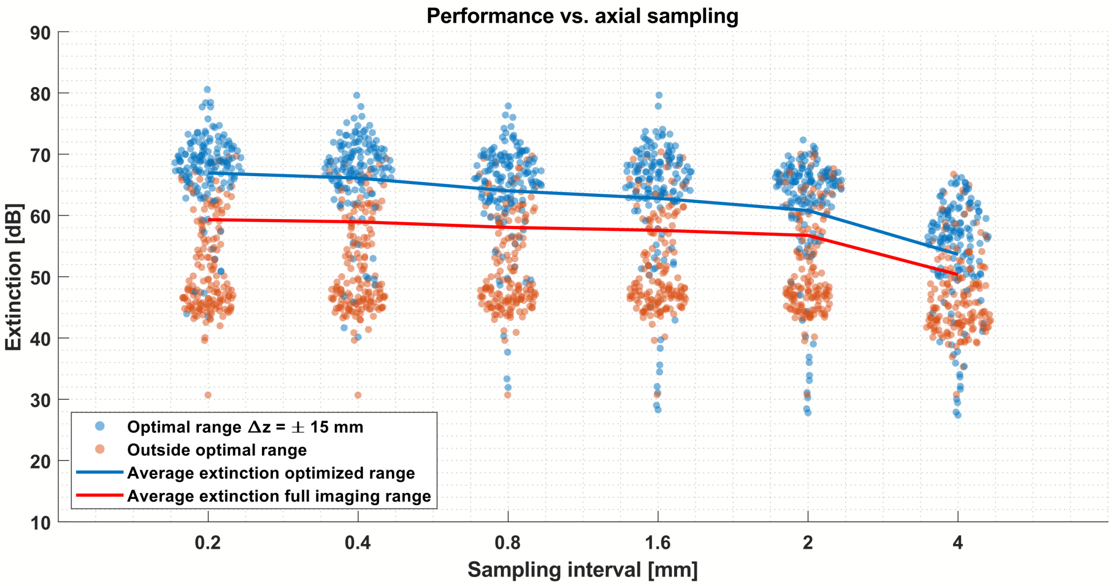

Figure 9.6 Performance of the calibration method vs. axial interval (i.e., the inverse of axial sampling). Decreasing number of sampling points used for calibration, from left to right, corresponding to 311, 155, 78, 39, 31, and 15 axial positions respectively. Average over full imaging range includes data points both in- and outside of optimal range.

9.4.3 Temporal stability analysis

Finally, the temporal stability of our method was assessed to verify how long a set of correction vectors would produce high mirror artifact extinction. Identical datasets of 311 measurement points were acquired over a period of 10 days. Figure 9.7 illustrates three different calibration strategies: (a) full calibration performed every day, (b) calibration parameters extracted on the first day were used at all subsequent time points, and (c) depth-dependent parameters calculated on the first day and chromatic parameters recalculated every day. Figure 9.7(b) shows that performance degrades over time across the entire imaging range. This gradual loss of performance is likely due to the sensitivity of the demodulation circuit to environmental changes such as temperature and humidity, as well as perturbations of the system from vibrations or manipulations during measurements. In line with findings reported by Siddiqui et al. [386], we observed that the depth-dependent vectors were very stable in time, while the chromatic vectors presented more significant variations. As such, it may be sufficient to re-compute the chromatic parameters only, rather than performing the complete calibration method. This implies using β_z and $\Delta\phi_z$ from day one or, in other words, skipping step 3 in the procedure (see Fig. 9.2). Figure 9.7(c) illustrates that this strategy performs only slightly worse than applying the entire procedure, even after ten days. Such a strategy is particularly interesting as it does not require a large number of measurements. Indeed, assuming that the depth-dependent vectors are still correct, only a single measurement at any axial position is necessary to measure the chromatic parameters. In practice, we recommend acquiring a few measurements and averaging the extracted β_k and $\Delta\phi_k$ vectors. This approach would still require significantly fewer measurements than the full protocol and can be performed quickly prior to other measurements. Moreover, as seen in Fig. 9.7(b), even without frequent calibration of the system's correction parameters, an extinction ratio of the mirror artifact peaks of ≥ 40 dB is consistently achieved, which may be sufficient for specific applications. Isolating the optical hybrid and photodetectors from environmental perturbations and immobilizing optical fibers are good practice measures that should improve the stability of the correction parameters over time.

9.4.4 Imaging

Once calibration is performed, correction vectors can be applied to measured data following Eqs. 9.12 through 9.14. To demonstrate this, we imaged a roll of tape at different axial positions. The images resulting from standard OCT processing, direct complex signal reconstruction, and calibrated complex signal reconstruction (from left to right) are shown in Fig. 9.8. The different images were acquired by changing the length of the reference arm so as to maintain the sample in focus. As expected, the images of the tape roll are doubled in the left column (no correction). In the central column (direct complex reconstruction) the mirror artifact is attenuated, but not fully removed. The last column of images on the right shows removal in excess of 45 dB (limited by the dynamic range) obtained with our method (calibrated complex reconstruction), which effectively removes the mirror artifact across the entire imaging range. The extinction of the mirror artifact peaks can also be observed directly in the A-line plots. The insets in the first row of images present a zoomed in view of the tape layers and demonstrate that the axial resolution

(a) Full calibration each day

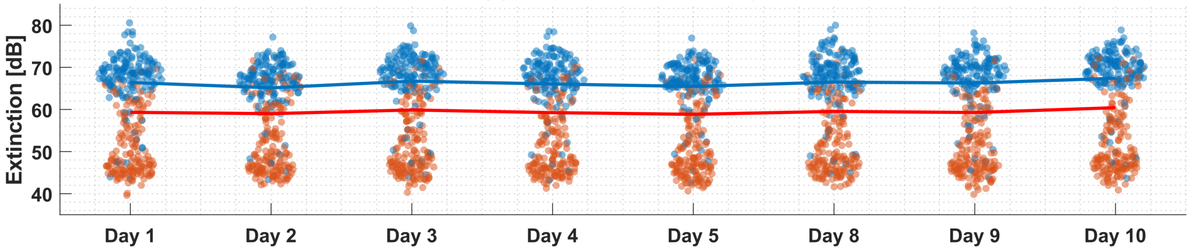

(b) Chromatic and spatial correction from day 1

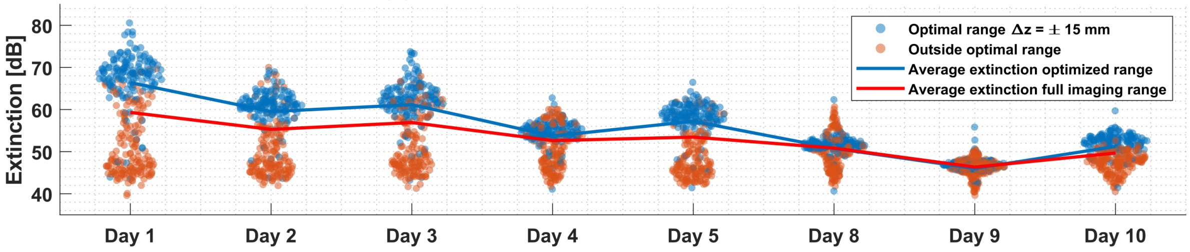

(c) Spatial correction from day 1 + daily chromatic correction

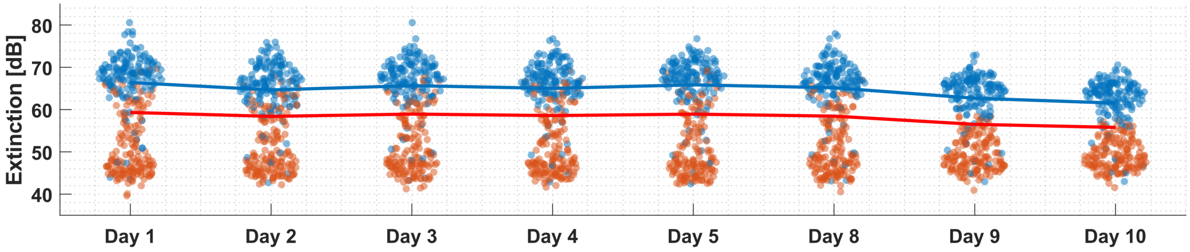

Figure 9.7 Stability of mirror artifact extinction ratio over time. (a) Full calibration (RF and chromatic vectors) performed daily (baseline). (b) Calibration vectors (RF and chromatic) calculated on day 1 and used for all subsequent time points. (c) RF calibration vectors calculated on day 1 and used for all subsequent time points & chromatic calibration parameters re-calculated every day. Average over full imaging range includes data points both in- and outside of optimal range.

of the images is not affected by the reconstruction of the complex signal.

While the calibration protocol may require some time to complete, the correction of the quadrature signal and reconstruction of the complex signal is compatible with real-time imaging applications. Indeed, real-time reconstruction can be achieved at relatively low computational cost as it requires only two additional FFTs on one of the two channels and a few simple arithmetic operations. Furthermore, this cost may be mostly offset by the gain made in numerical dispersion compensation, typically performed by multiplying the signal with a complex phase vector, which also requires two additional FFTs to compute the complex analytical signal from the measured, real signal [305]. In this instance, the calibrated reconstructed signal can be directly multiplied by the dispersion compensation vector. Lastly, to minimize the computational cost in real time application, it is recommended to pre-compute and store in memory several recurring factors such as $\beta_z e^{i\Delta\phi_z}$ in Eq. 9.12 as well as $\beta_k/\sin\Delta\phi_k$ and $\cos\Delta\phi_k/\sin\Delta\phi_k$ in Eq. 9.13.

9.5 Conclusion

In this work, we have described and demonstrated a calibration procedure enabling the numerical correction of imperfect quadrature signals obtained from a passive demodulation circuit. We first outlined a theoretical description of the interference signal produced by a non-ideal demodulation circuit. We then showed that non-ideal behaviors, including chromatic and depth-dependent components, can be summarized into two phasors, one in the wavelength-domain and one in the spatial domain. Both these phasors can be directly measured from mirror measurements at different positions in the imaging range. Once measured, these parameters can be used to correct the measured signal and accurately reconstruct the complex interference signal, resulting in high mirror artifact extinction across the entire imaging range. Furthermore, we investigated the method's stability in time and with respect to axial sampling. We found that dense sampling is beneficial, but only marginally. As such, it is possible to limit the number of sampling points to maintain a reasonable experimental load. Similar to prior art, we found that performance does degrade over time and that this is primarily due to variations in the chromatic error. As such, it is possible to re-measure only the chromatic correction vectors to maintain high performance over a longer period of time without having to repeat the complete procedure.

The proposed method's effectiveness, robustness, and experimental simplicity are also interesting because they open the door for the use of imperfect demodulation circuits to

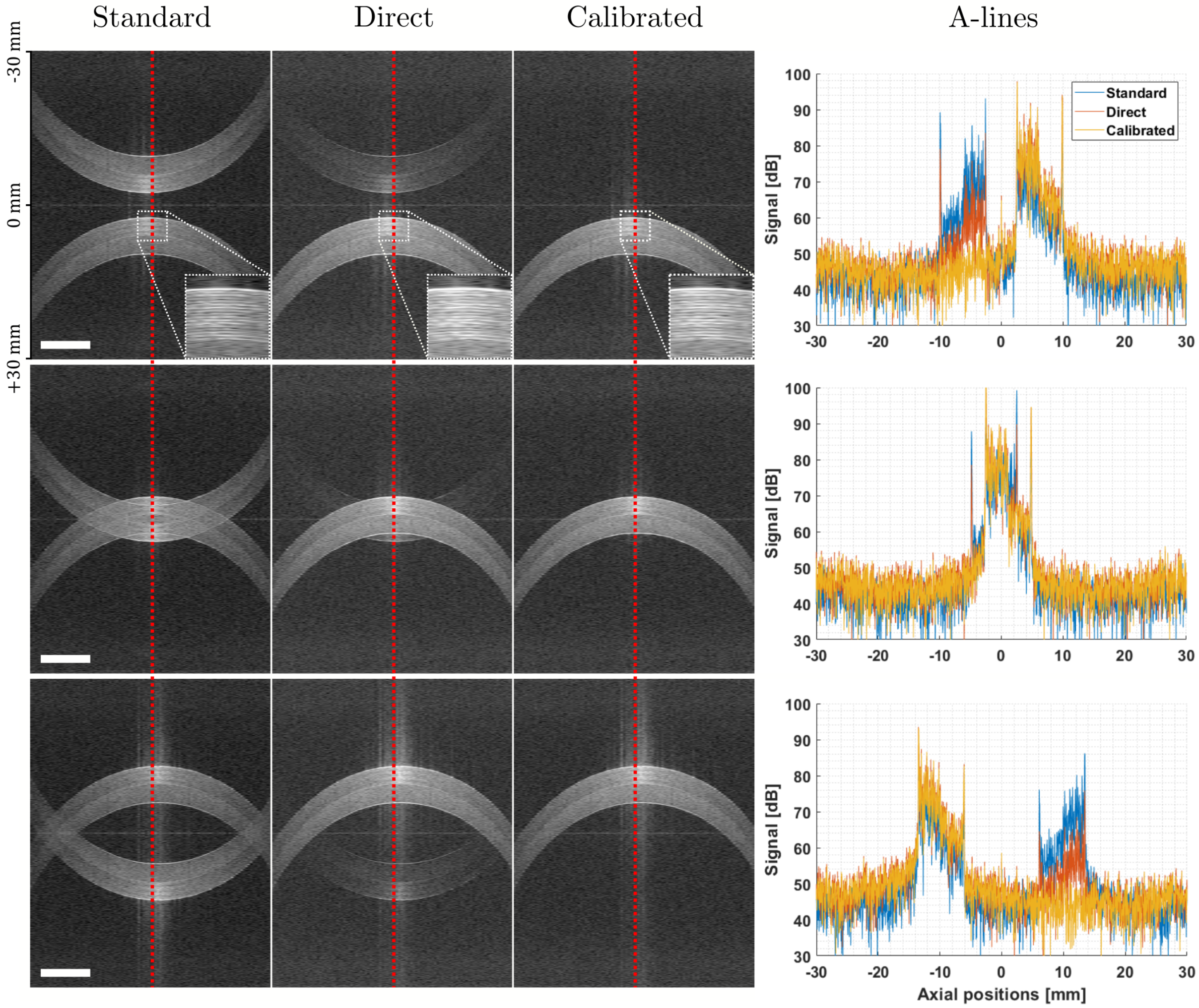

Figure 9.8 Images of a roll of tape at different axial positions. From top to bottom: after, overlapping with, and before zero-delay, respectively. From left to right for each row: standard processing with no complex reconstruction, direct complex reconstruction with no corrections to measured signals, and calibrated complex reconstruction (this method). Scale bars are equal to 5 mm. Dynamic range was purposefully fixed to [30,90] dB to enable the visualization of residual mirror artifacts. The plots on the right side depict the A-lines along the red dashed lines in each row of images. The insets in the top row provide a zoomed in view of the tape layers.

achieve FR-OCT. In particular, broadband $N \times N$ fiber couplers, which are exceedingly hard to manufacture with precisely matched outputs, may become a viable alternative to polarization-based demodulation circuits. Numerical correction of their imperfections may simplify manufacturing and thereby reduce component costs. Fiber-based demodulation comes with all the advantages of fiber optics, including robustness to vibration and other perturbations, laser safety advantages, and compactness. Furthermore, doubling the imaging range may also be beneficial in endoscopy systems as it would grant greater flexibility regarding the total fiber length of probes. It may also assist in moving undesirable back-reflections from micro-optics such as GRIN lenses from the useful imaging range. The extended imaging range can also be used for spatially multiplexed OCT applications in which several scans are acquired simultaneously, to increase overall acquisition speed. Finally, doubling the imaging range through FR-OCT rather than through increasing the sampling frequency and using sources with long coherence lengths provides more flexibility during system design. All these benefits may encourage the adoption of FR-OCT systems in clinical and industrial applications. Outside of the realm of OCT imaging, this method could also be of high interest for quadrature phase-shift keying (QPSK) demodulation in telecommunication systems using multiple wavelength channels per optical fiber.

9.6 Appendix

9.6.1 Accuracy requirement for complex signal reconstruction

Consider S_I and S_{II}, the two simplified signals in quadrature with slightly different amplitudes, $A_I(k)$ and $A_{II}(k)$, and a small phase offset, $\delta\phi(k)$, as described by Eqs. 9.16:

$$\begin{aligned} S_I(k) &= A_I(k) \cdot \cos(2k\Delta z) \\ S_{II}(k) &= A_{II}(k) \cdot \sin(2k\Delta z + \delta\phi(k)). \end{aligned} \tag{9.16}$$

The complex signal, $\tilde{S}$, can be obtained following Eq. 9.17:

$$\tilde{S}(k) = S_I(k) + i \cdot S_{II}(k). \tag{9.17}$$

By substituting Eq. 9.16 into Eq. 9.17 and applying several trigonometric identities it is possible to evaluate the impact of the amplitude and/or phase offsets. For example, in the event where the signal are phase-matched ($\delta\phi = 0$), but vary in amplitude ($A_I \neq A_{II}$), the complex signal becomes:

$$\begin{aligned}\tilde{S}(k) &= A_I\left[\cos(2k\Delta z) + i\cdot\sin(2k\Delta z)\right] + (A_{II} - A_I)\cdot i\cdot\sin(2k\Delta z)\\ &= \underbrace{A_I e^{i\cdot 2k\Delta z}}_{\text{complex signal}} + \underbrace{(A_{II} - A_I)\cdot i\cdot\sin(2k\Delta z)}_{\text{residual peak}}.\end{aligned} \tag{9.18}$$

Similarly, when the signals are equal in amplitude ($A_I = A_{II} = A$) but there exists a small phase offset ($\delta\phi \neq 0$), the complex signal becomes:

$$\begin{aligned}\tilde{S}(k) &= A\cos(2k\Delta z) + i\cdot A\sin(2k\Delta z + \delta\phi)\\ &= A\cos(2k\Delta z) + i\cdot A\left[\sin(2k\Delta z)\cancelto{1}{\cos(\delta\phi)} + \cos(2k\Delta z)\cancelto{\delta\phi}{\sin(\delta\phi)}\right]\\ &= \underbrace{Ae^{i\cdot 2k\Delta z}}_{\text{complex signal}} + \underbrace{i\cdot\delta\phi\cdot A\cos(2k\Delta z)}_{\text{residual peak}}.\end{aligned} \tag{9.19}$$

In both instances, the magnitude of the residual signal is directly proportional to the difference in the amplitudes or to the phase offset. As such, in order to achieve the target 60 dB of mirror artifact extinction, the accuracy of the quadrature signal must be ≤ 0.1% both in amplitude and phase. Such stringent accuracy requirements are extremely difficult, if not impossible, to achieve with standard electrical and optical components, especially when considering their chromatic behavior. As a result, some form of signal processing and associated system calibration are unavoidable for successful passive demodulation.

9.6.2 Derivation for quadrature correction

Equation 9.5 which derives the perfect quadrature relative to S_I can also be derived geometrically. Figure 9.9 illustrates how the ideal quadrature signal, S_Q, can be re-constructed from a linear combination of the two measured signals, S_I and S_{II}. As such, S_Q can be expressed as:

$$S_Q = a\cdot\vec{S}_{II} - b\cdot\vec{S}_I, \tag{9.20}$$

where the values of a and b can be derived trigonometrically, using $\Delta\phi$ and β which can be extracted from measurements as detailed in the main body of this paper. As such, we arrive at:

$$\begin{aligned}a\cdot|S_{II}|\sin\Delta\phi &= |S_I|,\\ a\cdot|S_{II}|\cos\Delta\phi &= b\cdot|S_I|.\end{aligned} \tag{9.21}$$

Solving for a and b:

$$\begin{aligned} a &= \frac{|S_I|}{|S_{II}|}\frac{1}{\sin\Delta\phi} = \frac{\beta}{\sin\Delta\phi}, \\ b &= \frac{a\cdot|S_{II}|\cos\Delta\phi}{|S_I|} = \frac{\cos\Delta\phi}{\sin\Delta\phi}. \end{aligned} \tag{9.22}$$

Finally inserting Eq. 9.22 into Eq. 9.20 we arrive back at Eq. 9.5:

$$\vec{S}_Q = \frac{\beta\cdot\vec{S}_{II} - \cos\Delta\phi\cdot\vec{S}_I}{\sin\Delta\phi}. \tag{9.23}$$

It is interesting to note that this equation can be used to reconstruct the ideal quadrature signal from any two measured signals that are related by a phase delay of $\Delta\phi$. In this paper, we use input signals that are offset by approximately $\pi/2$, and already close to the ideal quadrature. However, the same analysis could be performed with signals with a different phase delay, such as 120° as would be obtained with 3x3 optical fiber couplers. We expect that good results should be obtainable with this method as long as $\Delta\phi$ remains far from 0 and π and β is relatively close to 1.

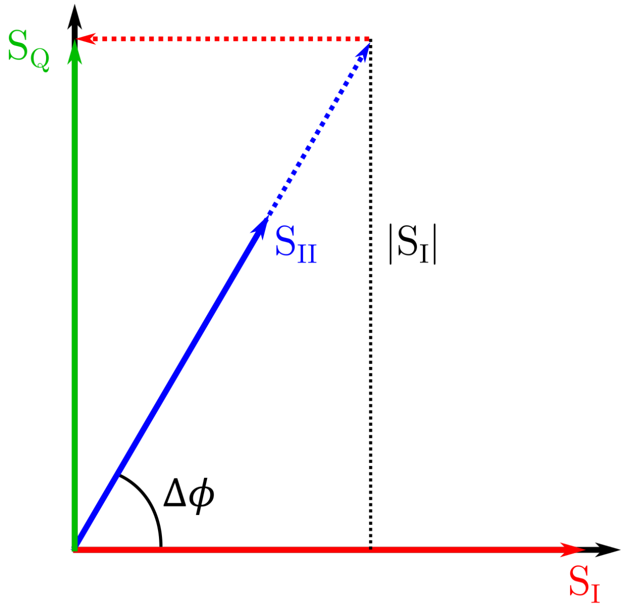

Figure 9.9 Geometric interpretation of Eq. 9.5

Acknowledgments

The authors would like to acknowledge Martin Poinsinet de Sivry-Houle and Rodrigo Itzamna Becerra Deana for helpful and insightful discussions regarding the behavior of fiber optic components. We would also like to thank Claudia Boily for her work on preliminary versions of the experimental setup. XA is supported by the Natural Sciences and Engineering Research Council of Canada (NSERC), a fellowship from TransMedTech, Canada First Research Excellence Fund (CFREF), and a travel grant from the Fonds de Recherche du Quebec—Nature et Technologies (FRQNT). This project was funded by the National Research Council Canada (NRC) through the Ideation Fund granted by the National Program Office (NPO) and the TKI-programme Life Sciences and Health 2017; "M-Cath: MEMS-catheter based 3D optical coherence tomography of bladder lesions", 22455, Dutch Ministry of Economic Affairs.

Disclosures

The authors have no relevant financial interests in this article and no potential conflicts of interest to disclose.

Data Availability Statement

All data underlying the results presented in this paper, as well as corresponding processing scripts are available in Dataset 1 and Code 1, in a Figshare repository [387, 388].

CHAPTER 10 GENERAL DISCUSSION

10.1 Achievement of research objectives

This thesis explores the development of novel implementations of multimodal endoscopic systems combining OCT with reflectance spectroscopy methods. In Chapter 1, several specific research objectives were outlined to achieve this goal. Below, the fulfillment of each research objective is discussed, and the key insights are summarized. Furthermore, context is provided about how the chapters of this dissertation relate to each other and ongoing and future research.

10.1.1 System development

Chapters 3–5 of this thesis presents three different implementations of bench-top systems combining OCT with some manner of spectral imaging (Chapters 3, 4 and 5). Each of these chapters represents a different attempt at accomplishing the first specific objective of this thesis: the development of a proof-of-concept, bench-top, multimodal imaging system. Developing these bench-top systems aims to identify, test, and validate hardware, software, and optical strategies that may then be transferred to endoscopic devices and implemented in vivo.

One of the core strengths of the systems presented in this thesis is their use of optical fibers and specialty fiber components. This significantly enhanced the robustness of each system, simplifying their use and transportation when necessary. Such qualities are essential to eventually translate the systems out of the laboratories and into a clinical setting. The use of specialty fibers and fiber components, such as double-clad fiber, double-clad fiber couplers, fiber-based wavelength division-multiplexers, and wideband multimode circulators, simultaneously replaced many free-space optical components, which are prevalent in previous literature, and enhanced the multimodal capabilities of the systems by providing alignment-free co-registration of the combined modalities. In Chapter 3, we demonstrated for the first time the use of a DCFC for combined OCT and hyperspectral imaging and validated the feasibility of collecting broadband light through the inner cladding without disrupting the OCT signal. However, in Chapter 3, the broadband illumination was external to the system, which led to a low resolution for the HSI channel. In Chapter 4, we investigated internal illumination for the spectroscopic channel by combining the OCT and VIS illumination in the core of an SMF28 through the use of a fiber-based, broadband wavelength-division multiplexer. VIS illumination through the DCF core resulted in multimode propagation, which led to reduced lateral resolution compared to diffraction-limited operation with single mode illumination. Moreover, it is difficult to estimate the theoretical spot size for multimode illumination because it depends on the launch conditions into the fiber, which was not assessed at the time. However, it is essential to note that despite sub-optimal lateral resolution with the VIS wavelengths, high-resolution imaging was still achievable, as depicted in Fig. 4.5. Moreover, the achieved resolution was approximately equivalent to that of OCT, preventing either technique from being over/under-sampled. Similar results are expected when using the system combining OCT and iSFR presented in Chapter 5, although the reflective scanner head will remove the contribution of chromatic aberrations. Using a WDM introduced distortions to the OCT signal in the form of a dispersion mismatch. However, this issue was addressed by developing a simple and quick calibration protocol, as outlined in Chapter 8, which allowed the recovery of optimal axial resolution for OCT in Chapter 4. Currently, in the project presented in Chapter 5 and ongoing projects introduced briefly in the following sections, we are investigating the use of wideband multimode circulators. These devices allow simultaneous injection and collection through the multimode port of bi-directional DCFCs and may hold the key to extending the multimodal capabilities of DCFC-based systems even further. As such, the objective of developing and validating novel fiber-based methods for multimodal imaging described in research objective 1.1 can be considered fully accomplished.

System engineering was a crucial part of the work presented in this thesis. Concepts such as data acquisition, data processing, synchronization, and control of the various subsystems within each imaging setup were essential to obtain high-quality multimodal data. Moreover, achieving optimal performance in each area was vital in determining the viability of different implementations for adaptation into endoscopic applications. For example, it is vital to evaluate signal-to-noise and signal-to-background ratios as a function of acquisition rate to determine whether the spectroscopic imaging technique can keep up with the high acquisition speed of OCT. Indeed, sequential acquisitions are not feasible in endoscopic applications as the probe will inevitably move (on the scale of the system's resolution). In Chapter 4, the VIS illumination was performed with modulated laser sources to overcome the speed limitation associated with the spectrometers and acquisition at a 16 kHz pixel rate. The sinusoidal modulation allowed the multiplexing of multiple laser sources without requiring complicated synchronization while using a single fast photodetector. However, the internal illumination proposed in Chapter 4 has the drawback that the choice of optics to focus the beam onto the sample can significantly impact the signal quality through backreflections and chromatic aberrations. While in the bench-top systems presented in Chapters 3 and 4 these aberrations were not prohibitive, in endoscopic probes, they dramatically reduce the viability of specific optical designs, as demonstrated through simulations in Chapter 6. This led to the development of the all-reflective system presented in Chapter 5, which bypasses all concerns of backreflections and chromatic effects. In light of these advances in system design and optical engineering, research objective 1.2 can also be considered fulfilled.

Finally, research objective 1.3 pertains to the investigation of different spectral imaging techniques for combination with OCT. In this thesis, we propose three such combinations: one with hyperspectral imaging (Chapter 3), one with multispectral imaging (Chapter 4), and one with a scanning variant of single fiber reflectance spectroscopy, dubbed imaging SFR (Chapter 5). However, it is important to realize that the three configurations differ only in the illumination/collection geometry and the resulting propagation regime of the collected photons. In Chapter 3, illumination is external resulting in the collection of diffuse photons, while in Chapters 4 and 5 the internal illumination results combined with cladding detection results in the collection of sub-diffuse photons. Both propagation regimes are relevant for biological imaging as they are respectively more sensitive to different optical properties [391]. For instance, sub-diffuse imaging is highly dependent on the scattering phase function, whereas diffuse imaging is less so. Diffuse imaging also provides information from much deeper in the sample (on the scale of millimeters), while sub-diffuse propagation is restricted to the most superficial layers (on the scale of hundreds of microns). A potential weakness in the presented research is that the more recent bench-top systems (as well as the endoscopic probes) rely primarily on sub-diffuse measurements and less on diffuse ones. Color reconstruction, a central theme in Chapter 4, could benefit from diffuse measurements as they more closely resemble the light perceived by our eye during color vision. While it is demonstrated in Chapters 4 and 5 that color reconstruction is feasible with internal illumination in certain instances, the general case requires advanced modeling to extract optical properties and subsequently perform forward light propagation simulations to determine the color as the human eye would perceive it. The difference between the two propagation regimes is also apparent in the quantitative comparison of the experimental and theoretical values for the color and spectral reflectance values presented in Figs. 4.7 and 4.6, respectively. Indeed the theoretical values were obtained in a diffuse regime using integrating spheres, while the experimental data was collected in the subdiffuse regime. More accurate characterization of the reference samples will be necessary in the future. In the spirit of multimodal imaging, it would be interesting to acquire measurements in both propagation regimes to determine if there is, in fact, an added value. Beyond spectroscopic imaging, incorporating other modalities such as autofluorescence or fluorescence lifetime imaging will also be highly relevant. Nonetheless, the target imaging modalities were investigated thoroughly in terms of spectral range and illumination/collection geometry, and research objective 1.3 can be deemed completed.

10.1.2 Endoscopic probes

Research objective two revolves around developing two different types of endoscopic probes. The first is GRIN-based (objective 2.1), and the second is the all-reflective capsule (objective 2.2). Chapter 6 presents a GRIN-based TCE and functioning OCT imaging. Through simulations and preliminary experiments, we found that GRIN-based designs offered limited performance for multimodal imaging due to chromatic aberrations and backreflections. This design was quickly abandoned in favor of the reflective TCE. One shortcoming of our approach is that we only investigated a simple GRIN design when other solutions existed, such as ball lenses or micro-lenses. GRIN lenses were favored for their technical simplicity and low cost, but assessing other solutions through simulations may have been worthwhile. In Chapter 7, we present the first prototype of an all-reflective TCE (RTCE). The great advantage of this design is that it offers achromatic performance across the entire VIS/NIR spectral range and is intended for operation with DCF. In principle, the RTCE can be used with any DCFC-based multimodal system, provided they are matched in terms of sample space numerical aperture. The lack of flexibility of the RTCE in terms of NA is its major limitation. The NA of the device may be fine-tuned by changing the focal lengths of the ellipsoidal mirror, but only within a finite range due to geometrical constraints. The achievable NA ranges between 0.01 and 0.03 approximately, with the device presented in Chapter 7 at NA=0.02. This limits the viability of certain higher-resolution techniques such as confocal microscopy, micro-OCT, or multiphoton techniques. Another limitation of the proposed RTCE design is the high cost and complexity of the device. However, these factors are offset by the fact that the RTCE is reusable. While the number of uses has not been thoroughly evaluated yet, we expect it to be at least 5-10 times, which would bring the cost per use of the endoscope down to values comparable to or below that of commercial, single-use OCT catheters. Although these considerations are less relevant from a scientific perspective, they are essential for the eventual commercialization of the device and the complete system, which represents one possible path to large-scale clinical trials in humans. Despite the limitations listed above, the RTCE remains highly promising for multimodal esophageal endoscopy and an exciting research avenue for the coming years. As such, we consider research objective 2 fully accomplished.

10.1.3 Signal analysis and processing

Research objectives 3.1–3.3 are centered around developing the necessary algorithms for the optimal operation of the proposed multimodal systems and analysis of the resulting data. In Chapter 8, we demonstrate a calibration procedure for k-linearization and dispersion compensation: two critical steps in the standard OCT processing pipeline. This methodology's development was essential in this thesis's context because the multimodal systems were often altered and, therefore, required frequent re-calibration. Moreover, specialty fiber components may introduce dispersion mismatches in the OCT signal, which can be challenging to correct other than with numerical methods. The proposed method is highly robust and efficient as it requires only two simple measurements of mirror surfaces. It was applied successfully to nearly all systems presented in this thesis, including the RTCE. Research objective 3.1 is therefore fully attained.

The method outlined in Chapter 9 enables high-quality, full-range OCT using passive quadrature demultiplexing. Full-range OCT is relevant for the development of endoscopic devices because it avoids having signals from interfaces inside the endoscope be folded back into the main imaging range. Such folded images reduce the overall useful imaging range and may degrade the image if the proper length adjustments are not performed (when switching endoscopes, for example). We are currently investigating the use of features on the glass window of the TCE as markers for the correction of rotational distortions. As such, the window must be located within the useful imaging range, further reducing the space available for the sample. With full-range OCT, the useful imaging range is doubled, providing more space for the glass window and the sample. Additionally, the extended imaging range slightly relaxes the tolerances on the total optical path length of the endoscope. Beyond its use in endoscopic applications, this method is related to the ongoing development of novel fiber-based optical hybrids. Indeed, the specifications required for calibration-free, full-range OCT are nearly impossible to achieve with fiber-based optical hybrids. Therefore, the proposed calibration method is necessary for deploying such optical hybrids in OCT systems. In Chapter 9, we implement the method successfully in a bench-top system at 1500 nm. In principle, the method should not be influenced by a change in spectral range or switching over to an endoscopic system. While we are confident that the proposed procedure will work, this remains to be validated experimentally. As such, we consider objective 3.2 only partially complete but have identified a pathway to allow experimental validation in the near future.

The final research objective (3.3) pertains to the development of light propagation models that enable the extraction of optical properties from the non-contact spectroscopy methods presented in Chapters 3–5, as well as analysis methods utilizing both spectroscopic and OCT data. Through the projects described in this thesis, we concluded that a strong connection exists between the signal measured with double-clad fibers and those measured with single fiber reflectance spectroscopy. Indeed, the different implementations described here effectively project the surface of the DCF onto the sample. This results in an equivalent fiber size and NA for illumination and collection in sample space, which is a sufficient parametrization for modern SFR models [230,241–243]. However, these models assume a single fiber geometry which is not respected in the case of core illumination with a DCF. As such, the models must be adapted to account for the difference in geometry. This research is ongoing but has not yet yielded any useful analysis of existing data. Another important aspect to consider in non-contact spectroscopy is the presence of glare. Glare refers to the specular reflections off of a surface with a certain unknown efficiency factor due to surface roughness, orientation, and optical properties. As this light has not interacted with the sample, it does not carry any useful information and obscures the signal of interest. Glare effects can be clearly visualized in Fig. 4.8(B), where they appear as brighter spots. The proportion of glare within the signal collected at each pixel is difficult to determine and influences the recovered spectroscopic information. One way the OCT and spectral data may be combined is by using the OCT signal, which can discriminate the origin of a signal based on depth, to determine the relative amount of glare vs. signal that has interacted with the sample. As such, we are exploring several ways in which OCT and spectral datasets may be used together. However, none of these initiatives have been completed yet. Objective 3.3, therefore, remains incomplete as of yet.

10.2 Advantages and limitations of proposed methodologies

10.2.1 Modularity

One key trait shared by the systems presented in this thesis is their modularity. They rely on a common base composed of the DCFC and a combiner that couples both light sources into the core of an SMF28 and on interchangeable illumination and detection modules. For example, in Chapter 4, the combiner is a fiber-based WDM, the illumination is a multi-laser device and the detection unit is a single fast photodetector. In Chapter 5, the combiner is a free-space system, the source is a supercontinuum laser, and the detection unit is composed of two spectrometers. Without oversimplifying the complexity of system design, this modularity can be exploited to achieve an accelerated turnaround in developing multimodal systems. This is also relevant in clinical validation because it implies that a system can be retrofitted to accommodate the additional modality with minimal influence on the rest of the system. As such, rather than developing several complete systems that combine OCT with all the possible modalities, it would be possible to construct several independent modules that could be rapidly switched in or out depending on the requirements at the time. While this would not achieve true sub-pixel level co-registration between all the modalities, the modular approach would significantly reduce the complexity of combining all illuminations and demultiplexing the signals before or after detection.

10.2.2 Lack of clinical experience

Aside from the technical difficulties and limitations encountered during the development of the proposed systems, there is one significant shortcoming in the overall research methodology: the lack of clinical data and experience. While the project presented in this thesis is centered around technological and scientific development and not clinical translation, biological data is essential to obtain representative performance data and to identify relevant biological features. While OCT has already been extensively studied in the esophagus and feature atlases have been developed, no such database of features exists for other modalities such as iSFR, multispectral imaging, or fluorescence imaging. In particular, considering the speed limitations of spectrometers as seen in Chapters 3 and 5, it is likely that a clinical system will operate with multispectral illumination, as demonstrated in Chapter 4. As such, it is relevant to establish if multispectral illumination is sufficient to obtain significant insight into tissue physiology and if this is the case, which wavelengths should be used. Fortunately, the ultra-broadband system presented in Chapter 5 was designed with this purpose in mind. However, a bench-top system will likely be limited to excised tissue, especially in the case of esophageal imaging. As such, several relevant physiological and molecular markers, including tissue perfusion or blood oxygenation, will not be accessible. Therefore, the further development and certification of endoscopic probes such as the RTCE presented in Chapter 7 are also essential to grant access to in vivo data.

10.3 Ongoing & future research

10.3.1 Modeling light-tissue interaction in iSFR

The systems in this thesis present spectroscopic imaging of a variety of samples. In most cases, this information is depicted as a reflectance map. However, reflectance alone is not the best tool for biochemical analysis as it also depends on the imaging geometry and not exclusively on the molecular composition of the sample. As such, modeling becomes an essential step in separating the contributions of the imaging geometry from that of the sample optical properties. As explained in Chapter 2 and illustrated in Fig. 2.13, the imaging geometries of the systems presented in this thesis closest resemble that of SFR measurements, albeit in a non-contact way. As such, we are currently in the process of adapting existing SFR models to the iSFR geometry. A key detail is that SFR measurements typically require at least two fiber sizes to obtain stable and reliable data. However, this problem may be overcome through the use of double-clad fiber. By performing two measurements, one with core illumination and one with cladding illumination, we hope to emulate multi-diameter SFR measurements with a single fiber. We are currently investigating the feasibility of this approach through extensive Monte Carlo simulations of a wide variety of optical properties. We hypothesize that if the propagation of the detected photons is sufficiently different between core and cladding illumination, then the two illumination modes may provide equivalent information to MDSFR.

Another interesting research avenue is the use of the OCT signal to sense the position of the sample relative to the focal plane. Such considerations are important because, in non-contact measurements, the surface of the sample may not always be in the exact same location, as illustrated by Fig. 4.8. Such depth variations may reach up to several millimeters while remaining in the OCT field of view, and can lead to differences in the iSFR signal by changing the illumination and collection spot sizes (see Fig. 7.7 for example values). As such, it will be important to incorporate the relative position of the sample surface into the models mentioned above.

This research offers two interesting potential outcomes. The first is the development of valid models for iSFR, which could then be incorporated into bench-top and endoscopic systems and used to extract quantitative maps of optical properties. The second is the potential improvement of conventional SFR measurements by removing the need for a second fiber. The technical implementation of the two illumination modes is made possible by using a novel fiber component called a wideband multimode circulator (WMC) and bi-directional DCFCs (discussed below).

10.3.2 Wideband multimode circulators in SFR and iSFR

As their name implies, wideband multimode circulators are multimode devices that act similarly to SM circulators in that they transfer light selectively from one port to the next (i.e., 1→ 2 and 2→ 3). However, these devices are composed of larger multimode fiber and have a considerable spectral bandwidth, ranging from 400–1600 nm. In iSFR, they can be implemented as presented in Fig. 10.1(A) to enable imaging with cladding illumination. The initial setup is the OCT+iSFR system presented in Chapter 5. Cladding illumination using the WMC allows for significantly simplified and higher light throughput, although at the cost of lateral resolution as illustrated in Figs. 10.1(B) and (C). Aside from the potential MDSFR measurements discussed previously, cladding illumination could also be used for high-speed acquisition, where signal levels may be too low with core illumination.

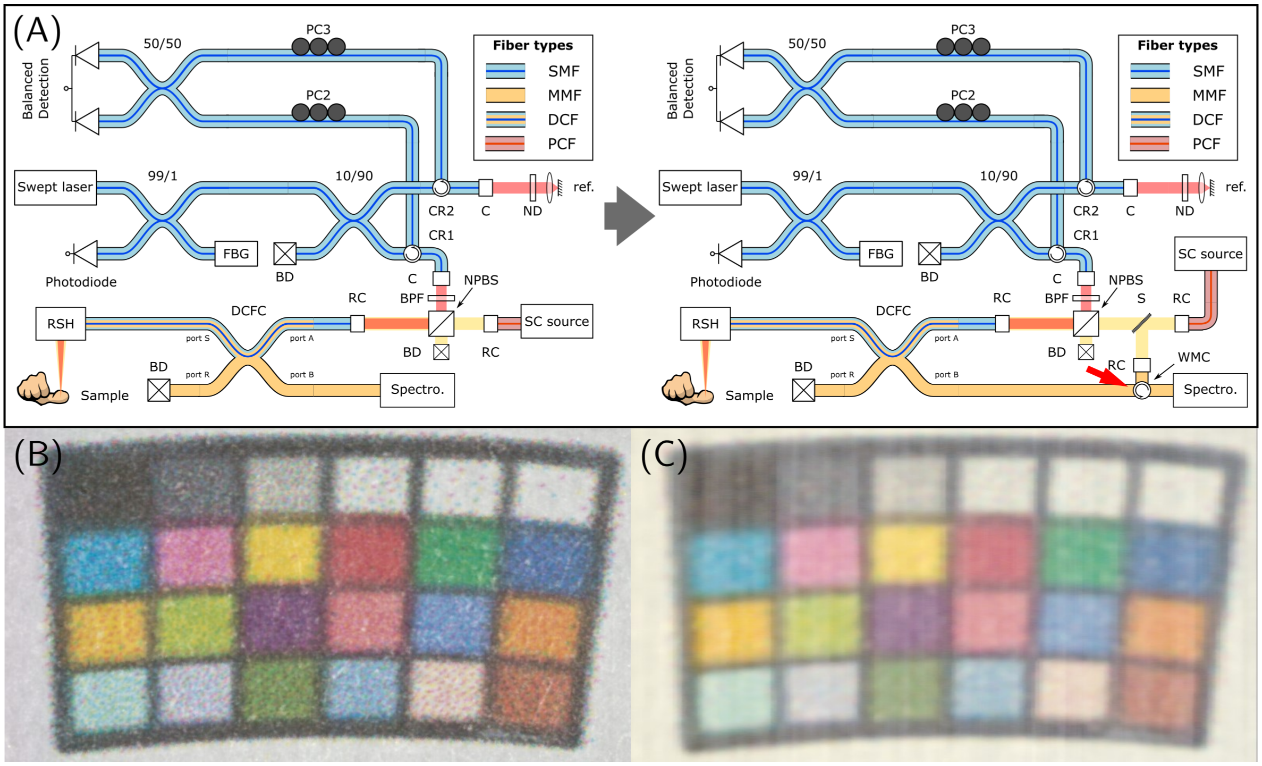

Figure 10.1 Reflectance imaging using cladding illumination with a WMC. (A) Changes implemented in the setup from Chapter 5 to incorporate the WMC, indicated by the red arrow. (B) iSFR image of a ColorChecker target with core illumination. (C) iSFR image of the same target with cladding illumination. Signal collection is performed through the cladding in both cases.

Another implementation of the WMC that we are currently exploring is in an improved experimental setup for conventional SFR measurements, illustrated in Fig. 10.2. Currently, SFR systems rely on bifurcated fibers to transport light from the source to the sample and then from the sample to the spectrometer. However, bifurcated fibers present a high sensitivity to modal content and fiber bends due to their asymmetry, which can distort the measured signal. On the other hand, multimode circulators are modally insensitive and more robust to experimental conditions. The improved SFR setup also includes a supercontinuum source rather than the usual lamps and a so-called reference arm to simultaneously measure signal variations due to bend losses (not shown). We hope to achieve improved measurement stability and speed for enhanced reliability in a clinical setting through these modifications.

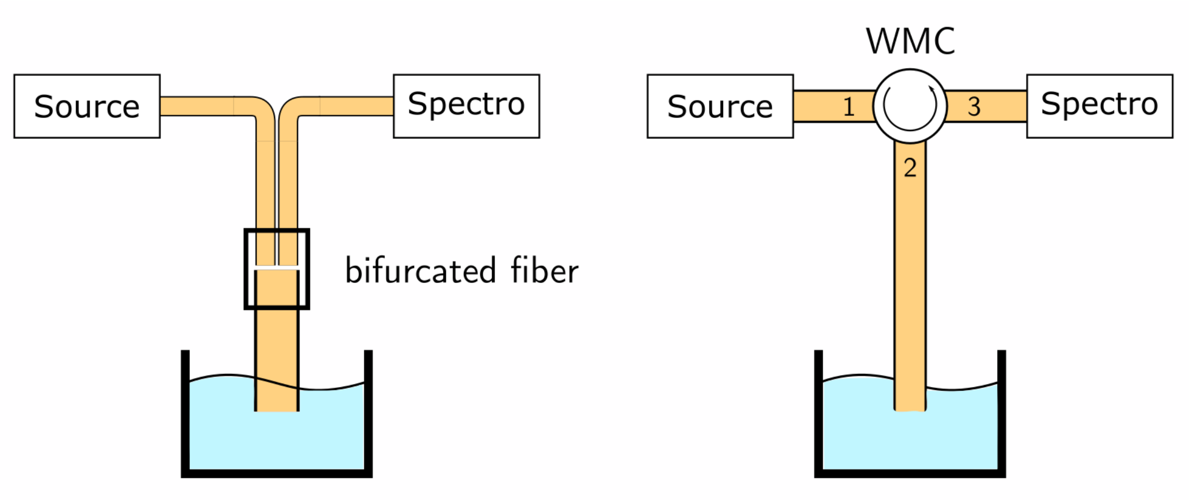

Figure 10.2 Schematic representations of SFR setups. (left) current implementation with a bifurcated fiber and (right) proposed setup with a WMC.

10.3.3 Tethered capsule endoscopy platform & clinical translation

Despite encouraging results, the tethered capsule endoscope presented in Chapter 7 is still at a prototype stage, and many more steps are required before it can be used in human trials. Obtaining certification for human use will be at the center of our priorities in the coming years. This includes verifying aspects such as toxicology, stress testing, electrical safety, and developing clinical protocols. As described in Chapter 7, the capsule itself was developed with versatility in mind such that it can be used for various combinations of modalities, including OCT, iSFR, MSI, fluorescence imaging, and laser marking or ablation. It is essential to keep this versatility in mind during the certification process such that it must not be repeated for each combination of techniques. In this way, we can leverage the modular nature of the systems and adopt a platform approach with interchangeable illumination/excitation and detection units, as depicted in Fig. 10.3. Moreover, all changes will occur on the proximal end of the system, which will not impact the endoscopic probe and its interaction with the patient. This will enable a single clinical system to perform highly multimodal imaging, perhaps even within a single patient, to assess the diagnostic potential of all modalities individually and combined. We will also endeavor to overcome the significant lack of biological data discussed previously by performing ex vivo esophageal imaging and potential animal studies. Obtaining OCT and spectroscopic data correlated to histology is critical to achieving optimal in vivo performance and simply knowing what to look for.

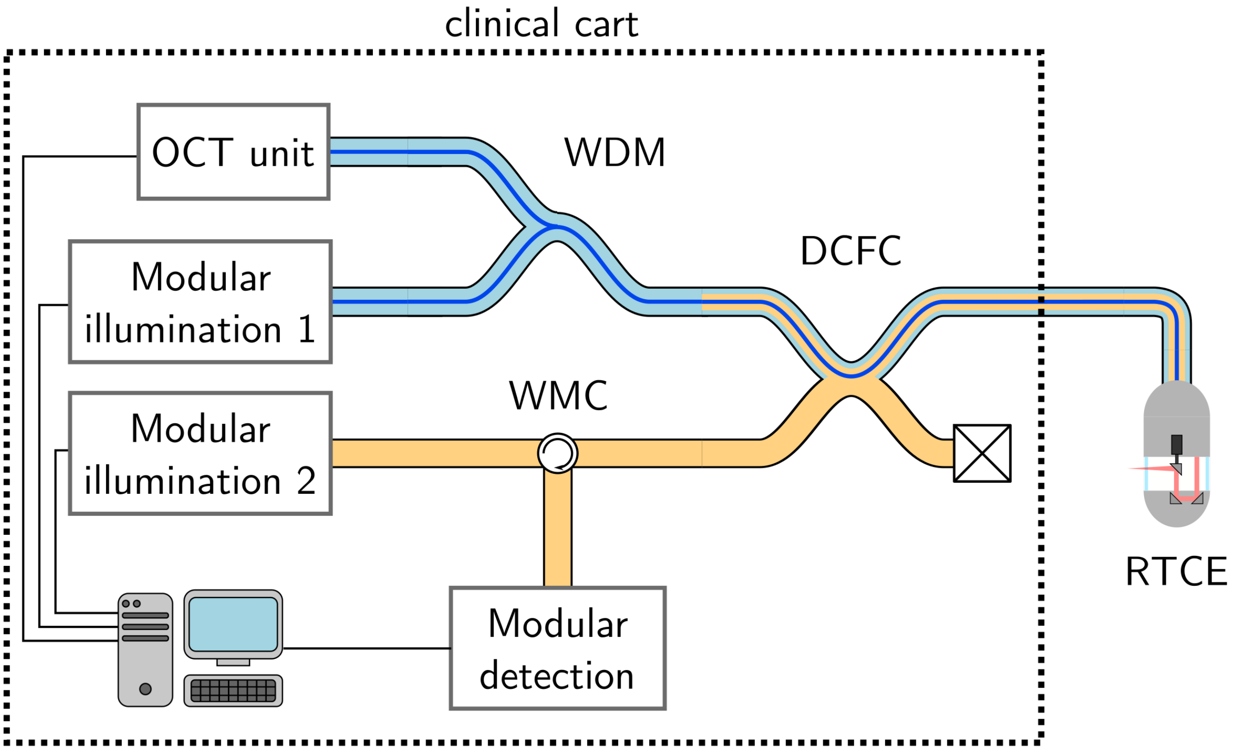

Figure 10.3 Schematic representation of the proposed multimodal imaging platform centered around the RTCE.

CHAPTER 11 CONCLUSION

11.1 Summary of works

Over the last 30 years, optical coherence tomography has shown tremendous promise in a wide variety of endoscopic fields, thanks to its ability to resolve the microscopic architecture of tissue in 3D. However, its application to various fields has been hampered by the development of specialized endoscopes and the intrinsic limits of the technique in terms of contrast. In this thesis, I worked towards overcoming both of these challenges by developing an endoscopy platform for multimodal optical coherence tomography in the esophagus.

Firstly, I investigated the combination of OCT with different spectroscopic techniques to overcome the limited molecular contrast achievable with OCT alone. Three different implementations based on the use of a double-clad fiber coupler were presented. These systems differed in their imaging geometry which was found to change to optical propagation regime of the collected photons and, therefore, the information that may be accessed from measurements. Furthermore, I developed technical solutions, including an achromatic, all-reflective imaging apparatus, to expand the spectral range of the spectroscopic techniques to the full visible and near-infrared ranges without compromising OCT imaging quality. Finally, I proposed signal multiplexing methods that enable concurrent, high-speed multispectral and OCT imaging. The proposed technical developments extend the possibilities for multimodal imaging. In addition to combining modalities, it is important to recognize the potential value of multiplexing of geometries. In this thesis, such geometries included external illumination, internal cladding illumination, and internal core illumination. These variations may provide enhanced insight into the sample compared to imaging with a single geometry. In parallel, developing broadband, achromatic, and backreflection-free imaging solutions is critical for expanding the system's sensitivity to diverse biological chromophores. Moreover, it enables the rapid prototyping of systems combining OCT with other modalities beyond the ones demonstrated in this dissertation. Finally, signal multiplexing strategies for both illumination and detection enable fast imaging, crucial for clinical applications, by maximizing the measurement density in time and minimizing cross-talk between channels.

Secondly, I developed endoscopic devices for multimodal imaging in the esophagus. Building on the lessons learned while working with benchtop systems, I designed and built a

DCFC-based, all-reflective tethered capsule endoscope (RTCE) for multimodal imaging in the esophagus. This device is intended for combined OCT and spectroscopic imaging but may, in principle, be used with other imaging or therapeutic modalities. This versatility is highly desirable as it enables a trial-and-error approach to in vivo imaging by reducing/removing repeated optomechanical design iterations and clinical certification processes.

Thirdly, I propose several algorithmic methods for OCT calibration and processing through advanced signal analysis. This enables optimal OCT imaging despite signal distortions caused by the multimodal system. As such, no compromises or performance trade-offs are necessary when combining OCT with the proposed spectroscopic imaging techniques or when implementing novel fiber components. The experimental simplicity of the developed calibration methods also enhances the robustness of OCT systems, as they can easily be repeated and automated. This is of great value in a clinical context where the system may frequently move between environments or be operated by non-expert personnel.

11.2 Outlook

The research presented in the thesis demonstrates several technical advancements in multimodal optical coherence tomography. All of these developments are aimed at the realization of a highly-multimodal, clinical endoscopy platform for the early detection of esophageal cancer. With this objective in mind, it will be imperative to take into account and further expand existing research on the the connection between the biological changes of pathological tissue and the variations measured with optical imaging. Through this analysis and extensive in vivo imaging, we hope to conclusively demonstrate, or perhaps invalidate, the diagnostic capabilities of different variations of multimodal OCT. This reasoning is compelling as it extends beyond esophageal cancer and may be helpful for endoscopic cancer detection at large as well as for other diseases. Similarly, the proposed technical developments may also be extended to other organs and pathologies.

The success of such clinical trials will undoubtedly be linked to the accumulation of substantial quantities of data in order to draw statistically significant conclusions. In addition to quantity, the high dimensionality of multimodal datasets will complicate their interpretation. Machine learning (ML) methods will undoubtedly play a meaningful role in analyzing this data and finding the proverbial needle in the haystack. However, ML is often applied in a one-size-fits-all way, where images and minimally processed data are fed into black-box algorithms. While this approach has its merits, the optical techniques discussed in this dissertation are founded on decades (if not centuries) of theoretical knowledge, which can be used to supplement ML algorithms in their analyses. It will be fascinating to develop diagnostic algorithms that rely on the combined insights of physics, biology, and computer sciences.

REFERENCES

[1] M. J. Suter, B. J. Vakoc, P. S. Yachimski, M. Shishkov, G. Y. Lauwers, M. Mino-Kenudson, B. E. Bouma, N. S. Nishioka, and G. J. Tearney, "Comprehensive microscopy of the esophagus in human patients with optical frequency domain imaging," *Gastrointestinal endoscopy*, vol. 68, no. 4, pp. 745–753, 2008.

[2] M. J. Gora, M. J. Suter, G. J. Tearney, and X. Li, "Endoscopic optical coherence tomography: technologies and clinical applications," *Biomedical Optics Express*, vol. 8, no. 5, pp. 2405–2444, 2017.

[3] R. Guay-Lord, X. Attendu, K. L. Lurie, L. Majeau, N. Godbout, A. K. Bowden, M. Strupler, and C. Boudoux, "Combined optical coherence tomography and hyperspectral imaging using a double-clad fiber coupler," *Journal of Biomedical Optics*, vol. 21, no. 11, p. 116008, 2016.

[4] T. Zhao, A. E. Desjardins, S. Ourselin, T. Vercauteren, and W. Xia, "Minimally invasive photoacoustic imaging: Current status and future perspectives," *Photoacoustics*, vol. 16, p. 100146, 2019. [Online]. Available: https://www.sciencedirect.com/science/article/pii/S2213597919300692

[5] I. Hussein, M. Raad, R. Safa, R. A. Jurjus, and A. Jurjus, "Once upon a microscopic slide: the story of histology," *Journal of Cytology & Histology*, vol. 6, 2015.

[6] D. J. Uhlenhopp, E. O. Then, T. Sunkara, and V. Gaduputi, "Epidemiology of esophageal cancer: update in global trends, etiology and risk factors," *Clinical journal of gastroenterology*, vol. 13, no. 6, pp. 1010–1021, 2020.

[7] H. Sung, J. Ferlay, R. L. Siegel, M. Laversanne, I. Soerjomataram, A. Jemal, and F. Bray, "Global cancer statistics 2020: Globocan estimates of incidence and mortality worldwide for 36 cancers in 185 countries," *CA: a cancer journal for clinicians*, vol. 71, no. 3, pp. 209–249, 2021.

[8] M. Arnold, I. Soerjomataram, J. Ferlay, and D. Forman, "Global incidence of oesophageal cancer by histological subtype in 2012," *Gut*, vol. 64, no. 3, pp. 381–387, 2015.

[9] S. C. Canadian Cancer Statistics Advisory Committee in collaboration with the Canadian Cancer Society and the Public Health Agency of Canada, "Canadian cancer statistics 2021," 2021 (accessed 24/04/2022), available at http:\www.cancer.ca/Canadian-Cancer-Statistics-2021-EN.

[10] R. L. Siegel, K. D. Miller, H. E. Fuchs, and A. Jemal, "Cancer statistics, 2022," *CA: a cancer journal for clinicians*, 2022.

[11] M. Arnold, J. Ferlay, M. I. van Berge Henegouwen, and I. Soerjomataram, "Global burden of oesophageal and gastric cancer by histology and subsite in 2018," *Gut*, vol. 69, no. 9, pp. 1564–1571, 2020.

[12] H. Pohl and H. G. Welch, "The role of overdiagnosis and reclassification in the marked increase of esophageal adenocarcinoma incidence," *Journal of the National Cancer Institute*, vol. 97, no. 2, pp. 142–146, 2005.

[13] A. P. Thrift, "Global burden and epidemiology of barrett oesophagus and oesophageal cancer," *Nature Reviews Gastroenterology & Hepatology*, vol. 18, no. 6, pp. 432–443, 2021.

[14] M. B. Cook and A. P. Thrift, "Epidemiology of barrett's esophagus and esophageal adenocarcinoma: implications for screening and surveillance," *Gastrointestinal Endoscopy Clinics*, vol. 31, no. 1, pp. 1–26, 2021.

[15] M. Arnold, M. Laversanne, L. M. Brown, S. S. Devesa, and F. Bray, "Predicting the future burden of esophageal cancer by histological subtype: international trends in incidence up to 2030," *Official journal of the American College of Gastroenterology| ACG*, vol. 112, no. 8, pp. 1247–1255, 2017.

[16] C. Hur, M. Miller, C. Y. Kong, E. C. Dowling, K. J. Nattinger, M. Dunn, and E. J. Feuer, "Trends in esophageal adenocarcinoma incidence and mortality," *Cancer*, vol. 119, no. 6, pp. 1149–1158, 2013.

[17] A. Dubecz, I. Gall, N. Solymosi, M. Schweigert, J. H. Peters, M. Feith, and H. J. Stein, "Temporal trends in long-term survival and cure rates in esophageal cancer: a seer database analysis," *Journal of Thoracic Oncology*, vol. 7, no. 2, pp. 443–447, 2012.

[18] M. J. D. Arnal, Á. F. Arenas, and Á. L. Arbeloa, "Esophageal cancer: Risk factors, screening and endoscopic treatment in western and eastern countries," *World journal of gastroenterology: WJG*, vol. 21, no. 26, p. 7933, 2015.

[19] J. Maret-Ouda, S. R. Markar, and J. Lagergren, "Gastroesophageal reflux disease: a review," *Jama*, vol. 324, no. 24, pp. 2536–2547, 2020.

[20] C. Gindea, R. Birla, P. Hoara, A. Caragui, and S. Constantinoiu, "Barrett esophagus: history, definition and etiopathogeny," *Journal of Medicine and Life*, vol. 7, no. Spec Iss 3, p. 23, 2014.

[21] J. Lagergren, R. Bergström, A. Lindgren, and O. Nyrén, "Symptomatic gastroesophageal reflux as a risk factor for esophageal adenocarcinoma," *New England journal of medicine*, vol. 340, no. 11, pp. 825–831, 1999.

[22] P. J. F. de Jonge, M. van Blankenstein, W. M. Grady, and E. J. Kuipers, "Barrett's oesophagus: epidemiology, cancer risk and implications for management," *Gut*, vol. 63, no. 1, pp. 191–202, 2014.

[23] P. J. de Jonge, M. van Blankenstein, C. W. Looman, M. K. Casparie, G. A. Meijer, and E. J. Kuipers, "Risk of malignant progression in patients with barrett's oesophagus: a dutch nationwide cohort study," *Gut*, vol. 59, no. 8, pp. 1030–1036, 2010.

[24] M. A. Eloubeidi and D. Provenzale, "Does this patient have barrett's esophagus? the utility of predicting barrett's esophagus at the index endoscopy," *The American journal of gastroenterology*, vol. 94, no. 4, pp. 937–943, 1999.

[25] S.-W. Lee, H.-C. Lien, C.-S. Chang, M.-X. Lin, C.-H. Chang, and C.-W. Ko, "Benefits of the seattle biopsy protocol in the diagnosis of barrett's esophagus in a chinese population," *World Journal of Clinical Cases*, vol. 6, no. 14, p. 753, 2018.

[26] M. di Pietro, M. I. Canto, and R. C. Fitzgerald, "Endoscopic management of early adenocarcinoma and squamous cell carcinoma of the esophagus: screening, diagnosis, and therapy," *Gastroenterology*, vol. 154, no. 2, pp. 421–436, 2018.

[27] J. E. McArdle, K. J. Lewin, G. Randall, and W. Weinstein, "Distribution of dysplasias and early invasive carcinoma in barrett's esophagus," *Human pathology*, vol. 23, no. 5, pp. 479–482, 1992.

[28] J. M. Inadomi, R. Sampliner, J. Lagergren, D. Lieberman, A. M. Fendrick, and N. Vakil, "Screening and surveillance for barrett esophagus in high-risk groups: a costutility analysis," *Annals of internal medicine*, vol. 138, no. 3, pp. 176–186, 2003.

[29] J. M. Barbiere and G. Lyratzopoulos, "Cost-effectiveness of endoscopic screening followed by surveillance for barrett's esophagus: a review," *Gastroenterology*, vol. 137, no. 6, pp. 1869–1876, 2009.

[30] R. Garside, M. Pitt, M. Somerville, K. Stein, A. Price, and N. Gilbert, "Surveillance of barrett's oesophagus: exploring the uncertainty through systematic review, expert workshop and economic modelling." *Health Technology Assessment (Winchester, England)*, vol. 10, no. 8, pp. 1–142, 2006.

[31] S. Sami, V. Subramanian, W. Butt, G. Bejkar, J. Coleman, J. Mannath, and K. Ragunath, "High definition versus standard definition white light endoscopy for detecting dysplasia in patients with barrett's esophagus," *Diseases of the Esophagus*, vol. 28, no. 8, pp. 742–749, 2015.

[32] S. A. Gross, J. Kingsbery, J. Jang, M. Lee, and A. Khan, "Evaluation of dysplasia in barrett esophagus," *Gastroenterology & Hepatology*, vol. 14, no. 4, p. 233, 2018.

[33] P. Sharma, R. H. Hawes, A. Bansal, N. Gupta, W. Curvers, A. Rastogi, M. Singh, M. Hall, S. C. Mathur, S. B. Wani *et al.*, "Standard endoscopy with random biopsies versus narrow band imaging targeted biopsies in barrett's oesophagus: a prospective, international, randomised controlled trial," *Gut*, vol. 62, no. 1, pp. 15–21, 2013.

[34] J. Mannath, V. Subramanian, C. Hawkey, and K. Ragunath, "Narrow band imaging for characterization of high grade dysplasia and specialized intestinal metaplasia in barrett's esophagus: a meta-analysis," *Endoscopy*, vol. 42, no. 05, pp. 351–359, 2010.

[35] G. Longcroft-Wheaton, M. Duku, R. Mead, D. Poller, and P. Bhandari, "Acetic acid spray is an effective tool for the endoscopic detection of neoplasia in patients with barrett's esophagus," *Clinical Gastroenterology and Hepatology*, vol. 8, no. 10, pp. 843–847, 2010.

[36] F. J. Chedgy, S. Subramaniam, K. Kandiah, S. Thayalasekaran, and P. Bhandari, "Acetic acid chromoendoscopy: Improving neoplasia detection in barrett's esophagus," *World journal of gastroenterology*, vol. 22, no. 25, p. 5753, 2016.

[37] A. L. Post, A. J. de Groof, X. U. Zhang, A.-F. Swager, K. N. Fockens, R. E. Pouw, B. L. Weusten, D. J. Faber, D. M. de Bruin, J. J. Bergman *et al.*, "Toward improved endoscopic surveillance with multidiameter single fiber reflectance spectroscopy in patients with barrett's esophagus," *Journal of Biophotonics*, vol. 14, no. 4, p. e202000351, 2021.

[38] D. Boerwinkel, J. Holz, M. Aalders, M. Visser, S. Meijer, M. Van Berge Henegouwen, B. Weusten, and J. Bergman, "Third-generation autofluorescence endoscopy for the detection of early neoplasia in barrett's esophagus: a pilot study," *Diseases of the Esophagus*, vol. 27, no. 3, pp. 276–284, 2014.

[39] W. L. Curvers, R. Singh, L. W.-K. Song, H. C. Wolfsen, K. Ragunath, K. Wang, M. B. Wallace, P. Fockens, and J. Bergman, "Endoscopic tri-modal imaging for detection of early neoplasia in barrett's oesophagus: a multi-centre feasibility study using high-resolution endoscopy, autofluorescence imaging and narrow band imaging incorporated in one endoscopy system," *Gut*, vol. 57, no. 2, pp. 167–172, 2008.

[40] D. Kohli, M. Schubert, A. Zfass, and T. Shah, “Performance characteristics of optical coherence tomography in assessment of barrett’s esophagus and esophageal cancer: systematic review.” *Diseases of the Esophagus*, vol. 30, no. 11, 2017.

[41] J. A. Evans, J. M. Poneros, B. E. Bouma, J. Bressner, E. F. Halpern, M. Shishkov, G. Y. Lauwers, M. Mino-Kenudson, N. S. Nishioka, and G. J. Tearney, “Optical coherence tomography to identify intramucosal carcinoma and high-grade dysplasia in barrett’s esophagus,” *Clinical Gastroenterology and Hepatology*, vol. 4, no. 1, pp. 38–43, 2006.

[42] J. A. Evans, B. E. Bouma, J. Bressner, M. Shishkov, G. Y. Lauwers, M. Mino-Kenudson, N. S. Nishioka, and G. J. Tearney, “Identifying intestinal metaplasia at the squamocolumnar junction by using optical coherence tomography,” *Gastrointestinal endoscopy*, vol. 65, no. 1, pp. 50–56, 2007.

[43] J. M. Poneros, S. Brand, B. E. Bouma, G. J. Tearney, C. C. Compton, and N. S. Nishioka, “Diagnosis of specialized intestinal metaplasia by optical coherence tomography,” *Gastroenterology*, vol. 120, no. 1, pp. 7–12, 2001.

[44] G. Isenberg, M. V. Sivak Jr, A. Chak, R. C. Wong, J. E. Willis, B. Wolf, D. Y. Rowland, A. Das, and A. Rollins, “Accuracy of endoscopic optical coherence tomography in the detection of dysplasia in barrett’s esophagus: a prospective, double-blinded study,” *Gastrointestinal endoscopy*, vol. 62, no. 6, pp. 825–831, 2005.

[45] D. Huang, E. A. Swanson, C. P. Lin, J. S. Schuman, W. G. Stinson, W. Chang, M. R. Hee, T. Flotte, K. Gregory, C. A. Puliafito *et al.*, “Optical coherence tomography,” *Science*, vol. 254, no. 5035, pp. 1178–1181, 1991.

[46] C. Boudoux, *Fundamentals of Biomedical Optics*. Pollux, 2017.

[47] B. E. A. Saleh and M. C. Teich, *Fundamentals of Photonics*, ser. Wiley Series in Pure and Applied Optics. New York, USA: John Wiley & Sons, Inc., Aug. 1991.

[48] A. M. Zysk, F. T. Nguyen, A. L. Oldenburg, D. L. Marks, and S. A. Boppart, “Optical coherence tomography: a review of clinical development from bench to bedside,” *Journal of Biomedical Optics*, vol. 12, no. 5, p. 051403, 2007.

[49] J. A. Izatt and M. A. Choma, “Theory of Optical Coherence Tomography,” in *Optical coherence tomography*. Springer, Berlin, Heidelberg, 2008, pp. 47–72.

[50] A. F. Fercher, “Optical coherence tomography – development, principles, applications,” *Zeitschrift für Medizinische Physik*, vol. 20, no. 4, pp. 251–276, Nov. 2010.

[51] L. Liu, J. A. Gardecki, S. K. Nadkarni, J. D. Toussaint, Y. Yagi, B. E. Bouma, and G. J. Tearney, “Imaging the subcellular structure of human coronary atherosclerosis using micro–optical coherence tomography,” *Nature medicine*, vol. 17, no. 8, pp. 1010–1014, 2011.

[52] J. Fujimoto and W. Drexler, “Introduction to optical coherence tomography,” in *Optical coherence tomography*. Springer, 2008, pp. 1–45.

[53] E. Hecht, *Optics*. Pearson Education, 2017.

[54] J. W. Goodman, *Statistical optics*. John Wiley & Sons, 2015.

[55] A. F. Fercher, "In vivo optical coherence tomography in ophthalmology," in *Medical optical tomography: functional imaging and monitoring*, vol. 10311. International Society for Optics and Photonics, 1993, p. 103110L.

[56] E. A. Swanson, J. A. Izatt, M. R. Hee, D. Huang, C. Lin, J. Schuman, C. Puliafito, and J. G. Fujimoto, "In vivo retinal imaging by optical coherence tomography," *Optics letters*, vol. 18, no. 21, pp. 1864–1866, 1993.

[57] G. Tearney, B. Bouma, and J. Fujimoto, "High-speed phase-and group-delay scanning with a grating-based phase control delay line," *Optics letters*, vol. 22, no. 23, pp. 1811–1813, 1997.

[58] C. Jesser, S. A. Boppart, C. Pitris, D. L. Stamper, G. P. Nielsen, M. E. Brezinski, and J. Fujimoto, "High resolution imaging of transitional cell carcinoma with optical coherence tomography: feasibility for the evaluation of bladder pathology." *The British journal of radiology*, vol. 72, no. 864, pp. 1170–1176, 1999.

[59] J. G. Fujimoto, S. A. Boppart, G. Tearney, B. E. Bouma, C. Pitris, and M. E. Brezinski, "High resolution in vivo intra-arterial imaging with optical coherence tomography," *Heart*, vol. 82, no. 2, pp. 128–133, 1999.

[60] B. E. Bouma, G. J. Tearney, C. C. Compton, and N. S. Nishioka, "High-resolution imaging of the human esophagus and stomach in vivo using optical coherence tomography," *Gastrointestinal endoscopy*, vol. 51, no. 4, pp. 467–474, 2000.

[61] A. V. D'Amico, M. Weinstein, X. Li, J. P. Richie, and J. Fujimoto, "Optical coherence tomography as a method for identifying benign and malignant microscopic structures in the prostate gland," *Urology*, vol. 55, no. 5, pp. 783–787, 2000.

[62] C. Pitris, M. E. Brezinski, B. E. Bouma, G. J. Tearney, J. F. Southern, and J. G. Fujimoto, "High resolution imaging of the upper respiratory tract with optical coherence tomography: a feasibility study," *American journal of respiratory and critical care medicine*, vol. 157, no. 5, pp. 1640–1644, 1998.

[63] M. R. Hee, J. A. Izatt, E. A. Swanson, D. Huang, J. S. Schuman, C. P. Lin, C. A. Puliafito, and J. G. Fujimoto, "Optical coherence tomography of the human retina," *Archives of ophthalmology*, vol. 113, no. 3, pp. 325–332, 1995.

[64] G. Tearney, B. Bouma, S. Boppart, B. Golubovic, E. Swanson, and J. Fujimoto, "Rapid acquisition of in vivo biological images by use of optical coherence tomography," *Optics letters*, vol. 21, no. 17, pp. 1408–1410, 1996.

[65] Y. Pan, E. Lankenou, J. Welzel, R. Birngruber, and R. Engelhardt, "Optical coherence-gated imaging of biological tissues," *IEEE Journal of selected topics in Quantum Electronics*, vol. 2, no. 4, pp. 1029–1034, 1996.

[66] J. Szydlo, N. Delachenal, R. Gianotti, R. Wälti, H. Bleuler, and R. Salathe, "Air-turbine driven optical low-coherence reflectometry at 28.6-khz scan repetition rate," *Optics communications*, vol. 154, no. 1-3, pp. 1–4, 1998.

[67] T. Pfeiffer, M. Petermann, W. Draxinger, C. Jirauschek, and R. Huber, "Ultra low noise fourier domain mode locked laser for high quality megahertz optical coherence tomography," *Biomedical Optics Express*, vol. 9, no. 9, pp. 4130–4148, 2018.

[68] J. Xu, X. Wei, L. Yu, C. Zhang, J. Xu, K. Wong, and K. K. Tsia, "High-performance multi-megahertz optical coherence tomography based on amplified optical time-stretch," *Biomedical Optics Express*, vol. 6, no. 4, pp. 1340–1350, 2015.

[69] A. Yasin Alibhai, C. Or, and A. J. Witkin, "Swept source optical coherence tomography: a review," *Current Ophthalmology Reports*, vol. 6, no. 1, pp. 7–16, 2018.

[70] P. Andretzky, M. Knauer, F. Kiesewetter, and G. Haeusler, "Optical coherence tomography by spectral radar: improvement of signal-to-noise ratio," in *Coherence Domain Optical Methods in Biomedical Science and Clinical Applications IV*, V. V. Tuchin, J. A. Izatt, and J. G. Fujimoto, Eds., vol. 3915. SPIE, Apr. 2000, p. 55.

[71] T. Mitsui, "Dynamic range of optical reflectometry with spectral interferometry," *Japanese Journal of Applied Physics, Part 1: Regular Papers and Short Notes and Review Papers*, vol. 38, no. 10, pp. 6133–6137, Oct. 1999.

[72] G. Häusler and M. W. Lindner, "Coherence radar and spectral radar - new tools for dermatological diagnosis," *Journal of Biomedical Optics*, vol. 3, no. 1, pp. 21–31, 1998.

[73] J. F. De Boer, B. Cense, B. H. Park, M. C. Pierce, G. J. Tearney, and B. E. Bouma, "Improved signal-to-noise ratio in spectral-domain compared with time-domain optical coherence tomography," *Optics letters*, vol. 28, no. 21, pp. 2067–2069, 2003.

[74] M. Choma, M. Sarunic, C. Yang, and J. Izatt, "Sensitivity advantage of swept source and Fourier domain optical coherence tomography," *Optics Express*, vol. 11, no. 18, p. 2183, Sep. 2003.

[75] S. Yun, G. Tearney, J. de Boer, N. Iftimia, and B. Bouma, "High-speed optical frequency-domain imaging," *Optics Express*, vol. 11, no. 22, p. 2953, Nov. 2003.

[76] R. Leitgeb, F. Placzek, E. Rank, L. Krainz, R. Haindl, Q. Li, M. Liu, M. Andreana, A. Unterhuber, T. Schmoll *et al.*, "Enhanced medical diagnosis for doctors: a perspective of optical coherence tomography," *Journal of Biomedical Optics*, vol. 26, no. 10, p. 100601, 2021.

[77] J. Fujimoto and E. Swanson, "The development, commercialization, and impact of optical coherence tomography," *Investigative ophthalmology & visual science*, vol. 57, no. 9, pp. OCT1–OCT13, 2016.

[78] E. Swanson and D. Huang, "Ophthalmic oct reaches $1 billion per year," *Retinal Physician*, vol. 8, no. 4, p. 45, 2011.

[79] Z. A. Ali, K. Karimi Galougahi, A. Maehara, R. A. Shlofmitz, O. Ben-Yehuda, G. S. Mintz, and G. W. Stone, "Intracoronary optical coherence tomography 2018: current status and future directions," *JACC: Cardiovascular Interventions*, vol. 10, no. 24, pp. 2473–2487, 2017.

[80] G. J. Tearney, E. Regar, T. Akasaka, T. Adriaenssens, P. Barlis, H. G. Bezerra, B. Bouma, N. Bruining, J.-m. Cho, S. Chowdhary *et al.*, "Consensus standards for acquisition, measurement, and reporting of intravascular optical coherence tomography studies: a report from the international working group for intravascular optical coherence tomography standardization and validation," *Journal of the American College of Cardiology*, vol. 59, no. 12, pp. 1058–1072, 2012.

[81] T. Kume, H. Okura, Y. Miyamoto, R. Yamada, K. Saito, T. Tamada, T. Koyama, Y. Neishi, A. Hayashida, T. Kawamoto *et al.*, "Natural history of stent edge dissection, tissue protrusion and incomplete stent apposition detectable only on optical coherence tomography after stent implantation–preliminary observation–," *Circulation Journal*, vol. 76, no. 3, pp. 698–703, 2012.

[82] T. Kume and S. Uemura, "Current clinical applications of coronary optical coherence tomography," *Cardiovascular intervention and therapeutics*, vol. 33, no. 1, pp. 1–10, 2018.

[83] J. E. Phipps, T. Hoyt, D. Vela, T. Wang, J. E. Michalek, L. M. Buja, I.-K. Jang, T. E. Milner, and M. D. Feldman, "Diagnosis of thin-capped fibroatheromas in intravascular optical coherence tomography images: effects of light scattering," *Circulation: Cardiovascular Interventions*, vol. 9, no. 7, p. e003163, 2016.

[84] G. Van Soest, T. P. Goderie, E. Regar, S. Koljenovic, A. G. J. van Leenders, N. Gonzalo, S. van Noorden, T. Okamura, B. E. Bouma, G. J. Tearney *et al.*, "Atherosclerotic tissue characterization in vivo by optical coherence tomography attenuation imaging," *Journal of Biomedical Optics*, vol. 15, no. 1, p. 011105, 2010.

[85] G. van Soest, E. Regar, T. P. Goderie, N. Gonzalo, S. Koljenović, G. J. van Leenders, P. W. Serruys, and A. F. van der Steen, "Pitfalls in plaque characterization by oct: image artifacts in native coronary arteries," *JACC: Cardiovascular Imaging*, vol. 4, no. 7, pp. 810–813, 2011.

[86] C. V. Bourantas, F. A. Jaffer, F. J. Gijsen, G. Van Soest, S. P. Madden, B. K. Courtney, A. M. Fard, E. Tenekecioglu, Y. Zeng, A. F. Van Der Steen *et al.*, "Hybrid intravascular imaging: recent advances, technical considerations, and current applications in the study of plaque pathophysiology," *European heart journal*, vol. 38, no. 6, pp. 400–412, 2017.

[87] A. Alex, M. Noti, E. D. T. Wojno, D. Artis, and C. Zhou, "Characterization of eosinophilic esophagitis murine models using optical coherence tomography," *Biomedical Optics Express*, vol. 5, no. 2, pp. 609–620, 2014.

[88] C. J. Sheil, A. Wartak, J. A. Gardecki, A. L. Gregg, and G. J. Tearney, "Characterizing subepithelial remodeling in eosinophilic esophagitis with ps-μoct," in *Endoscopic Microscopy XVII*. SPIE, 2022, p. PC119370J.

[89] A. M. Sergeev, V. Gelikonov, G. Gelikonov, F. I. Feldchtein, R. Kuranov, N. Gladkova, N. Shakhova, L. Snopova, A. Shakhov, I. Kuznetzova *et al.*, "In vivo endoscopic oct imaging of precancer and cancer states of human mucosa," *Optics Express*, vol. 1, no. 13, pp. 432–440, 1997.

[90] G. Zuccaro, N. Gladkova, J. Vargo, F. Feldchtein, E. Zagaynova, D. Conwell, G. Falk, J. Goldblum, J. Dumot, J. Ponsky *et al.*, "Optical coherence tomography of the esophagus and proximal stomach in health and disease," *The American journal of gastroenterology*, vol. 96, no. 9, pp. 2633–2639, 2001.

[91] E. Masci, B. Mangiavillano, G. Barera, B. Parma, L. Albarello, A. Mariani, C. Doglioni, and P. A. Testoni, "Optical coherence tomography in pediatric patients: a feasible technique for diagnosing celiac disease in children with villous atrophy," *Digestive and Liver Disease*, vol. 41, no. 9, pp. 639–643, 2009.

[92] E. Masci, B. Mangiavillano, L. Albarello, A. Mariani, C. Doglioni, and P. A. Testoni, "Pilot study on the correlation of optical coherence tomography with histology in celiac disease and normal subjects," *Journal of gastroenterology and hepatology*, vol. 22, no. 12, pp. 2256–2260, 2007.

[93] E. Zagaynova, N. Gladkova, N. Shakhova, G. Gelikonov, and V. Gelikonov, "Endoscopic oct with forward-looking probe: clinical studies in urology and gastroenterology," *Journal of Biophotonics*, vol. 1, no. 2, pp. 114–128, 2008.

[94] D. C. Adler, C. Zhou, T.-H. Tsai, J. Schmitt, Q. Huang, H. Mashimo, and J. G. Fujimoto, "Three-dimensional endomicroscopy of the human colon using optical coherence tomography," *Optics Express*, vol. 17, no. 2, pp. 784–796, 2009.

[95] P. Consolo, G. Strangio, C. Luigiano, G. Giacobbe, S. Pallio, and L. Familiari, "Optical coherence tomography in inflammatory bowel disease: prospective evaluation of 35 patients," *Diseases of the colon & rectum*, vol. 51, no. 9, pp. 1374–1380, 2008.

[96] M. Arvanitakis, L. Hookey, G. Tessier, P. Demetter, N. Nagy, A. Stellke, V. De Maertelaer, J. Devière, and O. Le Moine, "Intraductal optical coherence tomography during endoscopic retrograde cholangiopancreatography for investigation of biliary strictures," *Endoscopy*, vol. 41, no. 08, pp. 696–701, 2009.

[97] Y. Chen, A. D. Aguirre, P.-L. Hsiung, S.-W. Huang, H. Mashimo, J. M. Schmitt, and J. G. Fujimoto, "Effects of axial resolution improvement on optical coherence tomography (oct) imaging of gastrointestinal tissues," *Optics Express*, vol. 16, no. 4, pp. 2469–2485, 2008.

[98] Y. Chen, A. Aguirre, P.-L. Hsiung, S. Desai, P. Herz, M. Pedrosa, Q. Huang, M. Figueiredo, S.-W. Huang, A. Koski *et al.*, "Ultrahigh resolution optical coherence tomography of barrett's esophagus: preliminary descriptive clinical study correlating images with histology," *Endoscopy*, vol. 39, no. 07, pp. 599–605, 2007.

[99] H.-C. Lee, O. O. Ahsen, K. Liang, Z. Wang, M. Figueiredo, M. G. Giacomelli, B. Potsaid, Q. Huang, H. Mashimo, and J. G. Fujimoto, "Endoscopic optical coherence tomography angiography microvascular features associated with dysplasia in barrett's esophagus (with video)," *Gastrointestinal endoscopy*, vol. 86, no. 3, pp. 476–484, 2017.

[100] A.-F. Swager, G. J. Tearney, C. L. Leggett, M. G. van Oijen, S. L. Meijer, B. L. Weusten, W. L. Curvers, and J. J. Bergman, "Identification of volumetric laser endomicroscopy features predictive for early neoplasia in barrett's esophagus using high-quality histological correlation," *Gastrointestinal endoscopy*, vol. 85, no. 5, pp. 918–926, 2017.

[101] C. L. Leggett, D. K. Chan, E. C. Gorospe, A. Nehra, M. Anderson, L. S. Lutzke, and K. K. Wang, "Tu1542 diagnostic performance of in-vivo volumetric laser endomicroscopy for detection of barrett's esophagus dysplasia," *Gastrointestinal Endoscopy*, vol. 81, no. 5, p. AB502, 2015.

[102] A. J. Trindade, B. J. George, J. Berkowitz, D. V. Sejpal, and M. J. McKinley, "Volumetric laser endomicroscopy can target neoplasia not detected by conventional endoscopic measures in long segment barrett's esophagus," *Endoscopy international open*, vol. 4, no. 03, pp. E318–E322, 2016.

[103] M. A. C. Rodriguez, D. T. H. de Moura, I. B. Ribeiro, W. M. Bernardo, F. H. A. Morita, S. B. Marques, P. Sakai, and E. G. H. de Moura, "Volumetric laser endomicroscopy and optical coherence tomography in barrett's esophagus: a systematic review and meta-analysis," *Endoscopy International Open*, vol. 7, no. 09, pp. E1078–E1091, 2019.

[104] P. Sharma, T. J. Savides, M. I. Canto, D. A. Corley, G. W. Falk, J. R. Goldblum, K. K. Wang, M. B. Wallace, and H. C. Wolfsen, "The american society for gastrointestinal endoscopy pivi (preservation and incorporation of valuable endoscopic innovations) on imaging in barrett's esophagus," *Gastrointestinal endoscopy*, vol. 76, no. 2, pp. 252–254, 2012.

[105] J. F. De Boer, C. K. Hitzenberger, and Y. Yasuno, “Polarization sensitive optical coherence tomography–a review,” *Biomedical Optics Express*, vol. 8, no. 3, pp. 1838–1873, 2017.

[106] B. Baumann, “Polarization sensitive optical coherence tomography: a review of technology and applications,” *Applied Sciences*, vol. 7, no. 5, p. 474, 2017.

[107] F. Feroldi, “Endoscopic structural and molecular optical imaging: From lab to clinic,” Ph.D. dissertation, Vrije Universiteit Amsterdam, 2019.

[108] R. C. Haskell, F. D. Carlson, and P. S. Blank, “Form birefringence of muscle,” *Biophysical journal*, vol. 56, no. 2, pp. 401–413, 1989.

[109] K. H. Kim, M. C. Pierce, G. N. Maguluri, B. H. Park, S. J. Yoon, M. Lydon, R. L. Sheridan, and J. F. De Boer, “In vivo imaging of human burn injuries with polarization-sensitive optical coherence tomography,” *Journal of Biomedical Optics*, vol. 17, no. 6, p. 066012, 2012.

[110] D. C. Adams and M. J. Suter, “Processing-based approach for resolving the sample optic axis in endoscopic polarization-sensitive optical coherence tomography,” *Optics Express*, vol. 26, no. 19, pp. 24 917–24 927, 2018.

[111] M. Pircher, C. K. Hitzenberger, and U. Schmidt-Erfurth, “Polarization sensitive optical coherence tomography in the human eye,” *Progress in retinal and eye research*, vol. 30, no. 6, pp. 431–451, 2011.

[112] J. Li, F. Feroldi, J. de Lange, J. M. Daniels, K. Grünberg, and J. F. de Boer, “Polarization sensitive optical frequency domain imaging system for endobronchial imaging,” *Optics Express*, vol. 23, no. 3, pp. 3390–3402, 2015.

[113] F. Feroldi, J. Willemse, V. Davidoiu, M. G. Gräfe, D. J. van Iperen, A. W. Goorsenberg, J. T. Annema, J. M. Daniels, P. I. Bonta, and J. F. de Boer, “In vivo multifunctional optical coherence tomography at the periphery of the lungs,” *Biomedical Optics Express*, vol. 10, no. 6, pp. 3070–3091, 2019.

[114] D. C. Adams, A. Majid, and M. J. Suter, “Polarization mode dispersion correction in endoscopic polarization-sensitive optical coherence tomography with incoherent polarization input states,” *Biomed. Opt. Express*, vol. 13, no. 6, pp. 3446–3460, Jun 2022.

[115] M. Villiger, B. Braaf, N. Lippok, K. Otsuka, S. K. Nadkarni, and B. E. Bouma, “Optic axis mapping with catheter-based polarization-sensitive optical coherence tomography,” *Optica*, vol. 5, no. 10, pp. 1329–1337, 2018.

[116] S. K. Nadkarni, M. C. Pierce, B. H. Park, J. F. de Boer, P. Whittaker, B. E. Bouma, J. E. Bressner, E. Halpern, S. L. Houser, and G. J. Tearney, “Measurement of collagen and smooth muscle cell content in atherosclerotic plaques using polarization-sensitive optical coherence tomography,” *Journal of the American College of Cardiology*, vol. 49, no. 13, pp. 1474–1481, 2007.

[117] M. Vaselli, P. C. Wijsman, J. Willemse, A. W. Goorsenberg, F. Feroldi, J. N. d’Hooghe, J. T. Annema, J. F. de Boer, and P. I. Bonta, “Polarization sensitive optical coherence tomography for bronchoscopic airway smooth muscle detection in bronchial thermoplasty-treated patients with asthma,” *Chest*, vol. 160, no. 2, pp. 432–435, 2021.

[118] D. C. Adams, L. P. Hariri, A. J. Miller, Y. Wang, J. L. Cho, M. Villiger, J. A. Holz, M. V. Szabari, D. L. Hamilos, R. Scott Harris *et al.*, “Birefringence microscopy platform for assessing airway smooth muscle structure and function in vivo,” *Science translational medicine*, vol. 8, no. 359, pp. 359ra131–359ra131, 2016.

[119] M. Liu and W. Drexler, "Optical coherence tomography angiography and photoacoustic imaging in dermatology," *Photochem. Photobiol. Sci.*, vol. 18, pp. 945–962, 2019.

[120] M. Ulrich, L. Themstrup, N. de Carvalho, M. Manfredi, C. Grana, S. Ciardo, R. Kästle, J. Holmes, R. Whitehead, G. B. Jemec *et al.*, "Dynamic optical coherence tomography in dermatology," *Dermatology*, vol. 232, no. 3, pp. 298–311, 2016.

[121] B. J. Vakoc, D. Fukumura, R. K. Jain, and B. E. Bouma, "Cancer imaging by optical coherence tomography: preclinical progress and clinical potential," *Nature Reviews Cancer*, vol. 12, no. 5, pp. 363–368, 2012.

[122] A. J. Deegan, W. Wang, S. Men, Y. Li, S. Song, J. Xu, and R. K. Wang, "Optical coherence tomography angiography monitors human cutaneous wound healing over time," *Quantitative imaging in medicine and surgery*, vol. 8, no. 2, p. 135, 2018.

[123] K. Chalam and K. Sambhav, "Optical coherence tomography angiography in retinal diseases," *Journal of ophthalmic & vision research*, vol. 11, no. 1, p. 84, 2016.

[124] R. Reif and W. R.K., "Optical microangiography based on optical coherence tomography," in *Optical coherence tomography*. Springer, 2015, pp. 1373–1398.

[125] R. A. Leitgeb, R. M. Werkmeister, C. Blatter, and L. Schmetterer, "Doppler optical coherence tomography," *Progress in retinal and eye research*, vol. 41, pp. 26–43, 2014.

[126] V. X. Yang, S.-j. Tang, M. L. Gordon, B. Qi, G. Gardiner, M. Cirocco, P. Kortan, G. B. Haber, G. Kandel, I. A. Vitkin *et al.*, "Endoscopic doppler optical coherence tomography in the human gi tract: initial experience," *Gastrointestinal endoscopy*, vol. 61, no. 7, pp. 879–890, 2005.

[127] Y. Jia, O. Tan, J. Tokayer, B. Potsaid, Y. Wang, J. J. Liu, M. F. Kraus, H. Subhash, J. G. Fujimoto, J. Hornegger, and D. Huang, "Split-spectrum amplitude-decorrelation angiography with optical coherence tomography," *Opt. Express*, vol. 20, no. 4, pp. 4710–4725, Feb 2012.

[128] J. Enfield, E. Jonathan, and M. Leahy, "In vivo imaging of the microcirculation of the volar forearm using correlation mapping optical coherence tomography (cmoct)," *Biomedical Optics Express*, vol. 2, no. 5, pp. 1184–1193, 2011.

[129] M. S. Mahmud, D. W. Cadotte, B. Vuong, C. Sun, T. W. Luk, A. Mariampillai, and V. X. Yang, "Review of speckle and phase variance optical coherence tomography to visualize microvascular networks," *Journal of Biomedical Optics*, vol. 18, no. 5, p. 050901, 2013.

[130] A. Zhang, Q. Zhang, C.-L. Chen, and R. K. Wang, "Methods and algorithms for optical coherence tomography-based angiography: a review and comparison," *Journal of Biomedical Optics*, vol. 20, no. 10, p. 100901, 2015.

[131] T.-H. Tsai, H.-C. Lee, O. O. Ahsen, K. Liang, M. G. Giacomelli, B. M. Potsaid, Y. K. Tao, V. Jayaraman, M. Figueiredo, Q. Huang *et al.*, "Ultrahigh speed endoscopic optical coherence tomography for gastroenterology," *Biomedical Optics Express*, vol. 5, no. 12, pp. 4387–4404, 2014.

[132] K. Liang, Z. Wang, O. O. Ahsen, H.-C. Lee, B. M. Potsaid, V. Jayaraman, A. Cable, H. Mashimo, X. Li, and J. G. Fujimoto, "Cycloid scanning for wide field optical coherence tomography endomicroscopy and angiography in vivo," *Optica*, vol. 5, no. 1, pp. 36–43, Jan. 2018.

[133] H. S. Nam and H. Yoo, “Spectroscopic optical coherence tomography: A review of concepts and biomedical applications,” *Applied Spectroscopy Reviews*, vol. 53, no. 2-4, pp. 91–111, 2018.

[134] N. Bosschaart, T. van Leeuwen, M. Aalders, B. Hermann, W. Drexler, and D. J. Faber, “Spectroscopic low coherence interferometry,” in *Optical Coherence Tomography*. Springer, 2015, pp. 1163–1187.

[135] F. E. Robles, C. Wilson, G. Grant, and A. Wax, “Molecular imaging true-colour spectroscopic optical coherence tomography,” *Nature photonics*, vol. 5, no. 12, pp. 744–747, 2011.

[136] C. Xu, F. Kamalabadi, and S. A. Boppart, “Comparative performance analysis of time–frequency distributions for spectroscopic optical coherence tomography,” *Applied optics*, vol. 44, no. 10, pp. 1813–1822, 2005.

[137] S. Chang and A. K. Bowden, “Review of methods and applications of attenuation coefficient measurements with optical coherence tomography,” *Journal of Biomedical Optics*, vol. 24, no. 9, p. 090901, 2019.

[138] P. Gong, M. Almasian, G. Van Soest, D. M. De Bruin, T. G. Van Leeuwen, D. D. Sampson, and D. J. Faber, “Parametric imaging of attenuation by optical coherence tomography: review of models, methods, and clinical translation,” *Journal of Biomedical Optics*, vol. 25, no. 4, p. 040901, 2020.

[139] Y. Yang, T. Wang, N. C. Biswal, M. Brewer, Q. Zhu, X. Wang, and M. Sanders, “Optical scattering coefficient estimated by optical coherence tomography correlates with collagen content in ovarian tissue,” *Journal of Biomedical Optics*, vol. 16, no. 9, p. 090504, 2011.

[140] B. G. Muller, R. A. van Kollenburg, A. Swaan, E. C. Zwartkruis, M. J. Brandt, L. S. Wilk, M. Almasian, A. W. Schreurs, D. J. Faber, L. R. Rozendaal *et al.*, “Needle-based optical coherence tomography for the detection of prostate cancer: a visual and quantitative analysis in 20 patients,” *Journal of Biomedical Optics*, vol. 23, no. 8, p. 086001, 2018.

[141] A. Swaan, B. G. Muller, L. S. Wilk, M. Almasian, R. A. van Kollenburg, E. Zwartkruis, L. R. Rozendaal, D. M. de Bruin, D. J. Faber, T. G. van Leeuwen *et al.*, “One-to-one registration of en-face optical coherence tomography attenuation coefficients with histology of a prostatectomy specimen,” p. e201800274, 2019.

[142] J. A. Garcia, F. Benboujja, K. Beaudette, R. Guo, C. Boudoux, and C. J. Hartnick, “Using attenuation coefficients from optical coherence tomography as markers of vocal fold maturation,” *The Laryngoscope*, vol. 126, no. 6, pp. E218–E223, 2016.

[143] D. J. Faber, F. J. Van Der Meer, M. C. Aalders, and T. G. van Leeuwen, “Quantitative measurement of attenuation coefficients of weakly scattering media using optical coherence tomography,” *Optics Express*, vol. 12, no. 19, pp. 4353–4365, 2004.

[144] K. A. Vermeer, J. Mo, J. J. Weda, H. G. Lemij, and J. F. de Boer, “Depth-resolved model-based reconstruction of attenuation coefficients in optical coherence tomography,” *Biomedical Optics Express*, vol. 5, no. 1, pp. 322–337, 2014.

[145] M. Chen, J. Wang, W. Tan, Y. Feng, and G. Zheng, “Miniaturized all fiber probe for optical coherence tomography and ph detection of biological tissue,” *Journal of Biophotonics*, vol. 14, no. 2, p. e202000239, 2021.

[146] A. L. Buenconsejo, G. Hohert, M. Manning, E. Abouei, R. Tingley, I. Janzen, J. McAlpine, D. Miller, A. Lee, P. Lane, and C. MacAulay, "Submillimeter diameter rotary-pullback fiber-optic endoscope for narrowband red-green-blue reflectance, optical coherence tomography, and autofluorescence in vivo imaging," *Journal of Biomedical Optics*, vol. 25, no. 3, pp. 1 – 7, 2019.

[147] E. Brace, S. Bernard, J. Malone, A. Tanskanen, A. Lee, C. Poh, and P. Lane, "Micromotor OCTA-FLIM catheter for cancer screening," in *Endoscopic Microscopy XVII*, vol. PC11937, International Society for Optics and Photonics. SPIE, 2022.

[148] S. Y. Ryu, H. Y. Choi, J. Na, E. S. Choi, and B. H. Lee, "Combined system of optical coherence tomography and fluorescence spectroscopy based on double-cladding fiber," *Optics letters*, vol. 33, no. 20, pp. 2347–2349, 2008.

[149] Y. Li, J. Jing, J. Yu, B. Zhang, T. Huo, Q. Yang, and Z. Chen, "Multimodality endoscopic optical coherence tomography and fluorescence imaging technology for visualization of layered architecture and subsurface microvasculature," *Optics letters*, vol. 43, no. 9, pp. 2074–2077, 2018.

[150] Y. Li, Z. Zhu, J. J. Chen, J. C. Jing, C.-H. Sun, S. Kim, P.-S. Chung, and Z. Chen, "Multimodal endoscopy for colorectal cancer detection by optical coherence tomography and near-infrared fluorescence imaging," *Biomed. Opt. Express*, vol. 10, no. 5, pp. 2419–2429, May 2019.

[151] F. Feroldi, M. Verlaan, H. Knaus, V. Davidoiu, D. J. Vugts, G. A. van Dongen, C. F. Molthoff, and J. F. de Boer, "High resolution combined molecular and structural optical imaging of colorectal cancer in a xenograft mouse model," *Biomedical Optics Express*, vol. 9, no. 12, pp. 6186–6204, 2018.

[152] J. Mavadia, J. Xi, Y. Chen, and X. Li, "An all-fiber-optic endoscopy platform for simultaneous oct and fluorescence imaging," *Biomedical Optics Express*, vol. 3, no. 11, pp. 2851–2859, 2012.

[153] A. Wartak, A. K. Kelada, P. A. L. Alarcon, A. L. Bablouzian, O. O. Ahsen, A. L. Gregg, Y. Wei, K. Bollavaram, C. J. Sheil, E. Farewell *et al.*, "Dual-modality optical coherence tomography and fluorescence tethered capsule endomicroscopy," *Biomedical Optics Express*, vol. 12, no. 7, pp. 4308–4323, 2021.

[154] A. Wartak, Y. Wei, A. Bablouzian, P. L. Alarcon, K. Bollavaram, O. Ahsen, E. Farewell, S. VanTol, A. Kelada, A. Gregg *et al.*, "Multimodality optical coherence tomography based tethered capsule endomicroscopy for upper gastrointestinal tract imaging," in *Optical Coherence Tomography and Coherence Domain Optical Methods in Biomedicine XXV*, vol. 11630. International Society for Optics and Photonics, 2021, p. 116300P.

[155] D. Lorenser, B. C. Quirk, M. Auger, W.-J. Madore, R. W. Kirk, N. Godbout, D. D. Sampson, C. Boudoux, and R. A. McLaughlin, "Dual-modality needle probe for combined fluorescence imaging and three-dimensional optical coherence tomography," *Optics Letters*, vol. 38, no. 3, p. 266, Feb. 2013.

[156] L. Scolaro, D. Lorenser, W.-J. Madore, R. W. Kirk, A. S. Kramer, G. C. Yeoh, N. Godbout, D. D. Sampson, C. Boudoux, and R. A. McLaughlin, "Molecular imaging needles: dual-modality optical coherence tomography and fluorescence imaging of labeled antibodies deep in tissue," *Biomedical Optics Express*, vol. 6, no. 5, p. 1767, May 2015.

[157] H. Pahlevaninezhad, A. M. Lee, T. Shaipanich, R. Raizada, L. Cahill, G. Hohert, V. X. Yang, S. Lam, C. MacAulay, and P. Lane, "A high-efficiency fiber-based imaging system for co-registered autofluorescence and optical coherence tomography," *Biomedical Optics Express*, vol. 5, no. 9, pp. 2978–2987, 2014.

[158] X. Dai, L. Xi, C. Duan, H. Yang, H. Xie, and H. Jiang, "Miniature probe integrating optical-resolution photoacoustic microscopy, optical coherence tomography, and ultrasound imaging: proof-of-concept," *Optics letters*, vol. 40, no. 12, pp. 2921–2924, 2015.

[159] X. Dai, H. Yang, T. Shan, H. Xie, S. A. Berceli, and H. Jiang, "Miniature endoscope for multimodal imaging," *ACS Photonics*, vol. 4, no. 1, pp. 174–180, 2017.

[160] A. M. Fard, P. Vacas-Jacques, E. Hamidi, H. Wang, R. W. Carruth, J. A. Gardecki, and G. J. Tearney, "Optical coherence tomography–near infrared spectroscopy system and catheter for intravascular imaging," *Optics Express*, vol. 21, no. 25, pp. 30 849–30 858, 2013.

[161] S. Liang, C. Sun, A. Saidi, J. Jing, G. Liu, J. Li, J. Zhang, Z. Chen, and J. Narula, "Intravascular atherosclerotic imaging with combined fluorescence and optical coherence tomography probe based on a double-clad fiber combiner," *Journal of Biomedical Optics*, vol. 17, no. 7, p. 070501, 2012.

[162] H. Yoo, J. W. Kim, M. Shishkov, E. Namati, T. Morse, R. Shubochkin, J. R. McCarthy, V. Ntziachristos, B. E. Bouma, F. A. Jaffer *et al.*, "Intra-arterial catheter for simultaneous microstructural and molecular imaging in vivo," *Nature medicine*, vol. 17, no. 12, pp. 1680–1684, 2011.

[163] S. Lee, M. W. Lee, H. S. Cho, J. W. Song, H. S. Nam, D. J. Oh, K. Park, W.-Y. Oh, H. Yoo, and J. W. Kim, "Fully integrated high-speed intravascular optical coherence tomography/near-infrared fluorescence structural/molecular imaging in vivo using a clinically available near-infrared fluorescence–emitting indocyanine green to detect inflamed lipid-rich atheromata in coronary-sized vessels," *Circulation: Cardiovascular Interventions*, vol. 7, no. 4, pp. 560–569, 2014.

[164] G. J. Ughi, H. Wang, E. Gerbaud, J. A. Gardecki, A. M. Fard, E. Hamidi, P. Vacas-Jacques, M. Rosenberg, F. A. Jaffer, and G. J. Tearney, "Clinical characterization of coronary atherosclerosis with dual-modality oct and near-infrared autofluorescence imaging," *JACC: Cardiovascular imaging*, vol. 9, no. 11, pp. 1304–1314, 2016.

[165] H. Wang, J. A. Gardecki, G. J. Ughi, P. V. Jacques, E. Hamidi, and G. J. Tearney, "Ex vivo catheter-based imaging of coronary atherosclerosis using multimodality oct and niraf excited at 633 nm," *Biomedical Optics Express*, vol. 6, no. 4, pp. 1363–1375, 2015.

[166] X. Chen, W. Kim, M. J. Serafino, Z. Tan, J. A. Jo, and B. E. Applegate, "Dual-modality optical coherence tomography and frequency-domain fluorescence lifetime imaging microscope system for intravascular imaging," *Journal of Biomedical Optics*, vol. 25, no. 9, p. 096010, 2020.

[167] H. S. Nam, W. J. Kang, M. W. Lee, J. W. Song, J. W. Kim, W.-Y. Oh, and H. Yoo, "Multispectral analog-mean-delay fluorescence lifetime imaging combined with optical coherence tomography," *Biomedical Optics Express*, vol. 9, no. 4, pp. 1930–1947, 2018.

[168] M. W. Lee, J. W. Song, W. J. Kang, H. S. Nam, T. S. Kim, S. Kim, W.-Y. Oh, J. W. Kim, and H. Yoo, "Comprehensive intravascular imaging of atherosclerotic plaque in vivo using optical coherence tomography and fluorescence lifetime imaging," *Scientific reports*, vol. 8, no. 1, pp. 1–12, 2018.

[169] T. Wang, A. McElroy, D. Halaney, D. Vela, E. Fung, S. Hossain, J. Phipps, B. Wang, B. Yin, M. D. Feldman *et al.*, “Dual-modality fiber-based oct-tpl imaging system for simultaneous microstructural and molecular analysis of atherosclerotic plaques,” *Biomedical Optics Express*, vol. 6, no. 5, pp. 1665–1678, 2015.

[170] D. Vega, D. Galvez, G. Romano, N. Y. Pham, R. Cordova, M. Aitken, S. Suebka, J. Heusinkveld, and J. K. Barton, “Triple-modality co-registered endoscope featuring wide-field reflectance imaging, and high-resolution multiphoton and optical coherence microscopy,” *Journal of Optical Microsystems*, vol. 1, no. 4, p. 044502, 2021.

[171] B. E. Sherlock, J. E. Phipps, J. Bec, and L. Marcu, “Simultaneous, label-free, multispectral fluorescence lifetime imaging and optical coherence tomography using a double-clad fiber,” *Optics letters*, vol. 42, no. 19, pp. 3753–3756, 2017.

[172] Y. Yang, X. Li, T. Wang, P. D. Kumavor, A. Aguirre, K. K. Shung, Q. Zhou, M. Sanders, M. Brewer, and Q. Zhu, “Integrated optical coherence tomography, ultrasound and photoacoustic imaging for ovarian tissue characterization,” *Biomedical Optics Express*, vol. 2, no. 9, pp. 2551–2561, 2011.

[173] J. Malone, G. Hohert, J. McAlpine, L. Hoang, C. MacAulay, and P. Lane, “Co-registered optical coherence tomography (oct) and autofluorescence imaging (afi) of ex vivo fallopian tubes for early ovarian cancer detection,” in *Multimodal Biomedical Imaging XVII*. SPIE, 2022, p. PC1195206.

[174] P. K. Capon, J. Li, A. J. Horsfall, S. Yagoub, E. P. Schartner, A. Khalid, R. W. Kirk, M. S. Purdey, K. R. Dunning, R. A. McLaughlin *et al.*, “A silk-based functionalization architecture for single fiber imaging and sensing,” *Advanced Functional Materials*, vol. 32, no. 3, p. 2010713, 2022.

[175] A. C. Croce and G. Bottiroli, “Autofluorescence spectroscopy and imaging: a tool for biomedical research and diagnosis,” *European journal of histochemistry: EJH*, vol. 58, no. 4, 2014.

[176] R. Datta, T. M. Heaster, J. T. Sharick, A. A. Gillette, and M. C. Skala, “Fluorescence lifetime imaging microscopy: fundamentals and advances in instrumentation, analysis, and applications,” *Journal of Biomedical Optics*, vol. 25, no. 7, p. 071203, 2020.

[177] X. Liu, D. Lin, W. Becker, J. Niu, B. Yu, L. Liu, and J. Qu, “Fast fluorescence lifetime imaging techniques: A review on challenge and development,” *Journal of Innovative Optical Health Sciences*, vol. 12, no. 05, p. 1930003, 2019.

[178] S. R. Bloch, F. Lesage, L. McIntosh, A. H. Gandjbakhche, K. Liang, and S. Achilefu, “Whole-body fluorescence lifetime imaging of a tumor-targeted near-infrared molecular probe in mice,” *Journal of Biomedical Optics*, vol. 10, no. 5, pp. 1 – 8, 2005.

[179] P. Debie and S. Hernot, “Emerging fluorescent molecular tracers to guide intra-operative surgical decision-making,” *Frontiers in Pharmacology*, vol. 10, p. 510, 2019.

[180] A. B. E. Attia, G. Balasundaram, M. Moothanchery, U. Dinish, R. Bi, V. Ntziachristos, and M. Olivo, “A review of clinical photoacoustic imaging: Current and future trends,” *Photoacoustics*, vol. 16, p. 100144, 2019.

[181] B. T. Cox, J. G. Laufer, P. C. Beard, and S. R. Arridge, “Quantitative spectroscopic photoacoustic imaging: a review,” *Journal of Biomedical Optics*, vol. 17, no. 6, p. 061202, 2012.

[182] B. Vahabzadeh, A. B. Seetharam, M. B. Cook, S. Wani, A. Rastogi, A. Bansal, D. S. Early, and P. Sharma, “Validation of the prague c & m criteria for the endoscopic grading of barrett’s esophagus by gastroenterology trainees: a multicenter study,” *Gastrointestinal endoscopy*, vol. 75, no. 2, pp. 236–241, 2012.

[183] C. L. Booth and K. S. Thompson, “Barrett’s esophagus: a review of diagnostic criteria, clinical surveillance practices and new developments,” *Journal of gastrointestinal oncology*, vol. 3, no. 3, p. 232, 2012.

[184] K. Gono, T. Obi, M. Yamaguchi, N. Oyama, H. Machida, Y. Sano, S. Yoshida, Y. Hamamoto, and T. Endo, “Appearance of enhanced tissue features in narrow-band endoscopic imaging,” *Journal of Biomedical Optics*, vol. 9, no. 3, pp. 568–577, 2004.

[185] W. L. Curvers, F. J. van den Broek, J. B. Reitsma, E. Dekker, and J. J. Bergman, “Systematic review of narrow-band imaging for the detection and differentiation of abnormalities in the esophagus and stomach (with video),” *Gastrointestinal endoscopy*, vol. 69, no. 2, pp. 307–317, 2009.

[186] G. J. Tearney, S. Waxman, M. Shishkov, B. J. Vakoc, M. J. Suter, M. I. Freilich, A. E. Desjardins, W.-Y. Oh, L. A. Bartlett, M. Rosenberg *et al.*, “Three-dimensional coronary artery microscopy by intracoronary optical frequency domain imaging,” *JACC: Cardiovascular imaging*, vol. 1, no. 6, pp. 752–761, 2008.

[187] S. H. Yun, G. J. Tearney, B. J. Vakoc, M. Shishkov, W. Y. Oh, A. E. Desjardins, M. J. Suter, R. C. Chan, J. A. Evans, I.-K. Jang *et al.*, “Comprehensive volumetric optical microscopy in vivo,” *Nature medicine*, vol. 12, no. 12, pp. 1429–1433, 2006.

[188] M. Kirby, K. Ohtani, T. Nickens, R. M. L. Lisbona, A. M. Lee, T. Shaipanich, P. Lane, C. MacAulay, S. Lam, and H. O. Coxson, “Reproducibility of optical coherence tomography airway imaging,” *Biomedical Optics Express*, vol. 6, no. 11, pp. 4365–4377, 2015.

[189] J. Li, M. de Groot, F. Helderman, J. Mo, J. M. Daniels, K. Grünberg, T. G. Sutedja, and J. F. de Boer, “High speed miniature motorized endoscopic probe for optical frequency domain imaging,” *Optics Express*, vol. 20, no. 22, pp. 24 132–24 138, 2012.

[190] B. G. Muller, D. M. de Bruin, M. J. Brandt, W. van den Bos, S. van Huystee, D. Faber, D. Savci, P. J. Zondervan, T. M. de Reijke, M. P. Laguna-Pes *et al.*, “Prostate cancer diagnosis by optical coherence tomography: First results from a needle based optical platform for tissue sampling,” *Journal of Biophotonics*, vol. 9, no. 5, pp. 490–498, 2016.

[191] W.-J. Madore, E. De Montigny, A. Deschênes, F. Benboujja, M. Leduc, A.-M. Mes-Masson, D. M. Provencher, K. Rahimi, C. Boudoux, and N. Godbout, “Morphologic three-dimensional scanning of fallopian tubes to assist ovarian cancer diagnosis,” *Journal of Biomedical Optics*, vol. 22, no. 7, p. 076012, 2017.

[192] M. J. Gora, J. S. Sauk, R. W. Carruth, K. A. Gallagher, M. J. Suter, N. S. Nishioka, L. E. Kava, M. Rosenberg, B. E. Bouma, and G. J. Tearney, “Tethered capsule endomicroscopy enables less invasive imaging of gastrointestinal tract microstructure,” *Nature medicine*, vol. 19, no. 2, pp. 238–240, 2013.

[193] C.-P. Liang, J. Dong, T. Ford, R. Reddy, H. Hosseiny, H. Farrokhi, M. Beatty, K. Singh, H. Osman, B. Vuong *et al.*, “Optical coherence tomography-guided laser marking with tethered capsule endomicroscopy in unsedated patients,” *Biomedical Optics Express*, vol. 10, no. 3, pp. 1207–1222, 2019.

[194] K. Li, W. Liang, J. Mavadia-Shukla, H.-C. Park, D. Li, W. Yuan, S. Wan, and X. Li, “Super-achromatic optical coherence tomography capsule for ultrahigh-resolution imaging of esophagus,” *Journal of Biophotonics*, vol. 12, no. 3, p. e201800205, 2019.

[195] K. Liang, O. O. Ahsen, A. Murphy, J. Zhang, T. H. Nguyen, B. Potsaid, M. Figueiredo, Q. Huang, H. Mashimo, and J. G. Fujimoto, “Tethered capsule en face optical coherence tomography for imaging barrett’s oesophagus in unsedated patients,” *BMJ open gastroenterology*, vol. 7, no. 1, p. e000444, 2020.

[196] B. J. Vakoc, M. Shishko, S. H. Yun, W.-Y. Oh, M. J. Suter, A. E. Desjardins, J. A. Evans, N. S. Nishioka, G. J. Tearney, and B. E. Bouma, “Comprehensive esophageal microscopy by using optical frequency–domain imaging (with video),” *Gastrointestinal endoscopy*, vol. 65, no. 6, pp. 898–905, 2007.

[197] H.-C. Lee, O. O. Ahsen, K. Liang, Z. Wang, C. Cleveland, L. Booth, B. Potsaid, V. Jayaraman, A. E. Cable, H. Mashimo *et al.*, “Circumferential optical coherence tomography angiography imaging of the swine esophagus using a micromotor balloon catheter,” *Biomedical Optics Express*, vol. 7, no. 8, pp. 2927–2942, 2016.

[198] T.-H. Tsai, O. O. Ahsen, H.-C. Lee, K. Liang, M. Figueiredo, Y. K. Tao, M. G. Giacomelli, B. M. Potsaid, V. Jayaraman, Q. Huang *et al.*, “Endoscopic optical coherence angiography enables 3-dimensional visualization of subsurface microvasculature,” *Gastroenterology*, vol. 147, no. 6, pp. 1219–1221, 2014.

[199] K. Liang, G. Traverso, H.-C. Lee, O. O. Ahsen, Z. Wang, B. Potsaid, M. Giacomelli, V. Jayaraman, R. Barman, A. Cable *et al.*, “Ultrahigh speed en face oct capsule for endoscopic imaging,” *Biomedical Optics Express*, vol. 6, no. 4, pp. 1146–1163, 2015.

[200] W. Yuan, R. Brown, W. Mitzner, L. Yarmus, and X. Li, “Super-achromatic monolithic microprobe for ultrahigh-resolution endoscopic optical coherence tomography at 800 nm,” *Nature communications*, vol. 8, no. 1, pp. 1–9, 2017.

[201] H. Pahlevaninezhad, M. Khorasaninejad, Y.-W. Huang, Z. Shi, L. P. Hariri, D. C. Adams, V. Ding, A. Zhu, C.-W. Qiu, F. Capasso *et al.*, “Nano-optic endoscope for high-resolution optical coherence tomography in vivo,” *Nature photonics*, vol. 12, no. 9, pp. 540–547, 2018.

[202] J. Xi, A. Zhang, Z. Liu, W. Liang, L. Y. Lin, S. Yu, and X. Li, “Diffractive catheter for ultrahigh-resolution spectral-domain volumetric oct imaging,” *Optics letters*, vol. 39, no. 7, pp. 2016–2019, 2014.

[203] J. Bec, C. Li, and L. Marcu, “Broadband, freeform focusing micro-optics for a side-viewing imaging catheter,” *Optics Letters*, vol. 44, no. 20, pp. 4961–4964, 2019.

[204] D. Yelin, B. Bouma, S. Yun, and G. Tearney, “Double-clad fiber for endoscopy,” *Optics letters*, vol. 29, no. 20, pp. 2408–2410, 2004.

[205] S. Lemire-Renaud, M. Strupler, F. Benboujja, N. Godbout, and C. Boudoux, “Double-clad fiber with a tapered end for confocal endomicroscopy,” *Biomedical Optics Express*, vol. 2, no. 11, pp. 2961–2972, 2011.

[206] K. Beaudette, J. Li, J. Lamarre, L. Majeau, and C. Boudoux, “Double-clad fiber-based multifunctional biosensors and multimodal bioimaging systems: Technology and applications,” *Biosensors*, vol. 12, no. 2, p. 90, 2022.

[207] K. Beaudette, H. W. Baac, W.-J. Madore, M. Villiger, N. Godbout, B. E. Bouma, and C. Boudoux, “Laser tissue coagulation and concurrent optical coherence tomography through a double-clad fiber coupler,” *Biomedical Optics Express*, vol. 6, no. 4, p. 1293, Apr. 2015.

[208] R. Maltais-Tariant, C. Boudoux, and N. Uribe-Patarroyo, “Real-time co-localized oct surveillance of laser therapy using motion corrected speckle decorrelation,” *Biomedical Optics Express*, vol. 11, no. 6, pp. 2925–2950, 2020.

[209] W.-J. Madore, E. De Montigny, O. Ouellette, S. Lemire-Renaud, M. Leduc, X. Daxhelet, N. Godbout, and C. Boudoux, “Asymmetric double-clad fiber couplers for endoscopy,” *Optics letters*, vol. 38, no. 21, pp. 4514–4517, 2013.

[210] N. Godbout, C. Boudoux, W.-J. Madore, S. Lemire-renaud, X. Daxhelet, and M. Leduc, “Asymmetric optical fiber coupler,” Sep. 2017.

[211] T. Perrillat-Bottonet, M. Strupler, M. Leduc, L. Majeau, N. Godbout, and C. Boudoux, “All fiber nonlinear microscopy at 1550 nm using a double-clad fiber coupler,” in *Multiphoton Microscopy in the Biomedical Sciences XVII*, vol. 10069. SPIE, 2017, pp. 284–293.

[212] K. Beaudette, N. Godbout, and C. Boudoux, “Advances in multimodal imaging using double-clad fiber couplers,” *Journal of lightwave technology*, vol. 37, no. 22, pp. 5674–5685, 2019.

[213] G. Lu and B. Fei, “Medical hyperspectral imaging: a review.” *Journal of Biomedical Optics*, vol. 19, no. 1, p. 10901, 2014.

[214] N. A. Hagen and M. W. Kudenov, “Review of snapshot spectral imaging technologies,” *Optical Engineering*, vol. 52, no. 9, p. 090901, 2013.

[215] C. Williams, G. S. Gordon, T. D. Wilkinson, and S. E. Bohndiek, “Grayscale-to-color: scalable fabrication of custom multispectral filter arrays,” *ACS photonics*, vol. 6, no. 12, pp. 3132–3141, 2019.

[216] J. R. Bauer, A. A. Bruins, J. Y. Hardeberg, and R. M. Verdaasdonk, “A spectral filter array camera for clinical monitoring and diagnosis: Proof of concept for skin oxygenation imaging,” *Journal of imaging*, vol. 5, no. 8, p. 66, 2019.

[217] M. Ivančič, P. Naglič, F. Pernuš, B. Likar, and M. Bürmen, “Extraction of optical properties from hyperspectral images by monte carlo light propagation model,” in *Optical Interactions with Tissue and Cells Xxvii*, vol. 9706. SPIE, 2016, pp. 208–215.

[218] D. J. Waterhouse, W. Januszewicz, S. Ali, R. C. Fitzgerald, M. Di Pietro, and S. E. Bohndiek, “Spectral endoscopy enhances contrast for neoplasia in surveillance of barrett’s esophagus,” *Cancer Research*, vol. 81, no. 12, pp. 3415–3425, 2021.

[219] J. M. Benavides, S. Chang, S. Y. Park, R. Richards-Kortum, N. Mackinnon, C. MacAulay, A. Milbourne, A. Malpica, and M. Follen, “Multispectral digital colposcopy for in vivo detection of cervical cancer,” *Optics Express*, vol. 11, no. 10, pp. 1223–1236, 2003.

[220] Z. Han, A. Zhang, X. Wang, Z. Sun, M. D. Wang, and T. Xie, “In vivo use of hyperspectral imaging to develop a noncontact endoscopic diagnosis support system for malignant colorectal tumors,” *Journal of Biomedical Optics*, vol. 21, no. 1, p. 016001, 2016.

[221] M. Hohmann, R. Kanawade, F. Klämpfl, A. Douplik, J. Mudter, M. Neurath, and H. Albrecht, "In-vivo multispectral video endoscopy towards in-vivo hyperspectral video endoscopy," *Journal of Biophotonics*, vol. 10, no. 4, pp. 553–564, 2017.

[222] M. Hohmann, I. Ganzleben, A. Grünberg, J. Gonzales-Menezes, F. Klämpfl, B. Lengenfelder, E. Liebing, C. Heichler, C. Neufert, C. Becker *et al.*, "In vivo multi spectral colonoscopy in mice," *Scientific Reports*, vol. 12, no. 1, pp. 1–9, 2022.

[223] S. E. Martinez-Herrera, Y. Benezeth, M. Boffety, J.-F. Emile, F. Marzani, D. Lamarque, and F. Goudail, "Identification of precancerous lesions by multispectral gastroendoscopy," *Signal, Image and Video Processing*, vol. 10, no. 3, pp. 455–462, 2016.

[224] J. Yoon, J. Joseph, D. J. Waterhouse, C. Borzy, K. Siemens, S. Diamond, V. L. Tsikitis, and S. E. Bohndiek, "First experience in clinical application of hyperspectral endoscopy for evaluation of colonic polyps," *Journal of Biophotonics*, vol. 14, no. 9, p. e202100078, 2021.

[225] J. Yoon, J. Joseph, D. J. Waterhouse, A. S. Luthman, G. S. Gordon, M. Di Pietro, W. Januszewicz, R. C. Fitzgerald, and S. E. Bohndiek, "A clinically translatable hyperspectral endoscopy (hyse) system for imaging the gastrointestinal tract," *Nature communications*, vol. 10, no. 1, pp. 1–13, 2019.

[226] D. J. Waterhouse, S. Bano, W. Januszewicz, D. Stoyanov, R. C. Fitzgerald, M. Di Pietro, and S. E. Bohndiek, "First-in-human pilot study of snapshot multispectral endoscopy for early detection of barrett's-related neoplasia," *Journal of Biomedical Optics*, vol. 26, no. 10, p. 106002, 2021.

[227] B. Regeling, B. Thies, A. O. Gerstner, S. Westermann, N. A. Müller, J. Bendix, and W. Laffers, "Hyperspectral imaging using flexible endoscopy for laryngeal cancer detection," *Sensors*, vol. 16, no. 8, p. 1288, 2016.

[228] B. Fei, "Chapter 3.6 - hyperspectral imaging in medical applications," in *Hyperspectral Imaging*, ser. Data Handling in Science and Technology, J. M. Amigo, Ed. Elsevier, 2019, vol. 32, pp. 523–565.

[229] M. S. Patterson, B. C. Wilson, and D. R. Wyman, "The propagation of optical radiation in tissue. ii: Optical properties of tissues and resulting fluence distributions," *Lasers in medical science*, vol. 6, no. 4, pp. 379–390, 1991.

[230] A. L. Post, "Quantifying tissue optical properties with single fiber reflectance spectroscopy," Ph.D. dissertation, University of Amsterdam, 2020.

[231] S. H. Tabrizi, S. M. R. Aghamiri, F. Farzaneh, A. Amelink, and H. J. Sterenborg, "Single fiber reflectance spectroscopy on cervical premalignancies: the potential for reduction of the number of unnecessary biopsies," *Journal of Biomedical Optics*, vol. 18, no. 1, p. 017002, 2013.

[232] S. Hariri Tabrizi, F. Farzaneh, S. M. R. Aghamiri, M. Arab, M. Hosseini, T. Ashrafganjoei, and M. Chehrazi, "Comparison between performance of single-fiber reflectance spectroscopy (sfrs) system and colposcopy: a phase iii trial," *Lasers in Medical Science*, vol. 32, no. 9, pp. 2139–2144, 2017.

[233] U. Gamm, M. Heijblom, D. Piras, F. Van den Engh, S. Manohar, W. Steenbergen, H. Sterenborg, D. Robinson, and A. Amelink, "In vivo determination of scattering properties of healthy and malignant breast tissue by use of multi-diameter-single fiber reflectance spectroscopy (mdsfr)," in *Biomedical Applications of Light Scattering Vii*, vol. 8592. SPIE, 2013, pp. 106–111.

[234] A. Sircan-Kuçuksayan, T. Denkceken, and M. Canpolat, “Differentiating cancerous tissues from non-cancerous tissues using single-fiber reflectance spectroscopy with different fiber diameters,” *Journal of Biomedical Optics*, vol. 20, no. 11, p. 115007, 2015.

[235] P. L. Stegehuis, L. S. Boogerd, A. Inderson, R. A. Veenendaal, P. Van Gerven, B. A. Bonsing, J. S. Mieog, A. Amelink, M. Veselic, H. Morreau *et al.*, “Toward optical guidance during endoscopic ultrasound-guided fine needle aspirations of pancreatic masses using single fiber reflectance spectroscopy: a feasibility study,” *Journal of Biomedical Optics*, vol. 22, no. 2, p. 024001, 2017.

[236] L. v. Manen, I. Schmidt, A. Inderson, R. D. Houvast, J. J. Boonstra, J. Dijkstra, J. E. van Hooft, W. B. Nagengast, D. J. Robinson, A. L. Vahrmeijer *et al.*, “p single fiber reflectance spectroscopy for pancreatic cancer detection during endoscopic ultrasound guided fine needle biopsy: a prospective cohort study,” *International Journal of Medical Sciences*, vol. 19, no. 2, pp. 205–212, 2022.

[237] S. C. Kanick, C. Van der Leest, J. Aerts, H. C. Hoogsteden, S. Kascáková, H. J. Sterenborg, and A. Amelink, “Integration of single-fiber reflectance spectroscopy into ultrasound-guided endoscopic lung cancer staging of mediastinal lymph nodes,” *Journal of Biomedical Optics*, vol. 15, no. 1, p. 017004, 2010.

[238] A. L. Post, S. L. Jacques, H. J. Sterenborg, D. J. Faber, and T. G. Van Leeuwen, “Modeling subdiffusive light scattering by incorporating the tissue phase function and detector numerical aperture,” *Journal of Biomedical Optics*, vol. 22, no. 5, p. 050501, 2017.

[239] S. Kanick, D. Robinson, H. Sterenborg, and A. Amelink, “Monte carlo analysis of single fiber reflectance spectroscopy: photon path length and sampling depth,” *Physics in Medicine & Biology*, vol. 54, no. 22, p. 6991, 2009.

[240] S. Kanick, H. Sterenborg, and A. Amelink, “Empirical model of the photon path length for a single fiber reflectance spectroscopy device,” *Optics Express*, vol. 17, no. 2, pp. 860–871, 2009.

[241] A. L. Post, D. J. Faber, H. J. Sterenborg, and T. G. van Leeuwen, “Subdiffuse scattering and absorption model for single fiber reflectance spectroscopy,” *Biomedical Optics Express*, vol. 11, no. 11, pp. 6620–6633, 2020.

[242] A. L. Post, H. J. Sterenborg, F. G. Woltjer, T. G. van Leeuwen, and D. J. Faber, “Subdiffuse scattering model for single fiber reflectance spectroscopy,” *Journal of Biomedical Optics*, vol. 25, no. 1, p. 015001, 2020.

[243] D. J. Faber, A. L. Post, H. J. Sterenborg, and T. G. Van Leeuwen, “Analytical model for diffuse reflectance in single fiber reflectance spectroscopy,” *Optics Letters*, vol. 45, no. 7, pp. 2078–2081, 2020.

[244] A. L. Post, D. J. Faber, H. J. Sterenborg, and T. G. van Leeuwen, “Experimental validation of a recently developed model for single-fiber reflectance spectroscopy,” *Journal of Biomedical Optics*, vol. 26, no. 2, p. 025004, 2021.

[245] P. Hrynchak and T. Simpson, “Optical coherence tomography: an introduction to the technique and its use,” *Optometry and vision science*, vol. 77, no. 7, pp. 347–356, 2000.

[246] T.-H. Tsai, J. Fujimoto, and H. Mashimo, “Endoscopic optical coherence tomography for clinical gastroenterology,” *Diagnostics*, vol. 4, no. 2, pp. 57–93, May 2014.

[247] J. A. Burns, "Optical coherence tomography," *Current Opinion in Otolaryngology & Head and Neck Surgery*, vol. 20, no. 6, pp. 477–481, Dec. 2012.

[248] C. Pitris, A. Goodman, S. A. Boppart, J. J. Libus, J. G. Fujimoto, and M. E. Brezinski, "High-resolution imaging of gynecologic neoplasms using optical coherence tomography," *Obstetrics & Gynecology*, vol. 93, no. 1, pp. 135–139, 1999.

[249] M. Y. Kirillin, T. Motovilova, and N. M. Shakhova, "Optical coherence tomography in gynecology: a narrative review," *Journal of Biomedical Optics*, vol. 22, no. 12, p. 121709, 2017.

[250] T. Gambichler, V. Jaedicke, and S. Terras, "Optical coherence tomography in dermatology: technical and clinical aspects," *Archives of dermatological research*, vol. 303, no. 7, pp. 457–473, 2011.

[251] U. Morgner, W. Drexler, F. X. Kärtner, X. D. Li, C. Pitris, E. P. Ippen, and J. G. Fujimoto, "Spectroscopic optical coherence tomography," *Optics Letters*, vol. 25, no. 2, p. 111, Jan. 2000.

[252] C. P. Fleming, J. Eckert, E. F. Halpern, J. A. Gardecki, and G. J. Tearney, "Depth resolved detection of lipid using spectroscopic optical coherence tomography," *Biomedical Optics Express*, vol. 4, no. 8, pp. 1269–1284, 2013.

[253] D. J. Faber, E. G. Mik, M. C. Aalders, and T. G. van Leeuwen, "Light absorption of (oxy-) hemoglobin assessed by spectroscopic optical coherence tomography," *Optics letters*, vol. 28, no. 16, pp. 1436–1438, 2003.

[254] N. Bosschaart, T. G. van Leeuwen, M. C. Aalders, and D. J. Faber, "Quantitative comparison of analysis methods for spectroscopic optical coherence tomography," *Biomedical Optics Express*, vol. 4, no. 11, pp. 2570–2584, 2013.

[255] S. T. Monteiro, Y. Kosugi, K. Uto, and E. Watanabe, "Towards applying hyperspectral imagery as an intraoperative visual aid tool," in *Proc. 4th Int. Conf. on Visualization, Imaging and Image Processing*, 2004, pp. 483–488.

[256] S. V. Panasyuk, S. Yang, D. V. Faller, D. Ngo, R. A. Lew, J. E. Freeman, and A. E. Rogers, "Medical hyperspectral imaging to facilitate residual tumor identification during surgery," *Cancer Biology & Therapy*, vol. 6, no. 3, pp. 439–446, Mar. 2007.

[257] K. J. Zuzak, R. P. Francis, E. F. Wehner, M. Litorja, J. A. Cadeddu, and E. H. Livingston, "Active dlp hyperspectral illumination: a noninvasive, in vivo, system characterization visualizing tissue oxygenation at near video rates," *Analytical chemistry*, vol. 83, no. 19, pp. 7424–7430, 2011.

[258] A. Holmer, J. Marotz, P. Wahl, M. Dau, and P. W. Kämmerer, "Hyperspectral imaging in perfusion and wound diagnostics–methods and algorithms for the determination of tissue parameters," *Biomedical Engineering/Biomedizinische Technik*, vol. 63, no. 5, pp. 547–556, 2018.

[259] M. E. Martin, M. B. Wabuyele, K. Chen, P. Kasili, M. Panjehpour, M. Phan, B. Overholt, G. Cunningham, D. Wilson, R. C. DeNovo, and T. Vo-Dinh, "Development of an Advanced Hyperspectral Imaging (HSI) System with Applications for Cancer Detection," *Annals of Biomedical Engineering*, vol. 34, no. 6, pp. 1061–1068, Jun. 2006.

[260] H. Akbari, L. V. Halig, D. M. Schuster, A. Osunkoya, V. Master, P. T. Nieh, G. Z. Chen, and B. Fei, "Hyperspectral imaging and quantitative analysis for prostate cancer detection," *Journal of Biomedical Optics*, vol. 17, no. 7, p. 0760051, Jul. 2012.

[261] S. Kiyotoki, J. Nishikawa, T. Okamoto, K. Hamabe, M. Saito, A. Goto, Y. Fujita, Y. Hamamoto, Y. Takeuchi, S. Satori, and I. Sakaida, “New method for detection of gastric cancer by hyperspectral imaging: a pilot study,” *Journal of Biomedical Optics*, vol. 18, no. 2, p. 026010, Feb. 2013.

[262] W. R. Johnson, D. W. Wilson, W. Fink, M. Humayun, and G. Bearman, “Snapshot hyperspectral imaging in ophthalmology,” *Journal of Biomedical Optics*, vol. 12, no. 1, p. 014036, 2007.

[263] D. Cohen, M. Arnoldussen, G. Bearman, and W. Grundfest, “The use of spectral imaging for the diagnosis of retinal disease,” in *1999 IEEE LEOS Annual Meeting Conference Proceedings. LEOS’99. 12th Annual Meeting. IEEE Lasers and Electro-Optics Society 1999 Annual Meeting (Cat. No.99CH37009)*, vol. 1. IEEE, 1999, pp. 220–221.

[264] J. Schweizer, J. Hollmach, G. Steiner, L. Knels, R. H. W. Funk, and E. Koch, “Hyperspectral imaging - A new modality for eye diagnostics,” *Biomedical Engineering / Biomedizinische Technik*, vol. 57, no. SI-1 Track-P, pp. 293–296, Jan. 2012.

[265] D. Yudovsky, A. Nouvong, and L. Pilon, “Hyperspectral imaging in diabetic foot wound care.” *Journal of diabetes science and technology*, vol. 4, no. 5, pp. 1099–113, Sep. 2010.

[266] H. Akbari, Y. Kosugi, K. Kojima, and N. Tanaka, “Detection and Analysis of the Intestinal Ischemia Using Visible and Invisible Hyperspectral Imaging,” *IEEE Transactions on Biomedical Engineering*, vol. 57, no. 8, pp. 2011–2017, Aug. 2010.

[267] M. S. Holzer, S. L. Best, N. Jackson, A. Thapa, G. V. Raj, J. A. Cadeddu, and K. J. Zuzak, “Assessment of Renal Oxygenation During Partial Nephrectomy Using Hyperspectral Imaging,” *The Journal of Urology*, vol. 186, no. 2, pp. 400–404, Aug. 2011.

[268] M. C. Skala, A. Fontanella, H. Hendargo, M. W. Dewhirst, and J. A. Izatt, “Combined hyperspectral and spectral domain optical coherence tomography microscope for noninvasive hemodynamic imaging,” *Optics letters*, vol. 34, no. 3, pp. 289–291, 2009.

[269] P. Zhang, A. Zam, Y. Jian, X. Wang, Y. Li, K. S. Lam, M. E. Burns, M. V. Sarunic, E. N. Pugh Jr, and R. J. Zawadzki, “In vivo wide-field multispectral scanning laser ophthalmoscopy–optical coherence tomography mouse retinal imager: longitudinal imaging of ganglion cells, microglia, and müller glia, and mapping of the mouse retinal and choroidal vasculature,” *Journal of Biomedical Optics*, vol. 20, no. 12, p. 126005, 2015.

[270] S. Lemire-Renaud, M. Rivard, M. Strupler, D. Morneau, F. Verpillat, X. Daxhelet, N. Godbout, and C. Boudoux, “Double-clad fiber coupler for endoscopy,” *Optics Express*, vol. 18, no. 10, p. 9755, May 2010.

[271] W.-J. Madore, E. De Montigny, O. Ouellette, S. Lemire-Renaud, M. Leduc, X. Daxhelet, N. Godbout, and C. Boudoux, “Asymmetric double-clad fiber couplers for endoscopy,” *Optics Letters*, 2013.

[272] E. De Montigny, W.-J. Madore, O. Ouellette, G. Bernard, M. Leduc, M. Strupler, C. Boudoux, and N. Godbout, “Double-clad fiber coupler for partially coherent detection,” *Optics Express*, vol. 23, no. 7, p. 9040, Apr. 2015.

[273] E. De Montigny, N. Goulamhoussen, W.-J. Madore, M. Strupler, O. E. Gologan, T. Ayad, and C. Boudoux, “Tri-modal microscope for head and neck tissue identification,” *Biomedical Optics Express*, vol. 7, no. 3, pp. 732–745, 2016.

[274] R. W. G. Hunt and M. R. Pointer, *Measuring colour*. John Wiley & Sons, 2011.

[275] J. Dawson, D. Barker, D. Ellis, J. Cotterill, E. Grassam, G. Fisher, and J. Feather, "A theoretical and experimental study of light absorption and scattering by in vivo skin," *Physics in Medicine & Biology*, vol. 25, no. 4, p. 695, 1980.

[276] N. Keshava and J. F. Mustard, "Spectral unmixing," *IEEE signal processing magazine*, vol. 19, no. 1, pp. 44–57, 2002.

[277] S. Prahl, "Optical absorption of hemoglobin," *http://omlc. ogi. edu/spectra/hemoglobin*, 1999.

[278] M. Tsuboi, A. Hayashi, N. Ikeda, H. Honda, Y. Kato, S. Ichinose, and H. Kato, "Optical coherence tomography in the diagnosis of bronchial lesions," *Lung cancer*, vol. 49, no. 3, pp. 387–394, 2005.

[279] Y. Fradet, H. B. Grossman, L. Gomella, S. Lerner, M. Cookson, D. Albala, M. J. Droller, and P. B. S. Group, "A comparison of hexaminolevulinate fluorescence cystoscopy and white light cystoscopy for the detection of carcinoma in situ in patients with bladder cancer: a phase iii, multicenter study," *The Journal of urology*, vol. 178, no. 1, pp. 68–73, 2007.

[280] G. Tao, L. Xing-hua, Y. Ai-ming, Z. Wei-xun, Y. Fang, W. Xi, W. Li-yin, L. Chong-mei, F. Gui-jun, S. Hui-jun *et al.*, "Enhanced magnifying endoscopy for differential diagnosis of superficial gastric lesions identified with white-light endoscopy," *Gastric Cancer*, vol. 17, no. 1, pp. 122–129, 2014.

[281] D. Lorenser, B. C. Quirk, M. Auger, W.-J. Madore, R. W. Kirk, N. Godbout, D. D. Sampson, C. Boudoux, and R. A. McLaughlin, "Dual-modality needle probe for combined fluorescence imaging and three-dimensional optical coherence tomography," *Optics letters*, vol. 38, no. 3, pp. 266–268, 2013.

[282] C. Balas, C. Pappas, and G. Epitropou, "Multi/hyper-spectral imaging," in *Handbook of Biomedical Optics*. CRC Press, Apr. 2016, pp. 131–163.

[283] V. Tuchin, *Tissue Optics*. 1000 20th Street, Bellingham, WA 98227-0010 USA: SPIE, Sep. 2007, vol. 76, no. 10.

[284] A. Bjorgan, M. Milanic, and L. L. Randeberg, "Estimation of skin optical parameters for real-time hyperspectral imaging applications," *Journal of biomedical optics*, vol. 19, no. 6, p. 066003, 2014.

[285] D. G. Ferris, R. A. Lawhead, E. D. Dickman, N. Holtzapple, J. A. Miller, S. Grogan, S. Bambot, A. Agrawal, and M. L. Faupel, "Multimodal hyperspectral imaging for the noninvasive diagnosis of cervical neoplasia," *Journal of lower genital tract disease*, vol. 5, no. 2, pp. 65–72, 2001.

[286] R. Guay-Lord, K. Lurie, X. Attendu, L. Mageau, N. Godbout, A. Ellerbee Bowden, M. Strupler, and C. Boudoux, "Combined optical coherence tomography and hyper-spectral imaging using a double clad fiber coupler," in *Progress in Biomedical Optics and Imaging - Proceedings of SPIE*, vol. 9701, 2016.

[287] W. Drexler and J. G. Fujimoto, *Optical coherence tomography : technology and applications*, 2nd ed. Springer Science & Business Media, 2015.

[288] M. Wojtkowski, V. Srinivasan, J. G. Fujimoto, T. Ko, J. S. Schuman, A. Kowalczyk, and J. S. Duker, "Three-dimensional retinal imaging with high-speed ultrahigh-resolution optical coherence tomography," *Ophthalmology*, vol. 112, no. 10, pp. 1734–1746, 2005.

[289] E. Regar, J. Schaar, E. Mont, R. Virmani, and P. Serruys, “Optical coherence tomography,” *Cardiovascular Radiation Medicine*, vol. 4, no. 4, pp. 198–204, 2003.

[290] F. Benboujja, J. A. Garcia, K. Beaudette, M. Strupler, C. J. Hartnick, and C. Boudoux, “Intraoperative imaging of pediatric vocal fold lesions using optical coherence tomography,” *Journal of Biomedical Optics*, vol. 21, no. 1, p. 016007, 2016.

[291] G. Tearney, B. Bouma, and J. Fujimoto, “High-speed phase-and group-delay scanning with a grating-based phase control delay line,” *Optics letters*, vol. 22, no. 23, pp. 1811–1813, 1997.

[292] W. Drexler, M. Liu, A. Kumar, T. Kamali, A. Unterhuber, and R. A. Leitgeb, “Optical coherence tomography today: speed, contrast, and multimodality,” *Journal of Biomedical Optics*, vol. 19, no. 7, p. 071412, 2014.

[293] P. C. Enzinger and R. J. Mayer, “Esophageal cancer,” *New England Journal of Medicine*, vol. 349, no. 23, pp. 2241–2252, 2003.

[294] F. R. Hirsch, W. A. Franklin, A. F. Gazdar, and P. A. Bunn, “Early detection of lung cancer: clinical perspectives of recent advances in biology and radiology,” *Clinical Cancer Research*, vol. 7, no. 1, pp. 5–22, 2001.

[295] S. Tang, Y. Zhou, and M. J. Ju, “Multimodal optical imaging with multiphoton microscopy and optical coherence tomography,” *Journal of Biophotonics*, vol. 5, no. 5-6, pp. 396–403, 2012.

[296] C. A. Patil, N. Bosschaart, M. D. Keller, T. G. van Leeuwen, and A. Mahadevan-Jansen, “Combined raman spectroscopy and optical coherence tomography device for tissue characterization,” *Optics letters*, vol. 33, no. 10, pp. 1135–1137, 2008.

[297] R. Hunt and M. Pointer, *Measuring Colour*. John Wiley & Sons, 2011.

[298] M. D. Fairchild, *Color appearance models*. John Wiley & Sons, 2013.

[299] A. R. Choudhury, “3 - colour-difference assessment,” in *Principles of Colour and Appearance Measurement*, A. K. R. Choudhury, Ed. Oxford: Woodhead Publishing, 2015, pp. 55 – 116.

[300] W. Mokrzycki and M. Tatol, “Colour difference δe-a survey,” *Machine Graphics and Vision*, vol. 20, no. 4, pp. 383–411, 2011.

[301] G. Sharma, “Color fundamentals for digital imaging,” *Digital color imaging handbook*, vol. 20, 2003.

[302] I. CIE, “Improvement to industrial colour-difference evaluation,” 2001.

[303] M. R. Luo, G. Cui, and B. Rigg, “The development of the cie 2000 colour-difference formula: Ciede2000,” *Color Research & Application: Endorsed by Inter-Society Color Council, The Colour Group (Great Britain), Canadian Society for Color, Color Science Association of Japan, Dutch Society for the Study of Color, The Swedish Colour Centre Foundation, Colour Society of Australia, Centre Français de la Couleur*, vol. 26, no. 5, pp. 340–350, 2001.

[304] BabelColor. (2014) The color checker. [Online]. Available: http://www.babelcolor.com/colorchecker.htm

[305] X. Attendu, R. M. Ruis, C. Boudoux, T. G. van Leeuwen, and D. J. Faber, “Simple and robust calibration procedure for k-linearization and dispersion compensation in optical coherence tomography,” *Journal of Biomedical Optics*, vol. 24, no. 5, p. 056001, 2019.

[306] S. M. Nascimento, F. P. Ferreira, and D. H. Foster, "Statistics of spatial cone-excitation ratios in natural scenes," *JOSA A*, vol. 19, no. 8, pp. 1484–1490, 2002.

[307] T. P. Moffitt and S. Prahl, "Sized-fiber reflectometry for measuring local optical properties," *IEEE Journal of selected topics in quantum electronics*, vol. 7, no. 6, pp. 952–958, 2001.

[308] M. Canpolat and J. R. Mourant, "Particle size analysis of turbid media with a single optical fiber in contact with the medium to deliver and detect white light," *Applied Optics*, vol. 40, no. 22, pp. 3792–3799, 2001.

[309] S. Kanick, U. Gamm, M. Schouten, H. Sterenborg, D. Robinson, and A. Amelink, "Measurement of the reduced scattering coefficient of turbid media using single fiber reflectance spectroscopy: fiber diameter and phase function dependence," *Biomedical Optics Express*, vol. 2, no. 6, pp. 1687–1702, 2011.

[310] M. Adhi and J. S. Duker, "Optical coherence tomography-current and future applications," *Current Opinion in Ophthalmology*, vol. 24, no. 3, pp. 213–221, May 2013.

[311] R. F. Spaide, J. G. Fujimoto, N. K. Waheed, S. R. Sadda, and G. Staurenghi, "Optical coherence tomography angiography," *Progress in Retinal and Eye Research*, vol. 64, pp. 1–55, May 2018.

[312] S. Lam, B. Standish, C. Baldwin, A. McWilliams, J. LeRiche, A. Gazdar, A. I. Vitkin, V. Yang, N. Ikeda, and C. MacAulay, "In vivo optical coherence tomography imaging of preinvasive bronchial lesions." *Clinical cancer research : an official journal of the American Association for Cancer Research*, vol. 14, no. 7, pp. 2006–11, Apr. 2008.

[313] S. P. Lerner, A. C. Goh, N. J. Tresser, and S. S. Shen, "Optical Coherence Tomography as an Adjunct to White Light Cystoscopy for Intravesical Real-Time Imaging and Staging of Bladder Cancer," *Urology*, vol. 72, no. 1, pp. 133–137, Jul. 2008.

[314] P. G. Wagstaff, A. Ingels, D. M. De Bruin, M. Buijs, P. J. Zondervan, C. D. Savci Heijink, O. M. Van Delden, D. J. Faber, T. G. Van Leeuwen, R. J. A. Van Moorselaar, J. J. De La Rosette, and M. P. Laguna Pes, "Percutaneous needle based optical coherence tomography for the differentiation of renal masses: A pilot cohort," *Journal of Urology*, vol. 195, no. 5, pp. 1578–1584, 2016.

[315] B. G. Muller, A. Swaan, D. M. de Bruin, W. van den Bos, A. W. Schreurs, D. J. Faber, E. C. H. Zwartkruis, L. Rozendaal, A. N. Vis, J. A. Nieuwenhuijzen, R. J. A. van Moorselaar, T. G. van Leeuwen, and J. J. M. C. H. de la Rosette, "Customized Tool for the Validation of Optical Coherence Tomography in Differentiation of Prostate Cancer," *Technology in Cancer Research & Treatment*, vol. 16, no. 1, pp. 57–65, Feb. 2017.

[316] S. Tang, Y. Zhou, and M. J. Ju, "Multimodal optical imaging with multiphoton microscopy and optical coherence tomography," *Journal of Biophotonics*, vol. 5, no. 5-6, pp. 396–403, 2012.

[317] A. Varkentin, M. Mazurenka, E. Blumenröther, L. Behrendt, S. Emmert, U. Morgner, M. Meinhardt-Wollweber, M. Rahlves, and B. Roth, "Trimodal system for in vivo skin cancer screening with combined optical coherence tomography-Raman and colocalized optoacoustic measurements," *Journal of Biophotonics*, vol. 11, no. 6, p. e201700288, Jun. 2018.

[318] W. Chen, Z. Chen, and D. Xing, "Optical coherence hyperspectral microscopy with a single supercontinuum light source," *Journal of Biophotonics*, vol. 14, no. 8, p. e202000491, Aug. 2021.

[319] X. Attendu, M. H. Bourget, M. P. de Sivry-Houle, and C. Boudoux, "Coregistered optical coherence tomography and frequency-encoded multispectral imaging for spectrally sparse color imaging," *Journal of Biomedical Optics*, vol. 25, no. 3, p. 032008, 2019.

[320] S. C. Kanick, H. J. C. M. Sterenborg, and A. Amelink, "Empirical model of the photon path length for a single fiber reflectance spectroscopy device," *Optics Express*, vol. 17, no. 2, pp. 860–871, Jan. 2009.

[321] A. L. Post, F. Woltjer, S. Jacques, D. H. J. C. M. Sterenborg, D. J. Faber, and T. G. van Leeuwen, "Modeling subdiffusive scattering and absorption for an overlapping source-detector geometry, e.g. single fiber reflectance spectroscopy (SFR) (Conference Presentation)," in *Optical Interactions with Tissue and Cells XXX*, H. T. Beier and B. L. Ibey, Eds. SPIE, Mar. 2019, p. 28.

[322] I. Grulkowski, S. Manzanera, L. Cwiklinski, F. Sobczuk, K. Karnowski, and P. Artal, "Swept source optical coherence tomography and tunable lens technology for comprehensive imaging and biometry of the whole eye," *Optica*, vol. 5, no. 1, pp. 52–59, 2018.

[323] M. J. Gora, L. H. Simmons, L. Quénéhervé, C. N. Grant, R. W. Carruth, W. Lu, A. Tiernan, J. Dong, B. W. Corkery, A. Soomro *et al.*, "Tethered capsule endomicroscopy: from bench to bedside at a primary care practice," *Journal of Biomedical Optics*, vol. 21, no. 10, p. 104001, 2016.

[324] H. L. Fu, Y. Leng, M. J. Cobb, K. Hsu, J. H. Hwang, and X. Li, "Flexible miniature compound lens design for high-resolution optical coherence tomography balloon imaging catheter," *Journal of Biomedical Optics*, vol. 13, no. 6, p. 060502, 2008.

[325] W. Kim, X. Chen, J. A. Jo, and B. E. Applegate, "Lensless, ultra-wideband fiber optic rotary joint for biomedical applications," *Optics letters*, vol. 41, no. 9, pp. 1973–1976, 2016.

[326] M. J. Gora, J. S. Sauk, R. W. Carruth, W. Lu, D. T. Carlton, A. Soomro, M. Rosenberg, N. S. Nishioka, and G. J. Tearney, "Imaging the upper gastrointestinal tract in unsedated patients using tethered capsule endomicroscopy," *Gastroenterology*, vol. 145, no. 4, pp. 723–725, 2013.

[327] W. Jung, W. A. Benalcazar, A. Ahmad, U. Sharma, H. Tu, and S. A. Boppart, "Numerical analysis of gradient index lens-based optical coherence tomography imaging probes," *Journal of biomedical optics*, vol. 15, no. 6, p. 066027, 2010.

[328] W. Emkey and C. Jack, "Analysis and evaluation of graded-index fiber lenses," *Journal of Lightwave Technology*, vol. 5, no. 9, pp. 1156–1164, 1987.

[329] C. Gomez-Reino, M. V. Perez, and C. Bao, *Gradient-index optics: fundamentals and applications*. Springer Science & Business Media, 2002.

[330] A. M. Kowalevicz Jr and F. Bucholtz, "Beam divergence from an smf-28 optical fiber," NAVAL RESEARCH LAB WASHINGTON DC, Tech. Rep., 2006.

[331] R. Kashyap, *Fiber bragg gratings*. Academic press, 2009.

[332] Zemax OpticsStudio LLC., "Zemax Opticsstudio 20.3 User Manual," 2020.

[333] K. Beaudette, "Double-clad fiber-based systems and devices as a therapeutic and diagnostic tool for barrett's esophagus," Ph.D. dissertation, Ecole Polytechnique, Montreal (Canada), 2017.

[334] A. López-Marín, G. Springeling, R. Beurskens, H. van Beusekom, A. F. van der Steen, A. D. Koch, B. E. Bouma, R. Huber, G. van Soest, and T. Wang, "Motorized capsule for shadow-free oct imaging and synchronous beam control," *Optics Letters*, vol. 44, no. 15, pp. 3641–3644, 2019.

[335] J. Zhang, T. Nguyen, B. Potsaid, V. Jayaraman, C. Burgner, S. Chen, J. Li, K. Liang, A. Cable, G. Traverso *et al.*, "Multi-mhz mems-vcsel swept-source optical coherence tomography for endoscopic structural and angiographic imaging with miniaturized brushless motor probes," *Biomedical Optics Express*, vol. 12, no. 4, pp. 2384–2403, 2021.

[336] J. Bentley and C. Olson, "Field guide to lens design." Society of Photo-Optical Instrumentation Engineers (SPIE), 2012.

[337] K. Beaudette, M. Strupler, J. Ren, B. E. Bouma, and C. Boudoux, "Radiometric model for coaxial single-and multimode optical emission from double-clad fiber," *Applied Optics*, vol. 57, no. 5, pp. 1110–1118, 2018.

[338] P. H. Tran, D. S. Mukai, M. Brenner, and Z. Chen, "In vivo endoscopic optical coherence tomography by use of a rotational microelectromechanical system probe," *Optics letters*, vol. 29, no. 11, pp. 1236–1238, 2004.

[339] O. O. Ahsen, H.-C. Lee, M. G. Giacomelli, Z. Wang, K. Liang, T.-H. Tsai, B. Potsaid, H. Mashimo, and J. G. Fujimoto, "Correction of rotational distortion for catheter-based en face oct and oct angiography," *Optics letters*, vol. 39, no. 20, pp. 5973–5976, 2014.

[340] S. Yun, G. Tearney, B. Bouma, B. Park, and J. F. de Boer, "High-speed spectral-domain optical coherence tomography at 1.3 μm wavelength," *Optics Express*, vol. 11, no. 26, pp. 3598–3604, 2003.

[341] M. Wojtkowski, R. Leitgeb, A. Kowalczyk, T. Bajraszewski, and A. F. Fercher, "In vivo human retinal imaging by fourier domain optical coherence tomography," *Journal of Biomedical Optics*, vol. 7, no. 3, pp. 457–464, 2002.

[342] M. Wojtkowski, V. J. Srinivasan, T. H. Ko, J. G. Fujimoto, A. Kowalczyk, and J. S. Duker, "Ultrahigh-resolution, high-speed, fourier domain optical coherence tomography and methods for dispersion compensation," *Optics Express*, vol. 12, no. 11, pp. 2404–2422, 2004.

[343] Z. Hu and A. M. Rollins, "Fourier domain optical coherence tomography with a linear-in-wavenumber spectrometer," *Optics letters*, vol. 32, no. 24, pp. 3525–3527, 2007.

[344] W. Drexler and J. G. Fujimoto, *Optical coherence tomography: technology and applications*. Springer Science & Business Media, 2008.

[345] C. Dorrer, N. Belabas, J.-P. Likforman, and M. Joffre, "Spectral resolution and sampling issues in fourier-transform spectral interferometry," *JOSA B*, vol. 17, no. 10, pp. 1795–1802, 2000.

[346] A. K. Gaigalas, L. Wang, H.-J. He, and P. DeRose, "Procedures for wavelength calibration and spectral response correction of ccd array spectrometers," *Journal of research of the National Institute of Standards and Technology*, vol. 114, no. 4, p. 215, 2009.

[347] M. Mujat, B. H. Park, B. Cense, T. C. Chen, and J. F. de Boer, "Autocalibration of spectral-domain optical coherence tomography spectrometers for in vivo quantitative retinal nerve fiber layer birefringence determination," *Journal of Biomedical Optics*, vol. 12, no. 4, p. 041205, 2007.

[348] D. J. Faber and T. G. v. Leeuwen, "Doppler calibration method for spectral domain oct spectrometers," *Journal of Biophotonics*, vol. 2, no. 6-7, pp. 407–415, 2009.

[349] T. J. Eom, Y.-C. Ahn, C.-S. Kim, and Z. Chen, "Calibration and characterization protocol for spectral-domain optical coherence tomography using fiber bragg gratings," *Journal of Biomedical Optics*, vol. 16, no. 3, p. 030501, 2011.

[350] M. Szkulmowski, S. Tamborski, and M. Wojtkowski, "Spectrometer calibration for spectroscopic fourier domain optical coherence tomography," *Biomedical Optics Express*, vol. 7, no. 12, pp. 5042–5054, 2016.

[351] N. Uribe-Patarroyo, S. H. Kassani, M. Villiger, and B. E. Bouma, "Robust wavenumber and dispersion calibration for fourier-domain optical coherence tomography," *Optics Express*, vol. 26, no. 7, pp. 9081–9094, 2018.

[352] K. Wang and Z. Ding, "Spectral calibration in spectral domain optical coherence tomography," *Chinese Optics Letters*, vol. 6, no. 12, pp. 902–904, 2008.

[353] S. Makita, T. Fabritius, and Y. Yasuno, "1- μ m spectral-domain optical coherence tomography using BM-scan for volumetric imaging of the human posterior eye," *Optics Express*, vol. 16, no. 12, pp. 2067–2069, 2008.

[354] C. K. Hitzenberger, A. Baumgartner, W. Drexler, and A. F. Fercher, "Dispersion effects in partial coherence interferometry: implications for intraocular ranging," *Journal of Biomedical Optics*, vol. 4, no. 1, pp. 144–152, 1999.

[355] B. Bouma, G. Tearney, S. Boppart, M. Hee, M. Brezinski, and J. Fujimoto, "High-resolution optical coherence tomographic imaging using a mode-locked ti: Al 2 o 3 laser source," *Optics letters*, vol. 20, no. 13, pp. 1486–1488, 1995.

[356] M.-T. Tsai, I.-J. Hsu, C.-W. Lu, Y.-M. Wang, C.-W. Sun, Y.-W. Kiang, and C. Yang, "Dispersion compensation in optical coherence tomography with a prism in a rapid-scanning optical delay line," *Optical and quantum electronics*, vol. 37, no. 13-15, pp. 1199–1212, 2005.

[357] S. Iyer, S. Coen, and F. Vanholsbeeck, "Dual-fiber stretcher as a tunable dispersion compensator for an all-fiber optical coherence tomography system," *Optics letters*, vol. 34, no. 19, pp. 2903–2905, 2009.

[358] T. Xie, Z. Wang, and Y. Pan, "Dispersion compensation in high-speed optical coherence tomography by acousto-optic modulation," *Applied optics*, vol. 44, no. 20, pp. 4272–4280, 2005.

[359] Y. Chen and X. Li, "Dispersion management up to the third order for real-time optical coherence tomography involving a phase or frequency modulator," *Optics Express*, vol. 12, no. 24, pp. 5968–5978, 2004.

[360] L. Froehly, S. Iyer, and F. Vanholsbeeck, "Dual-fibre stretcher and coma as tools for independent 2nd and 3rd order tunable dispersion compensation in a fibre-based 'scan-free' time domain optical coherence tomography system," *Optics Communications*, vol. 284, no. 16-17, pp. 4099–4106, 2011.

[361] D. L. Marks, A. L. Oldenburg, J. J. Reynolds, and S. A. Boppart, "Autofocus algorithm for dispersion correction in optical coherence tomography," *Applied optics*, vol. 42, no. 16, pp. 3038–3046, 2003.

[362] Y. Yasuno, Y. Hong, S. Makita, M. Yamanari, M. Akiba, M. Miura, and T. Yatagai, "In vivo high-contrast imaging of deep posterior eye by 1-μm swept source optical coherence tomography and scattering optical coherence angiography," *Optics Express*, vol. 15, no. 10, p. 6121, 2007.

[363] K. Singh, G. Sharma, and G. J. Tearney, “Estimation and compensation of dispersion for a high-resolution optical coherence tomography system,” *Journal of Optics*, vol. 20, no. 2, p. 025301, 2018.

[364] G. Yurtsever, N. Weiss, J. Kalkman, T. G. van Leeuwen, and R. Baets, “Ultra-compact silicon photonic integrated interferometer for swept-source optical coherence tomography,” *Optics letters*, vol. 39, no. 17, pp. 5228–5231, 2014.

[365] V. D. Nguyen, N. Weiss, W. Beeker, M. Hoekman, A. Leinse, R. Heideman, T. van Leeuwen, and J. Kalkman, “Integrated-optics-based swept-source optical coherence tomography,” *Optics letters*, vol. 37, no. 23, pp. 4820–4822, 2012.

[366] R. M. Ruis, A. Leinse, R. Dekker, R. G. Heideman, T. G. van Leeuwen, and D. J. Faber, “Decreasing the size of a spectral domain optical coherence tomography system with cascaded arrayed waveguide gratings in a photonic integrated circuit,” *IEEE Journal of Selected Topics in Quantum Electronics*, vol. 25, no. 1, pp. 1–9, 2019.

[367] B. Cense, N. A. Nassif, T. C. Chen, M. C. Pierce, S.-H. Yun, B. H. Park, B. E. Bouma, G. J. Tearney, and J. F. de Boer, “Ultrahigh-resolution high-speed retinal imaging using spectral-domain optical coherence tomography,” *Optics Express*, vol. 12, no. 11, pp. 2435–2447, 2004.

[368] S. H. Yun, G. J. Tearney, J. F. de Boer, and B. E. Bouma, “Removing the depth-degeneracy in optical frequency domain imaging with frequency shifting,” *Optics Express*, vol. 12, no. 20, pp. 4822–4828, Oct. 2004.

[369] J. Zhang, J. S. Nelson, and Z. Chen, “Removal of a mirror image and enhancement of the signal-to-noise ratio in Fourier-domain optical coherence tomography using an electro-optic phase modulator,” *Optics Letters*, vol. 30, no. 2, p. 147, Jan. 2005.

[370] M. Wojtkowski, A. Kowalczyk, R. Leitgeb, and A. F. Fercher, “Full range complex spectral optical coherence tomography technique in eye imaging,” *Optics Letters*, vol. 27, no. 16, p. 1415, Aug. 2002.

[371] D. Y. Kim, J. S. Werner, and R. J. Zawadzki, “Comparison of phase-shifting techniques for in vivo full-range, high-speed Fourier-domain optical coherence tomography,” *Journal of Biomedical Optics*, vol. 15, no. 5, p. 056011, 2010.

[372] Y. K. Tao, M. Zhao, and J. A. Izatt, “High-speed complex conjugate resolved retinal spectral domain optical coherence tomography using sinusoidal phase modulation,” *Optics Letters*, vol. 32, no. 20, p. 2918, Oct. 2007.

[373] R. A. Leitgeb, C. K. Hitzenberger, A. F. Fercher, and T. Bajraszewski, “Phase-shifting algorithm to achieve high-speed long-depth-range probing by frequency-domain optical coherence tomography,” *Optics Letters*, vol. 28, no. 22, p. 2201, Nov. 2003.

[374] E. Götzinger, M. Pircher, R. A. Leitgeb, and C. K. Hitzenberger, “High speed full range complex spectral domain optical coherence tomography,” *Optics Express*, vol. 13, no. 2, pp. 583–594, Jan. 2005.

[375] N. Lippok, B. E. Bouma, and B. J. Vakoc, “Stable multi-megahertz circular-ranging optical coherence tomography at 1.3 μm,” *Biomedical Optics Express*, vol. 11, no. 1, pp. 174–185, 2020.

[376] S. Vergnole, G. Lamouche, and M. L. Dufour, “Artifact removal in Fourier-domain optical coherence tomography with a piezoelectric fiber stretcher,” *Optics Letters*, vol. 33, no. 7, p. 732, Apr. 2008.

[377] Y. Yasuno, S. Makita, T. Endo, G. Aoki, M. Itoh, and T. Yatagai, "Simultaneous bm-mode scanning method for real-time full-range fourier domain optical coherence tomography," *Applied Optics*, vol. 45, no. 8, pp. 1861–1865, 2006.

[378] R. K. Wang, "In vivo full range complex Fourier domain optical coherence tomography," *Applied Physics Letters*, vol. 90, no. 5, p. 054103, Jan. 2007.

[379] L. An and R. K. Wang, "Use of a scanner to modulate spatial interferograms for in vivo full-range Fourier-domain optical coherence tomography," *Optics Letters*, vol. 32, no. 23, p. 3423, Dec. 2007.

[380] K. Wang, Z. Ding, Y. Zeng, J. Meng, and M. Chen, "Sinusoidal B-M method based spectral domain optical coherence tomography for the elimination of complex-conjugate artifact," *Optics Express*, vol. 17, no. 19, p. 16820, Sep. 2009.

[381] B. Baumann, M. Pircher, E. Götzinger, and C. K. Hitzenberger, "Full range complex spectral domain optical coherence tomography without additional phase shifters," *Optics Express*, vol. 15, no. 20, pp. 13 375–13 387, 2007.

[382] B. J. Vakoc, S. H. Yun, G. J. Tearney, and B. E. Bouma, "Elimination of depth degeneracy in optical frequency-domain imaging through polarization-based optical demodulation," *Optics Letters*, vol. 31, no. 3, p. 362, Feb. 2006.

[383] X. Liu, M. Ke, X. Yao, J. Chua, L. Schmetterer, and B. Tan, "Stable complex conjugate artifact removal in OCT using circularly polarized light as reference," *Optics Letters*, vol. 45, no. 14, p. 3977, Jul. 2020.

[384] M. V. Sarunic, M. Choma, C. Yang, and J. A. Izatt, "Instantaneous complex conjugate resolved spectral domain and swept-source OCT using 3×3 fiber couplers," *Optics Express*, vol. 13, no. 3, pp. 957–967, Feb. 2005.

[385] M. V. Sarunic, B. E. Applegate, and J. A. Izatt, "Real-time quadrature projection complex conjugate resolved Fourier domain optical coherence tomography," *Optics Letters*, vol. 31, no. 16, p. 2426, Aug. 2006.

[386] M. Siddiqui, S. Tozburun, E. Z. Zhang, and B. J. Vakoc, "Compensation of spectral and RF errors in swept-source OCT for high extinction complex demodulation," *Optics Express*, vol. 23, no. 5, p. 5508, Mar. 2015.

[387] X. Attendu, D. J. Faber, G. Lamouche, T. G. Van Leeuwen, C. Boudoux, and M. Rivard, "Quadrature demultiplexing example matlab script," figshare (2022) [retrieved 25 March 2022], https://doi.org/10.6084/m9.figshare.19802836.

[388] ——, "Quadrature demultiplexing example matlab data," figshare (2022) [retrieved 25 March 2022], https://doi.org/10.6084/m9.figshare.19802815.v1.

[389] B. Vakoc, S.-H. Yun, J. De Boer, G. Tearney, and B. Bouma, "Phase-resolved optical frequency domain imaging," *Optics Express*, vol. 13, no. 14, pp. 5483–5493, 2005.

[390] X. Attendu, D. J. Faber, G. Lamouche, T. G. Van Leeuwen, C. Boudoux, and M. Rivard, "Animation of method validation," figshare (2022) [retrieved 25 March 2022], https://doi.org/10.6084/m9.figshare.19802848.

[391] M. Witteveen, D. J. Faber, H. J. C. M. Sterenborg, T. J. M. Ruers, T. G. van Leeuwen, and A. L. Post, "Opportunities and pitfalls in (sub)diffuse reflectance spectroscopy," *Frontiers in Photonics*, vol. 3, 2022.

APPENDIX A SCIENTIFIC CONTRIBUTIONS

Peer-reviewed scientific articles

- Robin Guay-Lord, **Xavier Attendu**, Kristen L. Lurie, Lucas Majeau, Nicolas Godbout, Audrey K. Bowden, Mathias Strupler, and Caroline Boudoux (2016). "Combined optical coherence tomography and hyperspectral imaging using a double-clad fiber coupler." Journal of Biomedical Optics vol. 21 no. 11.

- **Xavier Attendu**, Roosje M. Ruis, Caroline Boudoux, Ton G. Van Leeuwen, and Dirk J. Faber (2019). "Simple and robust calibration procedure for k-linearization and dispersion compensation in optical coherence tomography." Journal of Biomedical Optics vol. 24, no. 5.

- **Xavier Attendu**, Marie Hélène Bourget, Martin Poinsinet de Sivry-Houle, and Caroline Boudoux (2019). "Coregistered optical coherence tomography and frequency-encoded multispectral imaging for spectrally sparse color imaging." Journal of Biomedical Optics vol. 25, no. 3.

- **Xavier Attendu**, Dirk J. Faber, Guy Lamouche, Ton G. van Leeuwen, Caroline Boudoux, Maxime Rivard (2022). "Calibration procedure for enhanced mirror artifact removal in full-range optical coherence tomography using passive quadrature demultiplexing," submitted to Journal of Biomedical Optics.

- *[in preparation]* **Xavier Attendu**, Paul R. Bloemen, Niels H. Kind, Dirk J. Faber, Daniel M. de Bruin, Caroline Boudoux, Ton G. van Leeuwen. "All reflective tethered capsule endoscope for multimodal esophageal imaging."

- *[in preparation]* **Xavier Attendu**, Paul R. Bloemen, Niels H. Kind, Dirk J. Faber, Caroline Boudoux, Ton G. van Leeuwen. "Combined optical coherence tomography and ultra-broadband imaging single fiber reflectance spectroscopy."

- *[in preparation – not included in this thesis]* Aude Benk-Fortin, **Xavier Attendu**, Dirk J. Faber, Ton G. van Leeuwen, Caroline Boudoux. "Stabilized single fiber reflectance spectroscopy using wideband multimode circulators and bend loss compensation."

Oral presentations

- **Xavier Attendu**, Robin Guay-Lord et al. "Combined optical coherence tomography and hyperspectral imaging." IONS 2016.
- **Xavier Attendu**, Robin Guay-Lord, et al. "Combined optical coherence tomography and hyper-spectral imaging." Proc. SPIE 10057, Multimodal Biomedical Imaging XII, SPIE Photonics West 2017.
- **Xavier Attendu**, Camille Crunelle, et al. "Towards combined optical coherence tomography and hyper-spectral imaging for gastrointestinal endoscopy." Proc. SPIE 10487, Multimodal Biomedical Imaging XIII. SPIE Photonics West 2018.
- **Xavier Attendu**, Mathias Strupler et al. "Color OCT: Combined Optical Coherence Tomography and RGB Imaging Through a Double-Clad Fiber Coupler," 2018 IEEE Photonics Conference (IPC), 2018, pp. 1-2, doi: 10.1109/IPCon.2018.8527096.
- **Xavier Attendu**, Roosje Ruis, et al. "A simple and robust two-step calibration procedure for k-linearization and dispersion compensation in optical coherence tomography." European Optical Society Annual Meeting 2018.
- **Xavier Attendu**, Abel Swaan, et al. "Combined optical coherence tomography and single fiber reflectance spectroscopy in a rotating catheter probe." Proc. SPIE 11216, Multiscale imaging and spectroscopy I, SPIE Photonics West 2020.
- **Xavier Attendu**, Paul Bloemen, et al. "Towards combined optical coherence tomography and broadband single fiber reflectance spectroscopy." Proc. SPIE 11232, Multimodal Biomedical Imaging XV, SPIE Photonics West 2020.
- **Xavier Attendu**, Paul Bloemen, et al. "Combined optical coherence tomography and broadband single fiber reflectance spectroscopy." Proc. SPIE 11634, Multimodal Biomedical Imaging XVI, SPIE Photonics West 2021.

Poster presentations

- **Xavier Attendu**, Robin Guay-Lord et al. "Combined optical coherence tomography and hyper-spectral imaging" GRSTB symposium on biomedical nanotechnologies 2017.

- **Xavier Attendu**, Martin Poinsinet et al. "Towards combined optical coherence tomography and hyper-spectral imaging for gastrointestinal endoscopy." Gordon Research Seminar & Gordon Research Conference 2018.
- **Xavier Attendu**, Roosje Ruis et al. "Simple and robust two-step calibration procedure for k-linearization and dispersion compensation in optical coherence tomography." Proc. SPIE 10867-98. Optical Coherence Tomography and Coherence Domain Optical Methods in Biomedicine XXIII. Photonics West 2019.
- **Xavier Attendu**, Martin Poinsinet, et al. "Combined optical coherence tomography and multispectral reflectance imaging." SPIE Proc. 10871-35. Multimodal Biomedical Imaging XIV, SPIE Photonics West 2019.
- **Xavier Attendu**, Dirk J. Faber, et al. "Simple and robust calibration procedure for passive and instantaneous quadrature demultiplexing in full-range optical coherence tomography." Proc. SPIE PC11948, Optical Coherence Tomography and Coherence Domain Optical Methods in Biomedicine XXVI, Photonics West 2022.
- **Xavier Attendu**, Paul Bloemen, et al. "All reflective tethered capsule endoscope for highly multimodal and achromatic esophageal imaging." Gordon Research Seminar & Conference 2022.

Textbook

- Caroline Boudoux, **Xavier Attendu**, Jérémie Villeneuve (2017). "Introduction à la conception en ingénierie." Pollux 1st Edition. ISBN: 9781389109348.